Experimental and Computational Study of the Behaviour of Trabecular Bone-Cement Interfaces

Mr Sebastien Sikora

Submitted in accordance with the requirements for the degree of

Doctor of Philosophy

The University of Leeds

School of Mechanical Engineering

July, 2013

For my Dad, Edmund

Acknowledgements

Over the last four years, I have had the honour and privilege of being a member of a thriving and welcoming research community within the Institute of Medical and Biological Engineering (IMBE) here at the University of Leeds. There have been many people, past and present, near and far, to whom I am indebted, as without their contributions to my life and work I would not be typing this today.

In no particular order, I would like to extend my thanks to;

- Phil, Lee, Irvine, Keith, Jane, Amisha, Tarsam, and all the rest of the technical staff within the IMBE and the School of Mechanical Engineering, whose technical expertise and advice made my experimental work possible. Particular thanks go to Lee and Irvine, whose good-natured banter in the hallways always brightened my day, and to Jane, whose patience with my schoolboy errors was exemplary.
- Sami, Corrine, Beth, John, Kieran, Greg, Richard, Ju, Yuanyi, and all of my other PhD colleagues past and present, both for the entertaining office banter and their willingness to lend an ear whenever I needed a sounding board, or a hand whenever I needed help.
- Nagitha, Sarrawat, Alison, Daniel, Andre and all my other senior colleagues within the IMBE, whose willingness to make time to help me when asked and who have always made every effort to make me feel welcome. Special thanks go to Daniel and Andre, without whose help the development of the incremental compression and imaging device would have been far more arduous.
- My housemates past and present, Danielle, Theo, Aaron and Katie, who have endured more than their fair share of rants at the end of challenging days.
- My co-supervisor Professor Zhongmin Jin, without whose encouragement early on, I would almost certainly not be sitting here now.
- My girlfriend, Emma, who over the last two years has provided love, affection, encouragement and welcome distraction in abundance.

- Dr Nigel Askew, my favourite science teacher in high-school, and Dr Kevin Fancey, my undergraduate project supervisor. Both have been an inspiration to me, and I shall never forget the time they had for me.

I would like to give particular thanks to my Mum and Dad, Irène and Edmund. They have always believed in me, supported and encouraged me, and are in some way present in any endeavour in which I am successful.

Most importantly, I offer my thanks to my primary supervisor, Professor Ruth Wilcox. Without her seemingly inexhaustible patience and bonhomme, this work would never have been possible. Her academic and pastoral assistance has helped me through times of trial, both in and out of my University life, and words do a poor job of communicating my gratitude. I will be forever in her debt.

Lastly, I would like to thank the Engineering and Physical Sciences Research Council, who provided the funding that enabled my studies.

Abstract

Vertebroplasty is a treatment for vertebral compression fractures in which cement is injected into the vertebral body to relieve pain and stabilise the fracture site. Conflicting reports in the literature as to its efficacy indicate that further biomechanical evaluation of vertebroplasty is necessary to optimise the treatment variables (cement injection location, volume and composition) and to better understand which patients vertebroplasty will benefit. Finite element (FE) methods provide a means by which this can be undertaken under controlled conditions which are not possible experimentally, but existing vertebral FE models poorly reproduce the behaviour of cement-augmented vertebrae.

The aim of this study was to develop an improved, clinically practical FE method of representing the behaviour of the interface between the bone and cement augmentation. Appropriate homogenous finite element (hFE) micro-computed tomography (μCT) greyscale-modulus and yield strain relationships were derived for un-augmented ovine lumbar vertebral trabecular bone. Similar ovine vertebral bone specimens were then fractured and augmented with poly(methyl methacrylate) cement, and novel methods and equipment were developed to enable the imaging of these specimens using μCT as they were deformed to failure in axial compression. Proprietary software was then used to determine the specimen strain distribution from the images. hFE models that incorporated an explicitly modelled interfacial region were generated from the images and parametric studies undertaken to derive the most appropriate interfacial properties. Good agreement with the corresponding load-displacement and strain distribution data was achieved.

Finally, a preliminary study was conducted in which the new method of representing the interface was incorporated into existing hFE models of whole cement-augmented vertebrae. The predicted strain-distribution seen within the modified whole vertebral models more closely matched the behaviour of the earlier interfacial specimens, though this has yet to be validated experimentally against cement-augmented whole vertebrae.

Abbreviations

$BaSO_4$	–	Barium sulphate
BMD	–	Bone mineral density
CT	–	Computed tomography
DICOM	–	Digital communication and imaging in medicine
FE	–	Finite element
FEA	–	Finite element analysis
GS	–	Greyscale
GS->E	–	Greyscale-Young's modulus conversion factor
hFE	–	Homogenous finite element
MIL	–	Mean intercept length
PC	–	Personal computer
PMMA	–	Poly(methyl methacrylate)
pQCT	–	Peripheral quantitative computed tomography
QCT	–	Quantitative computed tomography
RMS	–	Root mean squared
TIFF	–	Tagged image file format
UK	–	United Kingdom
US	–	United States
VCF	–	Vertebral compression fracture
μCT	–	Micro computed tomography
μFE	–	Micro finite element
2D	–	Two dimensional
3D	–	Three dimensional

1. Introduction

The human spine is a complex composite structure that provides the main structural support connecting the upper and lower skeleton, while allowing mobility in flexion. The spine, typically considered to comprise four distinct sections (Figure 1-1), is composed of individual vertebrae separated by intervertebral discs, and interconnected with a system of muscles and ligaments that control flexion and provide stability.

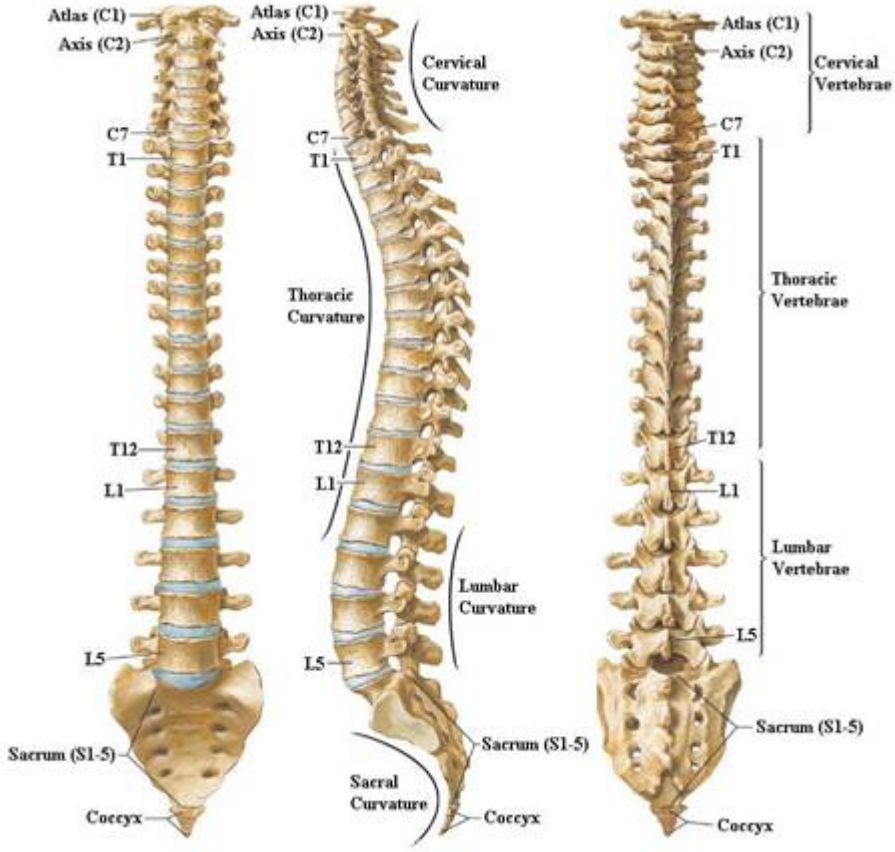

Figure 1-1. Anatomy of the human spine, showing the distinct sections (Netter 2006).

As a large and complex organ, the spine can be affected by a large number of pathologies. One of the most common, are vertebral compression fractures (VCFs) (Watts et al 2001), of which 40,000 were registered in the Netherlands alone in the year 2000 (Muijs et al 2011), and which were estimated to be responsible for 150,000 hospital admissions in the US annually (Evans et al 2002). VCFs generally involve a collapse of the anterior vertebral body wall (known as a wedge fracture due to the

resulting characteristic tilting of the vertebral endplates with respect to one another), typically leading to a loss of height and in some cases an increase in the curvature of the spine known as a kyphotic deformity (Evans et al 2002). In addition to substantially reduced mobility and quality of life (Ross et al 1991), VCFs impose an enormous cost on healthcare providers. It has been estimated that the total cost of treatment is as high as 1-2 % of the gross national product of several EU states, a total of over 100 Billion Euro per year (Van Tulder 2006), or over 2 Billion Euro per year in the UK alone (Maniadakis and Gray 2000). Though 85 % of cases can be successfully managed using conservative therapies including bed rest and pain medication (Muijs et al 2011), a significant number of sufferers remain in long term pain (Wilcox 2004).

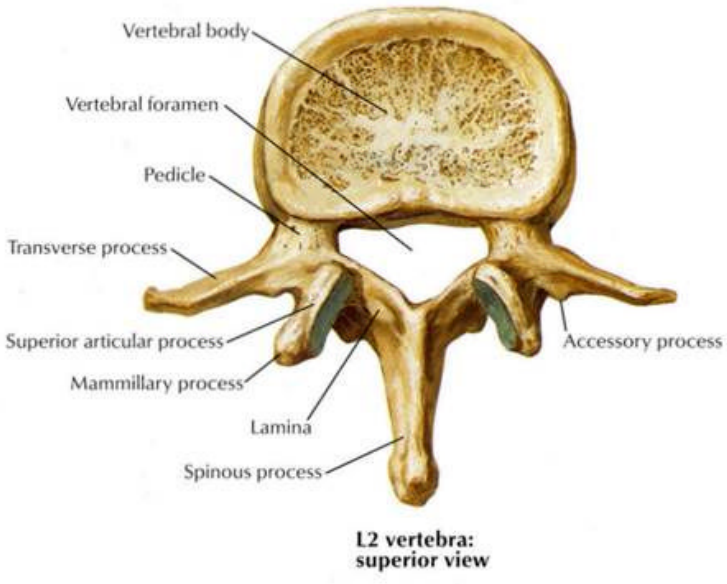

Figure 1-2. Anatomy of a human lumbar vertebra (Netter 2006).

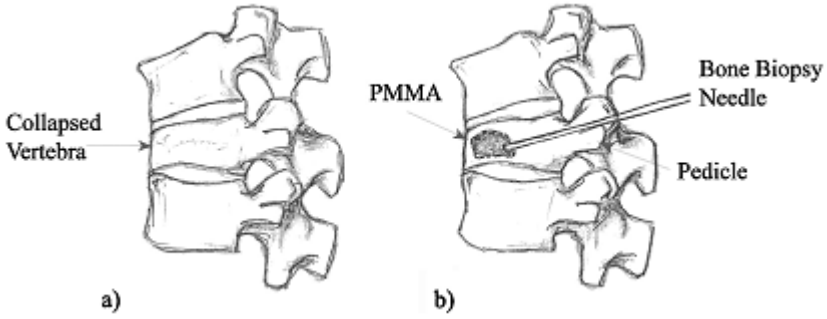

Figure 1-3. Typical location of cement inection during vertebroplasty (Sun and Liebschner 2004)

Since 1991 (Sun and Liebschner 2004), vertebroplasty, a therapy originally developed for the treatment of metastatic lesions (Wilcox 2004), has been used to stabilise fractured vertebrae to relieve pain (Muijs et al 2011). Acrylic bone cement, typically poly(methyl methacrylate) (PMMA) is injected into the fractured vertebra through one or both pedicles (Figures 1-2 and 1-3), preventing further fracture and relieving pain through prevention of micro-motions across the fracture site (Sun and Liebschner 2004).

While vertebroplasty has been reported to result in substantial immediate pain relief and restoration of motion in 70-80 % of cases (Wilcox 2004; Muijs 2011), the efficacy of the technique and likelihood of complication following treatment are not fully understood. Recent studies have indicated that vertebroplasty may be no more effective than a sham treatment (Buchbinder et al 2009), and may induce adjacent vertebral fracture (Trout and Kallmes 2006; Uppin et al 2003; Kim et al 2004), though a causal relationship has not been proven (Trout and Kallmes 2006). Furthermore, the detailed mechanics of vertebrae treated using vertebroplasty have yet to be fully characterised, with little consensus as to the ideal therapy configuration with respect to the quantity and material properties of the cement, and the ideal location for placement of the cement within the vertebral body (Wilcox 2004; Liebschner et al 2001; Sun and Liebschner 2004; Tschirhart et al 2005).

The development of an improved understanding of the effects of varying these parameters experimentally would involve a very large number of cadaveric vertebral specimens, due not only to the large number of possible parameter permutations, but also the significant variation in vertebral properties between donors (Sun and Liebschner 2004). In addition to the practical issues involved in conducting such large scale experimental testing, the use of such a large quantity of cadaveric tissue of limited availability would be ethically questionable.

Computational simulation using the finite element (FE) method has previously provided many useful predictions within the fields of biomechanics and orthopaedics (Prendergast 1997). The use of the FE method for the simulation and detailed study of cement-augmented vertebrae could be of great value (Sun and Liebschner 2004), and could offer numerous advantages over the use of physical experimental testing. These

advantages include, but are not limited to: the ability to explore the effects of multiple different cement augmentation configurations within a single vertebral specimen; the effects of a particular cement augmentation configuration within a large number of different vertebral specimens; the effect of varying the mechanical properties of the cement augmentation within a particular vertebral specimen; the fatigue failure properties of cement-augmented vertebrae over an accelerated timescale and the ability to closely control the range of bone material properties within the specimen set to explore the effects of treatment on particularly young, old or osteoporotic patients. However, the systematic use of the FE method to further develop and improve upon existing vertebroplasty techniques is contingent on the accuracy with which it can be shown to predict the mechanical and structural properties of cement-augmented vertebrae.

2. Literature review

A thorough review of the available literature concerning vertebral simulation using the FE method was conducted. Firstly, to assess the efficacy of existing attempts to use the FE method to predict the mechanical properties of cement-augmented vertebrae. Secondly, to identify the shortcomings of the existing attempts and thirdly, to explore existing efforts to better understand and mitigate these shortcomings.

2.1. Un-augmented whole vertebral body FE models

The first step towards developing finite element models of cement-augmented vertebrae suitable for the analyses and development of vertebroplasty is the development of accurate finite element models of whole, un-augmented vertebrae. These are important not only as a stepping stone towards building accurate finite element models of cement-augmented vertebrae but also as a clinical tool in their own right. For example, the models can be used in patient fracture risk assessment (Wang et al 2012), as a method of investigating variation in vertebral mechanical behaviour between different patient groups (Christiansen et al 2011) or simply to improve understanding of how aging and disease affect vertebral mechanics.

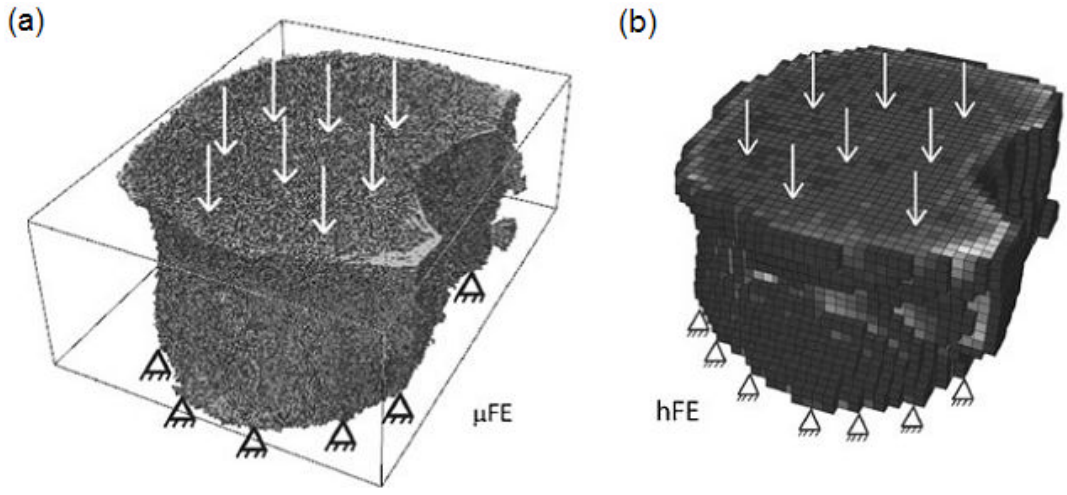

Figure 2-1. A comparison of (a) µFE and (b) hFE models of a vertebral specimen (Dall'ara et al 2012)

There are two main schools of vertebral body finite element analyses; (i) voxel-based continuum-level or ‘homogenised’ finite element (hFE) analyses and (ii) micro-finite element analysis (μFE).

2.1.2. μFE whole vertebral body modelling

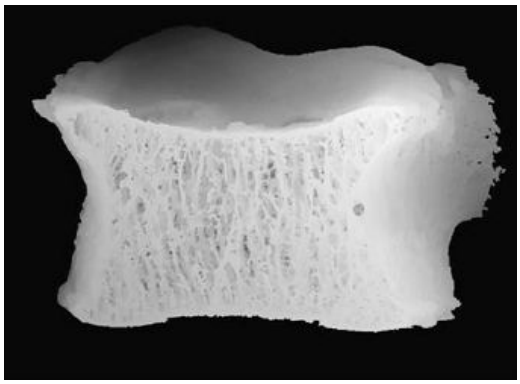

Figure 2-2 - A cross section of the detailed geometry of a μFE vertebral model (Homminga et al 2004)

In μFE analysis high-resolution μCT images of whole vertebral bodies are segmented and converted into a microstructurally representative mesh, comprising an accurate reproduction of the vertebral cortical shell and trabecular centrum (Figures 2-1(a) and 2-2). The elements therein are assigned a homogenous Young's modulus, typically based on nanoindentation studies of vertebral trabecular and cortical bone (Homminga et al 2004; Eswaran et al 2006; Eswaran, Gupta & Keaveny 2007).

These μFE models have been described as the modelling 'Gold standard' with regard to predicting vertebral stiffness and strength (Dall'ara et al 2012; Pahr & Zysset 2009). However, their clinical use is limited by the difficulty of obtaining the requisite high-resolution μCT images, due to the comparatively low-resolution of clinical CT equipment – of the order of 1 mm^3 as opposed to μCT resolutions of the order of 100 μm^3. In addition their solution times are prohibitive, even with the use of dedicated supercomputing facilities (Dall'ara et al 2012; Pahr & Zysset 2009; Homminga et al 2004; Eswaran, Gupta & Keaveney 2007).

While future improvement in the availability of high-speed computing facilities and further development of high-resolution clinical imaging tools may lead to vertebral μFE modelling becoming more practical from a clinical standpoint, at this time the majority of clinically relevant vertebral modelling is conducted using hFE models. For this reason, they will be the main focus of this review.

2.1.3. hFE whole vertebral body modelling

hFE vertebral modelling is a comparatively low resolution vertebral modelling approach developed predominantly over the last decade that represents the vertebral body as a continuum of solid elements, dispensing with detailed structural modelling of the internal trabecular architecture.

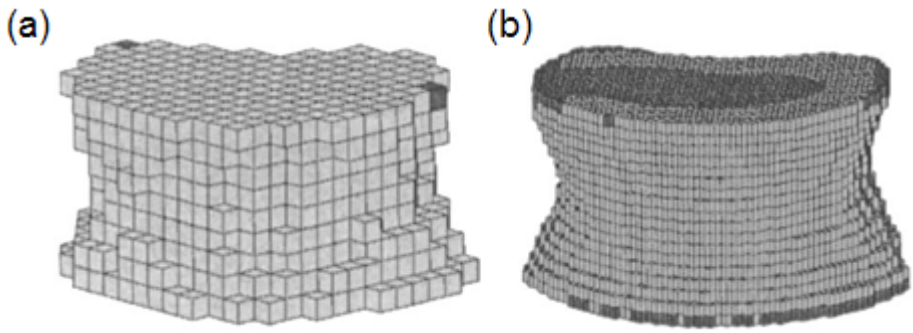

Figure 2-3 - A voxel-based vertebral hFE model meshed at a resolution (a) 3x3x3mm and (b) 1x1x1mm (Crawford, Rosenberg & Keaveny 2003)

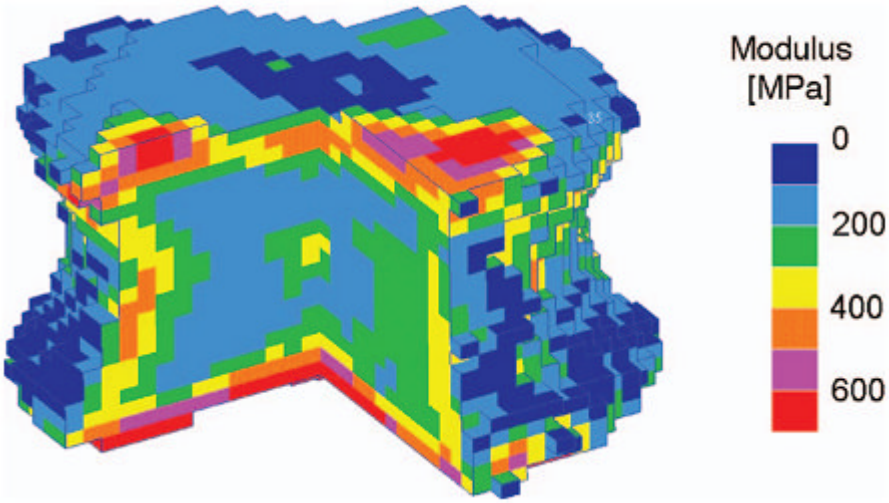

Figure 2-4 – A voxel-based vertebral hFE model cutaway, colour coded according to element Young's modulus (Buckley, Leang & Keaveny 2006)

2.1.3.1. Mesh generation

Specimen-specific vertebral hFE models are generated using one of two approaches; (i) voxel-based meshing, whereby clinical CT images or down-sampled μCT images of the specimen are directly converted into a finite element mesh on a one voxel to one element basis (Figures 2-3 and 2-4) and (ii) parametrically adjusted meshing, whereby an existing generic hexahedral vertebral mesh is adjusted by warping the geometry to match the specimen geometry (Sapin de Brosses et al 2012; Travert et al 2011; Wilcox 2007). Furthermore, voxel-based hFE meshes are often algorithmically smoothed to reduce the sharp changes in section caused by the low mesh resolution that can lead to unrealistic predicted stress (Figure 2-5)(Chevalier & Zysset 2012; Pahr & Zysset 2009).

Early efforts often did not explicitly model the vertebral cortical shell as it is difficult to resolve at typical clinical CT scan resolution (Crawford, Cann & Keaveny 2003) and it had been suggested in several studies that the cortical shell contributed little to the mechanical behaviour of vertebrae (Liebschner et al 2003; McBroom et al 1985). However, more recent studies have suggested that the contribution of the cortical shell to vertebral body mechanics is greater than previously proposed and explicit modelling of the cortical shell is important to maximise the predictive accuracy of whole body vertebral models (Pahr & Zysset 2009; Chevalier, Pahr & Zysset 2009; Sapin de Brosses et al 2012; Eswaran et al 2006; Andresen, Werner & Schober 1998).

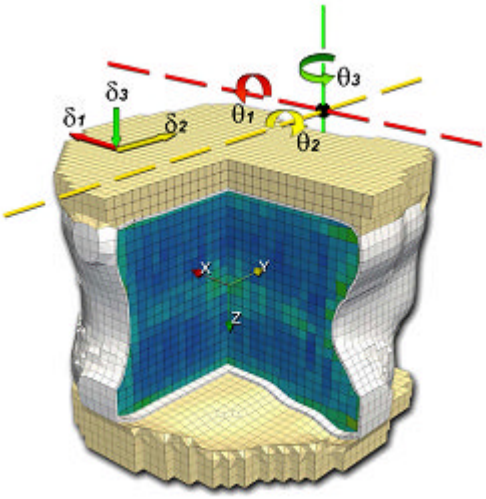

Figure 2-5 - Smoothed voxel-based vertebral hFE model. This model features explicitly modelled cortical bone (white elements) (Chevalier & Zysset 2012)

2.1.3.2. Material properties

The hFE modelling approach relies on the observation that the apparent mechanical behaviour of a volume of trabecular bone spanning more than five trabecular cells across its smallest dimension can be represented by considering the volume as a homogenous solid with a Young's modulus equal to some function of its average mineral density (Harrigan et al 1988). This is known as the 'continuum assumption'.

In this way, the vertebral hFE mesh is assigned Young's modulus values on an element-by-element basis according to the average greyscale value of the underlying CT voxel(s). These greyscale values are usually converted first into bone mineral density (BMD) values through the use of a calibrated scan phantom such as Dipotassium Phosphate (K_2HPO_4) to preserve CT-scanner independency (Crawford, Cann & Keaveney 2003) before being converted into equivalent Young's modulus values according to published BMD to Young's modulus relationships for human vertebral trabecular bone (Kopperdahl, Morgan & Keaveny 2002). Alternatively the CT greyscale values can be converted directly to element Young's moduli if the study derives a CT density-Young's modulus relationship for use with a particular CT scanner under fixed settings (Wijayathunga et al 2008), avoiding the need to use a calibrated scan phantom. The elements are typically assigned orthotropic material properties by calculating the

Young's moduli as described in the superior-inferior direction and then deriving the remaining direct and shear moduli from this value according to published anisotropy relationships for human vertebral trabecular bone (Crawford, Cann & Keaveney 2003; Buckley, Leang & Keaveny 2006).

Most recently a small number of studies have explored the use of density-fabric dependent material models. Proponents of this approach argue that hFE trabecular element material models that depend only on the underlying μCT density without considering the local structural morphology – or 'fabric' – do not adequately describe the apparent trabecular mechanical behaviour (Zysset 2003). Instead a method has been developed that relates the hFE trabecular element material properties to both the underlying μCT density values and a quantitative measure of the local fabric according to previously published relationships (Pahr & Zysset 2009; Chevallier, Pahr & Zysset 2009; Dall'ara et al 2010; Dall'ara et al 2012), typically the mean intercept length, a measure of architectural anisotropy calculated from the mean distance between bone-marrow interfaces along linear traverses over a range of orientations (Whitehouse WJ 1974).

In most of these studies the authors have implemented plastic damage behaviour through the use of a linear-elastic perfectly-plastic material model, representing trabecular bone failure by reducing to near-zero the elastic modulus of any element exceeding some pre-determined stress or strain limit (Buckley, Loo & Motherway 2007; Jones & Wilcox 2007; Wilcox 2007; Mirzaei et al 2009). More recently, several studies have tried to improve model strength predictions post-yield by instead using a linearly-elastic linearly-plastic material model based upon previously published studies of the post-yield behaviour of trabecular bone conducted by Garcia et al (2009)(Chevallier, Pahr & Zysset 2009; Dall'ara et al 2010; Zeinali, Hashemi & Akhlaghpoor 2010; Dall'ara et al 2012, Chevalier & Zysset 2012).

2.1.3.3. Mesh resolution

Published studies utilising vertebral hFE models typically make use of an average mesh resolution between 1-2mm^3 as shown from the examples presented in Table 2-1. While the majority of the studies examined do not test for mesh convergence, a number of published studies that did investigate the models' sensitivity to changes in mesh resolution have suggested that there was little improvement in predictive accuracy to be gained at higher resolutions (Zeinali, Hashemi & Akhlaghpoor 2010; Crawford, Rosenberg & Keaveny 2003; Vossou & Provatidis 2008; Jones & Wilcox 2007). Furthermore, the desire to generate clinically useful models imposes an upper limit on mesh resolution due the limited resolution of clinical CT equipment (Chevallier, Pahr & Zysset 2009; Mittra, Rubin & Qin 2005).

Study	Mesh resolution
Wang et al (2012)	1 mm^3
Chevalier & Zysset (2012)	1.312 mm^3
Dall'ara et al (2012)	1.3 mm^3
Zeinali, Hashemi & Akhlaghpoor (2010)	1 mm^3
Dall'ara et al (2010)	1.312 mm^3
Chevallier, Pahr & Zysset (2009)	1.312 mm^3
Mirzaei et al (2009)	1 mm^3
Wilcox (2007)	1-2 mm^3
Jones & Wilcox (2007)	1-4 mm^3
Buckley, Loo & Motherway (2007)	1 mm^3
Crawford, Rosenberg & Keaveny (2003)	1 mm^3

Table 2-1. Voxel-based vertebral hFE mesh resolutions by study

2.1.3.4. Boundary Conditions

The most common boundary conditions applied to the vertebral hFE models in the studies examined here replicated a simple axial compressive test. Nodes across the

entire inferior surface of the model were constrained both rotationally around all three principal axes and in translation in the lengthwise z-direction, while a displacement expected to instigate vertebral yield according to experimental testing applied either to all nodes across the superior model surface (Zeinali, Hashemi & Akhlaghpoor 2010; Mirzaei et al 2009; Crawford, Cann & Keaveny 2003) or to all nodes across the superior surface of a layer of elements assigned material properties of PMMA cement tied to the superior vertebral surface such as to mimic their experimental test conditions (Wang et al 2012; Chevalier & Zysset 2012; Chevallier, Pahr & Zysset 2009; Buckley, Loo & Motherway 2007).

In some cases, the experimental vertebral compressive testing was conducted using a ball-and-socket cross head such as to precipitate a vertebral wedge fracture, which as previously discussed often occurs in-vivo. In these cases the displacements were applied to the corresponding vertebral hFE models via a rigid surface, tied to the superior vertebral or PMMA surface but not constrained rotationally such as to allow toggling of the superior vertebral end plate (Dall'ara et al 2012; Dall'ara et al 2010; Jones & Wilcox 2007; Wilcox 2007). Loading hFE models in this way necessitates that great care be taken to ensure that the FE model loads (or displacements) are applied upon precisely the same point as they were upon the corresponding experimental specimens in each case. This is because previous studies have suggested that such models can be greatly sensitive to the position of the applied loads, with a small variation in the position of the applied displacement leading to a variation in predicted model stiffness as high as 40 % (Travert et al 2011; Wijayathunga et al 2008). This finding may have been in part due to the use of a displacement applied at a single point, as an earlier study suggested that varying between uniform displacement, uniform force, and a variety of strongly non-uniform force distributions cause variations in prediction that are not statistically significant (approx 14.2 % +/- 7 % S.D.) (Buckley, Leang & Keaveny 2006).

2.1.3.5. Performance and validation

The studies examined here that provide quantitative validation of their hFE model predictions are listed in Table 2-2. The hFE model predictions were compared like-for-like with corresponding experimental compressive test results, with the exception of those investigated by Pahr & Zysset (2009) which were compared with corresponding μFE model predictions.

				r^2 fitting slope	
Study	**Type**	**Stiffness**	**Strength**	**Stiffness**	**Strength**
Zeinali, Hashemi & Akhlaghpoor (2010)	r^2	N/A	**0.94**	N/A	1.14
Mirzaei et al (2009)	r^2	N/A	**0.84**	N/A	1.3
Sapin-de-brosses et al (2012)	r^2	N/A	**0.79**	N/A	0.88
Pahr & Zysset (2009)	r^2	**0.97**	N/A	1	N/A
Crawford, Cann & Keaveny (2003)	r^2	**0.82**	**0.86**	0.326	1.64
Crawford, Rosenberg & Keaveny (2003)	r^2	**0.71**	N/A	N/A	N/A
Chevalier, Pahr & Zysset (2009)	r^2	**0.64**	**0.77**	1	0.96
Dall'ara et al (2010)	r^2	**0.49**	**0.79**	0.59	0.86
Buckley, Loo & Motherway (2007)	r^2	**0.27**	**0.8**	N/A	1.02
Jones & Wilcox (2007)	CC	**0.98**	**0.88**	N/A	N/A
Wilcox (2007)	CC	**0.88**	**0.75**	N/A	N/A
Wijayathunga et al (2008)	rms error	**12.90%**	**14.40%**	N/A	N/A

Table 2-2 – Performance of un-augmented vertebral hFE models detailed quantitatively in the literature

The hFE model performance is usually expressed as the r^2 correlation coefficient between the hFE model and experimental or μFE model results and the selected arbitrary linear regression through them – the gradients of which are detailed in the rightmost two columns in Table 2-2. Jones & Wilcox (2007) and Wilcox (2007) instead opt to express their hFE model performance in terms of the concordance coefficient - a measure of the closeness of fit between their hFE model and experimental results and a 1:1 relationship between them (Lin 1989) - while Wijayathunga et al (2008) quote the root-mean-squared percentage error between their hFE model predictions and corresponding experimental results.

Unfortunately the wide range of linear regression gradients chosen to calculate the correlation coefficients makes it very difficult to draw anything but the coarsest performance comparisons between the different studies. An r^2 value close to 1 is only

indicative of close agreement between the hFE model predictions and the corresponding experimental or μFE model results if the gradient of the linear regression is close to 1. In studies such as these where the ideal relationship between the predicted and measured values is 1:1 the concordance coefficient is a far more useful measure of agreement, maximising comparability by dispensing with the need to select an arbitrary linear regression.

With this in mind, the study results broadly suggest that there is no obvious benefit with regard to predicting vertebral stiffness and strength in the use of complex orthotropic non-linear material models when compared to the simpler μCT density-dependent isotropic linear-elastic material models used by Wilcox (2007), Jones & Wilcox (2007) and Wijayathunga et al (2008). Though Pahr & Zysset (2009) achieved good agreement between their hFE model and μFE model predictions using a complex density-fabric dependent trabecular material model, their method is of doubtful clinical utility due to the high μCT resolution required to quantify the local trabecular morphology throughout the vertebrae. Furthermore, efforts to use the same density-fabric dependent trabecular material models with average values for vertebral trabecular fabric resulted in significantly poorer agreement between their hFE model predictions and corresponding experimental results (Chevalier, Pahr & Zysset 2009; Dall'ara et al 2010).

2.1.3.6. Discussion

To be able to judge the performance of the hFE models studied here it is first important to define the necessary level of accuracy. While the desired level of accuracy is in a sense always 100 %, from a pragmatic point of view a particular modelling approach could be considered to display reasonable performance if matches or improves upon existing methods of determining the output of interest. Commonly used BMD-based clinical predictors of vertebral stiffness and strength such as DXA or QCT-based approaches are capable of achieving a correlation between predicted and measured output of r^2=0.31-0.77 and 0.38-0.84 for stiffness and strength respectively (Chevalier, Pahr & Zysset 2009). In light of this, contemporary μCT image-based hFE vertebral modelling approaches are considered to demonstrate reasonable predictive accuracy,

and are well validated through numerous comparisons with experimentally derived results, in both simple axial compression and under loading boundary conditions that allow rotation of the vertebral endplates with respect to one another in the manner of a wedge fracture.

The remainder of the studies available in the literature are predominantly investigative in nature, aiming to use a previously developed vertebral hFE modelling approach to qualitatively explore vertebral mechanical behaviour, for example to determine the relationship between bulk vertebral body stiffness in the superior-inferior direction and medial-lateral, anterior-posterior and torsional stiffness (Chevalier & Zysset 2012), to explore the sensitivity of vertebral strength to variation in the direction and/or distribution of the applied loads or displacements (Matsumoto et al 2009; Travert et al 2011; Buckley, Leang & Keaveny 2006), or to quantify vertebral strength in-vivo by utilising more physiologically representative boundary conditions (Kazuhiro et al 2008). Some of the studies also include soft tissues such as the intervertebral disc (Whyne, Hu & Lotz 2001) and inter-vertebral muscles and ligaments (Boccaccio et al 2008).

When the studies detail any validation that the modelling approach has undergone, it has usually been conducted under non-physiologically representative simple axial compression boundary conditions. This is likely due to the increased difficulty of obtaining experimental compressive test data under more complex constraints possessing a greater number of degrees of freedom, particularly when soft tissues or multi-vertebral assemblies are to be included. Though the qualitative results and trends displayed by such studies may be of great interest and help inform the progression and development of vertebral hFE models, without explicit validation by quantitative comparison with experimental test results obtained under these alternative boundary conditions such models cannot be confidently considered to be exhibiting predictive behaviour. For this reason, great care should be taken if and when they are used to inform clinical judgements.

2.2. Cement-augmented whole vertebral body FE models

In more recent years, a number of groups have made efforts to develop vertebral hFE models that aim to reproduce the mechanical effects upon vertebrae of cement augmentation, generally by modifying or building upon methods developed for the purpose of modelling un-augmented vertebrae. There are two main modelling approaches used, those that model a single cement-augmented vertebral body (Figure 2-6)(Kinzl et al 2012; Chae et al 2012; Mirzaei et al 2009; Chevalier et al 2008; Wijayathunga et al 2008; Lewis & Xu 2007; Teo, Chang & Teoh 2007; Sun & Liebschner 2002; Liebschner, Rosenberg & Keaveney 2001) and those that model two or more connected vertebral bodies, one of which contains cement augmentation (Figure 2-7)(Zhang et al 2010; Rohlmann et al 2010; Villaraga et al 2005; Baroud et al 2003, Polikeit, Nolte & Ferguson 2003).

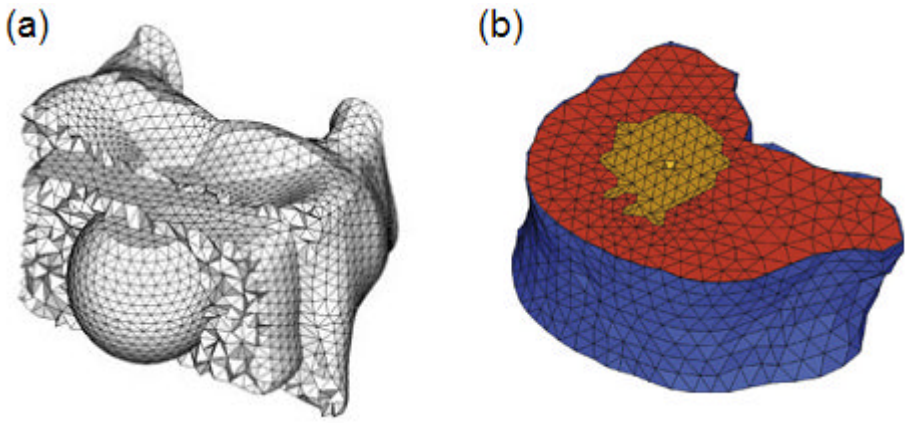

Figure 2-6 – Single vertebrae cement-augmented hFE models created by (a) Chae et al (2012) and (b) Kinzl et al (2012)

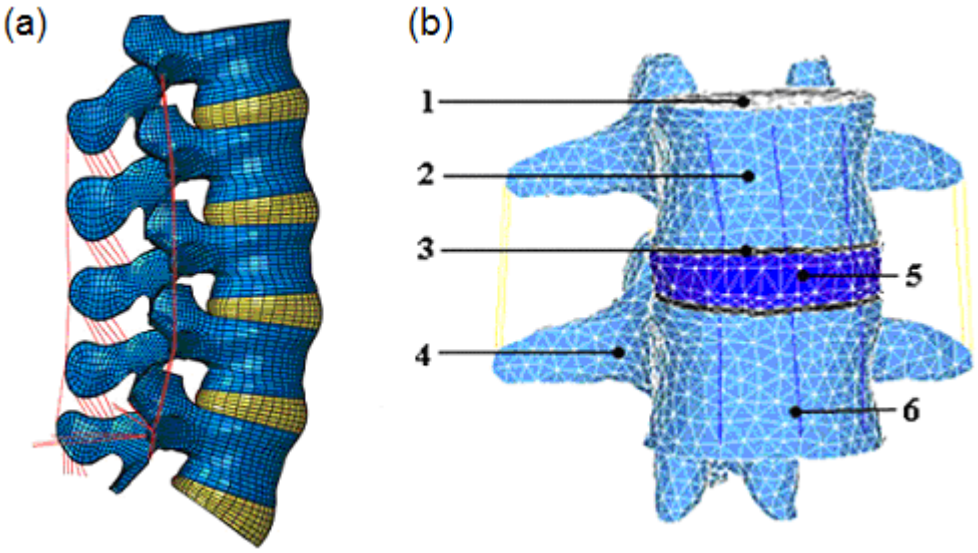

Figure 2-7 - Multi-vertebral body cement-augmented hFE models created by (a) Rohlmann et al (2010) and (b) Zhang et al (2010)

2.2.1. Geometry generation – Vertebral mesh

In the cases of both the single-vertebral body and multi-vertebrae models the vertebral geometry was generally generated using the common CT image-based method previously described whereby image processing tools are used to convert downsampled CT images directly into a hFE mesh. An exception was one of the multi-vertebrae studies, in which a commercially available spinal surface model was used following verification by comparison with dimensions of anatomic specimens previously reported in the literature (Villaraga et al 2005).

2.2.2. Geometry generation – Cement augmentation

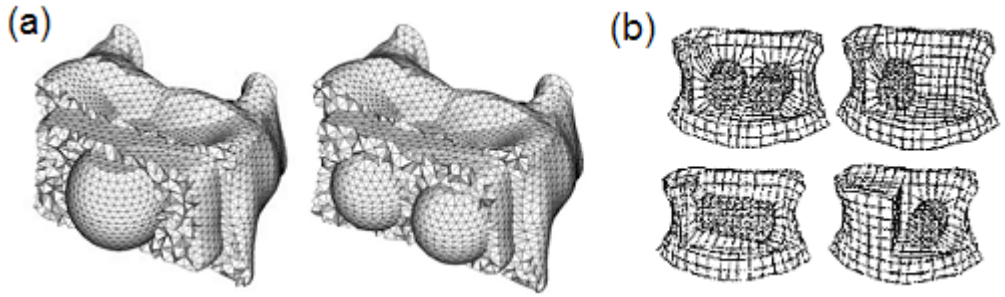

Figure 2-8 – Various generic cement augmentation geometries used by (a) Chae et al (2012) and (b) Sun & Liebschner (2002)

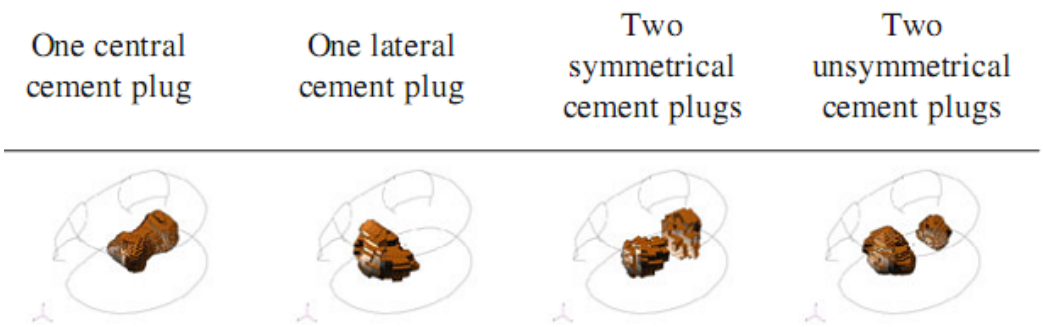

Figure 2-9 - Various 'clinically appropriate' cement augmentation geometries used by Rohlmann et al (2010)

While the manner in which the exterior vertebral geometry was generated was consistent across the available hFE studies of cement-augmented vertebrae, the manner in which the geometry of the cement augmentation was generated varied depending on the nature and aims of the studies.

The majority of the studies – both single-vertebra and multi-vertebrae – were primarily investigative studies that aimed to comparatively examine the effect on vertebral mechanics of the inclusion of one or more typical vertebral augmentation morphologies. As the vertebra(e) from which the model geometries were generated were un-augmented it was necessary to manually include a region of cement augmentation within the models' trabecular centrum.

In most cases arbitrary augmentation geometries were used, variously straight or convex sided cylinders (Figure 2-8b)(Lewis & Xu 2007; Villaraga et al 2005; Polikeit, Nolte & Ferguson 2003; Sun & Liebschner 2002; Liebschner, Rosenberg & Keaveney 2001), oblate spheroids (Figure 2-8a)(Chae et al 2012), a central cube with heavily rounded corners (Zhang et al 2010) or a variety of clinically appropriate cement distributions created by reference to a large number of clinical radiographs of augmented vertebrae (Figure 2-9)(Rohlmann et al 2010). In each case the chosen augmentation geometries were expected to provide a reasonable representation of either unipedicular or bipedicular vertebral cement augmentation in-vivo based on examination of clinical radiographs of treated vertebrae.

One interesting exception to this method was detailed in the study by Teo, Wang & Teoh (2007) in which computational fluid dynamics modelling was used to determine the cement augmentation geometry. Previously published density-fluid permeability relationships for trabecular bone were utilised in a computational fluid dynamics model generated from downsampled vertebral μCT images to predict the geometry of both bipedicular and unipedicular injection of each of two clinically relevant volumes of cement (Teo, Wang & Teoh 2007).

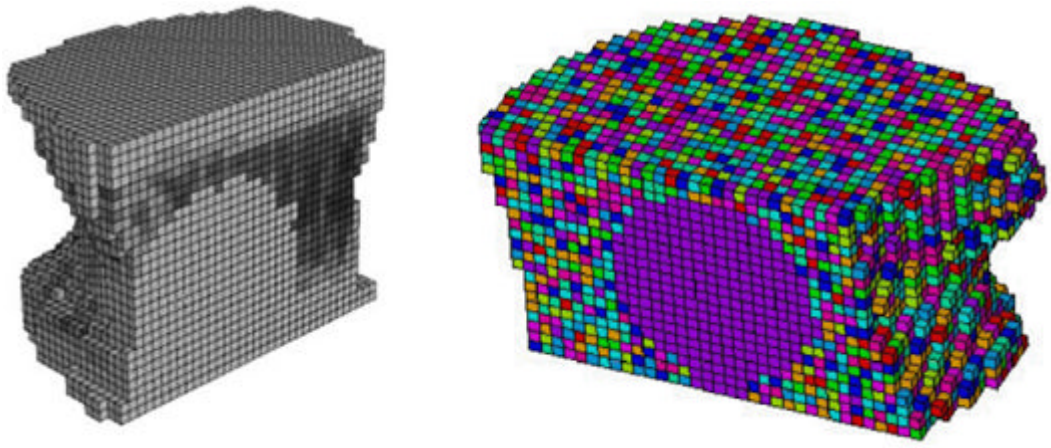

Figure 2-10 - Specimen-specific augmented vertebral hFE models featuring image-based cement augmentation geometries, Chevallier et al (2008) (left) and Mirzaei et al (2009) (right)

The remaining four published studies of hFE models of cement-augmented vertebrae could be considered exercises in model development that aimed to improve the performance of a particular cement-augmented vertebral hFE modelling approach. All

four studies used similar specimen-specific image-based mesh generation methods, and examined cement-augmented experimental vertebral specimens. As such the geometry of the cement augmentation was generated in the same manner as the vertebral geometry through processing of the downsampled specimen μCT images (Figure 2-10)(Kinzl et al 2012; Mirzaei et al 2009; Chevallier et al 2008; Wijayathunga et al 2008).

2.2.3. Bone material properties

Across all of the hFE studies of cement-augmented vertebrae the manner in which the material properties assigned to the trabecular bone were derived broadly depended on the nature of the models – single or multi-vertebra(e).

In all of the studies of cement-augmented single-vertebra hFE models the trabecular bone was assigned specimen-specific μCT greyscale-derived material properties in a similar manner to the un-augmented hFE models discussed previously. Similarly to the un-augmented vertebral hFE studies there has been an apparent trend over time towards increasingly complex trabecular material models, originally using simple linear-elastic perfectly-plastic definitions (Liebschner, Rosenberg & Keaveney 2001; Sun & Liebschner 2002; Teo, Wang & Teoh 2007; Lewis & Xu 2007; Wijayathunga et al 2008), progressing to linear-elastic linearly-plastic definitions (Mirzaei et al 2009), and most recently to a complex linear-elastic non-linearly-plastic model defined not only as a function of μCT greyscale but also accounting for local variations in the trabecular fabric (previously detailed in Section 2.1.3.) (Kinzl et al 2012), though a similar material model had been used previously by Chevallier et al (2008) & Pahr & Zysset (2009).

The multi-vertebral hFE models were assigned homogenous trabecular bone material properties taken from the literature, using isotropic linear-elastic material models with the exception of Rohlman et al (2010) who used a transversely-isotropic linear-elastic material model. The universal choice of homogenous trabecular bone material properties is surprising considering that with the exception of Villaraga et al (2005) the multi-vertebral hFE model geometries were generated from CT images that would have provided a means to derive specimen-specific greyscale-based trabecular material properties on an element-by-element basis in the same manner as in the single-vertebra studies discussed here.

Specimen-specific trabecular bone material properties have been demonstrated to result in significantly improved accuracy of vertebral hFE model predictions, Wilcox (2007)

reported that when compared to specimen-specific μCT greyscale-derived material properties, assigning homogenous trabecular bone material properties derived from the mean bone volume fraction across the specimens studied led to significantly reduced concordance between the experimentally determined and hFE predicted vertebral stiffness and strength (0.881 reduced to 0.724 and 0.752 reduced to 0.429 for stiffness and strength respectively). Furthermore, as previous studies have demonstrated that the apparent Young's modulus of trabecular bone can vary greatly even between specimens taken from a particular anatomic site (Ulricht et al 1999), it is suggested that using homogenous trabecular bone material properties taken from the literature as opposed to the mean across the study specimens is likely to lead to an even greater reduction in concordance between experimentally determined and finite element model predicted stiffness and strength than observed by Wilcox (2007).

The introduction of many additional sources of possible error in multi-vertebral hFE models due to their greater constitutional complexity, eg: soft and connective tissue material properties and morphology, may work to reduce the relative significance of the error contribution of homogenous trabecular bone material properties, and may explain their consistent use in these models.

2.2.4. Cement material properties

In all but four of the studies examined here the cement augmentation was assigned previously published homogenous isotropic linear-elastic material properties for pure PMMA bone cement, with a Young's modulus ranging from 2000-3000 MPa. Sensitivity studies were carried out as part of four of these studies in which the effect of varying the homogenous Young's modulus assigned to the cement augmentation on the model predictions was investigated. It was suggested that the influence of the cement Young's modulus on the mechanical behaviour of the models in both single-vertebrae and multi-vertebral models was negligible, with a 20 % reduction in cement Young's modulus leading to a < 2 % reduction in vertebral stiffness and strength (Wijayathunga et al 2008), while varying the cement Young's modulus from 300-3500 MPa in 100 MPa steps (Rohlmann et al 2010) or increasing it by 100 % from 2000 MPa to 4000

MPa (Villaraga et al 2005) lead to negligible variation in the maximum stress within the models. This seems reasonable in light of the fact that PMMA bone cement has a Young's modulus around 30 times that of the apparent modulus of trabecular bone (Zhang et al 2010), suggesting that unless the trabecular centrum is completely saturated with cement the majority of the overall deformation will occur in the bone rather than the cement augmentation.

Of the remaining four studies, two assigned the cement augmentation homogenous material properties for PMMA bone cement saturated trabecular bone derived in previous studies (Chae et al 2012; Baroud et al 2003), while two recent studies defined the material properties of the cement-augmented region in comparatively complex manners. Based on their previous work, Chevalier et al (2008) defined the material properties of the cement-augmented region according to a rule of mixtures that combined previously published bone volume fraction-dependent material property definitions for trabecular bone (anisotropic) and PMMA cement (isotropic) (Chevalier et al 2008).

In contrast to this, based on the results of a previous study Kinzl et al (2012) suggested that the elastic and yield properties of a PMMA-trabecular bone composite depended only on the porosity of the PMMA cement (Pore volume/(Total volume – Bone volume)) and not on the bone-volume fraction (Kinzl et al 2011). Instead the elements in the cement-augmented region were assigned an isotropic elastic-plastic material model that Guo et al (2008) suggested would account for the pressure-sensitivity of porous materials and assigned Young's modulus, yield stress and plastic stress hardening on an element-by-element basis according to previously derived PMMA porosity-Young's modulus and -yield stress relationships (Kinzl et al 2012). Problematically, there were sufficient artefacts in the μCT images from which the models were segmented to make it impossible to determine the porosity of the augmented region. Due to this, Kinzl et al (2012) instead assigned the whole cement-augmented region average porosity values for PMMA-trabecular bone composite determined as part of their previous study.

While these attempts to define more complex porosity or bone fraction dependent material property models for the cement augmentation are interesting, unfortunately the authors do not provide any information as to the resulting average cement elastic modulus, or a measure of it's variation throughout the cement-augmented zone. Given the trends seen in the aforementioned sensitivity studies that suggest that even significant variation of a homogenous cement elastic modulus leads to a negligible change in apparent vertebral behaviour, it is likely that unless these alternative material models produce drastic local variation in the cement properties that they will have negligible effect on the hFE model predictions when compared with the use of homogenous isotropic cement material properties. Furthermore, the practical problems experienced by Kinzl et al (2012) in determining the local cement porosity that lead to their use of average porosity values within the material model resulted in homogenous (though anisotropic) material properties throughout the cement-augmented zone. Thus, their method entails all of the additional complexity and computational expense of the use of an inhomogeneous material model for the cement, with none of the postulated advantages.

2.2.5. Interfacial configuration

All but two of the hFE studies of augmented vertebrae in the literature used a tied contact between the elements representing the trabecular centrum and those representing the internal cement augmentation. Villaraga et al (2005) defined a 1 mm deep region of the mesh at the boundary between the trabecular centrum and cement augmentation which joined to the adjacent bone and cement via a tied contact (Figure 2-11). The material properties of this interfacial region were calculated according to the rule of mixtures, assuming a 50/50 ratio of bone and cement.

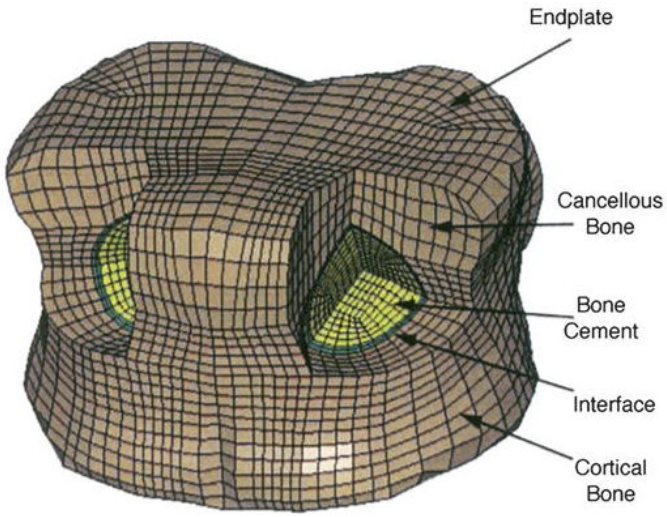

Figure 2-11 - Location of interfacial region in hFE models studied by Villaraga et al (2005)

In their more recent study, Kinzl et al (2012) defined a 2 mm deep region of the mesh at the boundary between the trabecular centrum and cement augmentation, defining a tied contact between the three regions in the same manner as Villaraga et al (2005). Their previous work had suggested that the mechanical properties of a trabecular bone-cement composite were dependent not on the bone volume-fraction but on the cement porosity (Kinzl et al 2011). According to this, in their models the mechanical properties of the interfacial region were calculated in the same manner as in the main cement-augmented region, but assuming a higher average porosity to account for the tapering-off in cement interdigitation at the interface.

2.2.6. Performance and validation

Of the hFE studies of cement-augmented vertebrae available in the literature, only three draw specimen-specific comparisons between their hFE model predictions and corresponding experimental test results, and of these only two make quantitative comparisons with respect to apparent vertebral stiffness and strength (Table 2-3).

	RMS % error between hFE & Experimental results		
Study	**Stiffness**	**Strength**	**Contact pressure**
Kinzl et al (2012)	12.5	15.4	19.4
Wijayathunga et al (2008)	65	68	N/A

Table 2-3 - Performance of augmented vertebral hFE models detailed quantitatively in the literature

Wijayathunga et al (2008) found that modeling cement-augmented vertebrae using the same approach as they had used to model un-augmented vertebrae lead to a marked reduction in the accuracy with which their models could predict apparent vertebral properties, from 12.9 to 65 % and 14.4 to 68 % average RMS error for stiffness and strength respectively. In their more recent study, Kinzl et al (2012) reported significantly better agreement between their hFE model predictions and corresponding experimentally derived results, describing average percentage RMS error of 12.5 % and 15.4 % for stiffness and strength respectively. There were a number of significant differences between the modeling approaches used by the two groups; the use by Kinzl et al (2012) of more complex material models for the cement augmentation and trabecular bone (previously described in Section 2.1.3.) and the definition of an interfacial region of increased compliance between the trabecular centrum and the cement-augmented zone. However, de-coupling the contributions of each of these differences in modeling approach to the apparent increase in predictive accuracy is not easy.

As discussed in Section 2.1.3, when modeling un-augmented vertebral bodies both Pahr & Zysset (2009) – using the same modeling approach as used here by Kinzl et al (2012), and Wilcox (2007) & Jones & Wilcox (2008) – using the same approach as used here by Wijayathunga et al (2008) reported good agreement between the hFE model predictions

for apparent vertebral stiffness and strength and their corresponding experimentally derived results. This suggests that it is not the use of the more complex density-fabric-based material model for trabecular bone that leads to the reduced error reported by Kinzl et al (2012).

Furthermore, in the same manner as Pahr & Zysset (2009), Kinzl et al (2012) defined a complex local porosity-based material model for the cement augmentation, in both cases μCT image artefacts precluded the calculation of local porosity values throughout the augmented zone. Instead, a homogenous average porosity value was applied throughout the augmented zone. Kinzl et al (2012) do not specify the resulting average effective elastic modulus, but it is presumed to be lower than that of pure cement. As Wijayathunga et al (2008) demonstrate that a significant reduction in the homogenous elastic modulus assigned to the augmented zone within their models leads to a negligible change in apparent vertebral properties it is suggested that the reduction in error reported by Kinzl et al (2012) is due primarily to the remaining significant difference between their modeling approach and that used by Wijayathunga et al (2008): the definition of an interfacial region of increased compliance between the trabecular centrum and the cement-augmented zone.

While Villaraga et al (2005) also included an interfacial region of increased compliance in their hFE models of cement-augmented vertebral bodies, the lack of specimen-specific comparisons with corresponding experimental results due to their use of generic vertebral geometries and homogenous material properties taken from the literature makes drawing comparisons between the models with regard to their predictive accuracy impossible.

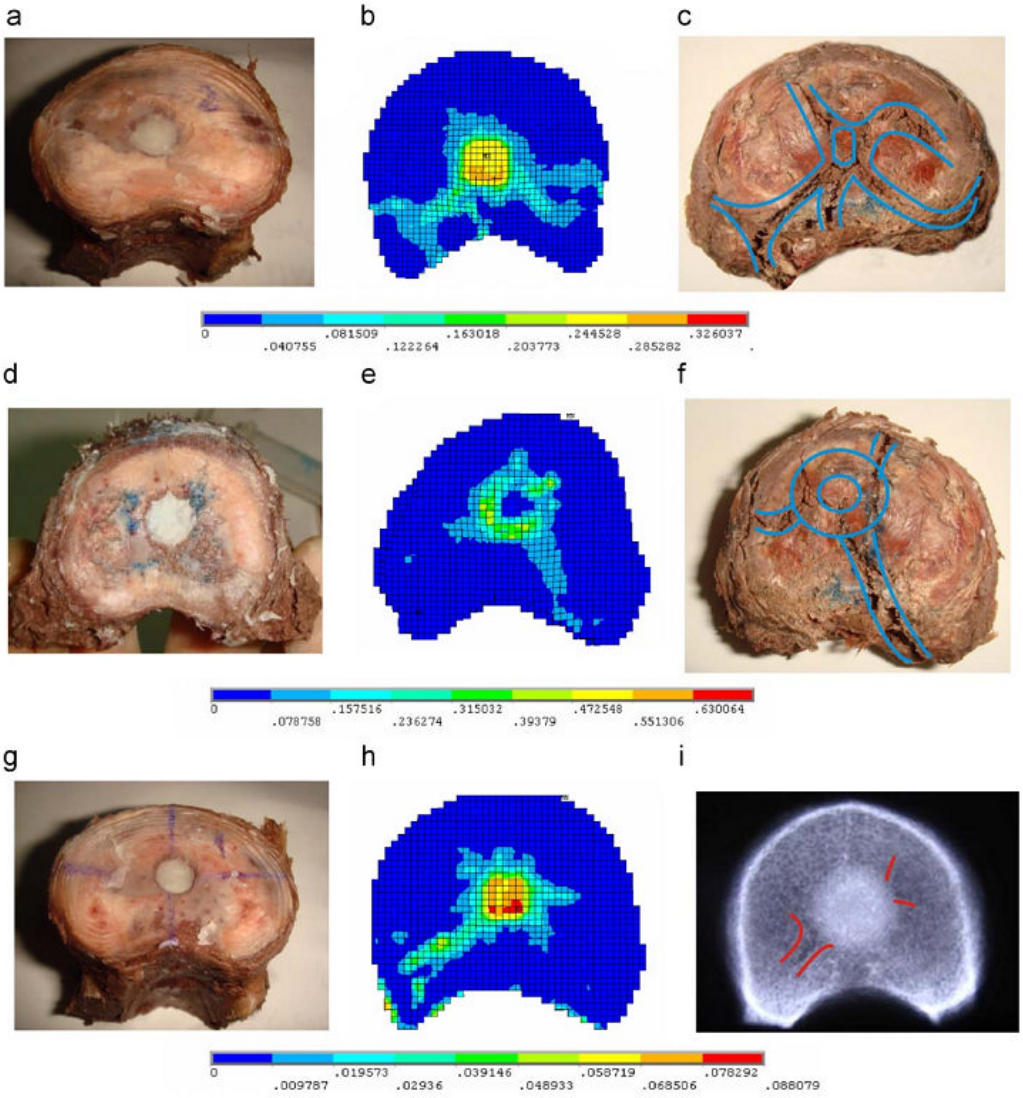

Figure 2-12 - Comparison of experimentally determined and hFE model predicted failure locations in PMMA-augmented vertebrae. Vertebral specimens post-augmentation with PMMA cement are shown in images (a), (d) and (g). Contour plots of the equivalent plastic strain (ie – damaged trabeculae) predicted by the corresponding specimen-specific FE models are shown in images (b), (e) and (h). Imges of the corresponding specimens following compressive testing are shown in images (c), (f) and (i), with blue or red lines superimposed to highlight the similarity between the FE-predicted and experimentally produced fracture patterns (Mirzaei et al 2009).

The remaining study that details specimen-specific comparison between hFE models predictions and corresponding experimentally-derived results of both their cement-augmented and un-augmented models (Mirzaei et al 2009). This makes it very difficult to evaluate the predictive accuracy of their cement-augmented models. However, their qualitative comparisons with respect to predicting the location of the initiation and progression of vertebral failure are of great interest.

The authors utilized a linearly-elastic linearly-plastic material model for the elements representing homogenized trabecular bone, and identified at each load step the trabecular elements that had reached a non-zero plastic strain. This enabled the location of the initiation of vertebral failure and how it progressed as the applied displacement was increased to be predicted. As shown in Figure 2-12, this approach produced good agreement with both visual and radiographic specimen-specific evidence collected experimentally. This suggests that an element-level strain-based failure criterion is an effective method of predicting the initiation and development of vertebral failure in simple axial compression.

The remainder of the single and multi-vertebral body hFE models discussed in Section 2.2. draw qualitative comparisons between their hFE model predictions and average properties and trends previously detailed in the literature, the lack of specimen-specific validation in these studies makes it difficult to have confidence that they are demonstrating genuinely predictive behaviour. The lack of efforts to validate the model behaviour, particularly in the case of the multi-vertebral body models, is likely due to the difficulty in conducting similar tests experimentally and of determining specimen-specific homogenous material properties for the soft and connective tissue included in the models. This leads to a similar conclusion to the investigative studies of un-augmented vertebral hFE models discussed in Section 2.1.3. While the qualitative comparisons and trends described in these studies are interesting and may help to inform the direction of further development of hFE models of cement-augmented vertebrae, without further efforts to explicitly validate their predictions experimentally, great care should be taken when using such models to inform clinical judgments.

2.3. Models of the total hip arthroplasty cement-bone interface

2.3.1. Introduction

There have been numerous hFE and pseudo-μFE finite element studies conducted with the aim of better understanding the mechanical behaviour of bone-cement interfaces. With the exception of a small number of very recent μFE studies, they have mainly focused on the interface found in the femur following total hip arthroplasty (THA). The most frequent cause of THA revision is aseptic loosening, whereby the steel or titanium implant stem becomes loose within the femur (Mann, Allen & Ayers 1998). Examination of radiographs and exploratory surgery of failed cemented implants has suggested that the behaviour of the bone-cement and cement-implant interfaces are amongst the most important factors involved in such failures, and that the cement-bone interface is the main site at which the de-bonding process initiates (Moreo, Garcia-Aznar & Doblare 2007). Likelihood of failure could be influenced by a number of clinical parameters such as the quantity or material properties of the cement, the geometry or surface treatment of the implant stem, or the surface characteristics of the bone within the treated femoral canal. It has been suggested that finite element modelling could be used to develop a better understanding of the mechanisms of failure of the bone-cement interface and how these parameters influence them (Moreo, Garcia-Aznar & Doblare 2007; Waanders et al 2009).

2.3.2. hFE modelling of the bone-cement interface

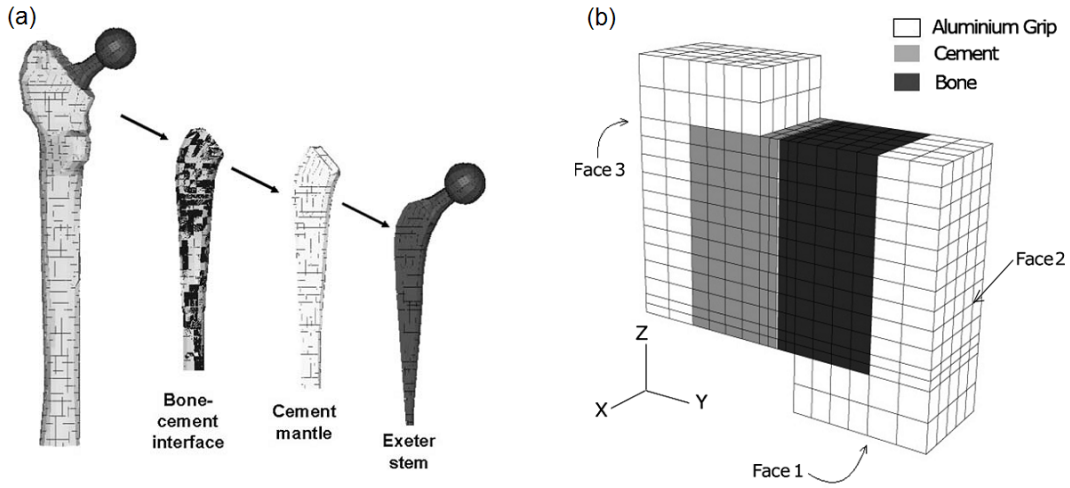

Figure 2-13 - Example hFE model geometries investigated by (a) Perez, Garcia-Aznar & Doblare (2009) and (b) Moreo, Garcia-Aznar & Doblare (2007)

Within the hFE studies the model geometry has represented either the entire femur, containing both the cement mantle and THA implant (Perez, Garcia-Aznar & Doblare 2009), or a small interfacial specimen representing an excised region of the femur containing cortical bone, the cement mantle and the interface between them (Figure 2-13)(Mann, Allen & Ayers 1998; Moreo, Garcia-Aznar & Doblare 2007). In all three cases the interfacial region between pure cortical bone and the cement mantle was explicitly modelled and assigned complex non-linear strain softening material properties derived from the level of local interdigitation between bone and cement (Moreo, Garcia-Aznar & Doblare 2007; Perez, Garcia-Aznar & Doblare 2009) or tuned by comparison with experimental results (Mann, Allen & Ayers 1998).

In contrast to the complexity of the interfacial region, the models typically featured homogenous isotropic linear-elastic material properties for the regions of bulk bone and cement. One exception is (Perez, Garcia-Aznar & Doblare 2009) who made use of an anisotropic heterogeneous material model for bone derived using a previously developed isotropic bone remodelling model and incorporated fatigue damage characteristics in their cement material model. While un-augmented vertebral hFE models utilising homogenous bone material properties have been shown to display poorer predictive accuracy in terms of apparent stiffness than those that utilise

specimen-specific μCT-greyscale dependent bone material properties (Wilcox 2007), the nature of the bone-cement interface within the femur is likely very different. THA involves broaching of the femoral canal such that the implant stem can be inserted into the femur. Broaching removes much of the trabecular bone within the canal, such that little remains, and the resulting post-THA bone-cement interface is largely a union between the cement and cortical bone, which as previously discussed is often modelled using homogenous material properties.

These studies predominantly focused on the shear stiffness, shear strength, tensile stiffness and fatigue-failure properties of the interface (Mann, Allen & Ayers 1998; Moreo, Garcia-Aznar & Doblare 2007), though Perez, Garcia-Aznar & Doblare (2009) also investigated the knock-on effects upon fatigue-failure within the cement mantle. While all three studies reported good agreement between the trends within their model predictions and their own experimental results and/or those previously published in the literature, there is little investigation of the effect of these interfacial material properties on the bulk compressive stiffness and strength of their models. As such, while their findings are of great interest in themselves, and potentially of great use with regard to hFE modelling of THA, there is little of immediate use in improving the predictive accuracy of augmented vertebral hFE models with respect to apparent stiffness and strength.

2.3.3. Pseudo-μFE modelling of the bone-cement interface

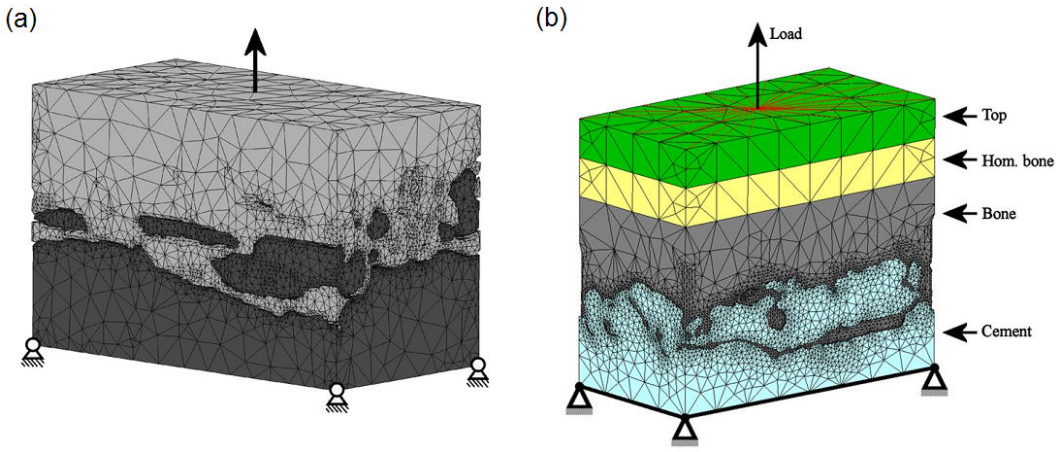

Figure 2-14 - Pseudo-μFE interfacial models studied by (a) Janssen, Mann & Verdonschott (2008) and (b) Waanders et al (2009)

The three pseudo-μFE studies were conducted by Janssen, Mann & Verdonschott (2008), Waanders et al (2009) and Waanders et al (2011). Their modelling approach is referred to here as pseudo-μFE as while larger microstructural details are preserved, smaller features of the interdigitated bone and cement were removed at the image processing stage to reduce the number of elements and hence the computational cost of solution (Figure 2-14) (Janssen, Mann & Verdonschott 2008). The model geometries and resulting surface-based meshes were generated from the corresponding downsampled specimen μCT images. Both the bone and the cement were assigned simple linear-elastic material models. The material properties of the bone were derived from the μCT image greyscale values according to previously a published density-modulus relationship while the cement was assigned homogenous material properties taken from the literature. The interface between the bone and cement surfaces was variously assigned a number of contact properties including fully tied, frictionless and frictional sliding according to a wide range of frictional coefficients.

Of the three studies, only one (Janssen, Mann & Verdonschott (2008) investigated interfacial stiffness, with the more recent studies focusing on fatigue failure and mixed-mode damage accumulation in the bone and cement. In the Janssen, Mann & Verdonschott (2008) study the models were tested in both tension and compression in

the same manner as the corresponding experimental specimens. It was demonstrated that closest agreement with the experimental results with regard to interfacial stiffness occurred when the interface was assigned a frictional sliding contact with a coefficient of friction of 0.3. The reasonable agreement between the experimental results and finite element predictions suggests that the assumption made by the authors that the mechanical behaviour of the femoral bone-cement interface would be dominated by the interlocking of the larger structural features is a reasonable one, at least within the elastic region before the onset of yield.

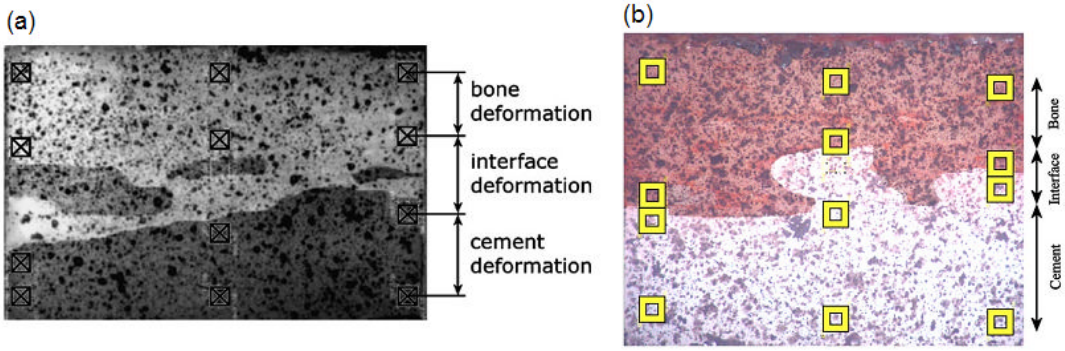

Figure 2-15 - Examples of DIC sampling points used by (a) Janssen, Mann & Verdonschott (2008) and (b) Waanders et al (2009)

One noteworthy aspect of these three studies is the use of an image-based strain measurement system by the name of digital image correlation (DIC). Prior to mechanical testing, the test specimen is treated with a dye that differentially stains the bone and cement to increase the contrast across the interface. A high resolution digital video camera is then trained on one of the specimen faces as it undergoes an applied deformation. By identifying a number of sampling points within the initial un-deformed images (Figure 2-15) which are then tracked between frames, and determining their movements relative to one-another, the local material strains across the specimen face can be measured.

By allowing the calculation of local strains and observation of the initiation and progression of failure across the interface, the technique is a great improvement over previous approaches that relied solely on apparent force/displacement data and visual inspection of the specimen post-failure. DIC does however possess a number of shortcomings; It's use is limited to specimen geometries including at least one planar

face parallel to the inferior-superior specimen axis, thus typically a cubic geometry is used (Janssen, Mann & Verdonschott 2008; Waanders et al 2009; Waanders et al 2011). DIC only facilitates strain measurement across the exterior of the specimen, where the nature of the interfacial strains are possibly quite different due to significantly different constraint conditions, and is incapable of imaging internal structural 'events' that may be driving the observed behaviour on the surface. Furthermore, the resolution with which the local strains can be measured is limited by the number of sampling points that can be reliably tracked between frames, which is likely to vary between specimens.

2.3.4. Discussion

The THA-centric nature of these studies casts significant doubt on the applicability of their findings to the mechanical behaviour of the bone-cement interface formed within the vertebral trabecular centrum following vertebroplasty. The primary difference - particularly in the case of the pseudo-μFE studies, is the greatly reduced interfacial interdigitation due to the removal of free trabeculae within the femoral canal by pre-implantation broaching. Additionally, due to the femoral morphology and the manner in which the specimens were prepared the interfaces studied in the pseudo-μFE models effectively lie along a plane. This leads to an interfacial region quite unlike the heavily interdigitated, near spherical or cylindrical shell interface within the vertebrae following vertebroplasty, and suggests that it is not unreasonable to expect significant qualitative differences between the mechanical behaviour of the bone-cement interfaces resulting from THA and vertebroplasty respectively. While the information derived from FE study of THA provide an insight into the types of modeling approaches possible, to increase understanding of the behaviour of the post-vertebroplasty bone-cement interface will require study of models that better represent these vertebroplasty-specific characteristics.

2.4. µFE modelling of the vertebral bone-cement interface

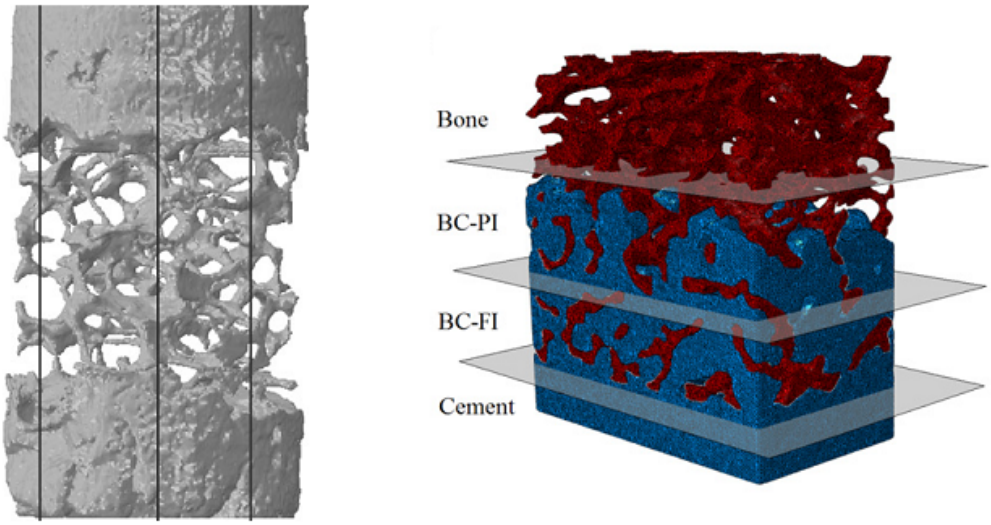

Figure 2-16 - Interfacial µFE models analysed by Zhao et al (2012) and Tozzi, Zhang & Tong (2012)

Three of the most recent finite element studies of bone-cement interfaces have made efforts to investigate interfacial morphologies that better represent those found in the vertebral centrum following vertebroplasty, exploring specimens comprising trabecular structures heavily interdigitated with cement.

In the same manner as in the pseudo-µFE studies conducted by Janssen, Mann & Verdonschott (2008), Waanders et al (2009) and Waanders et al (2011), the model geometries were generated from µCT images of the corresponding experimental specimens, cement-augmented human thoracic and lumbar vertebral trabecular bone, bovine trabecular bone taken from the iliac crest and polymer synthetic 'trabecular bone' in the cases of Kinzl et al (2012b), Tozzi, Zhang & Tong (2012) and Zhao et al (2012) respectively. Unlike in Janssen, Mann & Verdonschott (2008), Waanders et al (2009) and Waanders et al (2011), in these µFE studies the µCT images were not downsampled to the extent that the finer structural details of the interface were obliterated (Figure 2-16).

Zhao et al (2012) and Kinzl et al (2012b) assigned both the trabecular bone and cement homogenous, linear-elastic material properties taken from the literature, though Kinzl et al (2012b) also investigated the effects of including non-linear behaviour due to strain-dependent trabecular damage accumulation and the effects of porosity within the cement. Tozzi, Zhang & Tong (2012) assigned both the trabecular bone and cement orthotropic elastic-plastic material properties taken from the literature. While Tozzi, Zhang & Tong (2012) assigned to the interface a frictional sliding contact condition (coefficient of friction = 0.4), both Zhao et al (2012) and Kinzl et al (2012b) compared the effect of varying the interfacial contact condition from tied to frictionless-sliding, with Zhao et al (2012) also investigating the effect of a frictional sliding contact (coefficient of friction = 0.3). All three studies applied simple compressive boundary conditions under displacement control to their models to reflect the experimental test procedures. Both Tozzi, Zhang & Tong (2012) and Zhao et al (2012) utilised novel compression and imaging equipment that allowed μCT imaging of their specimens at each point in a stepwise compression to failure, thus facilitating direct comparisons between the experimental and μFE model predicted strain distribution.

In all three cases the model performance was evaluated quantitatively through comparison with corresponding experimental specimens. While Zhao et al (2012) and Tozzi, Zhang & Tong (2012) made direct like-for-like stiffness and strain distribution comparisons between their μFE models and experimental specimens, Kinzl et al (2012b) relied on comparisons of bulk model and specimen properties as their FE models only represented smaller sub-regions of their experimental specimens. This makes it more difficult to have complete confidence in the validity of their quantitative comparisons with regard to stiffness, as their cubic μFE sub-models measured only 4.2 mm on a side, less than the 6-8 trabecular cells recommended by Harrigan et al (1988) to ensure the ‘continuum behaviour’ necessary to negate the effect of local structural variation and allow like comparison of the model apparent mechanical properties with those of the larger experimental specimens from which they were generated.

There are some notable differences between the findings of the three studies. Zhao et al (2012) agreed with the earlier findings of Janssen, Mann & Verdonschott (2008) in suggesting that the degree of cement penetration into the trabecular structure was one of

the main determinants of the mechanical behaviour of the interface. This contradicts the findings of Tozzi, Zhang & Tong (2012) who found that the degree of cement penetration had little effect on interfacial mechanics, though they suggest that this was due to their exclusive use of compressive boundary conditions. This was unlike the mix of tensile and compressive deformations applied by Janssen, Mann & Verdonschott (2008), which led to failure occurring exclusively in the trabecular bone adjacent to the interdigitated region, primarily through trabecular buckling. This suggests that under tensile or shear boundary conditions, where trabecular pull-out is a failure mechanism, the degree of cement penetration may be far more important in determining interfacial behaviour.

While Kinzl et al (2012b) agreed with Janssen, Mann & Verdonschott (2008) in stating that the best agreement between their μFE model stiffness predictions and experimental results was found when the contact between bone and cement was defined as a frictionless sliding contact, Zhao et al (2012) found that varying the contact condition between synthetic polymer bone (Sawbone) and cement between tied and frictionless led to a variation of less than 4% and 1% for stiffness and stress respectively (compared to the representative 15.4% reduction in stress noted by Kinzl et al (2012b)). The lack of variation observed by Zhao et al (2012) is most likely due to the use of dry Sawbone for their experimental specimens, lacking the marrow and other soft tissue coating typically found in-vivo and in specimens fabricated from cadaveric tissue. It also seems reasonable to suggest that, due to the fact that Sawbone is fabricated from a polymer material, the liquid component of the PMMA cement may have had a solvent effect on the Sawbone itself and could have led to chemical bonding between them. While Tozzi, Zhang & Tong (2012) did not investigate the effect of varying the interfacial contact condition, good agreement was found between the strain distribution within their μFE models and corresponding experimental specimens. Though their μFE predicted stiffness was 50% higher than that experimentally measured, as the findings of Janssen, Mann & Verdonschott (2008) and Kinzl et al (2012b) indicated that a tied contact lead to increased over-prediction of stiffness, it is likely that the use of a tied contact would have lead to a greater over-prediction of the specimen stiffness.

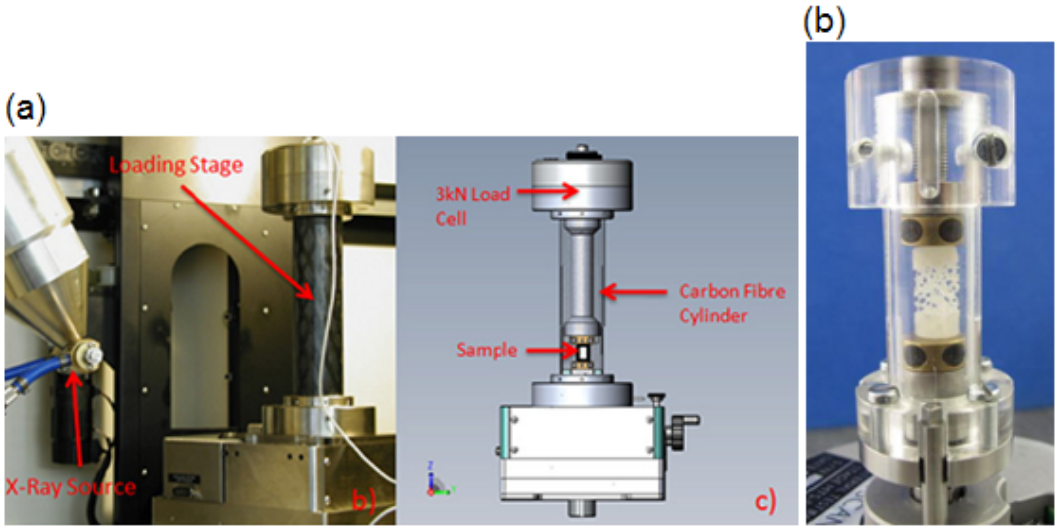

Figure 2-17 - uCT loading stages used by (a) Tozzi, Zhang & Tong (2012) and (b) Zhao et al (2012)

The use of novel stepwise compression and μCT imaging equipment used by Zhao et al (2012) and Tozzi, Zhang & Tong (2012) (Figure 2-17) demonstrates the power of such experimental equipment as a validation tool. These μCT loading stages improve markedly on the visible light based digital image correlation (DIC) systems used by Janssen, Mann & Verdonschott (2008), Waanders et al (2009) and Waanders et al (2011) due to their ability to determine tissue level strains not only on the specimen exterior but throughout the whole specimen volume. Another benefit is the ability to image cylindrical or irregularly-shaped specimens rather than the restriction to imaging only specimens with planar faces as is the case with DIC.

The ability to make comparisons of strain distribution and local material failure between the experimental specimens and finite element model predictions, at numerous points throughout the range of applied deformation, allows far greater confidence that the finite element models are accurately reproducing structural level specimen behaviour rather than merely bulk specimen properties. This is particularly important when aiming to show genuine predictive behaviour. Though there are some noteworthy shortcomings in these existing devices, with Zhao et al (2012) reporting that their small (6mm diameter, 12mm height) specimen size was due in part to the size constraints of their μCT loading stage, and that the design of the device led to the transfer of some torsional forces to their specimens that could not be accurately reproduced in their corresponding μFE models, it is likely that with further development such compression and imaging tools will become an indispensible part of the biomechanical FE modelling tool box.

Discussion

While these μFE studies present some interesting and well validated findings and demonstrate good agreement with experimentally observed interfacial behaviour, it is clear that further development of hFE representations of cement-augmented trabecular bone is necessary to produce clinically useful finite element tools for the analyses of vertebroplasty. As discussed earlier in this section, the computational cost of solving μFE models of un-augmented vertebrae is prohibitive even when taking advantage of high-speed computing facilities. Incorporating the sliding contact condition between the cement and trabecular bone suggested as necessary by these recent pseudo-μFE and μFE studies would greatly further increase these costs. As an example, Zhao et al (2012) reported that the time required to solve their μFE model increased from 20 hours in the case of the models featuring tied contact properties to over 700 hours when the interface was assigned a frictional sliding contact. Similarly, Kinzl et al (2012b) reported that their μFE models took as much as 60 hours to solve. In both cases, the models were very small compared with a whole vertebral body, let alone a spinal motion segment – 6 mm wide, 12 mm long cylindrical specimens in the case of Zhao et al (2012) and 4.22 mm edge-length cubes in the case of Kinzl et al (2012b). This indicates that, pending significant improvement in the clinical availability of what would currently be considered ‘super-computing facilities’, the μFE modelling approach is not a clinically practical tool for the analyses of cement-augmented vertebral bodies.

2.5. Conclusions

From this evaluation of existing efforts to better understand and model the apparent mechanical behaviour of both vertebrae with and without internal cement augmentation and the bone-cement interface in isolation, the following is clear:

- Specimen-specific hFE models of un-augmented vertebrae that make use of linear-elastic perfectly-plastic material models and μCT density-dependent material properties for the trabecular bone display reasonable concordance with experimentally derived results with respect to both apparent vertebral stiffness and strength.

- While some authors have advocated the use of more sophisticated density-fabric-dependent material properties for the trabecular bone, there is no evidence that their use significantly improves the accuracy of the model predictions.

- Incorporation of cement augmentation within hFE vertebral models typically greatly reduces their predictive accuracy when compared to hFE models of un-augmented vertebrae.

- Recent μFE model studies of the bone-cement interface following both vertebroplasty and THA suggest that the interface is more compliant in compression than either pure bone or cement.

- In agreement with this finding, one recent study of hFE models of cement-augmented vertebrae suggests that incorporating an interfacial region of increased compliance restores the model predictive accuracy to close to that of un-augmented hFE vertebral models.

2.6 Objectives

The issues identified during the review of the available literature concerning vertebral simulation using the FE method informed the determination of the following objectives:

- To obtain the necessary μCT greyscale dependent elastic and plastic material property parameters required to construct hFE models of un-augmented trabecular bone specimens using the existing image-based hFE modelling approach described by Wilcox et al (2007) and Wijayathunga et al (2008).

- To obtain experimental evidence of the deformation and failure processes that occur at the trabecular bone – cement interface under an applied load.

- To use this experimental evidence to inform modifications to hFE models generated using the existing image-based hFE modelling approach, and the material parameters previously derived, that result in better agreement between the hFE model predicted and experimentally observed interfacial apparent and structural behaviour.

3. µCT imaging and experimental axial compressive testing of un-augmented ovine vertebral trabecular bone

This chapter details the imaging using µCT of specimens of un-augmented ovine lumbar vertebral trabecular bone, and the experimental axial compressive testing conducted to determine their apparent stiffness and yield strain. This study formed the first part of the work conducted to meet the first objective set out in Section 2.6.

3.1. Selection of animal tissue

Selection of an appropriate source of non-human tissue is complicated by the fact that as the only large solely bipedal mammal, humans have no direct parallel in the animal kingdom (McLain, Yerby & Moseley 2002). While a number of larger species including dogs, mini pigs, poultry, dairy cows and non-human primates have previously been used in skeletal research (Zarrinkalam et al 2008), it is considered that there is no ideal large animal model for the study of all human bone disorders (Aerssens et al 1998).

Due to the fact that all commonly used animal species differ significantly from humans with respect to one or more anatomic and/or morphological vertebral parameters, it is important to select the best model for the needs of a particular study (McLain, Yerby & Moseley 2002). This work focuses on the compressive mechanical properties of trabecular bone and trabecular bone-cement composites. For this reason, ovine tissue was selected as previous studies had reported that correlation between ovine trabecular bone density and compressive properties (Young's modulus, compressive strength) agreed well with previously published values for human vertebral trabecular bone (Mitton et al 1998), and that while it was typically more dense, ovine trabecular bone exhibited similar anisotropic trends as human trabecular bone (Wang et al 2010).

3.2. Specimen design and fabrication

Ovine Lumbar spines were obtained from a local abattoir taken from sheep that were killed between the ages of 2-6 years. Only lumbar Ovine vertebrae were chosen for specimen fabrication. Vertebrae taken from the cervical and thoracic levels exhibited highly concave cortical walls that significantly 'necked' half way along the superior-inferior axis, and the superior endplates were deeply staggered in the anterior-posterior direction. This would have made it very difficult to fabricate cylindrical cores greater than a few millimetres in diameter.

The spines were sectioned and cleaned of soft tissue before being frozen for storage. The vertebrae were taken out of storage and, while still frozen, clamped across their superior and inferior end-plates using a custom jig that was developed for the purpose of assisting in the fabrication of vertebral trabecular core sections (Figure 3-1). A 10 mm internal diameter coring drill bit was then driven through the superior end-plate until it broke through the inferior end-plate allowing the extraction of the trabecular core. A 10 mm coring bit was chosen because it was the largest diameter specimen that could be fabricated while minimising amount of cortical shell incorporated within the specimen. As the average trabecular cell dimension within the vertebrae that were used was of the order of 1 mm, 10 mm diameter specimens still spanned sufficient trabecular cells to behave in a continuum manner under compression according to previously published work by Harrigan et al (1988). The trabecular cores were then trimmed to remove the cortical shell and cartilaginous end-plates on the superior and inferior faces (Figure 3-2). This did not reduce the axial dimension to less than 20 mm, ensuring that the height / diameter ratio remained greater than the 1.5:1 recommended by Keaveny et al (1993).

Figure 3-1. In-house developed vertebral coring jig

Figure 3-2. Ovine trabecular specimen following coring and trimming

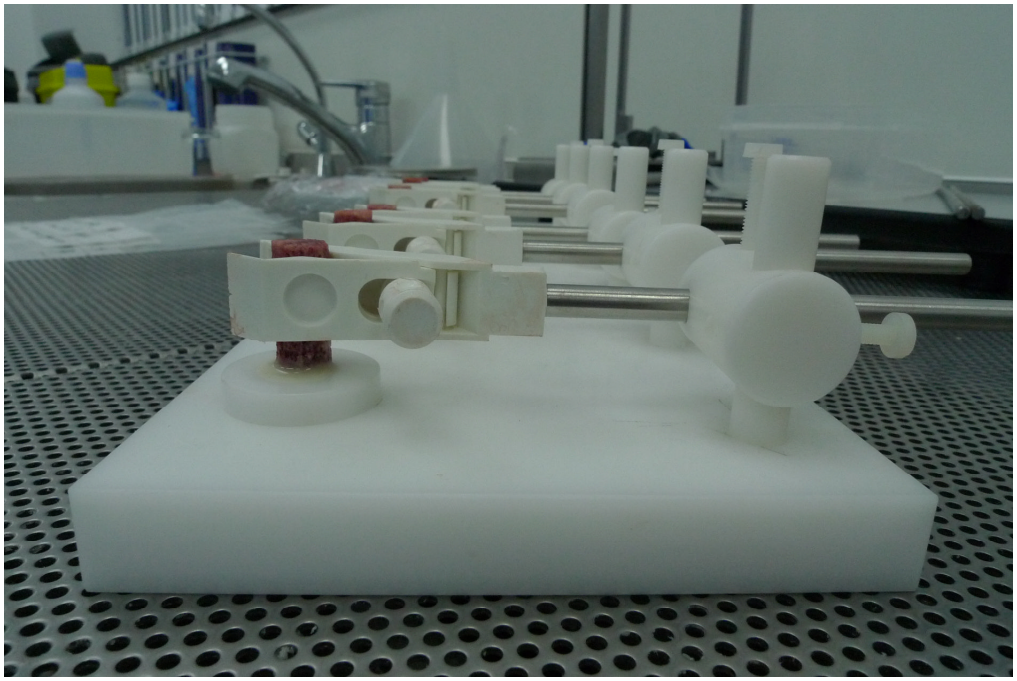

Figure 3-3. In-house developed trabecular core specimen potting jig

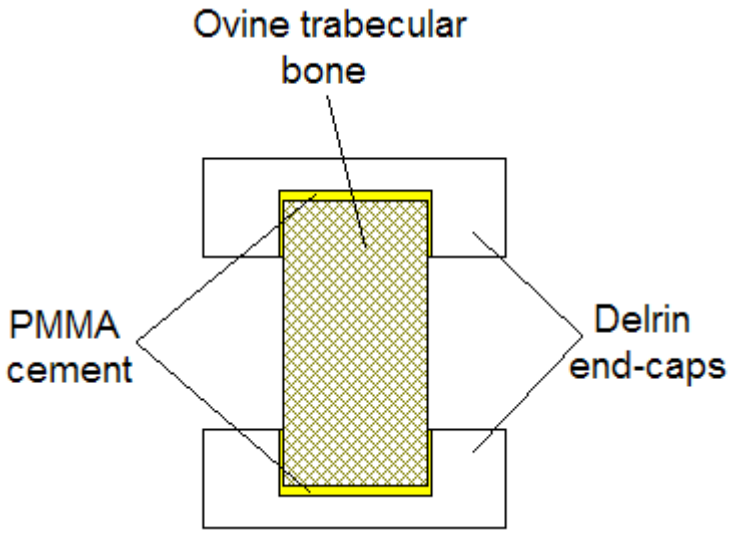

Figure 3-4. Schematic of completed specimen cemented into end caps

A previous study of sources of experimental error in compressive testing of trabecular bone specimens by Keaveny et al (1997) suggested that embedding the specimen ends would allow more accurate determination of the specimen apparent properties by reducing 'end artefacts', such as the splaying of free cut trabeculae at the specimen end-faces, which typically resulted in underestimation of the specimen apparent Young's modulus.

The trimmed trabecular cores were then potted into Delrin end-caps using a custom potting jig developed in-house for that purpose (Figure 3-3). The end-caps provided a loose sliding fit with the specimens. Before the specimens were inserted into the end-caps, a small quantity of PMMA cement, prepared at a 1:1 liquid-powder ratio, was injected into the end-caps to ensure full contact. The jig acted to hold the specimens concentric with the end caps until the PMMA hardened. Once all the specimens had been potted at one end, tubular Delrin jigs were used to pot the remaining ends into identical Delrin end-caps, ensuring that the end-caps were concentric and the loading faces plano-parallel (Figure 3-4).

Following potting into the Delrin end-caps, the specimens were wrapped in tissue paper moistened with water to prevent them from drying out and then kept frozen at minus 19°C prior to μCT scanning and mechanical testing.

3.3. Preliminary μCT scanning

Each specimen was imaged using a μCT scanner (XtremeCT, Scanco Medical AG, Brüttisellen, Switzerland). The scanner settings used were as shown in Table 2-1.

Energy (kVp)	60
Current (μA)	900
Integration time (ms)	300
Resolution (μm)	41

Table 3-1. XtremeCT μCT scanner settings used to image trabecular specimens

3.4. Mechanical testing

After μCT imaging, the experimental specimens were tested to destruction in compression using a materials testing machine (Instron, MA, USA) for the purposes of determining their apparent stiffness and yield strain.

The specimens were centrally located between the platens of the materials testing machine and, after the application of a 50 N pre-load, compressed under force control at a rate of 5 kN/min until failure. Preliminary testing conducted using ovine lumbar trabecular bone cores of the same cross-section suggested that this would produce a strain rate of approximately 0.5 %/sec.

Whilst there is not a ‘standard’ compressive testing procedure to determine the stiffness of trabecular bone specimens, this strain rate has been commonly used by a wide number of different groups in previous studies (Bevill, Farhamand & Keaveny 2009; Kopperdahl & Keaveny 1998; Morgan & Keaveny 2001; Bayraktar & Keaveny 2004). Though the strain-rate dependency of the mechanical properties of trabecular bone has been shown to be low (Keaveny & Hayes 1993), this strain rate was used to improve the comparability of the results with those previously published.

3.5. Derivation of apparent properties

For each specimen, the stiffness was determined by calculating the gradient of the linear portion of the force-displacement data as shown in Figure 3-5. The specimen yield stress and strain were determined according to the 0.2 % offset yield method, a common approach for materials that do not exhibit a well-defined yield region (Punmia, B. C. & Jain, A. K. Mechanics of Materials 2002, Page 14), illustrated in Figure 3-6. The apparent modulus was taken as the gradient of the straight-line portion of the stress-strain plot.

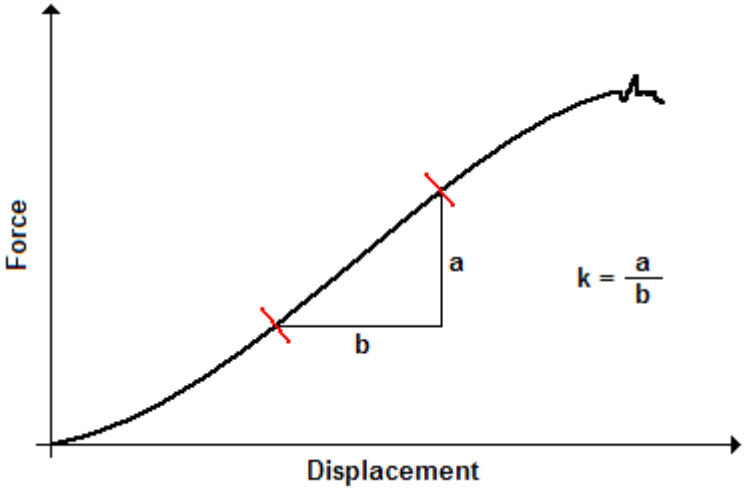

Figure 3-5. Method used for calculating specimen stiffness using the compressive force-displacement data

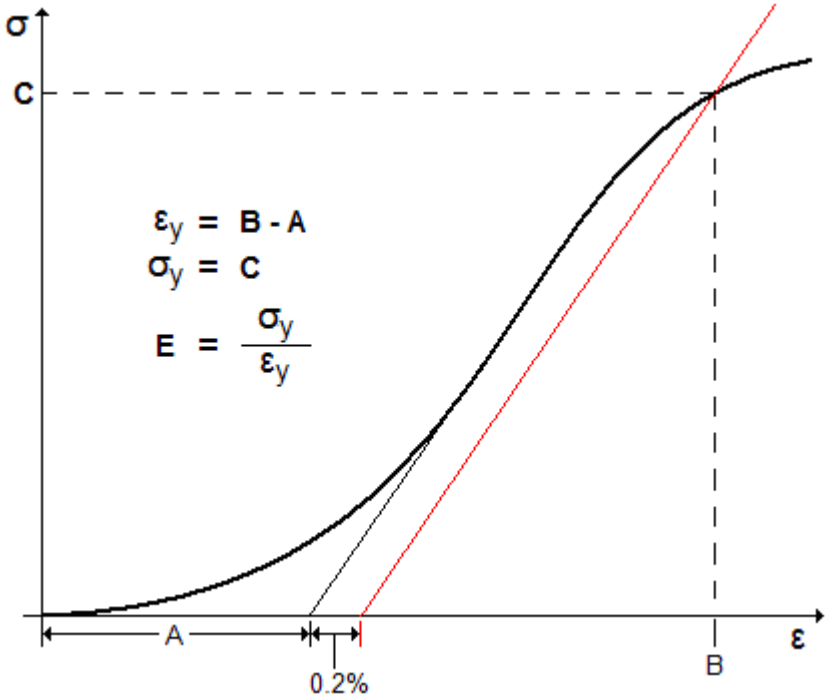

Figure 3-6. Methods used for calculating the apparent yield stress and strain from the specimen compressive stress-strain data using the 0.2% offset yield method

As trabecular bone does not exhibit a well-defined yield region (Bilezikian, Raisz & Martin, 2008), for the purposes of these tests failure was defined as the point at which the applied load dropped below 97.5 % of the peak load beyond a threshold of 500 N.

3.6. Results

The results are presented in Table 3-2 and Figures 3-7 to 3-10. Figures 3-11 and 3-12 show typical force-displacement and stress-strain plots, taken in this case from specimen 31-1-12_L4.

	Mean	S.D.
Stiffness (N/mm)	3650	743
Apparent Young's modulus (MPa)	956	225
Yield strain (%)	3.1	0.4
Yield stress (MPa)	26.6	4.4
Yield strength (N)	2090	347

Table 3-2. Average specimen properties determined via compressive testing

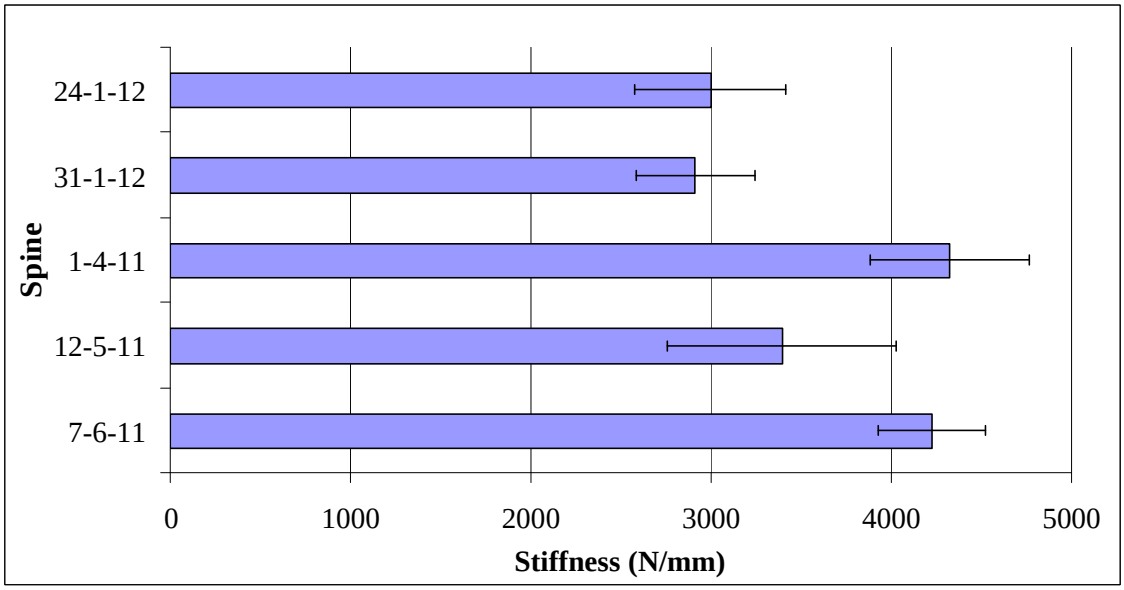

Figure 3-7. Average specimen stiffness grouped according to the spine from which they were fabricated. The error bars represent one standard deviation

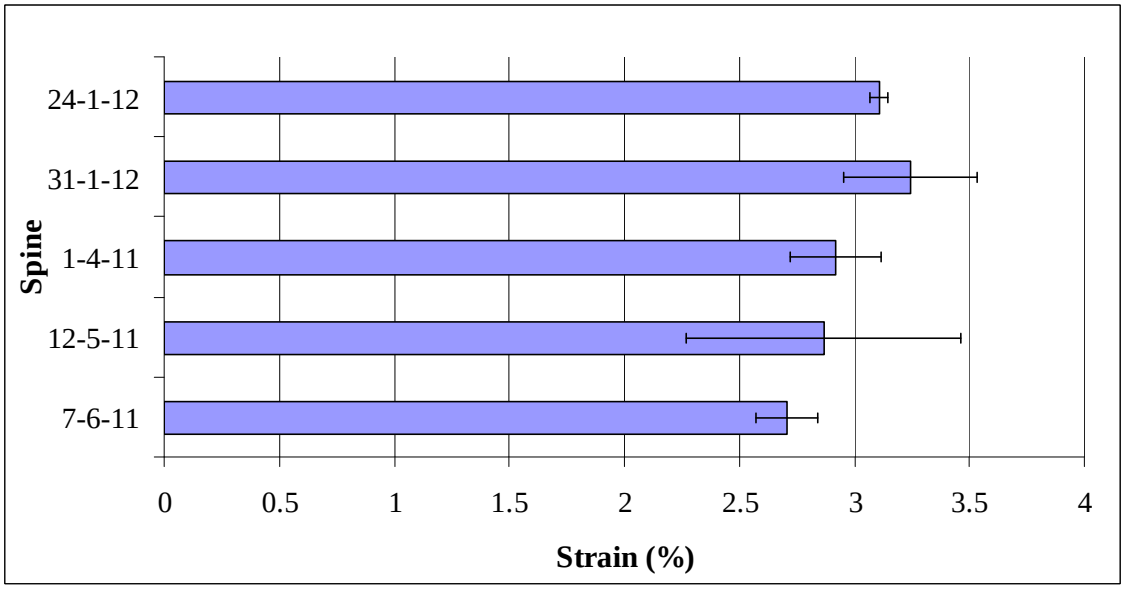

Figure 3-8. Average specimen apparent yield strain grouped according to the spine from which they were fabricated. The error bars represent one standard deviation

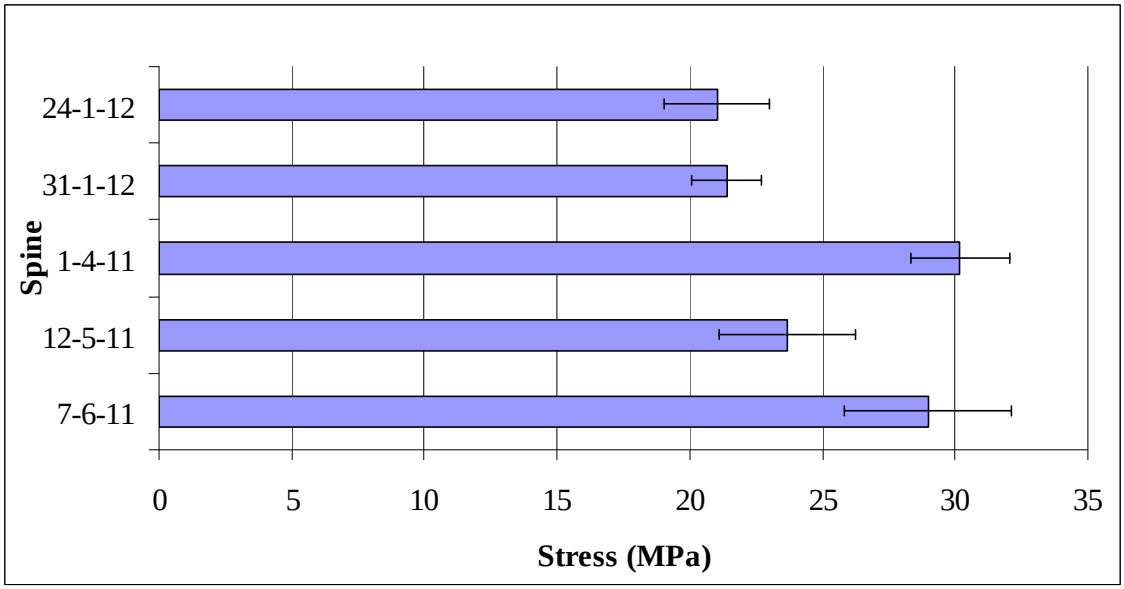

Figure 3-9. Average specimen yield stress grouped according to the spine from which they were fabricated. The error bars represent one standard deviation

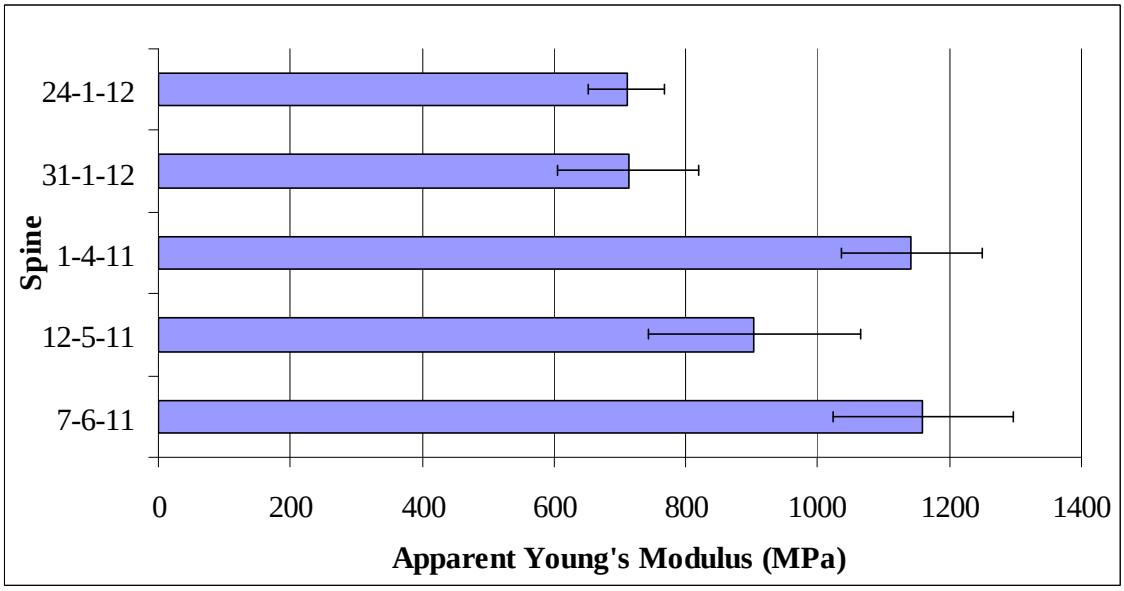

Figure 3-10. Average specimen apparent Young's modulus grouped according to the spine from which they were fabricated. The error bars represent one standard deviation

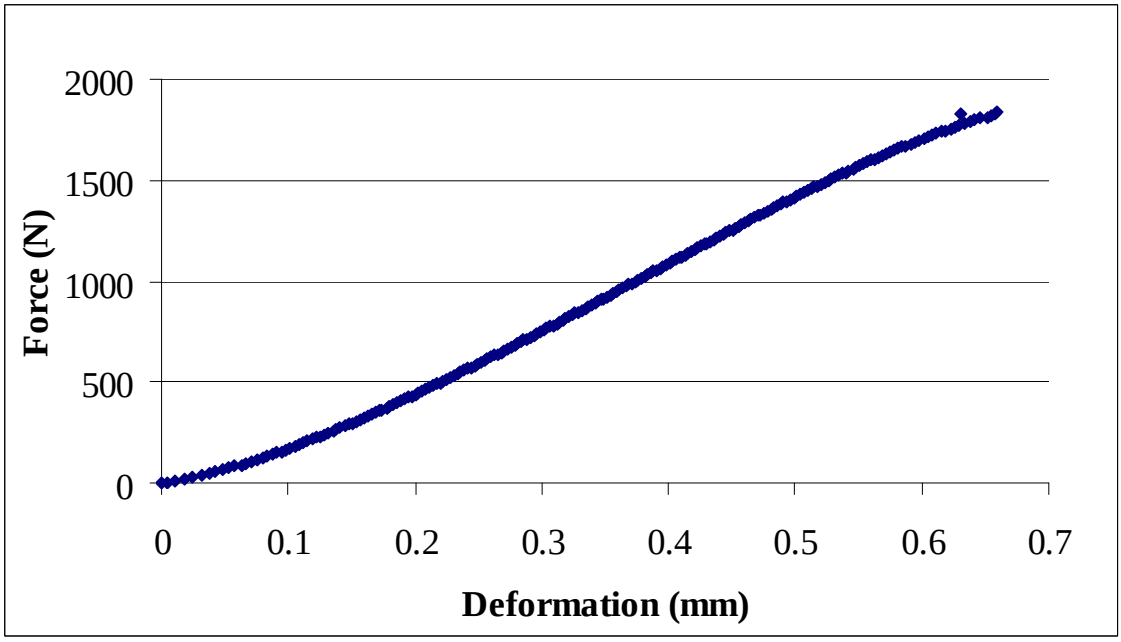

Figure 3-11. Example force-deformation data for specimen 31-1-12_L4

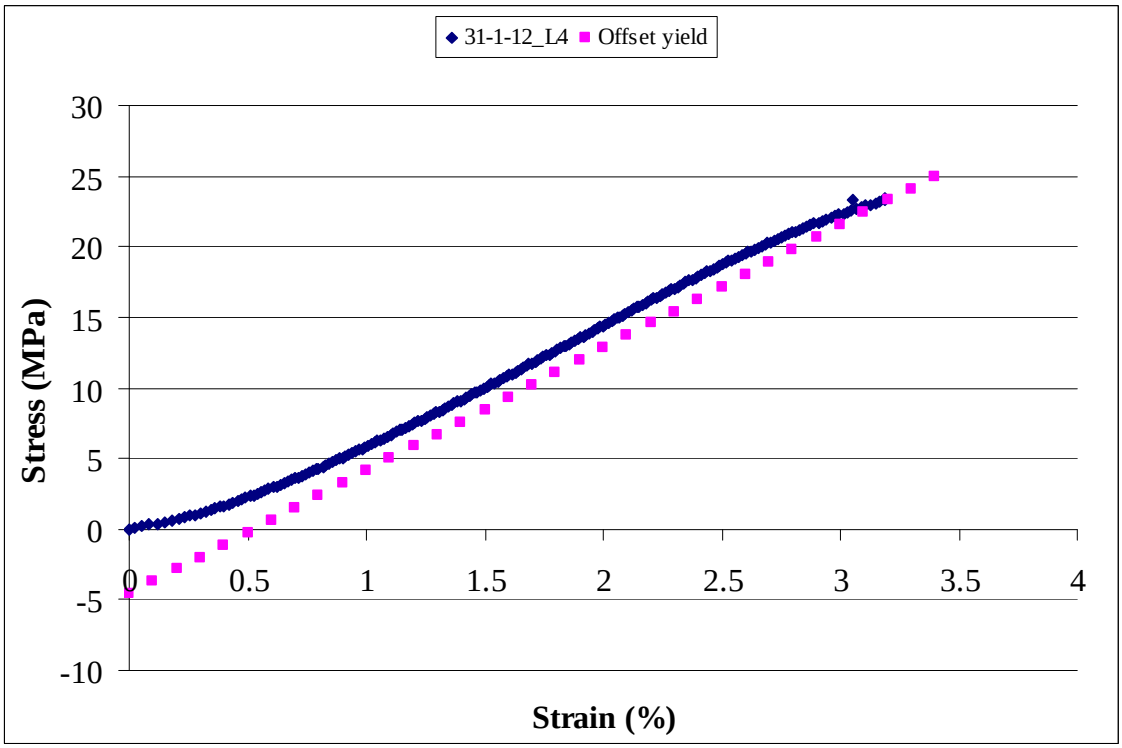

Figure 3-12. Example stress-strain data for specimen 31-1-12_L4 (blue). The pink data points represent the gradient and x-intercept of the 0.2 % offset yield intersection

3.7. Discussion

A comparison between the mean properties across all of the specimens tested and corresponding average values previously reported in the literature is presented in Tables 3-3 and 3-4. The results presented lie within the range of values for ovine lumbar vertebral, and in the case of Mittra, Rubin & Qin (2005) femoral trabecular bone.

	n =	E (Apparent) (MPa)
This study	27	956 (224)
Mitton, Rumelhart et al (1997)	32	1510 (784)
Mitton, Cendre et al (1998)	26	1347 (575)
Mittra, Rubin & Qin * (2005)	45	542 (78)

Table 3-3. Apparent Young's modulus properties for ovine trabecular bone from lumbar vertebra and femoral sites (marked *) previously published in the literature

		Yield			
	n =	Stress (MPa)		Strain (%)	
This study	27	26.6	(4.4)	3.1	(0.4)
Mitton, Rumelhart et al (1997)	32	22.3	(7.1)	3.21	(0.8)
Mitton, Cendre et al (1998)	26	23.4	(8.6)		
Mittra, Rubin & Qin * (2005)	45	17	(7)		

Table 3-4. Yield stress and strain properties for ovine trabecular bone from lumbar vertebra and femoral sites (marked *) previously published in the literature

Interestingly, while the specimens tested as part of this study lie within the upper range of previously published values with respect to yield stress, they lie within the lower range of previously published values with respect to their apparent Young's modulus, which would not be expected given that the yield strains are very similar. This is most likely because of differences between methods in defining the yield behaviour.

	n =	Age range (years)
This study	27	2 - 6
Mitton, Rumelhart et al (1997)	32	5.6 - 10.3 (mean = 9)
Mitton, Cendre et al (1998)	26	5.6 - 10.3 (mean = 8.9)
Mittra, Rubin & Qin * (2005)	45	6 - 8

Table 3-5. Sample sizes and tissue source age ranges for ovine trabecular bone from lumbar vertebra and femoral sites (marked *) studies previously published in the literature

Another interesting aspect of the results is the narrow range of specimen properties found here when compared to previously published values by Mitton et al (1997) and Mitton et al (1998). As ewes display age-related changes in bone volume and composition in a similar manner to that seen in humans (Newman, Turner & Wark 1995), it is suggested that the reduced variation in properties found in the specimens tested as part of this study is due to the significantly wider age range of the ewes involved in these two studies (Table 3-5).

3.8. Summary

- 27 cylindrical ovine lumbar vertebral trabecular bone specimens were fabricated and imaged using μCT.

- All specimens were deformed in axial compression until yield and the resulting force-displacement data was recorded.

- The force-displacement data for each specimen was used to calculate its stiffness, apparent yield strain, apparent Young's modulus, and apparent yield stress.

- For all specimens, the calculated apparent Young's modulus, apparent yield stress and apparent yield strain fell within the range of values previously reported in the literature.

4. Development of hFE models of un-augmented ovine vertebral trabecular bone

This chapter details the development of hFE models of the experimental specimens imaged and characterised in Chapter 3, and the derivation of the most appropriate μCT greyscale-modulus and element yield strain relationships from the image greyscale to the elastic modulus and yield strength. This study formed the second part of the work conducted to meet the first objective set out in Section 2.6.

4.1. Model development

The specimen μCT image data was initially converted into specimen-specific finite element meshes using commercial image processing and hFE model generation software (Scan-IP, version 4.2 – Build 140, Simpleware, Exeter, UK). Additional pre- and post-processing were then undertaken using ABAQUS CAE (Version 6.8, Dassault Systèmes, MA, USA). All models were solved using an implicit method in ABAQUS on a desktop PC (Intel® Xeon® X5260 CPU @ 3.33GHz, 3.25GB RAM, Microsoft Windows XP Professional, version 2002, service pack 3).

4.1.1. Choice of mesh resolution

In their study of hFE models of synthetic trabecular bone, Zhao et al (2010) conducted extensive testing of their models sensitivity to mesh resolution. Two regions of mesh convergence were identified; (i) Where the element size was approximately equal to the trabecular pore size, such that no element is assigned a near-zero stiffness (i.e. all pore) and (ii) where the element size approached the average trabecular strut thickness, such that there were effectively gaps in the model structure. While the results of Zhao et al (2010) were obtained using hFE models of synthetic bone, as it was suggested that mesh convergence behaviour was dependent on the relationship between element size and the specimens morphological parameters (average trabecular pore size and strut thickness)

it was considered reasonable to assume that hFE models of cadaveric trabecular bone would behave in the same way.

Zhao et al (2010) reported that choosing a mesh resolution resulting in an element size approaching the average trabecular strut thickness led to convergence at an average error of 1.4 % when compared to the corresponding experimentally derived results as opposed to an average error of 5 % when the element size was approximately equal to the trabecular pore size, a reduction in average error of 72 %. However, the increase in accuracy was accompanied by an approximately 15-fold increase in the number of elements and an approximately 60-fold increase in solution time. In light of both the magnitude of error present under existing approaches to computational simulation of cement-augmented vertebrae, and the small (<5 %) predictive error observed by Zhao et al (2010) at the coarser mesh resolution, a 60-fold increase in computational cost was not considered cost-effective and thus an element size approximately equal to the pore size was used. For the ovine lumbar vertebral trabecular bone from which the specimens were fabricated, this equated to an element size of 1 mm^3.

This agrees with the results of a number of sensitivity studies previously discussed in Section 2.1.3, that suggest that there is little benefit in using a mesh resolution smaller than 1 mm^3.

4.1.2. hFE mesh generation process

The mesh generation process is shown in Figures 4-1 to 4-4, which illustrate the main steps involved in converting a specimen μCT scan into a hFE mesh.

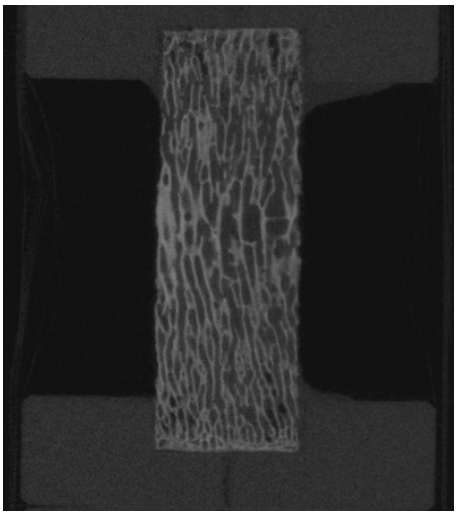

Figure 4-1. Vertical cross-section through specimen μCT image stack at full μCT scan resolution (0.041 mm^3).

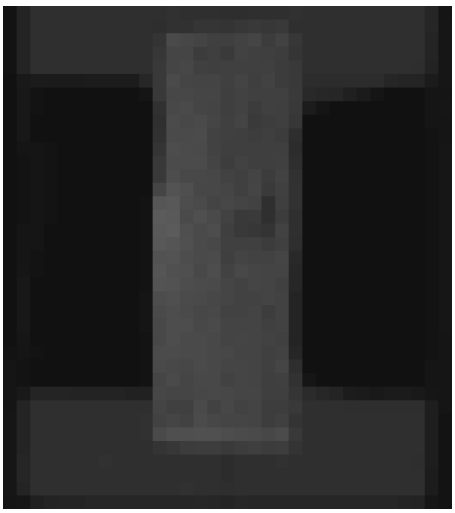

Figure 4-2. Vertical cross section through specimen μCT scan following downsampling to 1 mm^3 resolution.

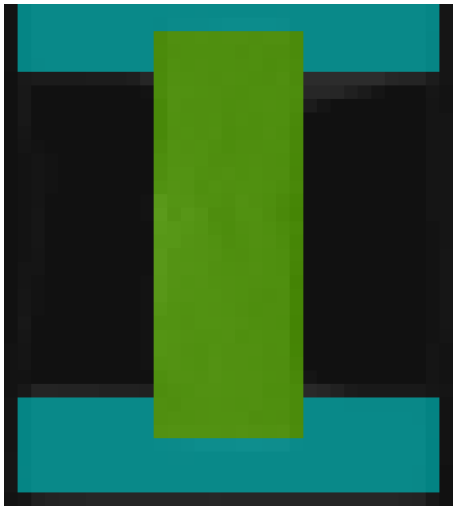

Figure 4-3. Vertical cross section through downsampled specimen scan following masking showing end-cap mask (blue) and trabecular core mask (green).

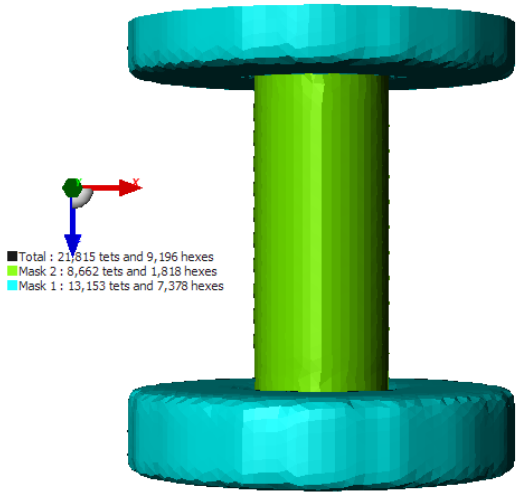

Figure 4-4. 3D view of resulting specimen mesh ready to be imported into ABAQUS.

The raw μCT data was firstly converted into stacks of .TIFF images using a Matlab code developed in-house (Figure 4-1). For each specimen, the .TIFF files were then loaded into Scan-IP and downsampled from their native resolution (0.041 mm^3) to a resolution of 1 mm^3 (Figure 4-2), and then masked into regions comprising the different constituent materials; Delrin end caps, trabecular bone and PMMA cement (Figure 4-3). This was achieved using a combination of threshold and binary subtraction operations; some manual intervention was also necessary. For one subset of models the PMMA cement, or both the PMMA cement and the Delrin end caps were not masked for inclusion in the final mesh for the purposes of exploring the models' sensitivity to problem simplification, which will be described in more detail in Section 4.2.1.

The Scan-IP meshing tool was then used to convert the masked regions directly into a finite element mesh that could be imported into ABAQUS (Figure 4-4). The mesh smoothing tool in Scan-IP, which was used to remove severe discontinuities in the mesh that arose as a result of the downsampling process, resulted in meshes comprising 4-node tetrahedral and 8-node hexahedral linear elements. Where two masks were in contact, a contact interface was defined. This allowed detailed contact properties between the different materials within the models to be defined in ABAQUS.

4.1.3. Additional pre-processing

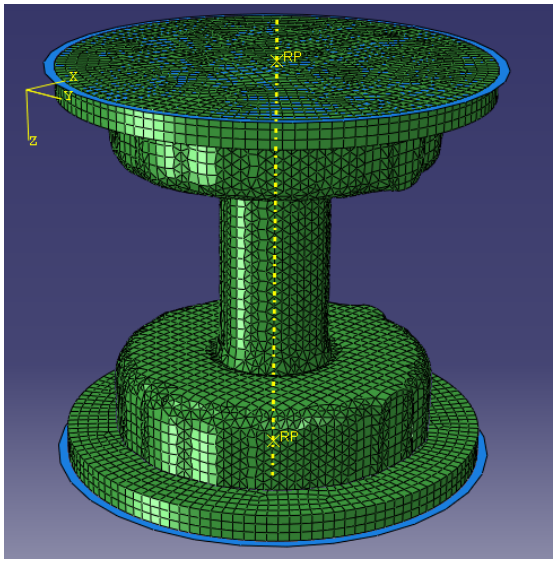

Figure 4-5. Specimen mesh and analytical rigid surfaces (blue) showing additional elements inserted to correct end-cap height.

The finite element meshes were then imported into ABAQUS and boundary conditions and internal interfacial contact properties were defined. In cases where the initial μCT images did not capture the full height of the Delrin end caps, additional layers of linear hexahedral 8-node elements were tied to the upper and lower surfaces of the mesh to increase the end cap thickness to 8 mm (Figure 4-5). These were of approximately the same element size as those in the imported mesh and were assigned the same material properties as the Delrin regions within the original mesh.

Analytical rigid plates were then created in tied contact with the upper and lower mesh surfaces to represent the loading platens of the compressive test equipment (Figure 3-5). A reference node was defined at the centre of the plate upon which the external boundary conditions were applied. For some specimens a number of different additional contact conditions were defined between the mesh and the analytical rigid plates to explore the models' sensitivity to the experimental boundary conditions, which will be described in more detail in Section 4.2.2.

4.1.4. Material property selection

For all models, the elements representing regions of PMMA cement or the Delrin end caps were assigned homogenous material properties, while the elements representing the trabecular bone cores were assigned either homogenous material properties or an elastic modulus dependent on the underlying μCT image greyscale values on an element-by-element basis.

4.1.4.1. Homogenous bone material properties

For the purpose of exploring the models' sensitivity to problem simplification a small number were generated with homogenous bone material properties. In these cases, the bone elements were assigned a Young's modulus based on the experimental compressive test data for that specimen (calculated as shown in Eq. 1).

$$E = \frac{\sigma}{\varepsilon} \qquad \therefore E = \left(\frac{F}{A}\right)\left(\frac{L}{\Delta L}\right)$$

Equation 1. E = elastic modulus, σ = stress, ε = strain, F = force, A = cross sectional area of specimen, L = length of specimen, Δ L = change in length of specimen.

Substituting the experimentally determined value of F at a deflection equal to that used throughout the hFE testing (ΔL = 0.5 mm) gave an overall Young's modulus for the specimen in each case. Across the four groups of specimen-specific models configured

in this way the mean Young's modulus was 906.8 MPa and the standard deviation was 271.7 MPa. In all cases a Poisson's ratio of $\nu = 0.3$ was used.

4.1.4.2. Greyscale-dependent bone material properties

As described previously (Section 2.1.3), generating specimen-specific hFE models directly from down sampled μCT image data allows the bone material properties to be assigned on an element-by-element basis according to the material density, which is itself related to the underlying μCT image greyscale values. Since all of the specimens in this study were imaged on the same calibrated μCT system with the same settings, a direct relationship between greyscale and elastic modulus was used, rather than first deriving a material density.

The relationship between the greyscale and the elastic modulus can be linear ($E = GS*k + C$), quadratic ($E = GS^2*k_1 + GS*k_2 + C$), cubic ($E = GS^3*k_1 + GS^2*k_2 + GS*k_3 + C$), or higher order. Previous work published by Wijayathunga et al (2008) compared the load-displacement curves produced using a specimen-specific finite element model of a single human vertebrae assigned bone material properties according to μCT image greyscale-modulus relationships of increasing order (Figure 4-6).

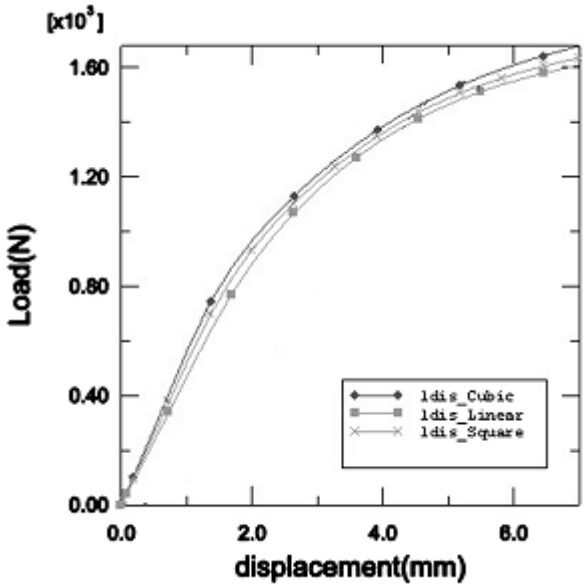

Figure 4-6. Load-displacement data previously published by Wijayathunga et al (2008) detailing how whole vertebral hFE model response varies depending on the order of the chosen grayscale-modulus relationship.

The difference between the hFE model predictions varied negligibly as the order of the relationship increased, and it was suggested that the error due to the use of a linear greyscale-modulus relationship would be likely insignificant compared to other possible sources of model prediction error, while greatly simplifying the derivation process. For this reason the greyscale-dependent bone material properties were assigned according to a linear relationship of the form E = GS*k.

A subset of models generated for the purpose of exploring the models' sensitivity to changes in the experimental boundary conditions were assigned greyscale-dependent bone material properties according to a preliminary μCT grayscale-modulus relationship derived during initial testing of the models whereby k = 43.259. The main series of models generated for the purpose of determining a generalised μCT grayscale-modulus relationship for ovine lumbar vertebral trabecular bone were initially assigned greyscale-dependent bone material properties according to a μCT grayscale-modulus relationship whereby k = 1.

4.1.4.3. Non-bone material properties

The two non-bone materials included in the models: PMMA bone cement and Delrin, were both assigned homogenous, isotropic material properties.

The PMMA regions featured in a small number of models run as part of the sensitivity testing were assigned a Young's modulus taken from the literature of 2.45 GPa (Wijayathunga et al 2008).

Some initial tests suggested that the Delrin from which the end-caps were machined was less stiff than suggested by the literature, so a series of compressive tests were conducted to ascertain the correct value. A 25 mm diameter, 35 mm height cylindrical specimen was machined from the same piece of Delrin used in the fabrication of the endcaps and cyclically compressed to a maximum load of 1 kN at a load rate of 2 kN/min twelve times. Taking the mean gradient of the straight-line portions of the force-extension data gave a Young's modulus for the Delrin of 757 MPa, which was used throughout all of the models utilised in this study.

For both the PMMA bone cement and Delrin, a Poisson's ratio (v) of 0.3 was used throughout.

4.2. Sensitivity testing

4.2.1. hFE model sensitivity to problem simplification

The iterative derivation of a generalised greyscale-modulus relationship for ovine lumbar vertebral trabecular bone would require the solution of a large number of hFE models. The inclusion of the end caps and the PMMA cement used to pot the specimens greatly increases the computational expense involved in solving the models. It not only increases the total number of elements but also requires the solution of two contact interfaces: between the end caps and the PMMA cement and between the PMMA cement and the bone.

To determine the minimum level of complexity necessary to adequately model the specimens, and thus minimize the computational expense, the variation in the stiffness predictions of a subset of hFE models as they were increasingly simplified was investigated.

4.2.1.1. Methods

The hFE models were generated directly from the μCT images as previously described (Section 4.1.2). For each of four specimens, four hFE models were created to include: (1) all three material regions – bone, PMMA cement and end-caps – and the contact interfaces between them (Figures 4-7b and 4-8a); (2) only the bone and end-caps and corresponding contact interface (Figures 4-7c and 4-8b), and (3) only the bone (Figure 4-7d and 4-8c). The fourth and final version of each specimen model included only the bone, but the boundary conditions at the specimen ends were set up such that they would provide the same radial constraints as would be provided by the end-caps (4).
Case (1) most closely matched the experimental set-up so was used as the baseline against which the other, more simplified, cases were compared.

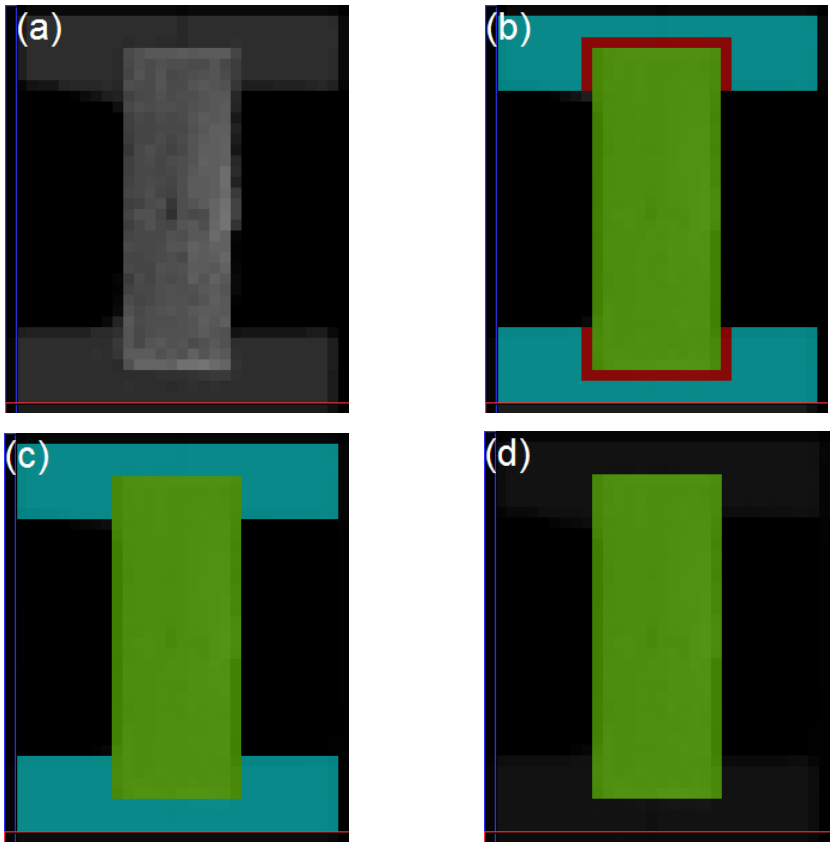

Figure 4-7. Vertical cross sections through (a) unmasked downsampled specimen image stack, and the same specimen image stack with masks applied for (b) bone (green), cement (red) & endcap (blue), (c) bone and endcap and (d) bone only.

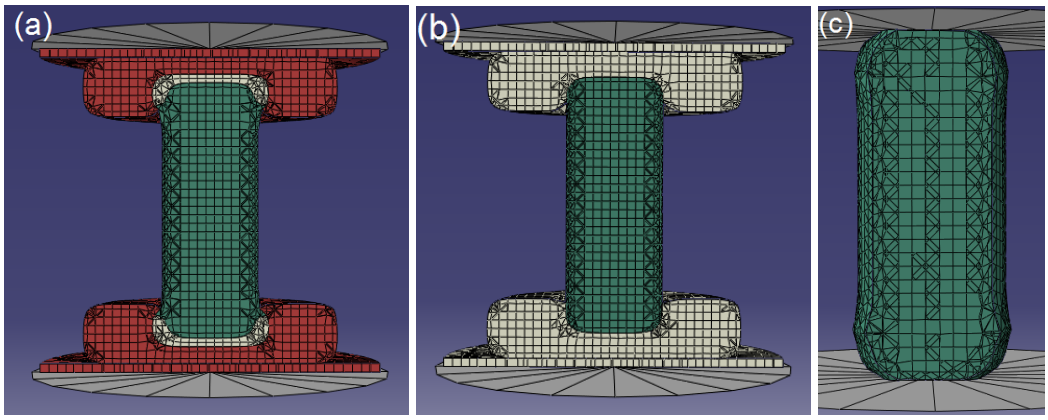

Figure 4-8. Vertical cross sections through example hFE models meshes corresponding to cases (a) 1, (b) 2 and (c) 3.

The contact conditions between each of the regions of the model (bone, cement and endcaps) were uniformly set to the 'rough' setting (no slip between the contact surfaces) and did not allow separation in the direction normal to the interface.

In all four cases boundary conditions were applied to the reference node in the centre of each analytical rigid surface (Figure 4-9) to provide similar constraints to the contact with the loading platens in the experimental compressive test.

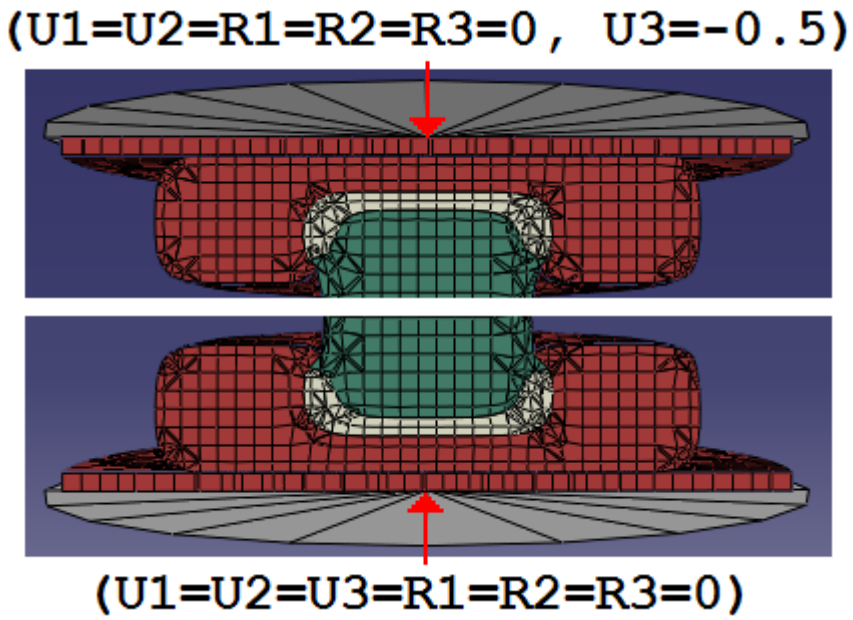

Figure 4-9. Initial constraint and applied displacement boundary conditions applied to the hFE models.

In the case of (4), additional boundary conditions were applied around the end-surfaces of the bone to provide a radial constraint in a similar manner to the end caps. The nodes that formed the 'bone' half of the contact region between the bone and end caps were then constrained in the x and y directions (Figure 4-10). This prevented any barrelling and radial deformation at the ends of the specimen.

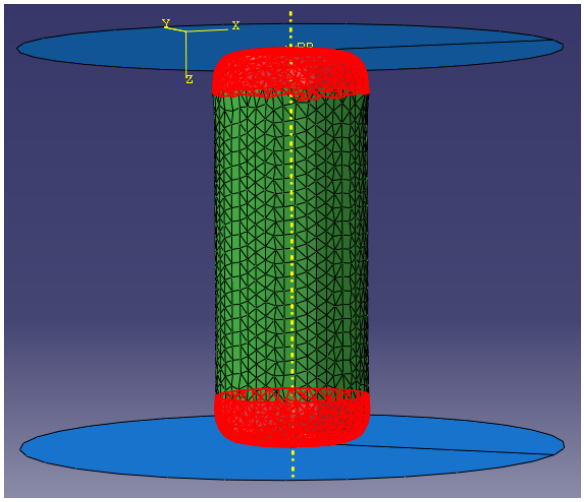

Figure 4-10. Location of nodes constrained on models using case (4) in x and y directions to replicate constraint effect due to the end-caps.

In each case, all the model regions were assigned homogeneous material properties (Section 4.1.4.1) to minimize the influence of specimen-specific material or structural properties.

4.2.1.2. Results

The results are presented in Figure 4-11. The absolute mean error was calculated by taking the percentage difference in stiffness between cases (2), (3) and (4), and case (1), and taking an average across all four specimens. The mean solution time was the average time in seconds required to solve the hFE models in ABAQUS. The error bars give the standard deviation of the percentage error in each case.

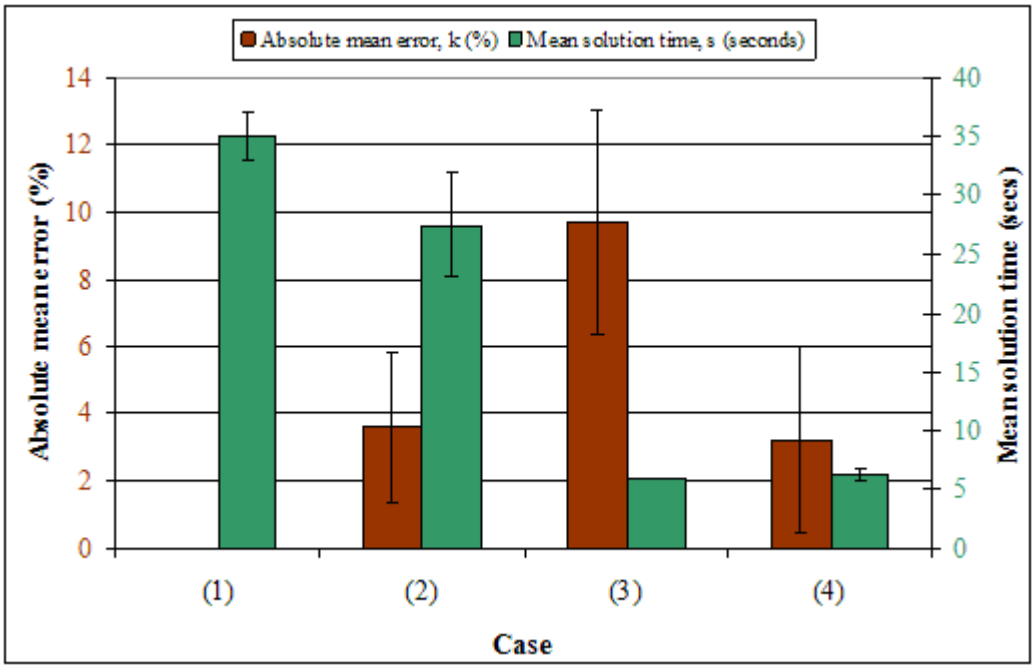

Figure 4-11. Results for the sensitivity study specimen hFE models. The error bars give the standard deviation of the percentage error between cases (2), (3) and (4), and the reference case (1).

4.2.1.3. Discussion

As shown in Figure 4-11, case (2) led to a small increase in error when compared to the full model (1) and a small decrease in solution time. Case (3) led to a considerable (approximately 83 %) reduction in solution time, but at the cost of an approximately three-fold increase in error when compared to (1). The best performance in terms of trade-off between accuracy and solution time was provided by case (4), which led to the same reduction in solution time, with less than one-third of the associated increase in error.

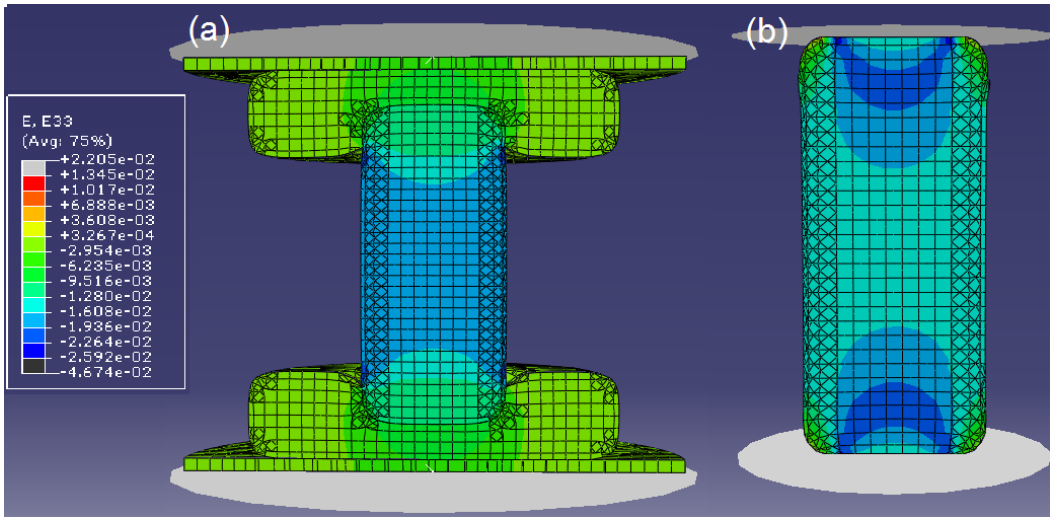

Figure 4-12. Vertical cross-section through contour plot of strain in the z-direction for Specimen 4 in (a) case (b) and (c). The contour scaling is the same in both cases.

The distribution of strain in the z-direction across a specimen in cases (2) and (3) is compared in Figure 4-12 on a common contour scale. From this it is clear that the removal of the endcaps changes the strain distribution within the specimen, reducing the strain in the main body of the specimen and increasing the strain at the specimen ends - particularly in the region at approximately 20 % of the specimen end-midpoint distance.

The strain in the z-direction across the same specimen in case (4) is shown in Figure 4-13. From this it is clear that the difference in strain distribution between cases (2) and (4) is even greater than between cases (2) and (3). While the level of strain around the centre of the specimen is closer to that seen in case (2) than in case (3), the pattern of strain distribution at the specimen ends is markedly different. This difference in strain distribution at the specimen ends between cases (2) and (4) suggests that the application of radial constraints around the specimen ends does not adequately reproduce the effects of the end caps within the model.

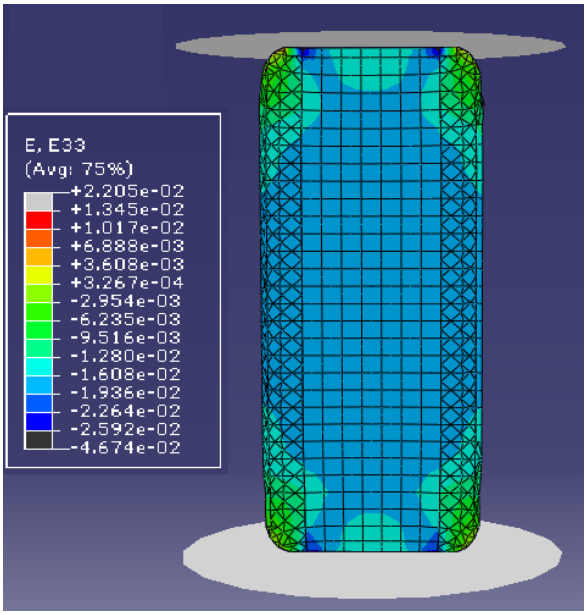

Figure 4-13. Vertical cross-section through contour plot of strain in the z-direction for Specimen 4 in case (4). The contour scaling is the same as in Figure 4-12.

Figure 4-14. Close-up of vertical cross-section through contour plot of strain in the z-direction for Specimen 4 in case (4) showing reduction is specimen cross-sectional area due to ScanIP image smoothing algorithms. The contour scaling is the same as in Figure 4-12.

Another important point to consider is that in cases (2) and (4), the removal of the end caps exposes the specimen ends. Although the specimens themselves were sharply trimmed perpendicularly to the lengthwise specimen axis, the smoothing algorithms used by the ScanIP hFE model generation software effectively put a radius on the edges of the specimen within the model. As seen in Figure 4-14, this clearly leads to a reduction in the specimen cross-sectional area at the points at which the boundary conditions are applied and an overall increase in strain in the z-direction at the specimen ends when compared to case (2), and would lead to a corresponding reduction in stiffness.

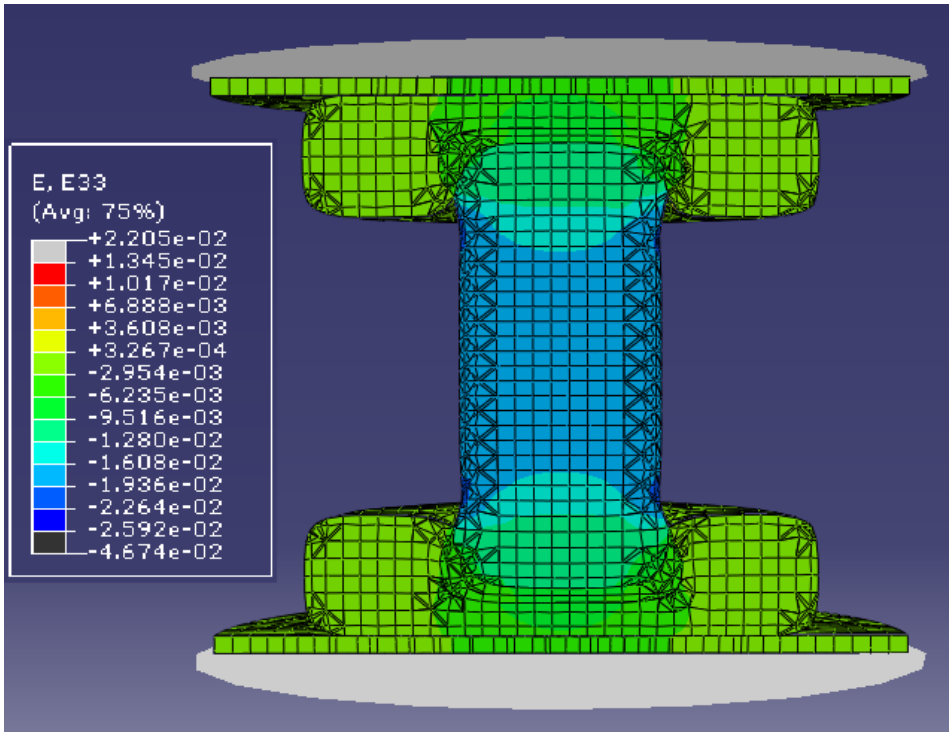

Figure 4-15. Vertical cross-section through contour plot of strain in the z-direction for Specimen 4 in case (1).

As can be seen in Figure 4-15 the inclusion of the cement layer between the bone and endcaps does not affect the strain distribution within the specimen. As this is the case, the small percentage difference in overall stiffness between cases (1) and (2) can be ignored.

4.2.1.4. Conclusions

Removal of the end caps led to non-negligible changes in the magnitude and more importantly the strain distribution within the models. As it was considered important that the hFE models accurately reproduce the strain distribution present in the experimental specimens as closely as possible, all further models featured explicitly modelled end caps. Including the end cap PMMA cement layer in the models – as in case (1) – led to a negligible change in overall stiffness and strain distribution when compared to case (2) while increasing the solution time and it was thus was omitted from future models.

4.2.2. hFE model sensitivity to experimental boundary conditions

Further sensitivity tests were carried out to explore the effect of varying the boundary conditions at the specimen ends on the stiffness predictions of a subset of hFE models. Such tests are important as they give an indication as to the robustness of the hFE model predictions with regard to the expected differences between the experimental and hFE testing, and can lead to a better understanding of the likely sources of error.

Two sets of tests were conducted; firstly to explore the hFE model sensitivity to the direction of the applied deformation and secondly, to explore the hFE model sensitivity to the nature of the contact condition between the analytical rigid plates and the specimen end caps. In both cases models featuring μCT grayscale-dependent bone material properties were used as the non homogenous nature of the specimens may affect the outcome of the tests.

4.2.2.1. Direction of the applied deformation

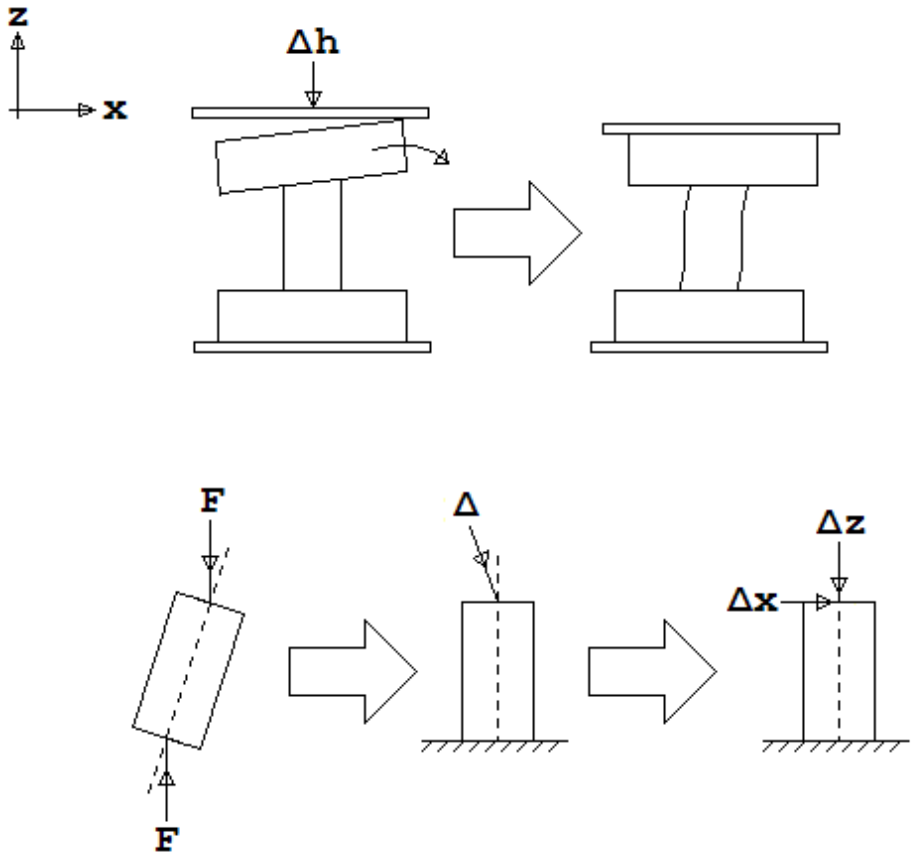

Figure 4-16. Example of non-parallel end-cap loading surfaces and the resulting effect on the applied displacement.

Upon loading the specimens between the compression platens of the materials testing machine, it appeared that in some cases the Delrin end caps at the specimen ends were not exactly plano-parallel with one-another (shown greatly exaggerated in Figure 4-16). The specimen and hFE model stiffness values were calculated from the reaction force measured in the z-axis only and as such an off-axis applied deformation in the experimental compressive test would result in underestimation of the specimen stiffness.

Though the angle between the end caps was very small – of the order of 1 degree – and as such considered likely to have a negligible effect on the measured stiffness, a sensitivity study was conducted to investigate the effect of varying the direction of the

applied deformation and ascertain if this could be discounted as a source of error between the experimental and hFE results.

Methods

Three models featuring μCT grayscale-dependent bone material properties (Section 4.1.4.2), generated from specimens taken from one spine, were selected at random. Models featuring μCT grayscale-dependent bone material properties were selected as it was considered likely that the mechanical response of the specimens would be affected by the stiffness distribution throughout the bone, such that models featuring homogenous bone material properties would likely underestimate the specimens' sensitivity to changes in the constraints.

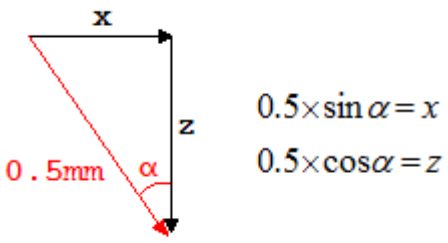

Figure 4-17. Calculation of applied displacements in the x and z directions due to off-axis loading.

Component deflections in the x-axis and z-axis that were assumed to be equivalent to an off-axis overall applied deformation (as shown in Figure 4-16) were calculated as shown in Figure 4-17 and applied to a reference node at the centre of the rigid plate tied to the upper surface of the model. Each of the three models was solved in ABAQUS for four values of α ranging from 0 degrees to 1.5 degrees in 0.5 degree increments.

Results

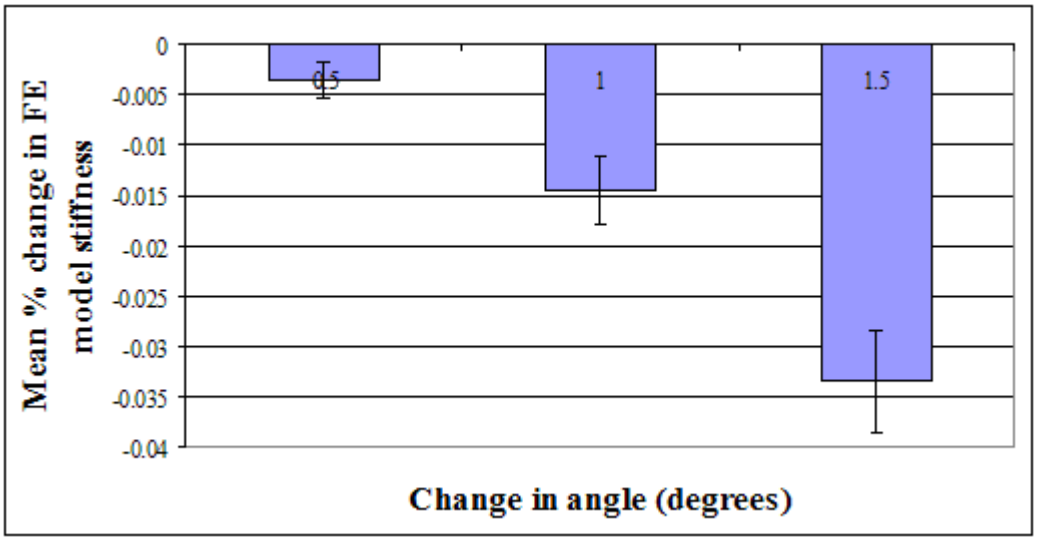

Figure 4-18. hFE model sensitivity to off-axis application of the applied displacement in terms of mean percentage change in predicted stiffness. The error bars denote the standard deviation.

The results are presented in Figure 4-18, which shows mean percentage change in hFE model stiffness across the three specimens as α increases. It can be seen that the hFE model stiffness predictions demonstrate low sensitivity to varying the direction of the applied displacement, decreasing by only 0.03-0.04 % as α varies from 0 to 1.5 degrees.

4.2.2.2. End cap boundary conditions

One aspect of the experimental setup that was simplified in the construction of the hFE models was the contact interface between the endcaps and the analytical rigid plates used within the model (Figure 4-19) to represent the loading platens of the Instron compressive testing device.

In the experimental tests the endcaps were not clamped or fastened in place except by the frictional force acting between them and the surface of the loading platens. The computational complexity of the hFE models was greatly reduced by defining a tied

contact (no relative motion between the surfaces). This was thought to be a reasonable simplification as the lateral forces acting on the endcaps were expected to be negligible.

A sensitivity study was conducted to investigate the effect of this simplification on the hFE model stiffness predictions.

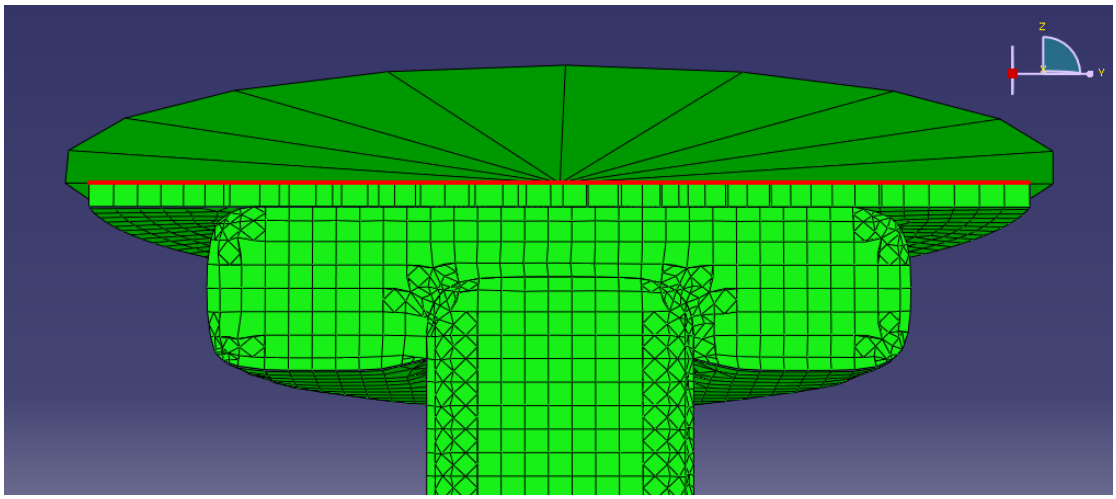

Figure 4-19. Vertical cross-section through an example specimen hFE model showing the location of the tied contact between the elements inserted to restore full end-cap height and the analytical rigid surfaces representing the loading platens.

Methods

Models generated from six corresponding specimens were selected at random. For the same reasons described in the previous study all six featured μCT grayscale-dependent bone material properties. In each case, in addition to the 'standard' tied contact between the analytical rigid plates and the upper and lower end caps, three further contact condition cases were simulated:

A tied contact was applied between the rigid plates and end caps but the constraints in the x and y directions applied to the rigid node at the centre of the upper rigid plate were removed such that it could translate laterally in both axes. This represented the possibility of relative lateral motion between the top and bottom end caps. The rotational constraints applied to the reference node were maintained to ensure that the top and bottom surfaces of the model remained plano-parallel.

A sliding frictional contact was defined between the upper rigid plate and the surface of the upper end cap, using a coefficient of friction of $\mu = 0.35$ – the coefficient of sliding friction specified for steel on Delrin contact (Delrin Design Guide – Module III, Dupont). The coefficient of sliding friction was chosen as it was stated to be higher than the coefficient of static friction ($\mu = 0.2$). The interface between the lower rigid plate and the surface of the lower endcap was tied.

A sliding frictional contact was applied to the interface between both rigid plates and their respective end caps, in both cases using the same coefficient of friction as in (ii).

Results

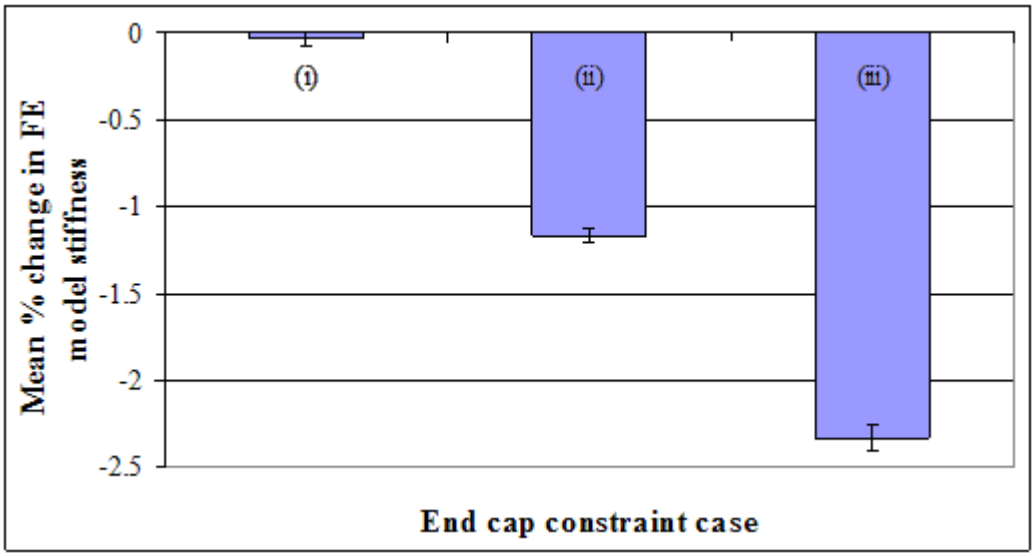

Figure 4-20. hFE model sensitivity to the nature of the end-cap constraints in terms of mean percentage change in predicted stiffness. The error bars denote the standard deviation.

The results of the sensitivity study are presented in Figure 4-20, which shows the mean percentage change across the six specimens in hFE model stiffness compared with the standard end cap – platen contact conditions and translational constraints.

Specimen	X force (N)	Y force (N)
7-6-11_L2	15.11	10.90
7-6-11_L5	0.88	5.84
12-5-11_L1	0.33	9.50
12-5-11_L3	3.57	3.12
12-5-11_L5	4.86	4.90
12-5-11_L6	1.42	4.21

Table 4-1. hFE model reaction forces in x and y directions measured at the point of application of a 0.5 mm displacement.

Table 4-1 presents the reaction forces in the x- and y-axis at the reference point at the centre of the upper analytical rigid plate to which the deformation is applied measured under the standard end cap – platen contact conditions and translational constraints.

4.2.2.3. Discussion

The results presented in Figure 4-18 show that the hFE model stiffness predictions demonstrate low sensitivity to varying the direction of the applied displacement. The change as α was varied from 0 to 1.5 degrees was several orders of magnitude lower than the maximum error between the experimentally measured and hFE model predicted stiffness values. This suggests that it is unnecessary to reproduce the slight off-axis loading seen to be present in some of the experimental compressive tests.

The results in Figure 4-20 show a consistent pattern of decreasing hFE model stiffness in all cases as the lateral boundary conditions applied to the models become progressively less restrictive. The magnitude of the reduction in hFE model stiffness between the stiffest (standard BCs) and least stiff (both interfaces sliding) boundary condition cases is small – a mean average of 2.3 % - suggesting that the model predictions are robust with regard to the contact conditions applied between the endcaps and the corresponding rigid plates.

Measuring the lateral reaction forces acting in the x- and y-axes in the hFE models when a tied contact is used throughout (Table 4-1) suggests that this is a reasonable result, as the forces in each case are very small by comparison with the reaction forces acting in the direction of the applied displacement.

4.2.2.4. Conclusions

The results of the two sets of sensitivity analyses carried out on random subsets of the specimen-specific greyscale-dependent hFE models suggested that the simplified representations of the experimental test setup were unlikely to cause significant error in the hFE model stiffness predictions when compared to the experimentally measured specimen stiffness values. It is therefore appropriate to simplify the model by (i) assuming tied contact between the analytical rigid plates representing the compressive loading platens and the end caps and (ii) assuming that the deformation was applied solely along the z-axis.

4.3 Standard hFE model configuration

The results of the hFE model sensitivity testing were used to define a standard model configuration (Figure 4-21). All of the hFE models used to derive a generalised μCT greyscale-modulus relationship were configured in this manner.

In summary:

- The Delrin end caps were modelled explicitly. In cases where the original μCT images did not capture the full height of the end caps, additional layers of identically configured elements were tied to the end cap faces to restore them to their full height (8 mm). (Section 4.2.1)

- The PMMA cement layer between the trabecular bone core and the Delrin end caps was not modelled. Instead a tied contact was defined between the bone and end caps. (Section 4.2.1)

- A tied contact was defined between the upper and lower end cap surfaces and the analytical rigid plates representing the loading platens of the materials testing equipment. (Section 4.2.2)

- The boundary conditions applied to the top-most analytical rigid plate – representing the applied deformation – completely constrained the central reference node along the x- and y-axes in translation, and around the x-, y- and z-axes in rotation (U1=U2=UR1=UR2=UR3=0). A -0.5 mm displacement was applied along the z-axis. (Section 4.2.2.)

- The boundary conditions applied to the lower analytical rigid plate – representing the fixation of the lower platen – completely constrained the central reference node along the x-, y- and z-axes in translation, and around the x-, y- and z-axes in rotation (U1=U2=U3=UR1=UR2=UR3=0).

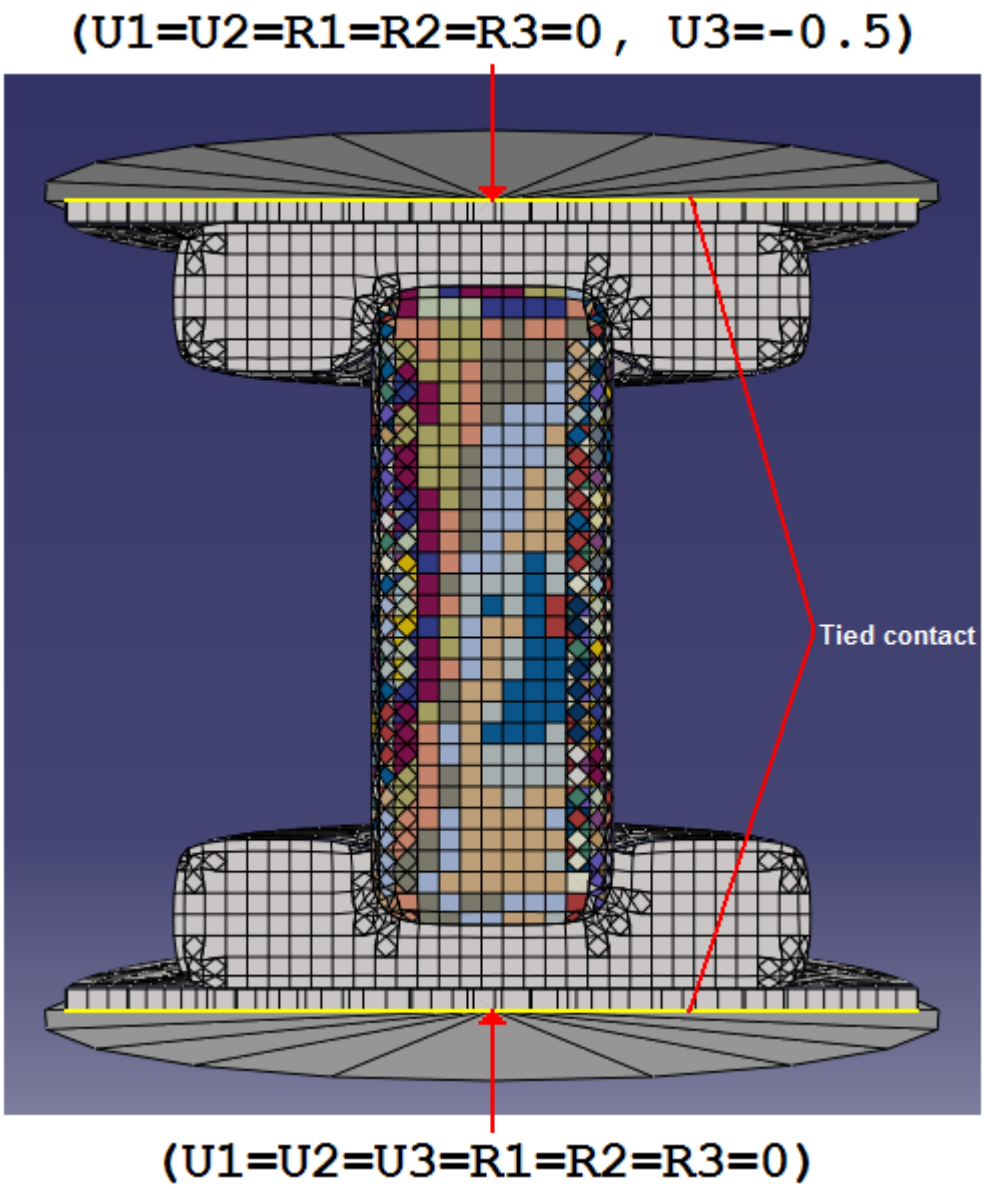

Figure 4-21. Standard hFE model constraint configuration.

4.4. Greyscale-modulus relationship derivation

Having finalised the degree of simplification to be utilised in the specimen-specific hFE models and explored the sensitivity of their stiffness predictions to the applied boundary conditions, the hFE models were then used to derive a generalised μCT greyscale-modulus relationship for ovine lumbar vertebral trabecular bone.

hFE models of all of the experimental specimens were generated utilising μCT greyscale-dependent material properties whereby the Young's modulus of each of the elements representing trabecular bone was assigned according to the linear relationship E = GS*k (see Section 4.1.4.2). In this case k was initially set to equal 1.

The general procedure was as follows: a chosen set of the hFE models was divided into Build and Validate subsets. Models in the Build subset were then tuned by iteratively adjusting k until the average percentage error between the hFE model predicted stiffness values and the corresponding experimentally measured stiffness values was minimised. This value of k was then applied to the hFE models within the Validate subset and the models solved in ABAQUS. This enabled the predictive accuracy of similar hFE models – outside of the derivation subset – assigned bone material properties according to the same μCT greyscale-modulus relationship to be evaluated.

4.4.1. Reduced dataset runs

To determine the effect that the choice of specimens used in the Build subset would have on the resulting μCT greyscale-modulus relationship, a number of sets of runs were carried out utilising different Build and Validate subsets taken from a chosen initial set of hFE models. This would allow estimation of the likely error in terms of predicted stiffness, when using a generalised μCT greyscale-modulus relationship determined from an available set of experimental specimens which is applied to other greyscale-dependent specimen-specific hFE models of ovine lumbar trabecular bone.

4.4.1.2. Methods

Copies of the twelve specimen-specific hFE models generated from specimens fabricated from two ovine lumbar spines (12-5-11 and 7-6-11) were randomly allocated to a Build and Validate subset, each comprising six models. This process was repeated five times, resulting in five different Build and Validate subsets.

In each case, the hFE models were generated using μCT greyscale-dependent bone material properties based on the linear μCT greyscale-Young's modulus relationship E = GS*k, where k = 1 (see Section 4.1.4.2). For each of the five sets the process is described below. A flowchart outlining the work flow for Build subset 1 is shown in Figure 4-23.

The hFE models in the Build subset were configured and solved in ABAQUS as described in Section 4.3 and the average difference between the hFE model stiffness predictions and the corresponding experimentally derived stiffness values (Δk_{mean}) was calculated.

A Matlab script developed in-house was then used to modify k within the hFE models such as to reduce Δk_{mean}. Thusly modified, the FE models were then solved in ABAQUS again, and the process of modifying k to reduce Δk_{mean} was repeated a second time.

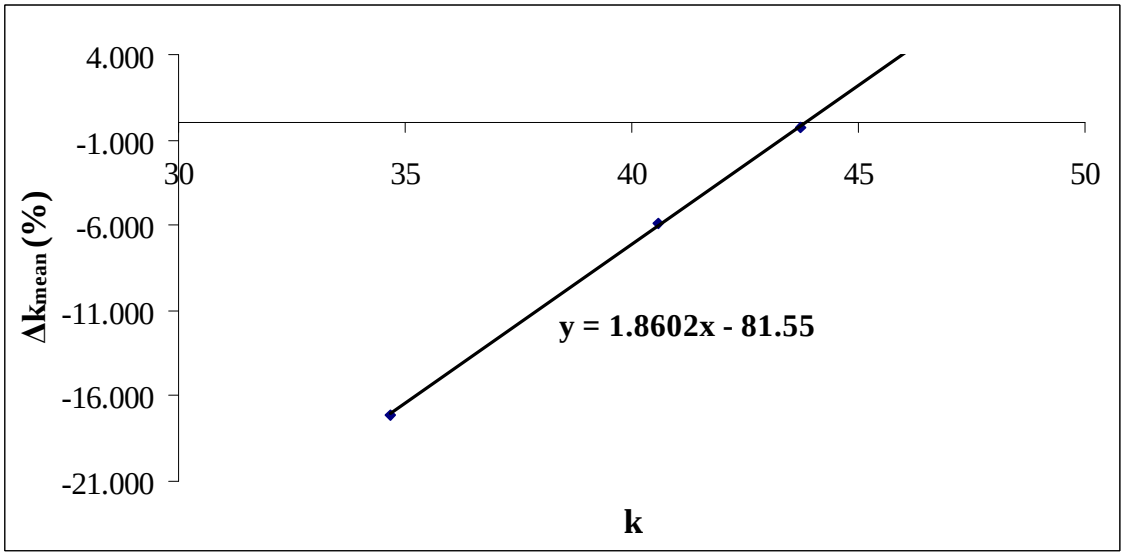

Figure 4-22. Mean percentage error between hFE predicted and experimentally determined specimen stiffness plotted against µCT grayscale-modulus conversion factor.

By plotting the two values of Δk_{mean} against k (Figure 4-22) and assuming a linear relationship between them, the resulting equation was solved for y=0 to give the value of k required to reduce Δk_{mean} to zero. This was confirmed by repeating the process of modifying k within the FE models to this value and solving them in ABAQUS once more.

Lastly, the same Matlab script was then used to modify the value of k within the models in the Validate subset to equal the final value of k used within the models in the Build subset. The models were then solved in ABAQUS.

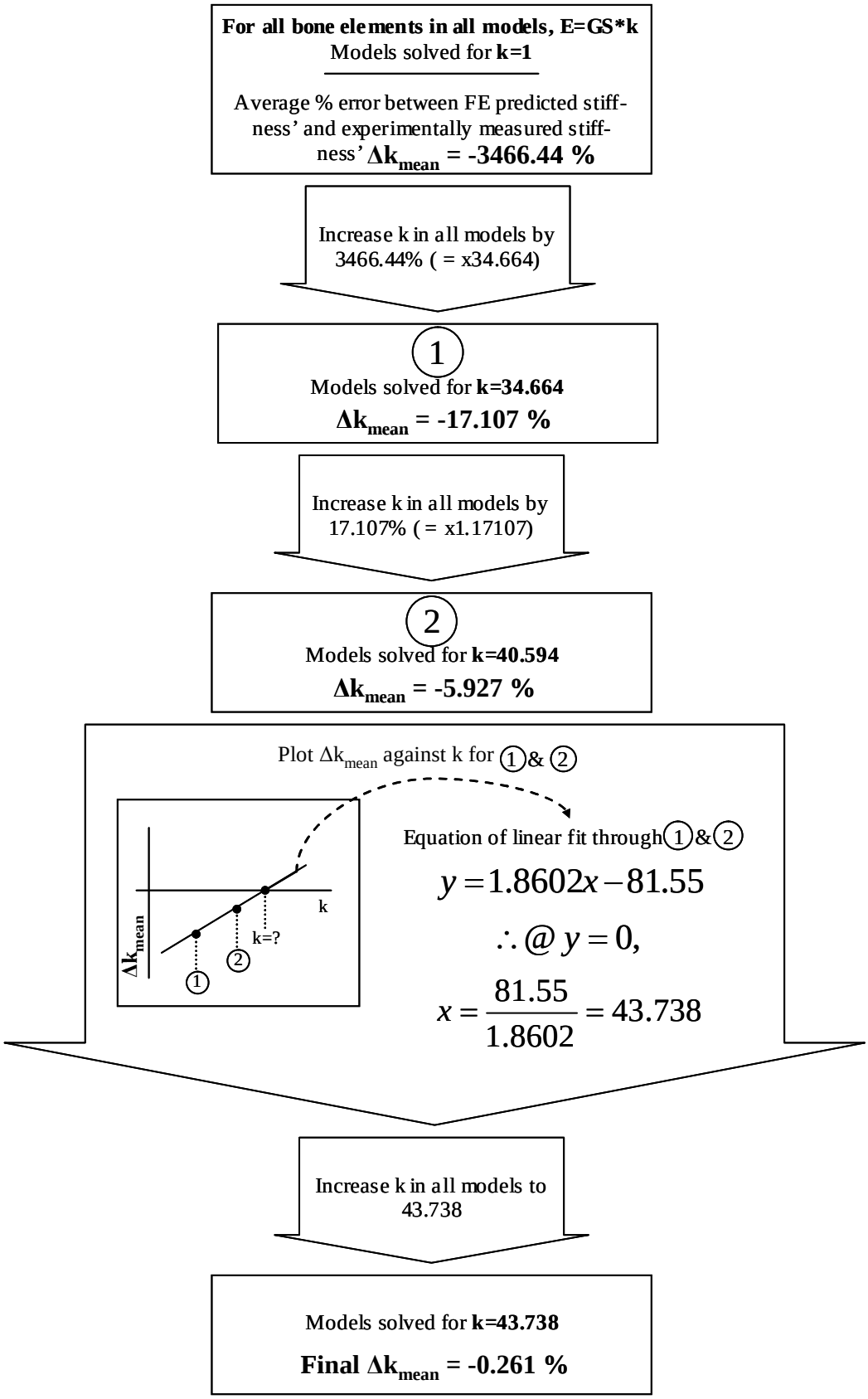

Figure 4-23. µCT grayscale-modulus relationship derivation workflow.

4.4.1.3. Results

The results of the five sets of greyscale-modulus relationship derivation runs are shown in Figure 4-24 and Table 4-2. The average percentage error for the Build and Validate subsets - and the overall average error across both – for each of the five sets are shown in Figure 4-24. The final value of k iteratively derived using each of the five Build subsets, alongside the mean and standard deviation are given in Table 4.2.

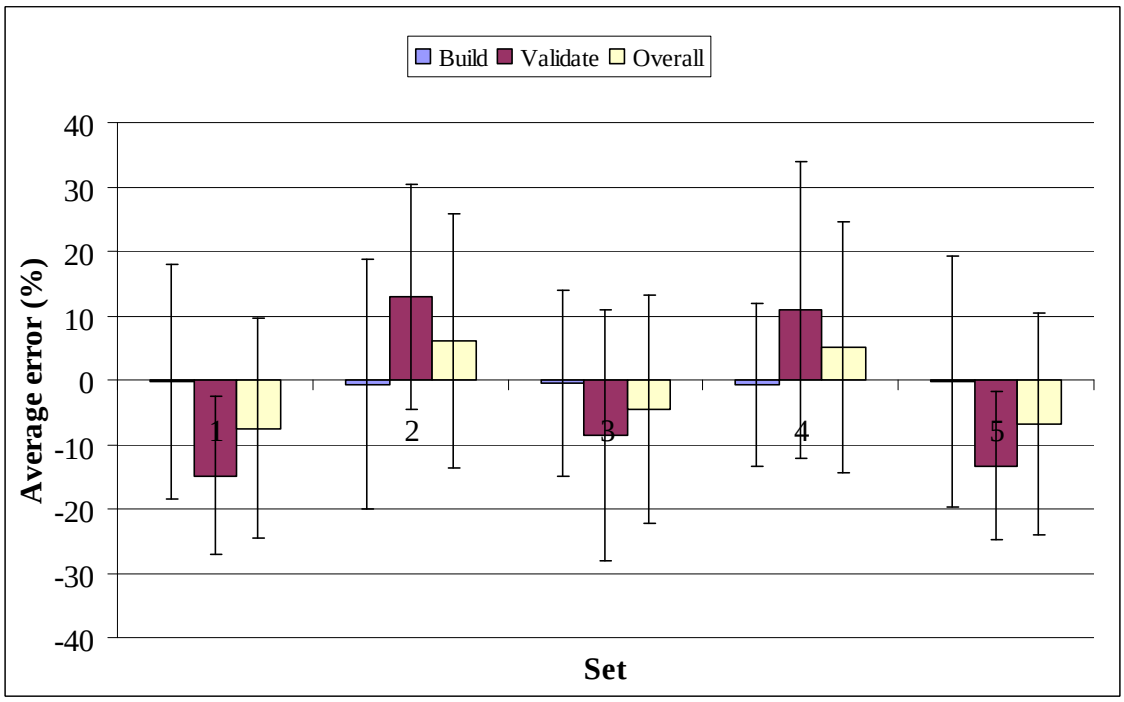

Figure 4-24. Mean percentage error across the Build subset, Validate subset and overall, for each of the five µCT grayscale-modulus relationships. The error bars denote the standard deviation in each case.

Build subset	1	2	3	4	5	Mean	S.D.	S.D. (%)
GS->E	43.74	52.44	45.56	51.78	44.21	47.54	3.78	7.95

Table 4-2. µCT greyscale-modulus relationship (GS->E) derived using each of the five Build subsets. Included are the mean and standard deviation of the five conversion factors, and the standard deviation expressed as a percentage of the mean.

4.4.1.4. Discussion

While the variation in the μCT greyscale-modulus relationship within the sub-population of specimens fabricated from two ovine lumbar spines is expected to be smaller than that which would be observed across the global population, as shown in Table 4-2, the resulting conversion factor (k) varied by almost +/- 10 % depending on which specimens from this sub-population were used to derive it.

As shown in Figure 4-24, the average absolute percentage error in hFE model predicted stiffness across all five Validate subsets is approximately 12 %. Unless the sub-population from which the specimens used in the Build subsets were chosen to exhibit an average μCT greyscale-modulus relationship similar to the average across the global population, the absolute average percentage error in hFE model stiffness predictions would be expected to increase for specimens chosen from outside this sub-population.

Ideally, the way to minimise the average error in hFE model predicted stiffness across any given group of specimen-specific models would be to ensure that the μCT greyscale-modulus relationship within the specimens used in the Build set is as close to as possible to the global population average. However, as the global population average is unknown, it is recommended that the widest possible range of specimens should be used to derive k.

4.4.2. Full dataset runs

4.4.2.1. Methods

Other than the composition of the Build and Validate subsets, the methods were the same as used in the previous study in Section 4.4.1. Of the entire available set of specimen-specific hFE models, copies of 20 models generated from specimens

fabricated from all five available ovine lumbar spines were randomly allocated to either the Build or Validate subsets – comprising 15 and five models respectively.

4.4.2.2. Results

The final value of k that produced the minimum mean percentage difference between the hFE model predicted stiffness values and experimentally derived specimen stiffness values was k = 45.054.

The results in terms of average percentage error between hFE predicted stiffness and experimentally measured stiffness are presented in Figure 4-25, for specimens in the Build subset, the Validate subset and ‘All’, encompassing both.

Figure 4-26 shows the concordance between the hFE model predicted stiffness values and the experimentally derived specimen stiffness values, with the linear plot denoting an ideal 1:1 agreement. Figure 4-27 compares the hFE model predicted stiffness values and the experimentally derived specimen stiffness values by rank, from most to least stiff. The number of places on the list gained or lost by each specimen is indicated.

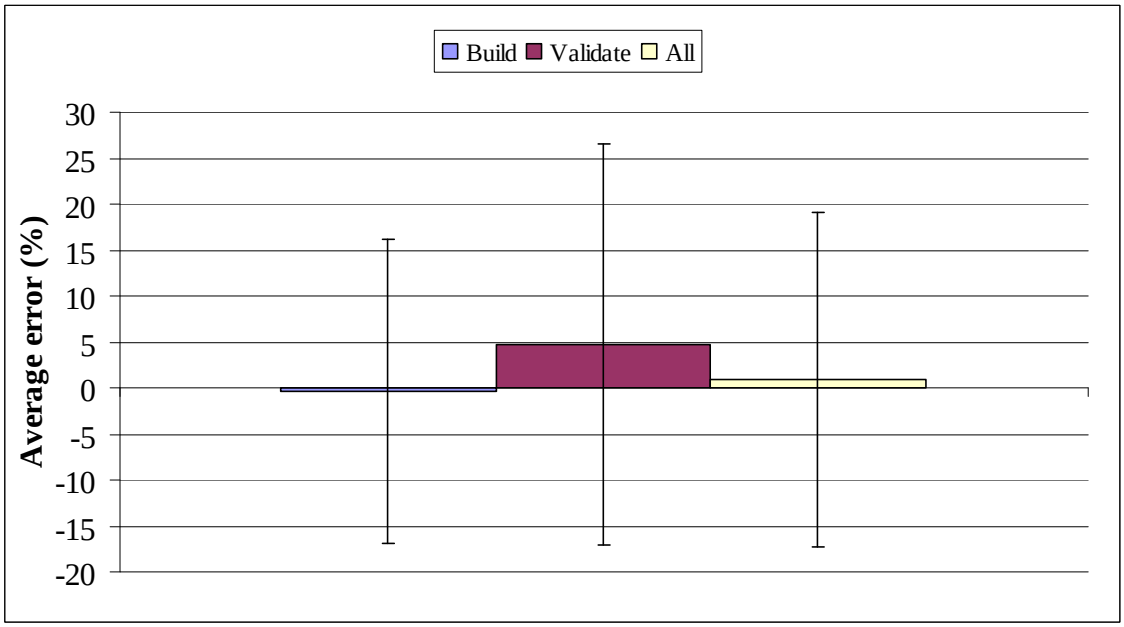

Figure 4-25. Mean percentage error between hFE predicted and experimentally determined stiffness across the Build subset, Validate subset and overall. The error bars denote the standard deviation in each case.

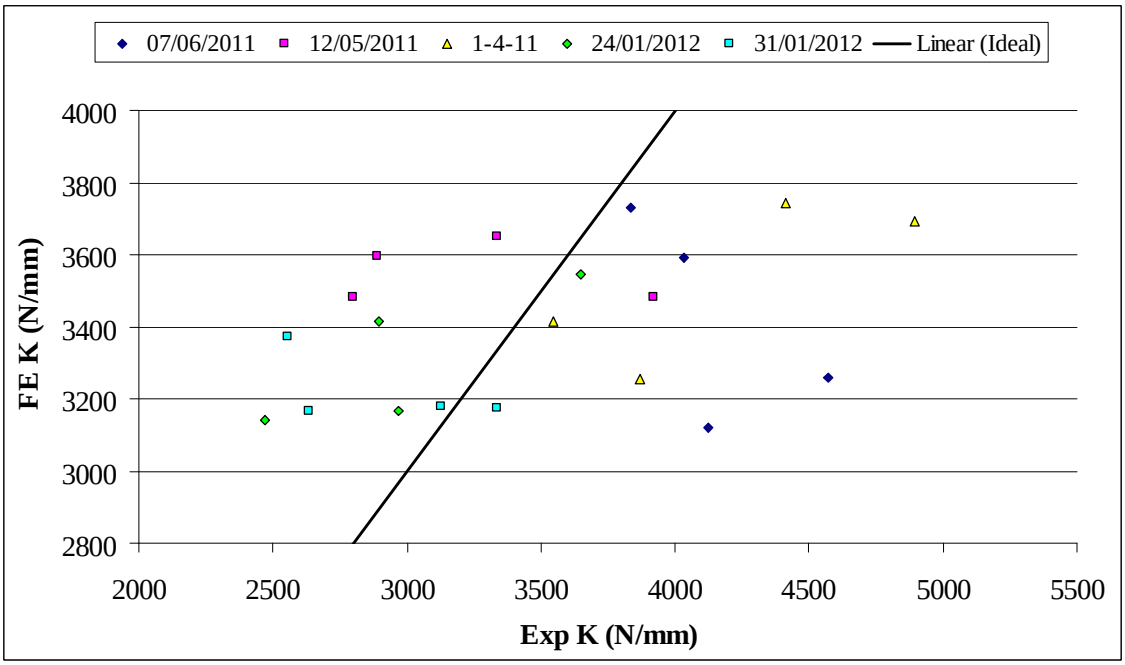

Figure 4-26. Concordance between hFE predicted and experimentally determined stiffness for all 20 specimens in the Build and Validate subsets. The linear plot denotes the ideal 1:1 relationship between hFE predicted and experimentally determined stiffness.

Key	
+11 & up	
+9 to +11	
+5 to +8	
+2 to +4	
+1 to -1	
-2 to -4	
-5 to -8	
-9 to -11	
-12 & down	

Specimen	Exp K (N/mm)	Specimen	FE K (N/mm)
1-4-11_L5	4895	1-4-11_L6	3744.640
7-6-11_L5	4573	7-6-11_L6	3730.240
1-4-11_L6	4412	1-4-11_L5	3694.540
7-6-11_L7	4127	12-5-11_L1	3649.020
7-6-11_L2	4033	12-5-11_L6	3595.8
12-5-11_L4	3919	7-6-11_L2	3590.68
1-4-11_L2	3868	24-1-12_L7	3546.6
7-6-11_L6	3835	12-5-11_L4	3483.58
24-1-12_L7	3645	12-5-11_L5	3482.220
1-4-11_L4	3545	1-4-11_L4	3413.98
31-1-12_L4	3338	24-1-12_L4	3412.74
12-5-11_L1	3337	31-1-12_L7	3371.260
31-1-12_L6	3126	7-6-11_L5	3258.46
24-1-12_L6	2968	1-4-11_L2	3254.1
24-1-12_L4	2896	31-1-12_L6	3180.460
12-5-11_L6	2891	31-1-12_L4	3173.86
12-5-11_L5	2799	24-1-12_L6	3166.660
31-1-12_L5	2632	31-1-12_L5	3166.08
31-1-12_L7	2554	24-1-12_L5	3141.3
24-1-12_L5	2473	7-6-11_L7	3120.06

Figure 4-27. hFE predicted and experimentally determined specimen stiffness ranked from most to least stiff. The colour-coding denotes the number of places on the list gained or lost by each specimen (see key).

4.4.2.3. Discussion

Firstly, it is clear from the results presented in Figure 4-25 that the average accuracy of the stiffness predictions of the hFE models in the Validate subset is improved compared to the Validate subsets in the previous study, with a mean percentage error of 4.7 % in this case, down from a mean absolute percentage error across all five previous Validate subsets of 12.1 %. The final µCT greyscale-modulus conversion factor in this case (45.054) is also approximately equal to the average of the µCT grayscale-modulus conversion factors resulting from the previous study (47.54).

These results support the idea that using a larger Build subset, presumably comprising more diverse specimens, has the effect of reducing the influence of outlying specimens and leads to a µCT greyscale-modulus relationship more representative of ‘average’ bone. However, the similar standard deviation suggests that even though the use of a larger Build subset can lead to good accuracy on average across the whole population, the percentage error in individual cases can be significant.

Secondly, although the average accuracy of the hFE model predictions was improved there were a number of aspects of the results which were contrary to expectations:

Figure 4-27 ranks the specimens by both their experimentally measured stiffness and their hFE predicted stiffness, colour-coded to denote how the hFE predicted stiffness varies from the experimentally measured stiffness. The hFE predicted and experimentally measured stiffness rankings are significantly different.

The spread of the experimentally measured specimen stiffness values is substantially greater than the spread of the hFE predicted stiffness values (Figure 4-26), exhibiting standard deviations as a proportion of the mean of 19.7% and 6.1% respectively.

Groups of specimens fabricated from a particular ovine spine tend not to straddle the 1:1 ideal concordance line in Figure 4-26, the hFE predicted stiffness either being typically higher or lower than the corresponding experimentally measured stiffness. This seems to suggest that the lack of concordance between the experimentally measured and hFE predicted stiffness is due to some commonality within each spine, be it structural or material property related.

The hFE model sensitivity studies reported in Section 4.2.2. discounted the chosen simplifications and boundary conditions as sources of significant differences between the experimentally-derived and hFE-predicted stiffness results. This suggests that the differences were more likely caused by an inability of the downsampled hFE models and their material properties, assigned according to a linear μCT greyscale-modulus relationship, to fully reproduce some aspects of the mechanical behaviour of the specimens.

This is supported by further investigation of the results of the previous study. The average experimentally measured stiffness values of each of the five Build subsets is plotted in Figure 4-28 against its respective μCT greyscale-modulus multiplier (k). There is a non-negligible correlation between them (r^2 = 0.8657). This would not be expected if the μCT greyscale distribution were the main driver of specimen stiffness, as if there was a global population wide linear μCT greyscale-modulus relationship higher stiffness would simply follow from higher specimen density.

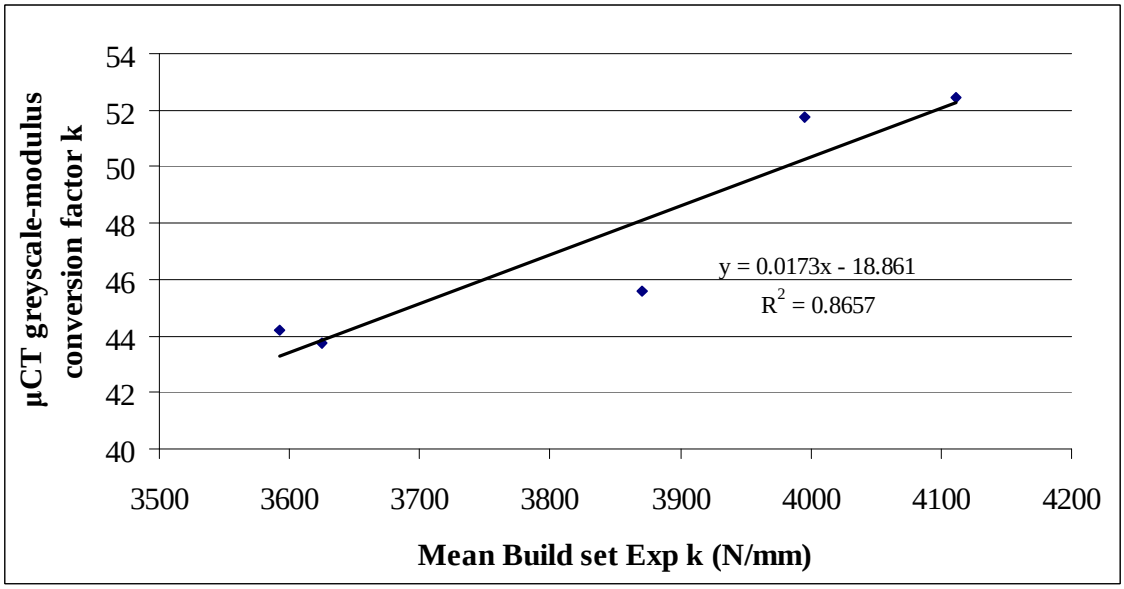

Figure 4-28. Average experimentally determined stiffness of each of the five Build subsets against resulting µCT grayscale-modulus conversion factor derived in each case.

This could suggest that the µCT grayscale-modulus relationship is not linear as previously assumed, but instead follows a power law relationship. As shown in Figure 4-29, if the relationship between µCT greyscale and modulus across the whole population followed a power law then the linear µCT grayscale-modulus conversion factor derived using specimens at B would be higher than that derived using specimens at A.

However, as shown in Figure 4-30, while the use of a power law µCT grayscale-modulus relationship could conceivably correct for the difference in *spread* between the experimentally-measured and hFE-predicted stiffness values, it would have negligible effect on the specimen stiffness *rankings*. As such it is considered unlikely to be the cause of the observed lack of concordance between the experimentally-measured and hFE-predicted stiffnesses.

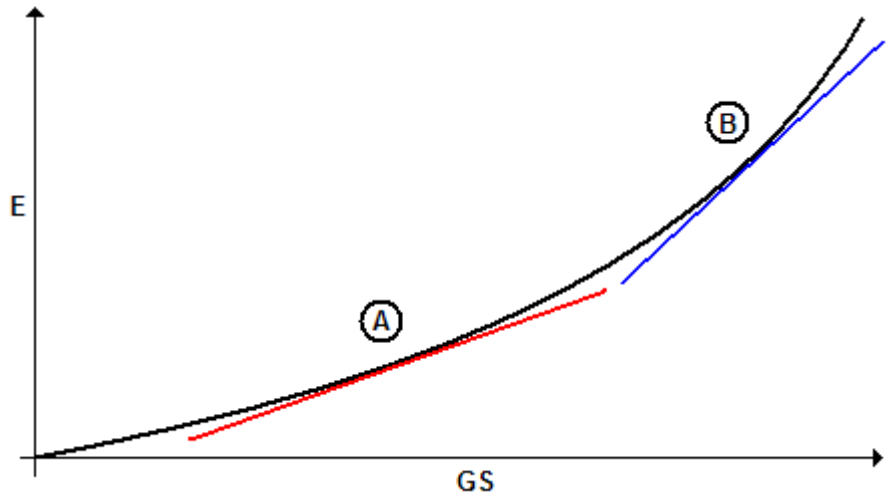

Figure 4-29. If relationship between µCT greyscale and modulus varies according to a power law, a linear µCT grayscale-modulus relationship derived as described would vary depending on where the properties of the Build subset lie within the global range.

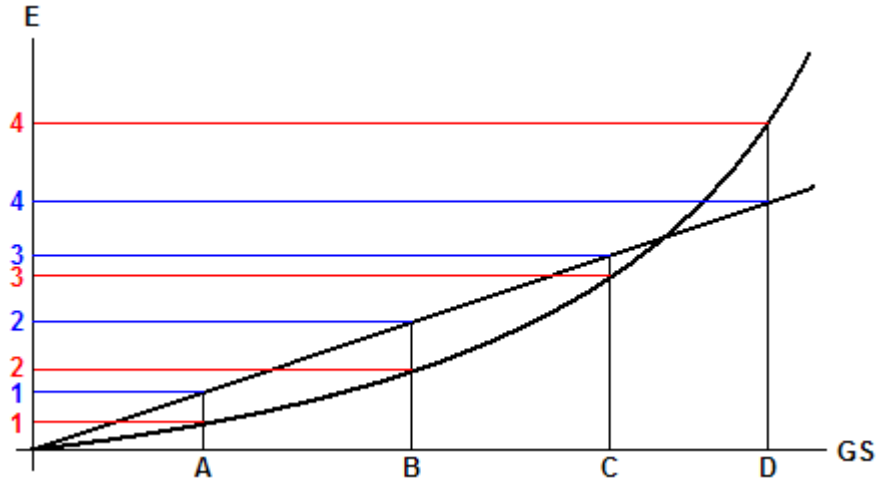

Figure 4-30. Examination of modulus spread and ranking across a given grayscale range for linear and power-law µCT grayscale-modulus relationships.

4.4.2.4. Summary

- In conclusion, a linear µCT greyscale-modulus relationship has been derived from a large subset of the models.

- Whilst the average error in predicted stiffness is relatively small, the models are not able to predict the spread of the experimental results or their ranking.

- This does not appear to be due to the choice of the linear μCT grayscale-modulus relationship, or due to simplifications in modelling the experimental set-up.

- It is suggested that it is likely to be caused by the more general assumptions necessary to develop hFE models that do not capture all the variation in bone morphology and tissue properties from one specimen to another.

4.5 Derivation of a scanner-indipendent μCT density-modulus relationship

4.5.1. Introduction

As previously discussed in Section 2.1.3.2, the use of a μCT greyscale – Young's modulus relationship to assign material properties to bone in hFE models rests on the observation that the apparent behaviour of a volume of trabecular bone spanning more than five trabecular cells across its smallest dimension can be represented by considering the volume as a homogenous solid with a Young's modulus equal to some function of its average bone mineral density (BMD), known as the 'continuum assumption' (Harrigan et al 1988).

In this study, the chosen measure of bone density was the μCT greyscale value as described by Wijayathunga et al (2008). μCT greyscale, however, is a function not only of the underlying material composition, but also the x-ray spectrum, the characteristics of the x-ray detector and the operating mode of the μCT scanner itself (Scanco Medical AG, Brüttisellen, Switzerland. General FAQ: Support). The result of this is that without further calibration the relationship between μCT greyscale and BMD is not consistent between different μCT scanners, or even between different scans made using a particular scanner using varying scan settings. As such, the μCT greyscale – Young's modulus relationship derived in this study would be unlikely to produce appropriate material property values for hFE models generated from specimen μCT scans obtained using an alternative μCT scanner or scan settings.

To preserve scanner independency, μCT greyscale values are often converted into BMD values through the use of a calibrated scan phantom (Crawford, Cann and Keaveny 2003), typically a sample comprising graded concentrations of calcium hydroxyapetite, the main mineral component of bone, used in isolation as the other materials of which bone is comprised have little effect on it's radiopacity (Scanco Medical AG, Brüttisellen, Switzerland. General FAQ: Support). Scanning the calibration phantom using the same scan settings as those used to derive the μCT greyscale – Young's modulus relationship enables the derivation of a BMD - μCT greyscale relationship for

the particular μCT scanner and scan settings. This allows the previously derived μCT greyscale – Young's modulus relationship to be expressed in terms of BMD rather than μCT greyscale, and thus enables it's use to assign bone material properties to hFE models generated from scans created using different μCT equipment and/or scan settings.

4.5.2. Methods

A commercially available calibrated scan phantom (Scanco Medical AG, Brüttisellen, Switzerland) comprising five rods of known calcium hydroxyapetite density was scanned using the same scan settings as were used to image the ovine lumbar vertebral trabecular bone specimens, detailed in Table 3-1. The raw μCT data was converted into a .TIFF image stack using the same approach described in Section 4.1.2, which were then analysed using a proprietary image processing software package (Scan-IP, version 4.2 – Build 140, Simpleware, Exeter, UK) to determine the mean image greyscale of each of the five rods. A function relating BMD - μCT greyscale was then derived by taking the gradient and intercept of a linear fit through the a plot of the mean μCT greyscale values against the known BMD for each rod.

4.5.3. Results

A slice taken from the μCT scan of the calibrated scan phantom is shown in Figure 4-31. The brightness and contrast of the image as reproduced here have been adjusted for clarity.

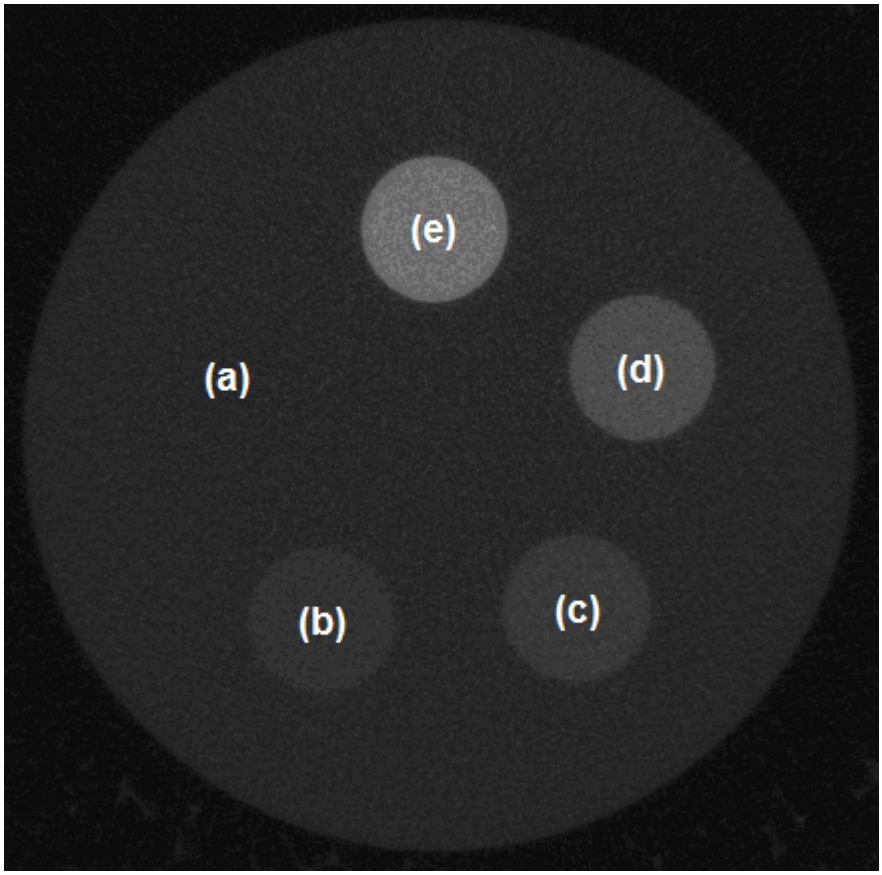

Figure 4-31. μCT cross-section through the calibrated calcium hydroxyapetite scan phantom, showing the 5 rods of increasing calcium hydroxyapetite density (a-e). Rod (a) shares the same calcium hydroxyapetite density as the matrix within which the rods are set, and as such is not discernable from it within the μCT images.

A plot of μCT greyscale against calcium hydroxyapetite density (BMD) is shown in Figure 4-32. The equation shown on the plot describes a linear fit through the data, giving a function relating μCT greyscale to BMD for the particular μCT scanner and scan settings that were used.

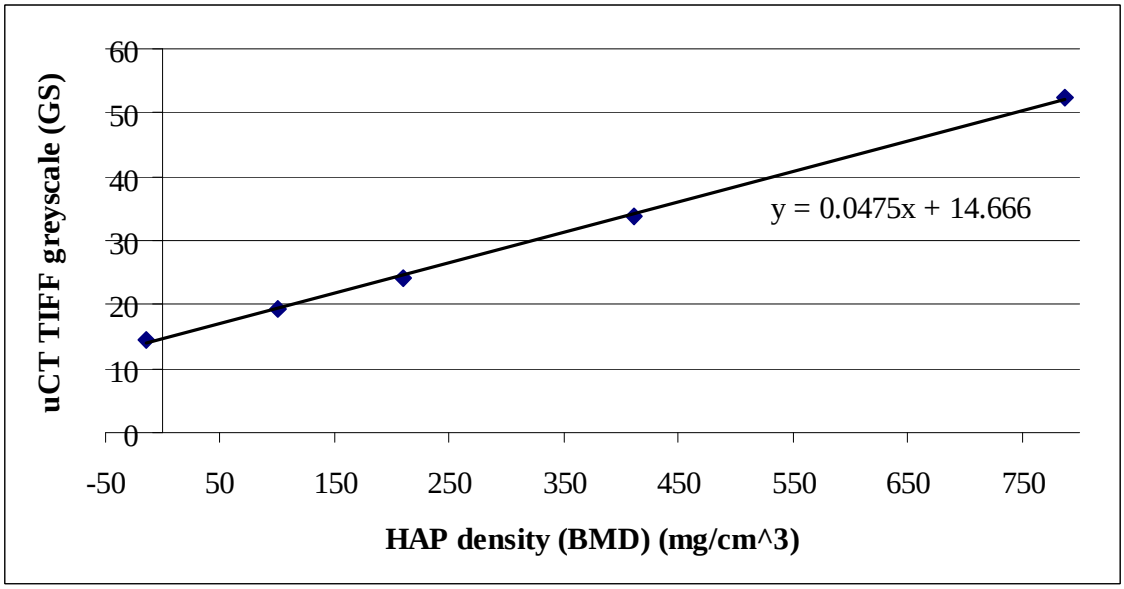

Figure 4-32. Plot of calcium hydroxyapetite density against µCT greyscale derived from inspection of the µCT TIFF images. The function overlaid on the plot is the equation of a linear fit through the data.

The substitution of the resulting BMD – µCT greyscale relationship into the previously derived µCT greyscale – Young's modulus relationship to give a BMD – Young's modulus relationship is shown in Figure 4-33.

µCT greyscale – Young's modulus relationship previously derived :

$$E = GS \times 45.054$$

From Figure (? Above) :

$$GS = (0.0475 \times BMD) + 14.666$$

$$\therefore E = (2.14 \times BMD) + 660.76$$

Figure 4-33. Substitution of the BMD – µCT greyscale relationship derived from the µCT TIFF images of the calibrated scan phantom into the µCT greyscale – modulus relationship derived in Section 4.4, resulting in a µCT scanner and scan settings independent µCT density – modulus relationship.

4.5.4. Summary

- A calibrated μCT scan phantom comprising rods of known calcium hydroxyapetite density (BMD) was imaged using μCT. The scan settings and raw μCT data to .TIFF image conversion methods were the same as used previously to image the ovine lumbar vertebral trabecular bone specimens used in the derivation of a μCT greyscale – Young's modulus relationship.

- The resulting .TIFF image files were used to derive a BMD – μCT greyscale relationship at these scan settings.

- By substituting this BMD – μCT greyscale relationship into the previously derived μCT greyscale – Young's modulus relationship, a μCT scanner and scan settings independent BMD – Young's modulus relationship for hFE representation of ovine lumbar vertebral trabecular bone was derived.

4.6. Yield strain determination

4.6.1. Specimen selection

The modelling process used to derive appropriate yield properties was based on the same approach as was used to determine a μCT greyscale-modulus relationship for ovine lumbar vertebral trabecular bone. A Build subset of specimen-specific models was used to determine appropriate hFE model yield properties through an iterative tuning process. A Validate subset of specimen-specific models was then solved using the same yield properties to validate their applicability to specimen-specific models outside of the derivation subset.

The ‘Build and Validate subsets contained modified versions of the same specimen-specific models as in the μCT greyscale-modulus relationship derivation study (Section 4.4), with modified elastic-plastic properties.

4.6.2. Material property configuration

4.6.2.1. Elastic material properties

The Young’s modulus and Poisson’s ratio assigned to the elements representing the Delrin end-caps were the same as in the μCT grayscale-modulus relationship derivation study (Section 4.4).

Elastic material properties were assigned to the elements representing ovine trabecular bone according to the final μCT grayscale-modulus relationship derived in Section 4.4.

4.6.2.2. Plastic material properties

The existing hFE models of the experimental ovine trabecular bone specimens were configured to use linear-elastic material models throughout. To determine appropriate yield properties the material model for the elements representing ovine trabecular bone were modified to include plastic behaviour.

An elastic-perfectly plastic material model with a strain-based failure criterion was chosen. This was because (as previously discussed in Section 2.1.3) hFE studies of whole vertebral bodies reported in the literature that used this approach had demonstrated good agreement between experimentally-determined and hFE-predicted results with respect to both apparent specimen strength, and the location of the initiation and progression of failure.

An in-house developed Matlab code was used to modify the material property definitions within each of the models in both the Build and Validate subsets to include elastic-perfectly plastic behaviour, with the elastic-plastic transition defined in terms of a constant element yield strain (ε_y).

4.6.3. Boundary conditions

4.6.3.1. Constraints

In all cases the models were configured with the same constraint and contact boundary conditions as described by the 'Standard hFE model configuration' (Section 4.3).

4.6.3.2. Applied displacement

Accurate determination of the apparent yield strain of a given model requires closely spaced data points on the model's predicted stress-strain plot, particularly as the applied strain approaches the apparent yield strain (Figure 4-34).

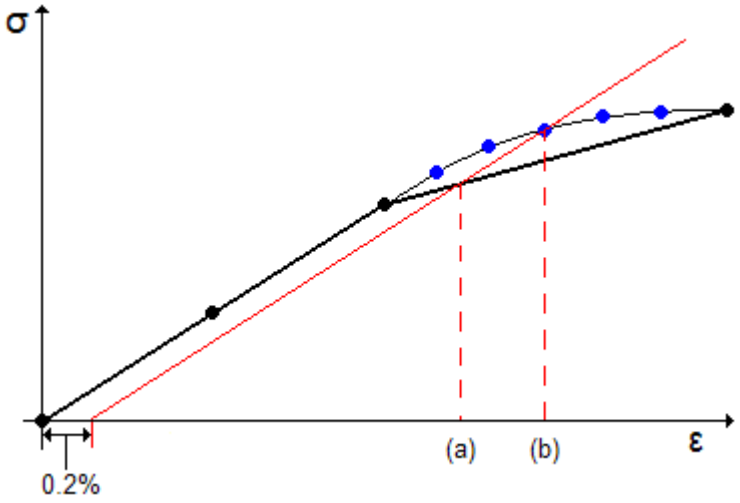

Figure 4-34. Example variation in specimen apparent yield strain (a and b) determined using the 0.2 % offset yield method, depending on the size of the increments in the applied strain as the specimen approaches apparent yield.

This involves splitting the total applied displacement into a number of smaller increments, or load steps. The computational cost of solving the models can be minimised by reducing the total number of load steps. This was achieved by estimating an applied deformation that would be more than sufficient to cause apparent-level yield for each model at a given applied ε_y. In each case this applied deformation was then

subdivided into multiple load steps of varying magnitude, such that the smallest increments were in the deformation range expected to cause apparent-level yield (Figure 4-35).

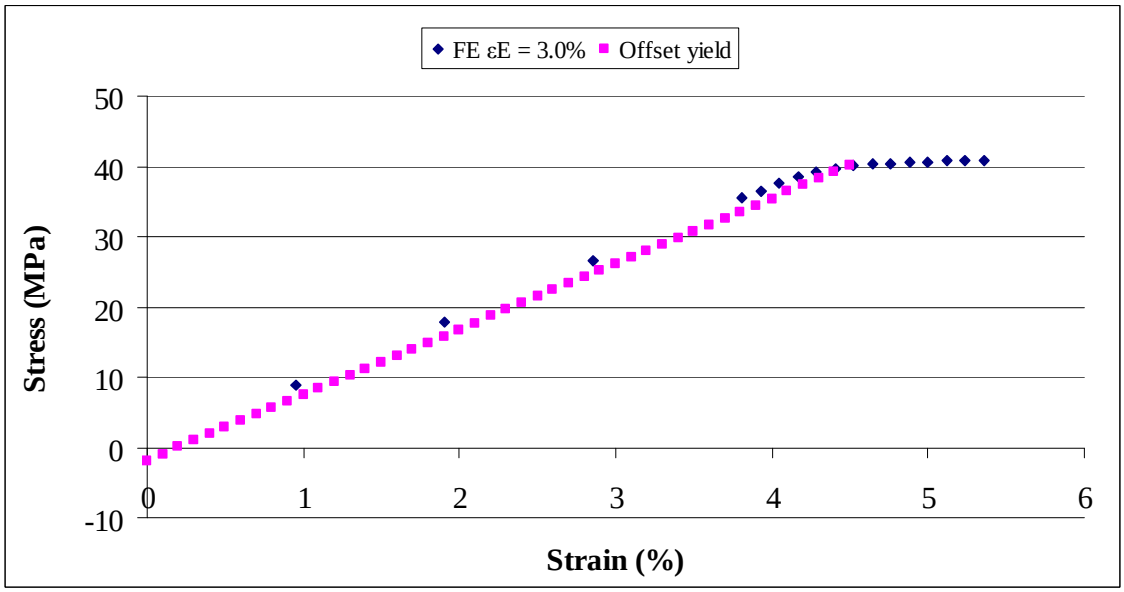

Figure 4-35. Example stress-strain plot for specimen 12-5-11_L4 showing small increments in the applied strain within the apparent strain range where it was estimated that failure would occur, for the selected value of ε_y (3.0 %). The pink data points plot the gradient and x-axis intercept of the 0.2 % offset yield line.

4.6.4. Determining the element-level yield strain

The model solution workflow followed to determine an appropriate value for ε_y was similar to that used to determine an appropriate μCT greyscale-modulus relationship for ovine vertebral trabecular bone (Section 4.4).

Preliminary modelling had suggested that the value of ε_y that would produce the closest agreement between the hFE predicted and experimentally determined apparent yield strain was approximately 2 %. Two copies of each model in the Build subset were created and assigned to one of two groups, Build_low and Build_high. Using the in-house developed Matlab code, the models were then assigned values of ε_y = 1.0 % and ε_y = 3.0 % respectively, and solved in ABAQUS.

For each model in both Build subsets the apparent yield strain was determined using the 0.2 % offset yield method as previously described in Section 3.5 (Figure 3-6). The average percentage error between hFE predicted and experimentally determined apparent yield strain was then calculated across all of the models in each of the Build subsets, and plotted against ε_y (Figure 4-36). The predicted value for ε_y that would result in an average percentage error between hFE predicted and experimentally determined apparent yield strain of zero was calculated assuming a linear fit through the two data points and solving the resulting equation for y = 0. This was confirmed by using the in-house developed Matlab code to assign this value of ε_y to the models in the Build_low subset, which were then solved in ABAQUS.

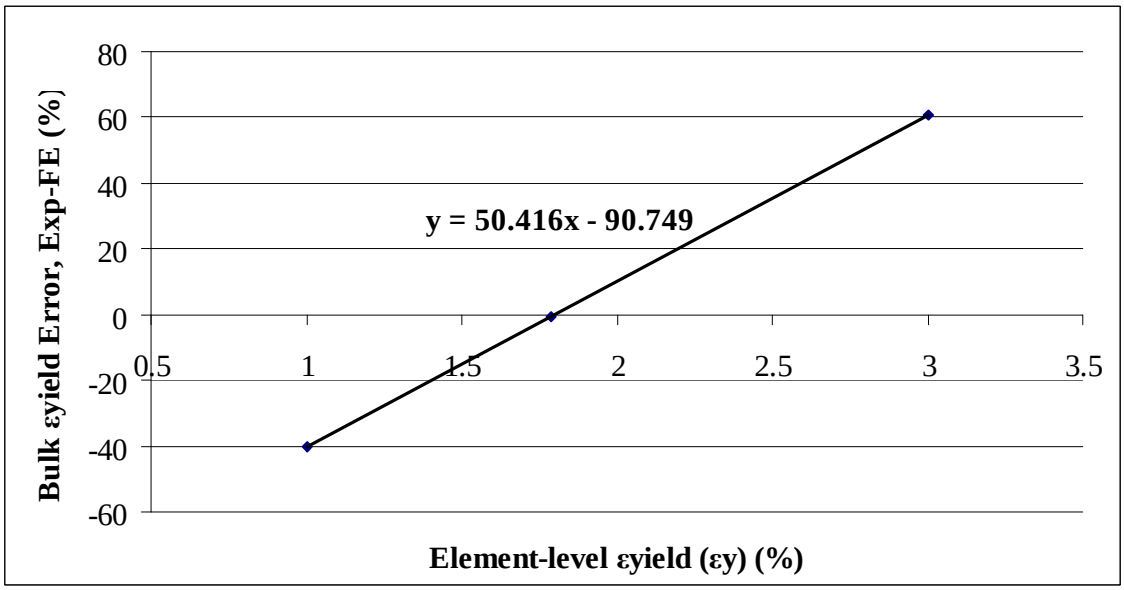

Figure 4-36. Mean percentage error between hFE predicted and experimentally determined apparent yield strain plotted against element-level yield strain (ε_y).

The applicability of this value for ε_y to specimen-specific models outside of the derivation subset was checked by using the in-house developed Matlab code to assign this value of ε_y to the models in the Validate subset. The models in this subset were then solved in ABAQUS, and the apparent yield strain in each case was determined using the 0.2 % offset yield method.

4.6.5. Results

The results are shown in Figures 4-37 and 4-38. The value of ε_y that produced the closest agreement between the hFE predicted and experimentally determined apparent yield strain across all specimens in the Build subset was ε_y = 1.79 %, leading to an average percentage error of -0.59 %, with a standard deviation of 14.11 %. When this value of ε_y was assigned to the models in the Validate subset the average percentage error was -6.5 %, with a standard deviation of 10.8 %. The average percentage error across the models in both subsets was -2.1 %, with a standard deviation of 13.6 %.

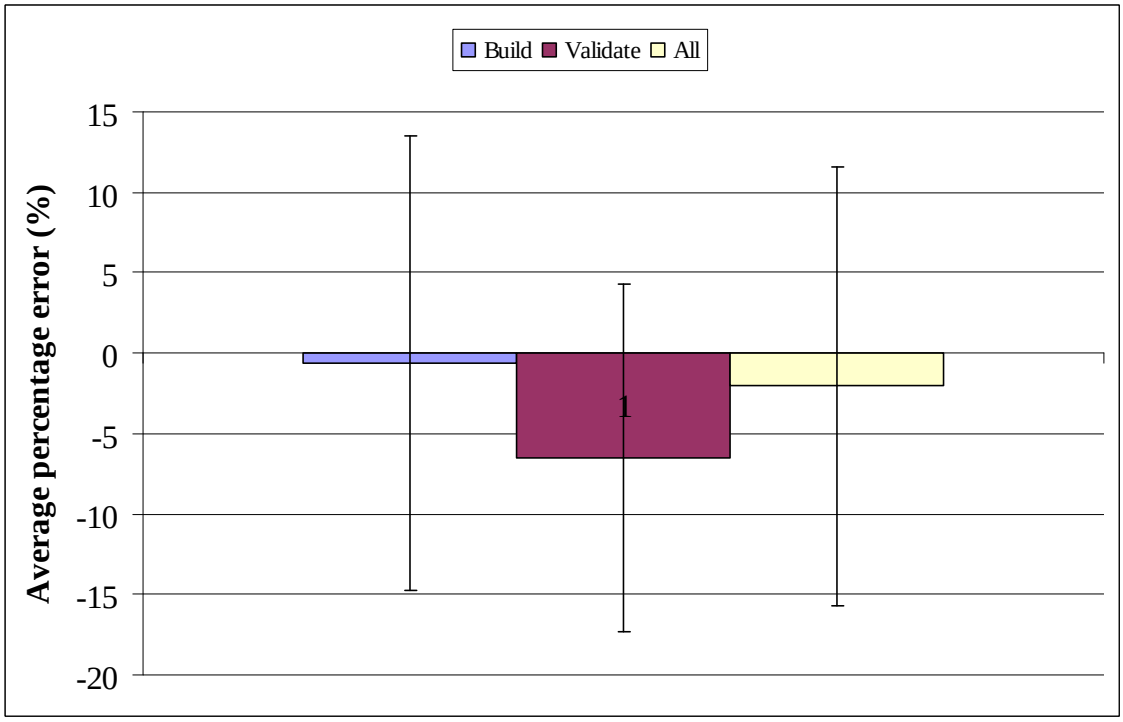

Figure 4-37. Mean percentage error between hFE predicted and experimentally determined apparent yield strain across the final Build subset, Validate subset and overall. The error bars denote the standard deviation in each case.

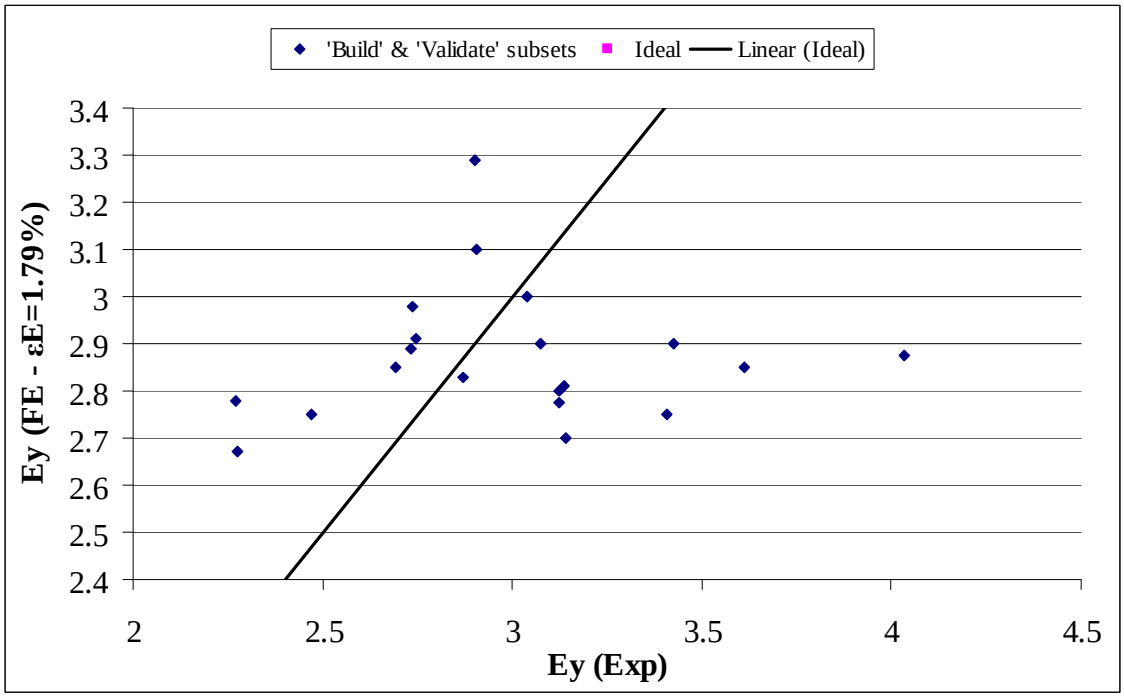

Figure 4-38. Concordance between hFE predicted and experimentally determined apparent yield strain for all 20 specimens in the Build and Validate subsets. The linear plot denotes the ideal 1:1 relationship between hFE predicted and experimentally determined apparent yield strain.

4.6.6. Discussion

The good agreement between the hFE predicted and experimentally determined apparent yield strain for specimens in the Validate subset (average percentage error of -6.5 %) suggests that ε_y = 1.79 % is an appropriate constant 'tissue level' yield strain for hFE representations of ovine lumbar vertebral trabecular bone generated using the approaches and equipment described here.

The magnitude of the average percentage error between hFE-predicted and experimentally-determined yield strain for all specimens is approximately double the average percentage error between hFE-predicted and experimentally- determined stiffness for all specimens (-2.07 % vs 0.946 %). This, coupled with the reasonable correlation between $\Delta\varepsilon$ and Δk (Figure 4-39), suggests that any aspects of the mechanical behaviour of the specimens that could not be reproduced by the hFE models have approximately twice the influence on apparent specimen yield strain as they have

on apparent specimen stiffness, with an average gradient of the linear fits through the Build and Validate subset comparisons of -0.542 (Figure 4-39).

Figure 4-38 shows a plot of the hFE predicted apparent yield strain against experimentally determined apparent yield strains for all specimens in both the Build and Validate subsets. In a similar manner to the results of the μCT greyscale-modulus relationship derivation study, the hFE-predicted apparent specimen yield strains occupy a narrower range than the experimentally-determined specimen apparent yield strains ($S.D._{(EXP)}$ = 3.02 x $S.D._{(hFE)}$ for yield strain, $S.D._{(EXP)}$ = 3.21 x $S.D._{(hFE)}$ for stiffness). The close similarity between the difference in variation between hFE predicted and experimentally determined apparent properties with respect to both yield strain and stiffness suggests that the origin of the suboptimal concordance between hFE-predicted and experimentally-determined apparent properties is the same in both cases.

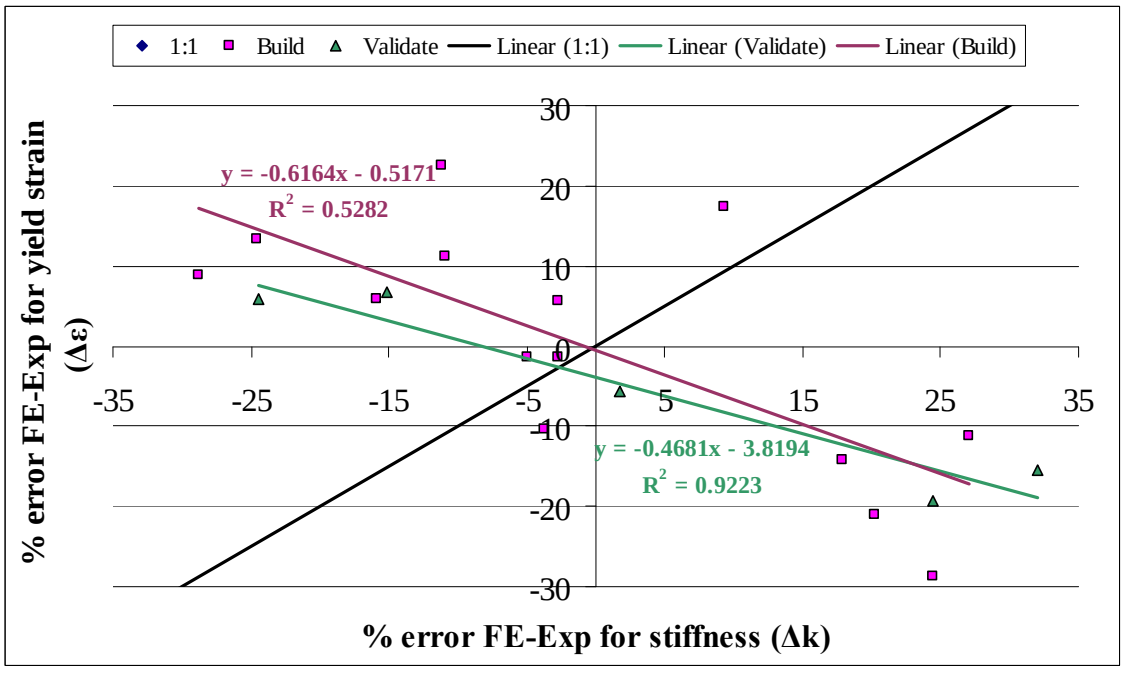

Figure 4-39. Average percentage error between hFE predicted and experimentally determined apparent yield strain plotted against average percentage error between hFE predicted and experimentally determined stiffness for all specimens in the Build and Validate subsets.

4.7 Summary

- A linear μCT grayscale-modulus relationship and constant element-level yield strain were derived using specimen-specific hFE models generated from the widest available range of ovine lumbar vertebral trabecular tissue.

- A μCT scanner and scan settings independent μCT density-modulus relationship was then derived by deriving a BMD - μCT grayscale relationship for the chosen μCT scanner and scan settings using a calibrated calcium hydroxyapetite scan phantom, and then substituting this relationship into the previously derived μCT grayscale – modulus relationship.

- The μCT grayscale-modulus relationship and element-level yield strain enabled the prediction of the compressive stiffness and apparent yield strain of similar specimen-specific ovine lumbar vertebral trabecular bone models outside of the derivation set to within an average error of 4.7 % and -6.5 % respectively.

- The problem simplifications, choice of boundary conditions and the order of the μCT grayscale-modulus relationship do not appear to explain the lack of concordance between the experimentally-determined and hFE-predicted specimen stiffnesses or apparent yield strains, in terms of their ranking or spread.

- It is proposed that these discrepancies, with regard to both stiffness and apparent yield strain, were caused by specimen structural properties other than the μCT greyscale distribution that were not captured by the downsampled hFE models. Exploring this would require extensive further modelling at an increased resolution and will therefore not be included in this study.

5. Experimental characterisation of the compressive structural behaviour of the bone-cement interface

This chapter details the development of the test specimens, equipment and methods required to image cement-augmented vertebral trabecular bone specimens under an incrementally applied deformation, and their use. This study formed the first part of the work conducted to meet the second objective set out in Section 2.6.

5.1. Introduction and aims

As discussed in Chapter 2, it was expected that improving the predictive accuracy of hFE representations of the bone – cement interface required both apparent and structural level characterisation of the behaviour of trabecular bone – cement specimens in compression, the purpose of which was twofold;

- To provide μCT images of undeformed trabecular bone – cement interface specimens from which specimen-specific interfacial hFE models were generated.
- To provide apparent-level force/displacement and structural-level strain distribution data for each specimen as it was deformed up to and beyond apparent-level failure, against which the specimen specific hFE model predictions could be validated.

To achieve this, each part of the necessary experimental equipment and protocols had to be developed, including;

- Development and fabrication of ovine lumbar vertebral trabecular bone – cement interface test specimens (section 5.2).
- Development of a compression and μCT imaging device (section 5.3).
- Implementation of a suitable experimental compression and imaging protocol (section 5.4).

5.2. Development of interfacial test specimens

The development of suitable bone-cement interface specimens was a multi-stage process. Initially, synthetic bone prototype specimens were used to develop a specimen fabrication and augmentation methodology, test the principles of operation of the compression and imaging device and assist in the development of a standard testing protocol. Ovine trabecular bone – cement specimens were then developed. Differences between the augmentation behaviour of synthetic bone and ovine lumbar trabecular bone necessitated the exploration of a number of alternative augmentation methods. This process resulted in the fabrication of ovine bone – cement specimens exhibiting the desired level of cement fill and trabecular interdigitation using the 'break and fill' approach.

5.2.1. Initial proof of concept synthetic bone specimens

The initial 'trabecular bone' - cement specimens were fabricated from an open cell rigid foam (Sawbone pcf7.5, Sawbones Europe AG, Malmö, Sweden) augmented with PMMA cement. The main advantages in using the synthetic bone were that it was readily available, relatively easy to machine into cylindrical core specimens and structurally provided a good approximation of open-celled trabecular bone as found in the centrum of osteoporotic human vertebrae (Homminga et al 2004).

5.2.1.1. Specimen dimensions

The specimen dimensions were determined according to the recommendations of Harrigan, Jasty et al (1988), Keaveny, Borchers et al (1993) and Keaveny, Pinilla et al (1997), in the same manner as for the ovine lumbar vertebral trabecular bone specimens described in Section 3.2.

These considerations, and the Sawbone 'trabecular' cell size of 1 – 2 mm, led to the fabrication of cylindrical specimens of 13 mm diameter and 25 mm height.

5.2.1.2. Specimen preparation

Due to the difficulties involved in clamping bulk synthetic bone, the material was immersed in water, which was then frozen. A 13 mm internal diameter hole-cutting drill was then used to produce 12 cores, which were trimmed to length such that the ends of each specimen were plano-parallel as far as possible. Upon thawing and drying the synthetic bone cores were potted into Delrin end-caps as previously described in Section 3.2.

5.2.1.3. Cement augmentation

A small quantity of PMMA was then prepared at a 1:1 liquid-powder ratio and allowed to thicken slightly before a syringe fitted with a 1.2 mm (18 gauge) needle was used to inject approximately 1 ml of PMMA into each specimen such that it formed a central bolus. The needle was inserted into each specimen half-way along its length such that the tip penetrated to approximately one-third of the specimen diameter, taking care to cause as little damage to the surrounding trabecular structure as possible. The PMMA was then allowed to cure at room temperature (Figure 5-1).

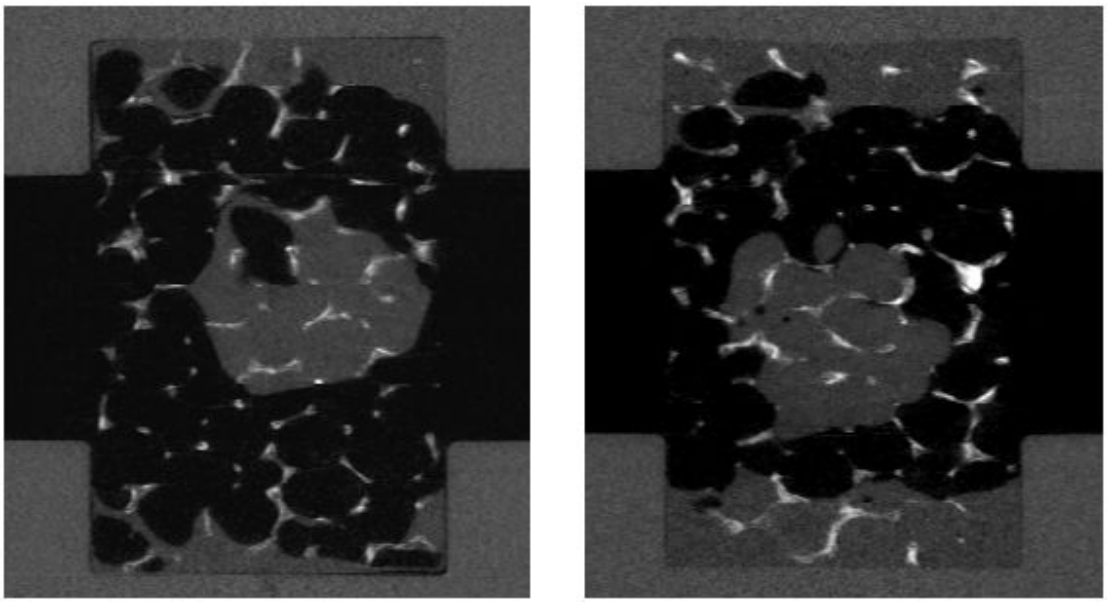

Figure 5-1. Example μCT image cross-sections of two of the end-capped synthetic bone specimens augmented with PMMA cement.

These initial test specimens were then used to carry out the first set of tests using the first prototype μCT compression and imaging device, leading to a number of design modifications that were applied to the revised μCT compression and imaging device. They were a successful proof of concept, demonstrating that it would be possible to image the deformation and failure of the trabecular bone - PMMA interface under an incrementally increased applied displacement.

5.2.2. Ovine trabecular bone specimens

Ovine lumbar vertebrae were chosen for the fabrication of animal tissue test specimens, for a number of morphological and geometric reasons previously discussed in Section 3.1.

5.2.2.1. Specimen dimensions

The specimen dimensions were determined according to the recommendations of Harrigan, Jasty et al (1988), Keaveny, Borchers et al (1993) and Keaveny, Pinilla et al (1997), in the same manner as for the ovine lumbar vertebral trabecular bone specimens described in Section 3.2.

These considerations led to the fabrication of 13 mm diameter cylindrical specimens with a height that ranged between 25.7 mm and 27.1 mm depending on the inferior-superior body height of the vertebrae from which they were extracted in each case.

5.2.2.2. Specimen preparation

The specimen cores were fabricated according to a modified version of the methodology outlined in Section 3.2. The difference in this instance was the addition of cement augmentation, which was carried out before the specimens were potted into Delrin end caps.

5.2.2.3. Cement augmentation

As ovine trabecular bone is considerably harder than Sawbone, it was not possible to insert the augmentation needle directly into the specimens. Instead, a 1 mm diameter drill bit was used to bore into the specimen to provide a guide hole for the needle injection. To provide maximum similarity to in-vivo conditions, the specimens were

then placed in polythene bags and submerged in a water bath at 37 °C for approximately 30 minutes. As the viscosity of the marrow, fats and other soft-tissues within the trabecular structure varies with temperature (Bryant et al, 1993), the ease with which the PMMA could displace the marrow and penetrate the trabecular structure could have been significantly reduced at the low temperatures at which the cored specimens were stored.

Several different methods of cement injection were investigated which are described below. In all cases, a small quantity of PMMA was prepared using a 1:1 liquid to powder ratio. In some cases a radiopacifier agent was also added as described in Section 5.2.3. The specimens were removed from the water bath one at a time and immediately augmented by injecting the cement through a 1.2 mm (18 gauge) needle inserted through the pre-drilled hole.

After augmentation, the specimens were returned to their polythene bags to prevent them from drying out and left for approximately 30 minutes to allow the PMMA to initially cure. The specimens were then potted into Delrin end-caps as previously described in Section 3.2.

Radially augmented specimens

Initially, a hole was bored radially into the specimens to a depth of half of the diameter, mid way along the superior-inferior axis. Cement was injected into each specimen until either approximately 1 ml was injected, or until it began to leak out of the specimen from the opposite side of its circumference from that through which the needle was inserted.

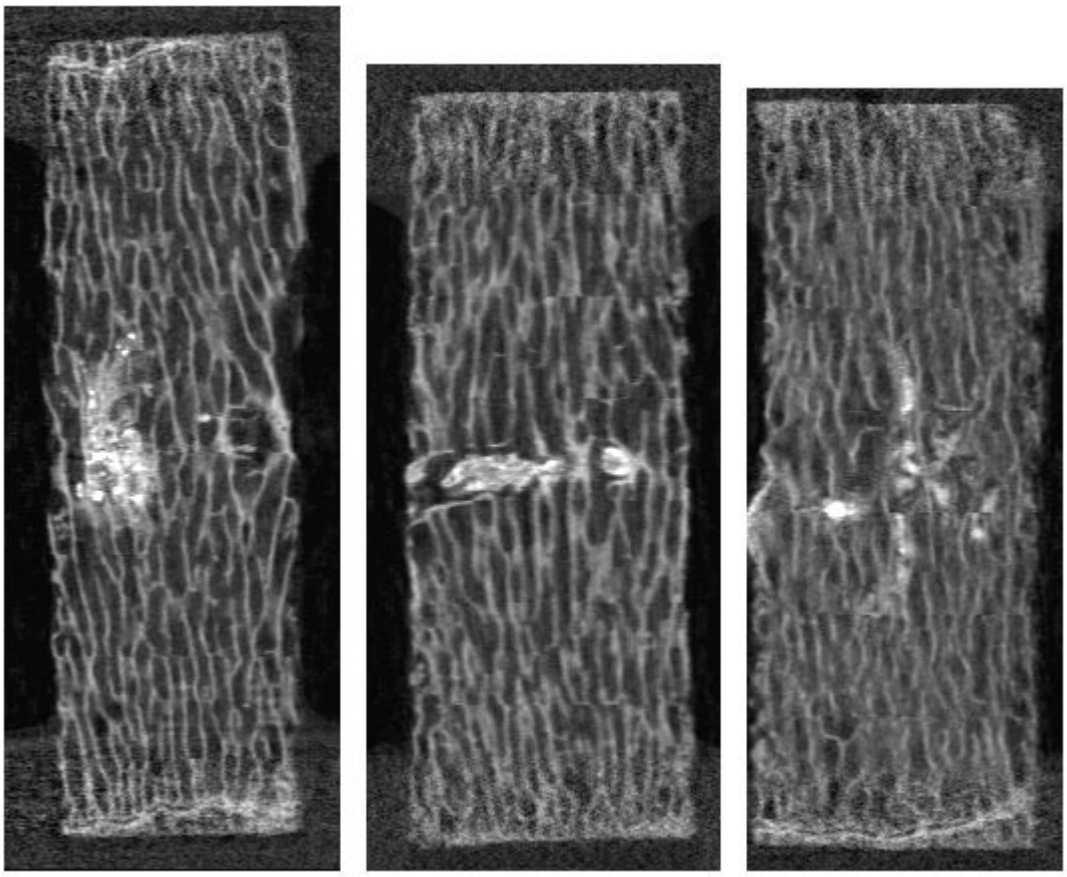

Figure 5-2. Example µCT image cross-sections of radially cement-augmented ovine specimens showing minimal evidence of inter-trabecular cement penetration.

Initial scans of the first batch of specimens prepared from ovine lumbar vertebrae using this method showed little cement penetration or interdigitation with the trabecular structure, agreeing with the similarity between apparent injected cement volume and observed cement leakage at the time of augmentation (Figure 5-2). This was likely caused by the PMMA following the path of least resistance and flowing directly through the centre of the specimen and out of the side of the specimen directly opposite the point at which the needle was inserted, rather than penetrating the trabecular structure above and below the needle tip. To avoid this, an alternative augmentation approach was utilised.

Axially augmented specimens

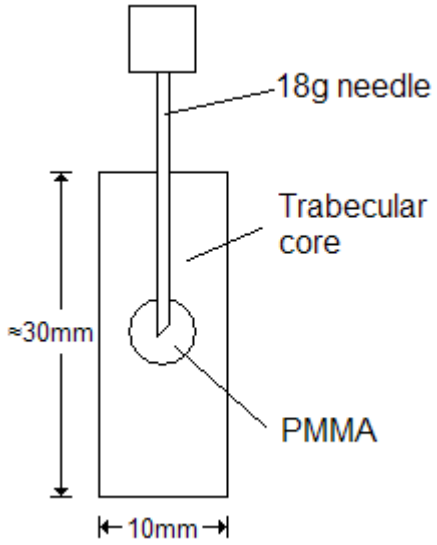

Figure 5-3. Needle tip placement for axial cement augmentation.

The revised augmentation approach remained largely unchanged except that the hole was drilled perpendicularly into one of the end-faces along the superior-inferior axis to a depth of approximately half of the total specimen length (Figure 5-3).

Again, a needle was inserted and used to inject approximately 1 ml of the cement , or until cement began to leak out of the sides of the specimen. As the axially bored hole disturbed the trabecular structure more than the previously used radially bored hole, a small amount of additional augmentation was injected as the needle was withdrawn from the specimens to back-fill the hole and ensure that the structural stability of the specimens was compromised as little as possible.

Inspection of the resulting μCT scans of the specimens suggested that the use of axial PMMA augmentation was an improvement over the radial augmentation and resulted in an increased volume of cement augmentation and a greater degree of bone-cement interdigitation. However, the total volume of cement augmentation and size of the surrounding interfacial region was still lower than necessary for accurate representaiton in the computational models. As in the case of the radially augmented specimens, this seemed to stem from the tendency of the injected cement to follow the path of least

resistance. Once the flow of cement reached the perimeter of the specimen and 'burst out' into empty space there was no further increase in interdigitation as beyond this point further injection of cement would merely displace that already injected via this opening (Figure 5-4).

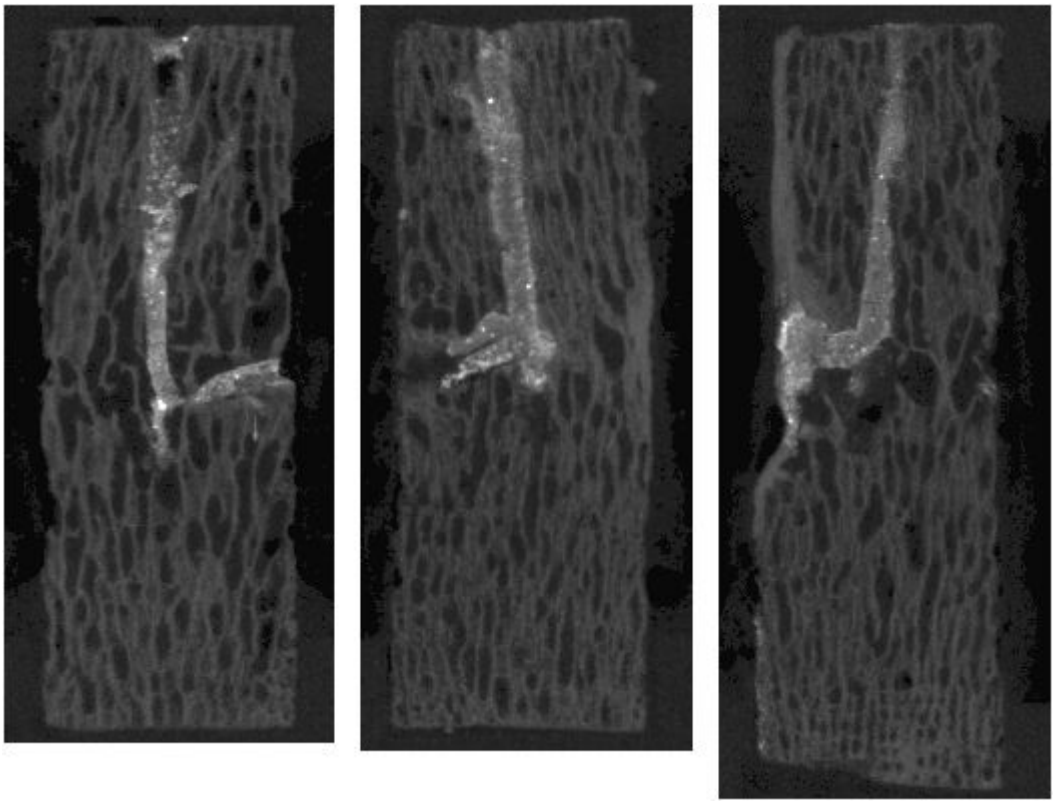

Figure 5-4. Example µCT image cross-sections of axially cement-augmented ovine specimens showing minimal evidence of inter-trabecular cement penetration.

'Break & fill' augmented specimens

In an effort to improve the augmentation method, consideration was given to the manner in which bone-cement interdigitation occurs in-vivo. In the case of traumatically fractured vertebrae, there are likely to be a number of significant cracks in the vertebral body. Vertebrae affected by osteoporosis are likely to have experienced trabecular 'thinning' to the extent that large voids will have formed within the centrum, and collapsed vertebrae that have undergone height-restoration using a balloon (Garfin et al 2001) will similarly feature a large central void. When these vertebrae are treated using vertebroplasty the cement is likely to flow into these cracks and voids, with the majority

of the interdigitation between the trabecular bone and cement occurring at the periphery of the augmented region.

A number of specimens were fabricated using a different approach in an effort to reproduce a section of such an interdigitated region within the ovine bone cores used in this study.

As before, a 1 mm diameter drill was used to bore into each specimen axially to approximately half its length prior to immersion in a water bath at 37 °C as previously described. Following removal from the water bath, a small saw was then used to score the specimens along their circumference along one side, to a depth of approximately 2 mm. Each specimen was then inserted into a short length of rubber tubing to protect it from crushing damage while a pair of forceps was used to break it across its cross-section (resulting in Figure 5-5(a)). After fracture, a moistened soft brush was used to dislodge a small amount of marrow and any trabecular fragments from the fractured ends such as to maximise potential bone-cement interdigitation. The two ends of each specimen were then wrapped in thick transparent polythene sheeting and positioned a short distance apart, secured by tightly bound adhesive tape immediately adjacent to the gap between the two specimen halves.

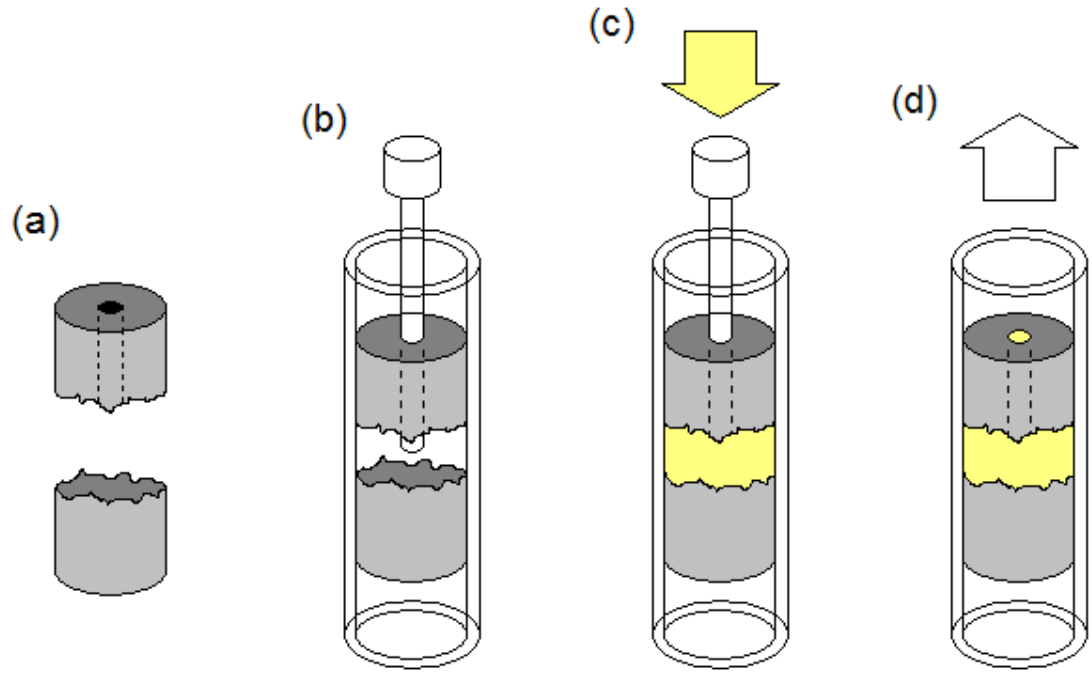

Figure 5-5. 'Break and fill' cement augmentation procedure showing (a) the specimen following fracture, (b) the insertion of the needle after the cement was inserted into the rubber tubing, (c) the injection of the cement and (d) the removal of the needle and back-filling of the needle track with PMMA cement.

With the specimens prepared in this manner, an 18 gauge needle was introduced axially and cement was injected (Figure 5-5(b) & (c)). The pressure on the syringe was maintained until cement could be seen leaking past the adhesive tape bindings on either side of the gap, and the specimens were each gently agitated and tapped a number of times during augmentation to try and dislodge any trapped air-pockets such that they would be released via leakage. The needle was then withdrawn while pressure was continually applied to the syringe to ensure that the needle path was completely back-filled with PMMA (Figure 5-5(d)). The specimens were set aside for approximately 15 minutes to allow the PMMA to partially cure. The polythene sheeting was then cut away such that any PMMA that had leaked past the adhesive tape bindings could be carefully trimmed using a scalpel before it had fully cured. An example of a specimen prepared in this manner following potting into Delrin end-caps is shown in Figure 5-6.

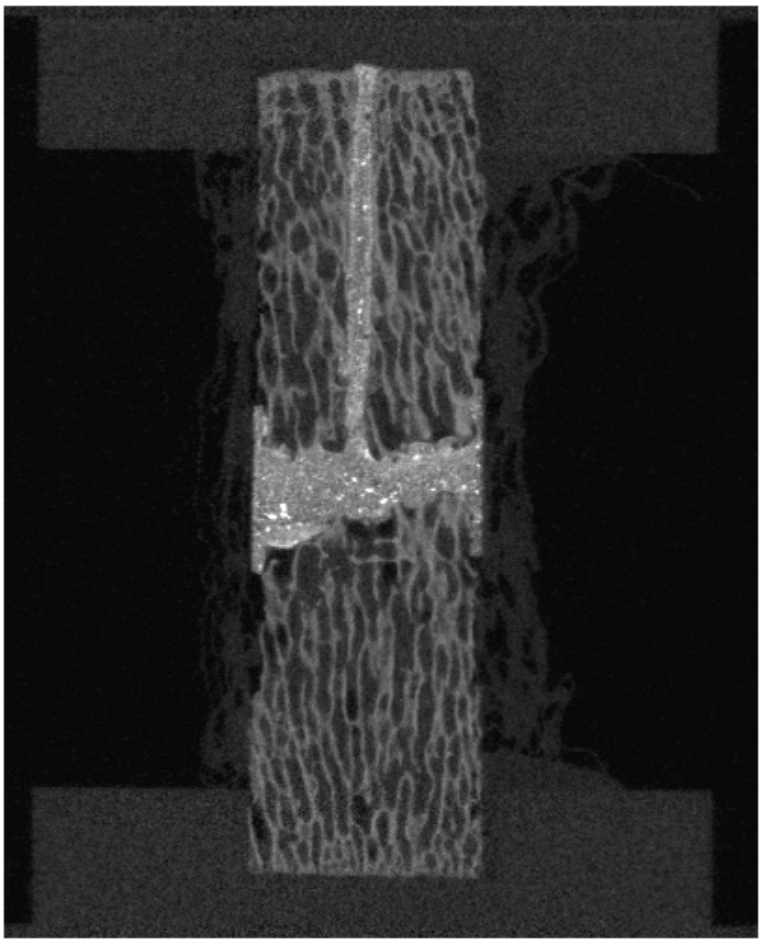

Figure 5-6. Example µCT image cross-section of one of the ovine specimens cement-augmented using the 'break and fill' approach and potted into Delrin end-caps.

5.2.3. Use of Barium Sulphate radiopacifier

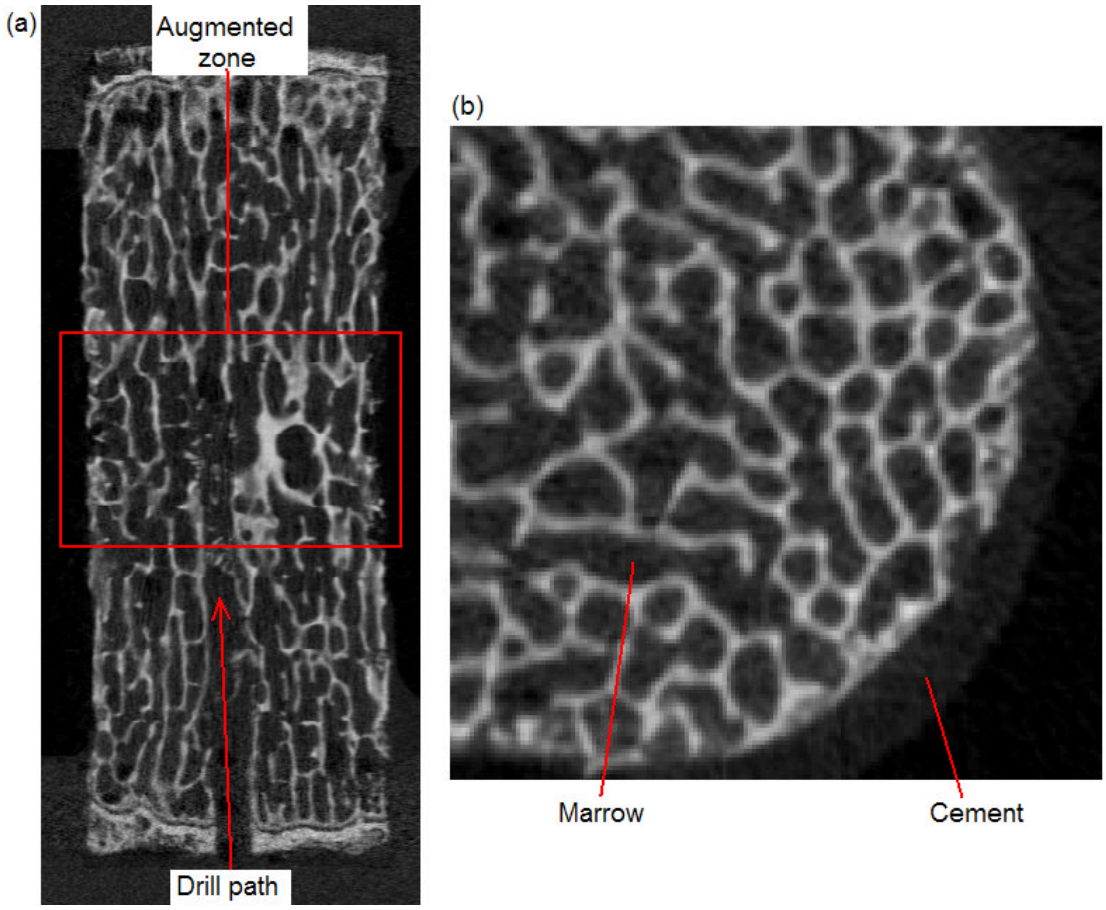

Figure 5-7. Example µCT image cross-sections of one of the axially cement-augmented ovine specimens augmented with unmodified PMMA cement.

Initially, specimens were augmented with an unmodified PMMA cement. When the specimens were augmented axially, comparison between the apparent quantity of cement injected according to the graduated syringe barrel and observed cement leakage suggested that this approach resulted in a greater degree of cement fill than the radial augmentation method. However, when the specimens were imaged using µCT, negligible cement penetration and fill was apparent (Figure 5-7(a)). Closer inspection of regions of the specimens adjacent to the endcaps (Figure 5-7(b)) where regions of cement were definitely visible suggested that the radiolucency, and hence µCT greyscale values, of the PMMA cement and the marrow present within the trabecular architecture were sufficiently similar that it would not be possible to differentiate them

within the μCT scans. There was therefore a need to include a radiopacifier agent within the cement to enable the cement and marrow to be differentiated on the images.

5.2.3.1. Clinical use of radiopacifier

Clinical use of vertebroplasty / kyphoplasty frequently includes the use of PMMA cement combined with a radiopacifier material, such as barium sulphate, to allow the use of a fluoroscope to assist the clinician in controlling the location and quantity of cement injected (Kurtz et al 2005).

Commercially available clinical PMMA cement formulations already include barium sulphate, for example Simplex P contains 10% barium sulphate (Kurtz et al 2005). However, typical clinical practice involves increasing the barium sulphate content to provide increased fluoroscope contrast by combining the cement with additional barium sulphate at the time of cement preparation (Theodorou et al 2002). A typical example of this practice involves combining a 14.7:6 Simplex P powder and barium sulphate mixture with 10 ml cement monomer liquid, resulting in a final barium sulphate content of 36% (Kurtz et al 2005).

5.2.3.2. Preliminary study: Use of Barium Sulphate radiopacifier

To increase the contrast seen on the Micro-CT images between the cement augmentation and the marrow, a series of studies were undertaken to investigate the effects of combining the PMMA cement with barium sulphate.

Methods

As this trial involved a comparatively small quantity of cement, plain PMMA powder and barium sulphate powder were combined at a ratio of approximately 2:1 to simplify the measurements involved, leading to a barium sulphate content of approximately 33%. This mixture was combined with PMMA monomer liquid at a 1:1 ratio to increase the

available working time and hand mixed using a spatula for approximately 1 minute as described by Kurtz et al (2005).

This mixture was then used to augment a number of ovine trabecular bone cores in the same manner as in the axially augmented specimen preparation section.

Results

Two μCT views of a representative specimen augmented thusly are shown in Figure 4-8.

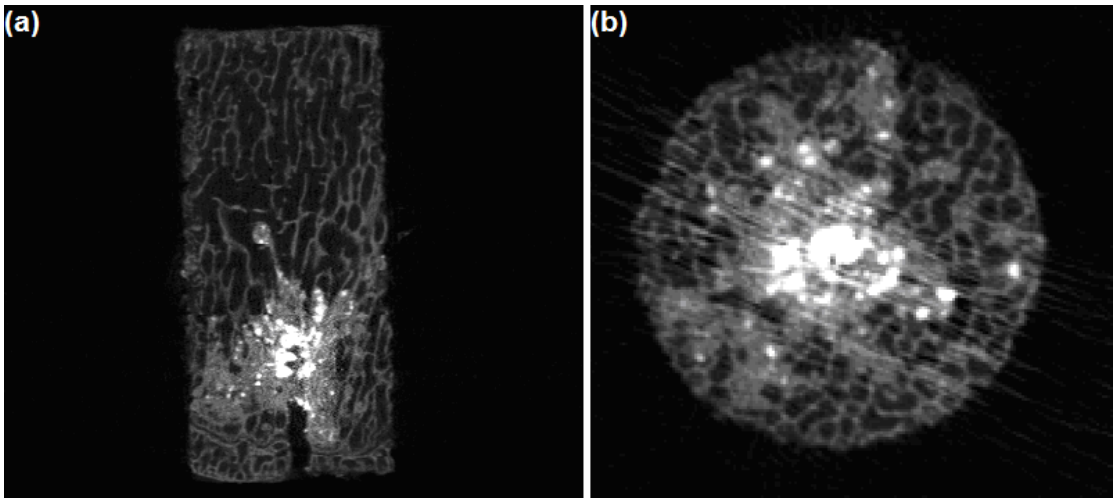

Figure 5-8. Example μCT image cross-sections of one of the axially cement-augmented ovine specimens augmented with a 2:1 PMMA cement and barium sulphate mixture prepared as described by Kurtz et al (2005).

It is apparent that the process led to significant barium sulphate agglomeration indicated by the bright white regions in the scans, causing streaking artefacts in Figure 5-8(b). Figure 5-9 shows the uneven distribution of barium sulphate more clearly. Areas where the barium sulphate and PMMA are well-mixed resulted in a μCT greyscale value similar to that of trabecular bone and considerably brighter than the unmodified PMMA cement.

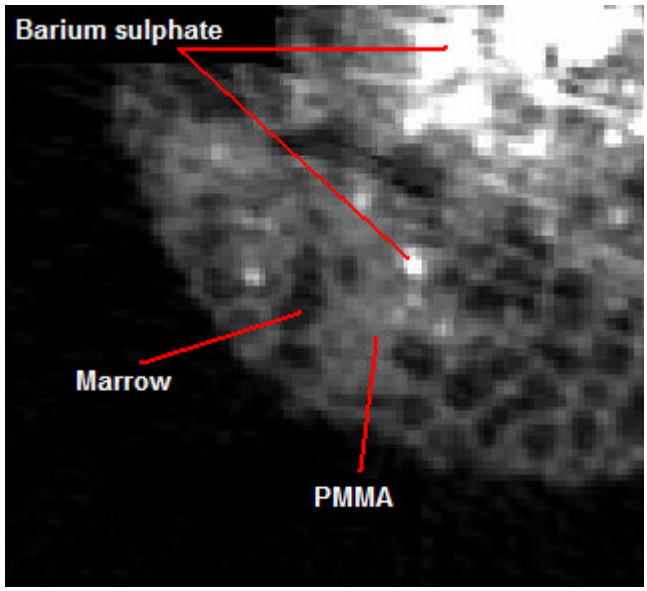

Figure 5-9. Close up of Figure 4-8(b) showing barium sulphate agglomeration and areas of well-mixed PMMA and barium sulphate.

Discussion

The significant barium sulphate agglomeration was likely a combination of two factors. Firstly, the barium sulphate powder used for the study was not anhydrous, and seemed prone to clumping when weighed out. It could be that the duration of the hand-mixing of PMMA and barium sulphate was insufficient to fully break up and disperse these clumps of barium sulphate powder throughout the cement. Secondly, previous work at Leeds (Tarsuslugil et al 2013) using calcium phosphate based cements demonstrated that significant filter pressing could occur upon injection. As the barium sulphate was not soluble in the PMMA monomer liquid or the combined cement, filter pressing was a possible partial cause of the barium sulphate agglomeration.

5.2.3.3. Main study: Revised mixing approach and evaluation of radiopacifier concentration

In an effort to distribute the barium sulphate radiopacifier more evenly throughout the cement augmentation a revised mixing approach was tested. The initial mixing approach followed the procedure outlined in the literature – hand mixing the barium sulphate with the mixture of cement powder and monomer liquid for approximately 1 minute immediately prior to injection. The limited working time before the cement became too viscous to inject into the specimen precluded greatly increasing the mixing time to try and more evenly distribute the barium sulphate.

Instead, the barium sulphate was first mixed with the liquid cement monomer using a magnetic stirrer. Although the barium sulphate was not soluble in the monomer, it was thought that vigorously agitating a mixture of the two in a sealed container using the magnetic stirrer would create a suspension of fine particles of barium sulphate, leading to greatly reduced agglomeration following the addition of the PMMA powder.

Methods

A small amount of PMMA powder and barium sulphate were weighed out at a given ratio, and the barium sulphate powder was then placed in a screw-top polyethylene container along with a quantity of PMMA monomer liquid which would produce a 1:1 powder-liquid ratio by weight. A magnetic stirrer bead was then sealed into the container and the contents agitated for a given time. Several different ratios of barium sulphate to PMMA powder and agitation times were investigated as outlined in Table 5-1.

Specimen group	1	2	3	4	5
Agitation time (mins)	**30**	**1**	**1**	**1**	**1**
PMMA powder: barium sulphate (wt:wt)	**2 : 1**	**1 : 0**	**2 : 1**	**4 : 1**	**8 : 1**
Number of specimens	4	4	4	4	4

Table 5-1. Details of specimens studied to evaluate barium sulphate radiopacifier concentration

The PMMA powder was then added to the barium sulphate suspension and hand-mixed for a further 1 minute, before a syringe and 18 gauge needle were used to transfer the cement into a mould. The Delrin end-caps described in Section 3.2 were used for this purpose. A separate syringe and needle were used to transfer each batch of cement to prevent cross-mixing. Once the cement had cured, the end-caps were imaged using μCT.

Results & Discussion

An initial agitation period of approximately 30 minutes was selected, but it was noticed that the PMMA monomer liquid had an etching effect on the polyethylene containers within which the barium sulphate and PMMA monomer liquid were mixed using the magnetic stirrer. In one instance, this caused the seam at the base of the container to fail. The polymer coating on the magnetic stirrer bead was also affected, creating a tendency for the stirrer bead to adhere to the floor of the container. For this reason it was desirable for the agitation time be reduced such as to minimise the quantity of container and magnetic stirrer bead coating material dissolved into the cement augmentation.

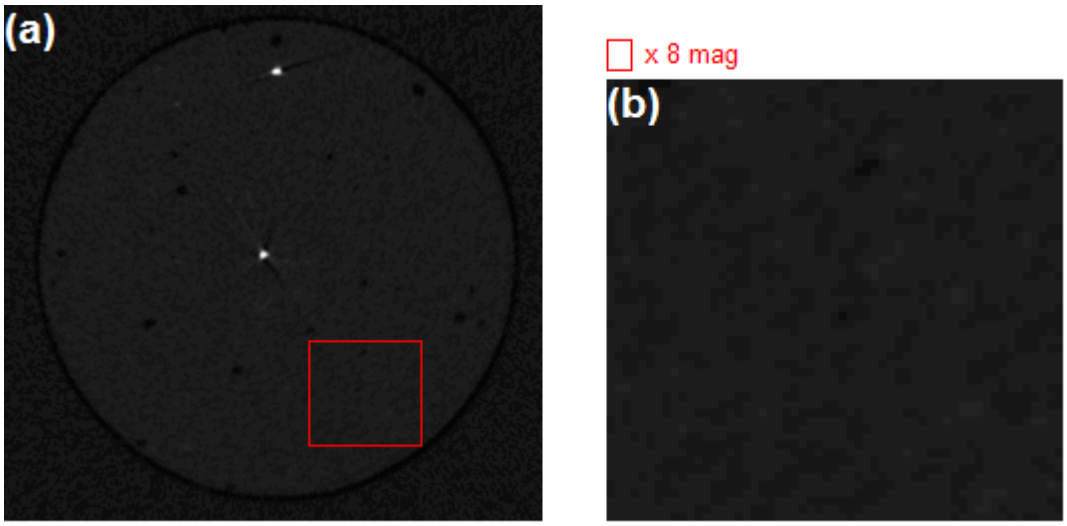

Figure 5-10. Example µCT image slices of a specimen of a 2:1 PMMA cement and barium sulphate mixture from group 1.

An example slice from the µCT images of one of the specimens from Group 1 is shown in Figure 5-10(a). There are two bright spots present in the image indicative of barium sulphate agglomerations. However, a close up of a region of the cement (Figure 5-10(b)) suggests that most of the barium sulphate had been finely dispersed throughout the cement, and that using a magnetic stirrer to create a suspension of barium sulphate particles in the cement monomer liquid before adding the powder component was an effective method of reducing barium sulphate agglomeration when compared to simultaneous hand mixing of all three component parts.

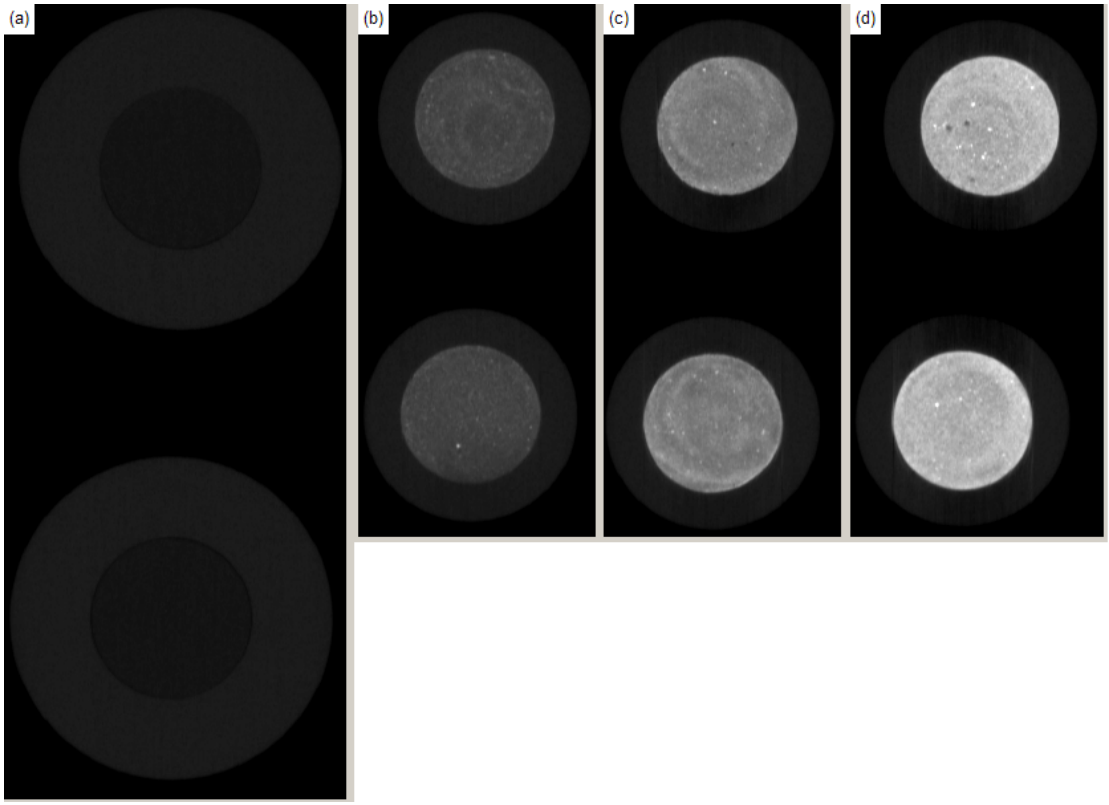

Figure 5-11. µCT image slices chosen at random of specimens from PMMA cement/barium sulphate mixture groups (a) 2 (1:0), (b) 3 (2:1), (c) 4 (4:1) and (d) 5 (8:1). In all four images, the brightness and contrast have been boosted to make it easier to see the Delrin endcaps.

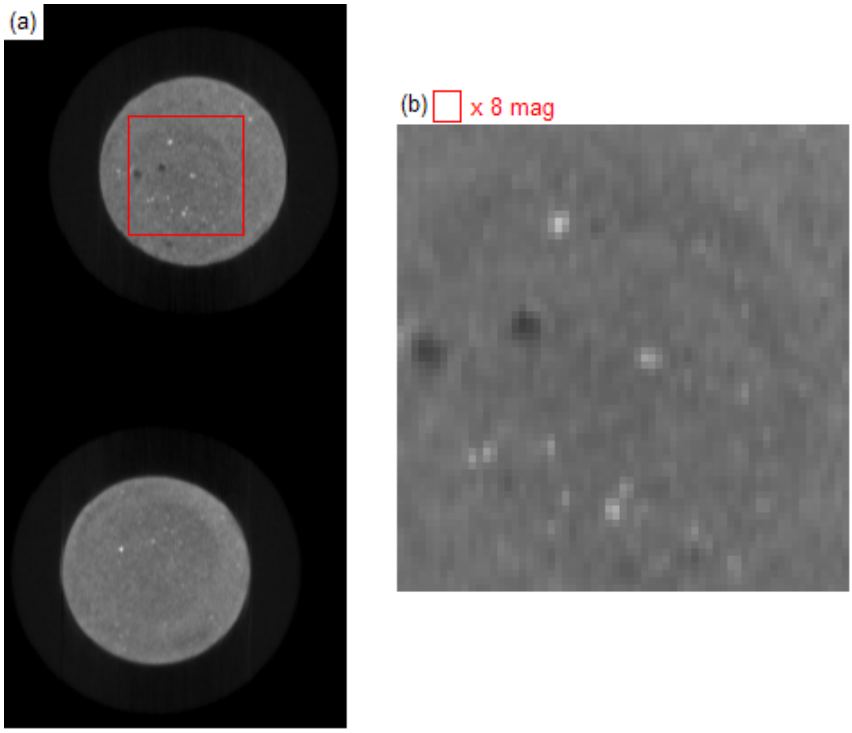

Figure 5-12. Example µCT image slices of specimens from PMMA cement/barium sulphate mixture group 3 (2:1).

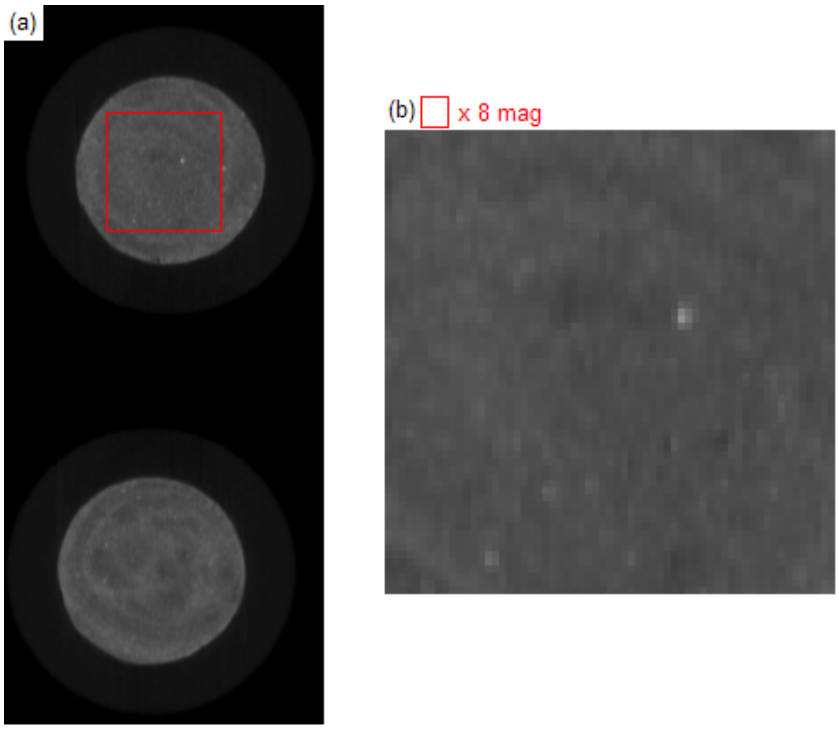

Figure 5-13. Example µCT image slice of specimens from PMMA cement/barium sulphate mixture group 4 (4:1).

Example µCT image slices from specimen Groups 2 to 5 are shown in Figure 5-11(a)-(d) respectively, with mixtures ranging from (a) 1:0 to (d) 8:1 PMMA powder to barium sulphate powder. In all four images, the brightness and contrast have been boosted to make it easier to see the Delrin endcaps. Figures 5-12 and 5-13 show slices chosen at random from specimen Groups 3 and 4, comprising 2:1 and 4:1 PMMA powder to barium sulphate respectively, using default brightness and contrast settings.

Comparing Figures 5-10, 5-12 and 5-13, it is clear that reducing the mixing time has the effect of increasing the incidence of barium sulphate agglomeration, while reducing the proportion of barium sulphate in the cement has the opposite effect, and in addition, appears to reduce the average µCT brightness of well-mixed cement regions. The ideal is to balance the requirement to be able to differentiate the cement from both the bone and the intra-trabecular soft tissues against the desire to reduce the incidence of barium sulphate agglomeration.

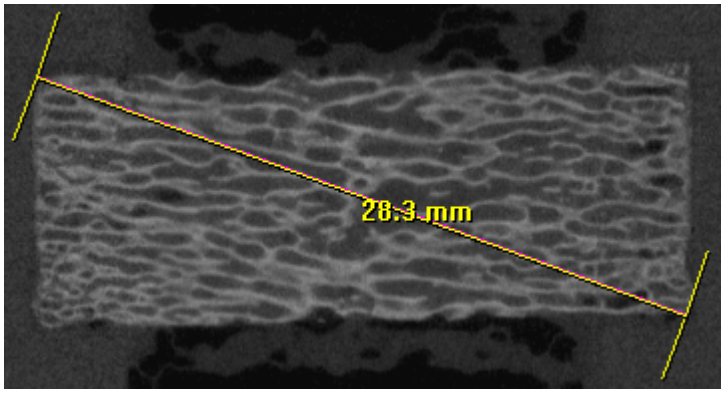

Figure 5-14. Location of the diagonal axis across a cross-section through a µCT scan of an un-augmented ovine specimen, along which the µCT grayscale profile was determined (shown in Figure 5-15).

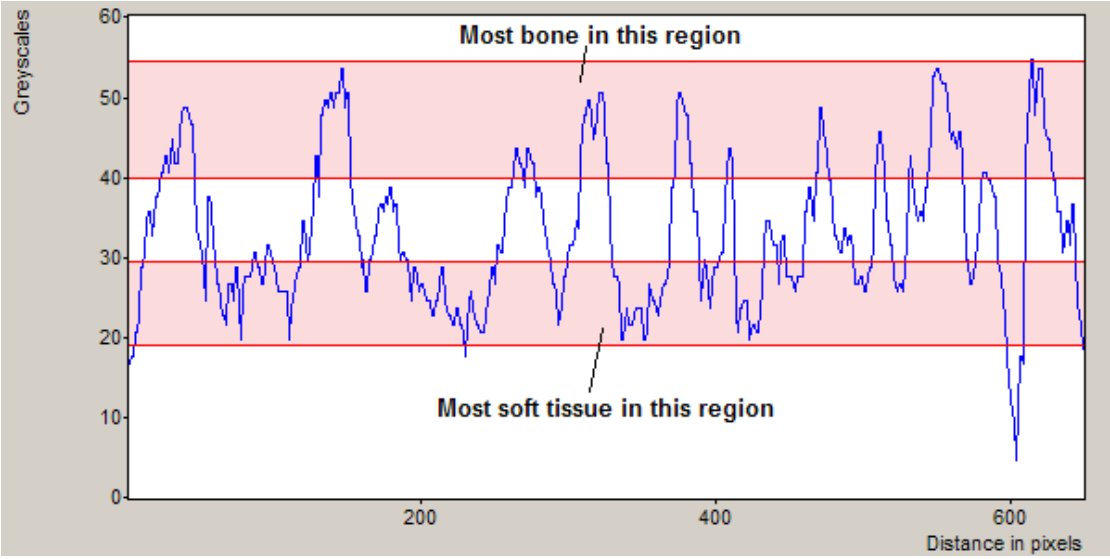

Figure 5-15. µCT ovine specimen grayscale profile along the diagonal axis shown in Figure 5-14.

A histogram representing the µCT grayscale profile along the diagonal of a cross-section of an un-augmented specimen of ovine lumbar vertebral trabecular bone (Figure 5-14) is shown in Figure 5-15. Most of the peaks representing the bone lie the µCT greyscale range 40-55, while most of the intra-trabecular soft-tissues lie in the µCT greyscale range 20-30. So that it can be easily differentiated from the trabecular bone, the cement µCT brightness needs to lie outside these greyscale ranges, ie > 55.

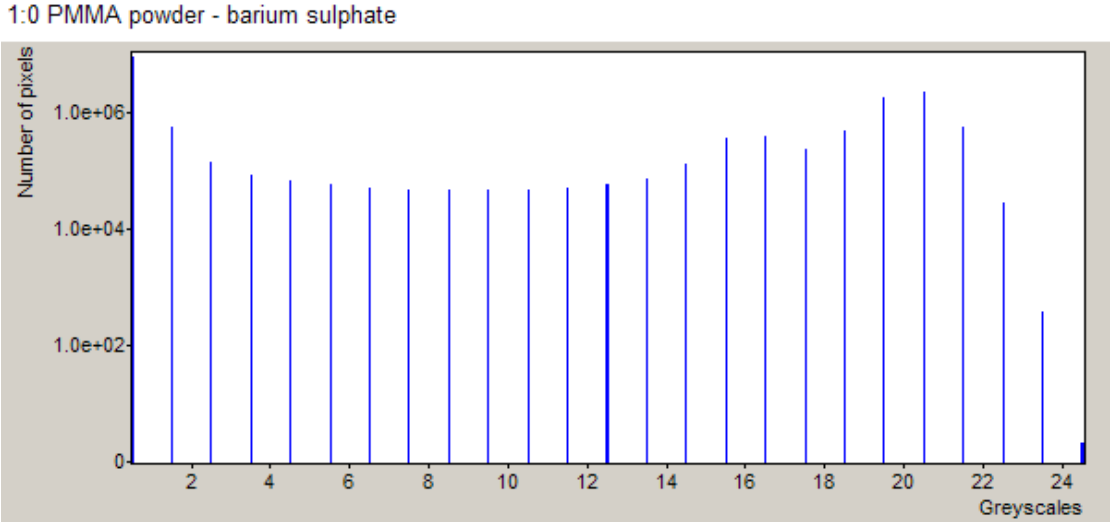

Figure 5-16. µCT grayscale profile for a µCT image slice selected at random from a specimen in Group 2 (1:0).

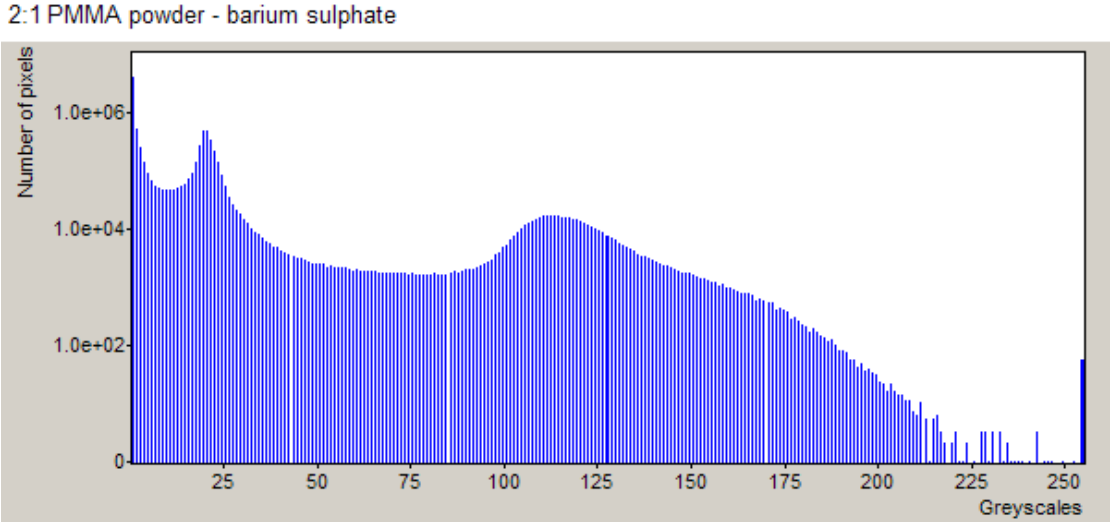

Figure 5-17. µCT grayscale profile for a µCT image slice selected at random from a specimen in Group 3 (2:1).

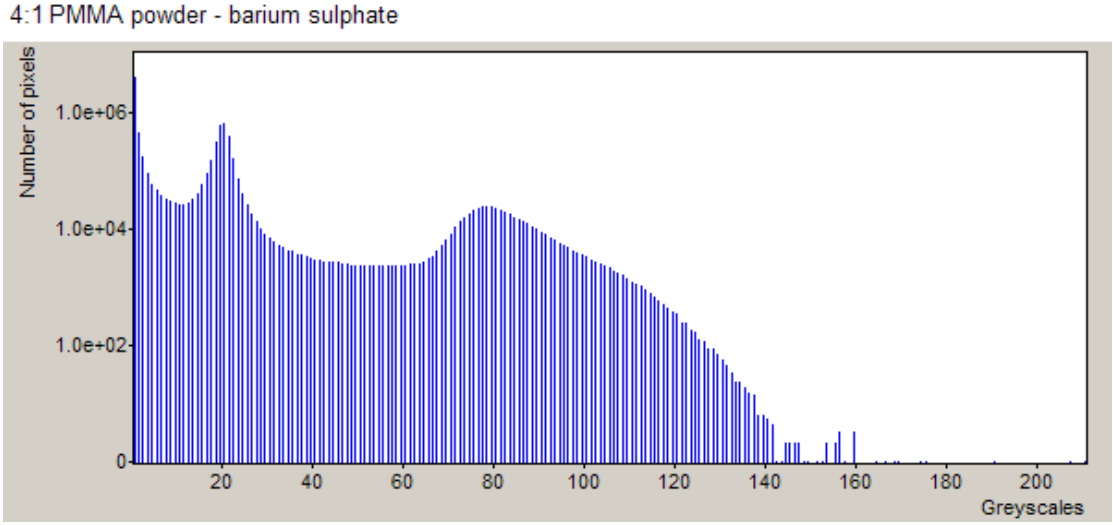

Figure 5-18. µCT grayscale profile for a µCT image slice selected at random from a specimen in Group 4 (4:1).

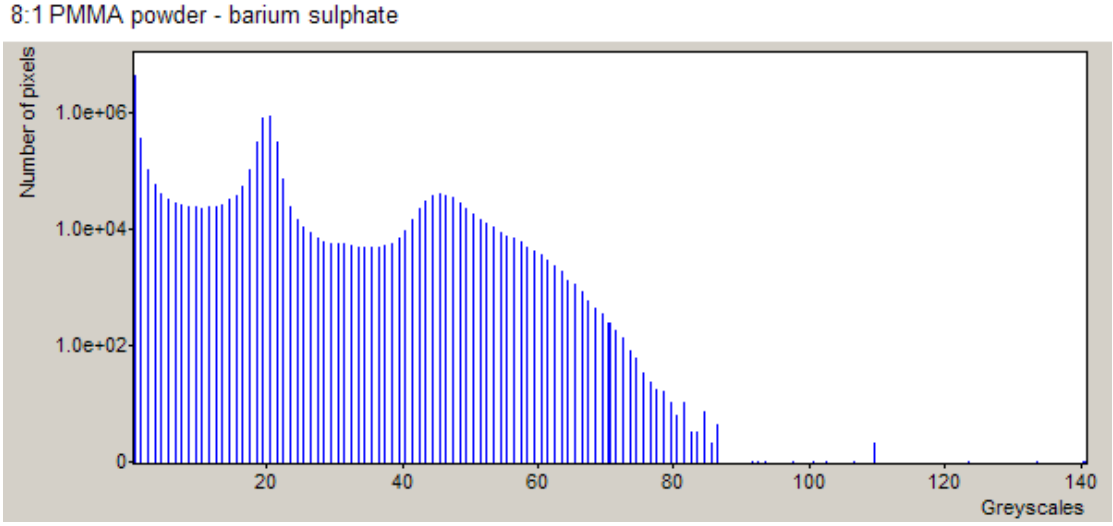

Figure 5-19. µCT grayscale profile for a µCT image slice selected at random from a specimen in Group 5 (8:1).

Figures 5-16 to 5-19 show the µCT greyscale histograms for the image slices from specimen Groups 2 to 5 shown in Figure 5-11(a)-(d). All four histograms exhibit a peak at a µCT greyscale value of approximately 20, which are presumed to be caused by the Delrin cups, as in the µCT images of the unmodified PMMA specimens (Figure 5-11(a)) the Delrin is markedly brighter than the PMMA it contains, suggesting that the unmodified PMMA occupies the greyscale range below 20. The next peak visible in Figures 5-16 to 5-19 is due to the barium sulphate augmentation added to the PMMA, the centre of which increases in brightness as the ratio of barium sulphate to PMMA

increases, and as such the concentration of barium sulphate particles in the evenly mixed regions of cement.

These are less well-defined than the peaks denoting the Delrin cups, featuring a broader main peak and gradual tail-off in the direction of increasing brightness. It is suggested that this is due to a wide range of barium sulphate particle sizes distributed throughout the cement by the mixing process. As the proportion of the cement mixture comprising barium sulphate increases, the quantity of very fine particles of barium sulphate distributed throughout the cement, and hence the average cement brightness, will increase. However at the same time it is likely that the number of progressively larger particles that have failed to be dispersed throughout the cement by the mixing process will also increase. This leads to an overall increase in cement brightness variation, and hence the increasing tail-off seen as the barium sulphate concentration increases (ie: from Figures 5-17 to 5-19).

While the high average cement brightness exhibited by the 2:1 PMMA to barium sulphate ratio specimens (μCT greyscale = approx 100+, (Figure 5-17)) would make it easy to differentiate the cement from the bone, and soft tissues, the increased barium sulphate agglomeration visible in the μCT images (Figure 5-11(d)) is clearly indicated by the narrow peak at a maximum brightness value of 255. Such a high incidence of barium sulphate agglomeration would be likely to cause the sort of destructive image artefacts seen in Figure 5-8. Conversely, while the histogram for the specimens containing an 8:1 PMMA to barium sulphate ratio show greatly reduced barium sulphate agglomeration (Figure 5-19), the majority of the cement lies between μCT greyscale values of approximately 40-60, tailing off by a μCT greyscale value of around 90. This suggests that significant amounts of the cement augmentation might be hard to differentiate from the surrounding bone.

Of the cases examined here, the ideal cement composition for these purposes appears to be a PMMA to barium sulphate ratio of 4:1. As can be seen in Figure 5-18, this leads to the majority of the cement occupying a μCT greyscale range above 70, markedly higher than the range in which the bone lies (μCT greyscale = approx 40-55). This allows the bone and cement to be easily differentiated while avoiding the significant barium

sulphate agglomeration exhibited by the higher barium sulphate concentration, and the image artefacts this would likely introduce.

5.3. Development of a compression and imaging device

As detailed earlier, the overall aim of this work was to better understand the behaviour of the interdigitated interface between trabecular bone and cement resulting from the injection of PMMA bone cement into a vertebral body during vertebroplasty, for the purposes of improving the predictive accuracy of continuum-level finite element models of cement-augmented vertebrae.

This would be accomplished by imaging specimens of this interface using μCT as they underwent deformation to failure such as to allow the interfacial behaviour and strain distribution throughout the specimen to be studied. This necessitated the design and fabrication of a piece of new test equipment able to compressively deform each specimen to failure in a number of discrete steps, holding the deformation constant between each step such that the specimen could be imaged using μCT.

5.3.1. Proof of concept apparatus

As detailed in Section 3.2, initial test specimens were fabricated from Sawbone for the purposes of developing a specimen fabrication and augmentation methodology. In parallel to this, a proof of concept device was developed to test the efficiacy of the proposed compression and imaging technique and develop and refine the experimental methodology.

5.3.1.1. Design requirements

The proof of concept device had to comply with the initial test specimen requirements:

- Accommodate a specimen diameter of at least six to eight trabecular ‘cells’, i.e.: Approximately 13 mm for a specimen fabricated from Sawbone with a 1.5-2 mm average pore size (without endcaps)
- Accommodate specimen height-width ratio of at least 1.5:1, i.e.: Approximately

20 mm (without endcaps)

- Resist significant elastic deformation or structural yield due to reaction forces applied by specimen at or approaching failure strain. For specimens fabricated as described above, this was estimated to be approximately 100 N

There were a number of other operational requirements:

- No metal components could be placed in the μCT x-ray beam path. This was important to minimise x-ray backscatter that can cause distortion and artefacts within the resulting images
- The overall dimensions of the rig were restricted by the size of the largest sample container available for the μCT scanner (μCT-80, Scanco Medical AG, Brüttisellen, Switzerland), which had a height of 100 mm and diameter of 74 mm
- The device had to allow the application of sub-millimetre increases to the applied deformation in order to capture a series of images of the specimen through loading.

5.3.1.2. Description of design

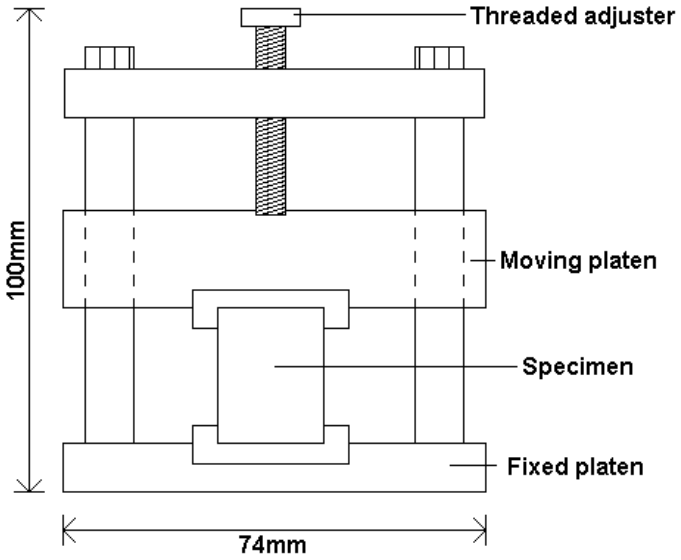

Figure 5-20. Cross-section schematic outlining the proposed design of the proof of concept compression and imaging device.

Based on these requirements a simple design was proposed (Figure 5-20). The end-capped specimen would be mounted between the fixed platen at the base and a movable platen able to slide on the four parallel uprights. Advancing a bolt threaded through the top plate would drive the movable platen towards the fixed platen, applying a compressive deformation on the mounted specimen.

To minimise x-ray back scatter, the device was completely fabricated from a polymer (Polyoxymethylene, commonly known as Delrin). This was chosen as it possesses a high stiffness and strength compared to many polymers and is easily machined. A bolt with a 1 mm thread pitch was chosen such as to allow sub-millimetre deformations to be easily applied. The dimensions of the fixed and movable platens, the bolt and the uprights were chosen to ensure that the maximum stresses within them, due to the reaction forces applied by a specimen at or approaching failure strain, would be at least one order of magnitude below the published failure stress for Delrin. The resulting axial elastic deformation would also be at least one order of magnitude below the applied deformation. These requirements were met whilst the dimensions remained within the limits set by the internal dimensions of the μCT scanner sample holder. The final fabrication of the device was completed in house (Figure 5-21).

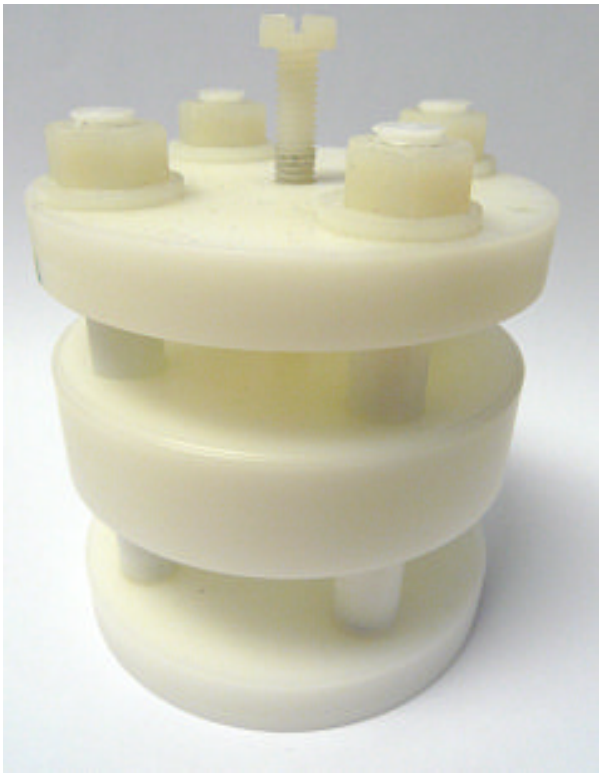

Figure 5-21. Proof of concept compression and imaging device as fabricated in-house.

5.3.1.3. Initial proof of concept μCT images

A series of μCT images of the incremental compression to failure of one of the synthetic bone interfacial specimens using the proof of concept compression and imaging device is shown in Figure 5-22. The proof of concept compression and imaging device and synthetic bone specimens demonstrated that it was possible to incrementally deform interfacial specimens to failure under screw thread driven deformation control, and informed both further development of the compression and imaging devices and the development of an appropriate test protocol to facilitate the study of ovine trabecular bone – cement interface specimens.

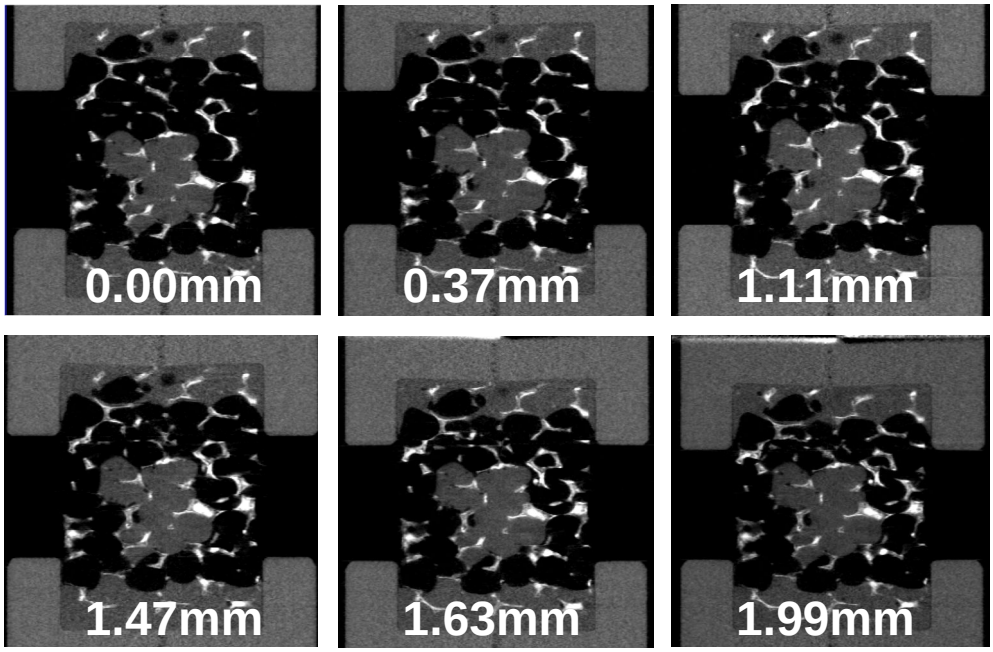

Figure 5-22. µCT images of the incremental deformation to failure of one of the synthetic bone interfacial specimens. The captions denote the applied deformation at each stage, measured from the µCT images.

5.3.2. Modifications to initial apparatus: Inclusion of load sensor

5.3.2.1. Introduction

The proof of concept compression and imaging device successfully demonstrated the feasibility of using a screw-thread driven compression and imaging device to image the incremental deformation of specimens of a simulated trabecular bone – cement interface. While the intention was to use image-based analysis tools to quantify the strains throughout the specimen and across the interface, results from previous studies (Zhao 2010) highlighted the need to be able to record the reaction forces resulting from a given applied specimen deformation for the purposes of validating the resulting image-based finite element models.

Efforts were thus made to incorporate a method of measuring the reaction force. Any modification made to the device had to comply with the limitations on size and material composition imposed by the available μCT scanner. It was essential to avoid placing metallic components in the x-ray beam path, however operation of the μCT scanner required that the device not protrude above the top of the specimen container and therefore precluded the installation of a load cell away from the specimen.

5.3.2.2. Methods

In order to comply with the space requirements, the only means of measuring the load was to use a non-metallic resistive force sensor installed between the specimen and the fixed platen of the compression and imaging device. A suitable sensor (FlexiForce A201, Tekscan, inc. MA. USA.) was identified and the device was modified to incorporate it.

An initial calibration test was conducted using the sensor. The sensor was clamped between two Delrin spacers within a compressive test machine. The Delrin spacers served to ensure that the applied load acted only on the force-sensitive central region of the force sensor (Figure 5-23). The applied load was ramped up to 1300 N in 50 N

increments, and the resistance of the force sensor was measured using a digital multi-meter following each load increment. This was repeated seven times.

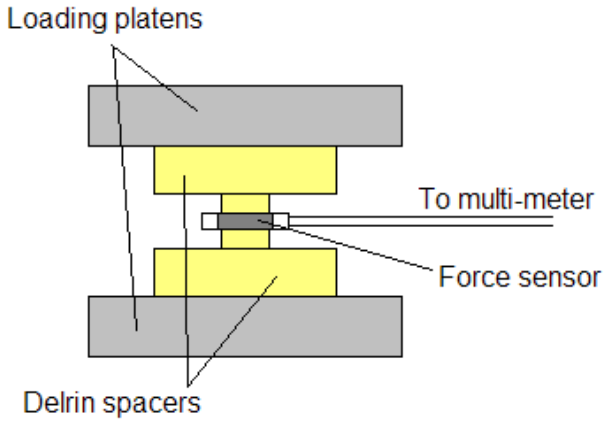

Figure 5-23. Cross section schematic of the compressive test setup used for initial calibration of the resistive force sensor.

5.3.2.3. Results

A plot of the measured resistance against the applied load, and the standard deviations of this is shown in Figure 5-24.

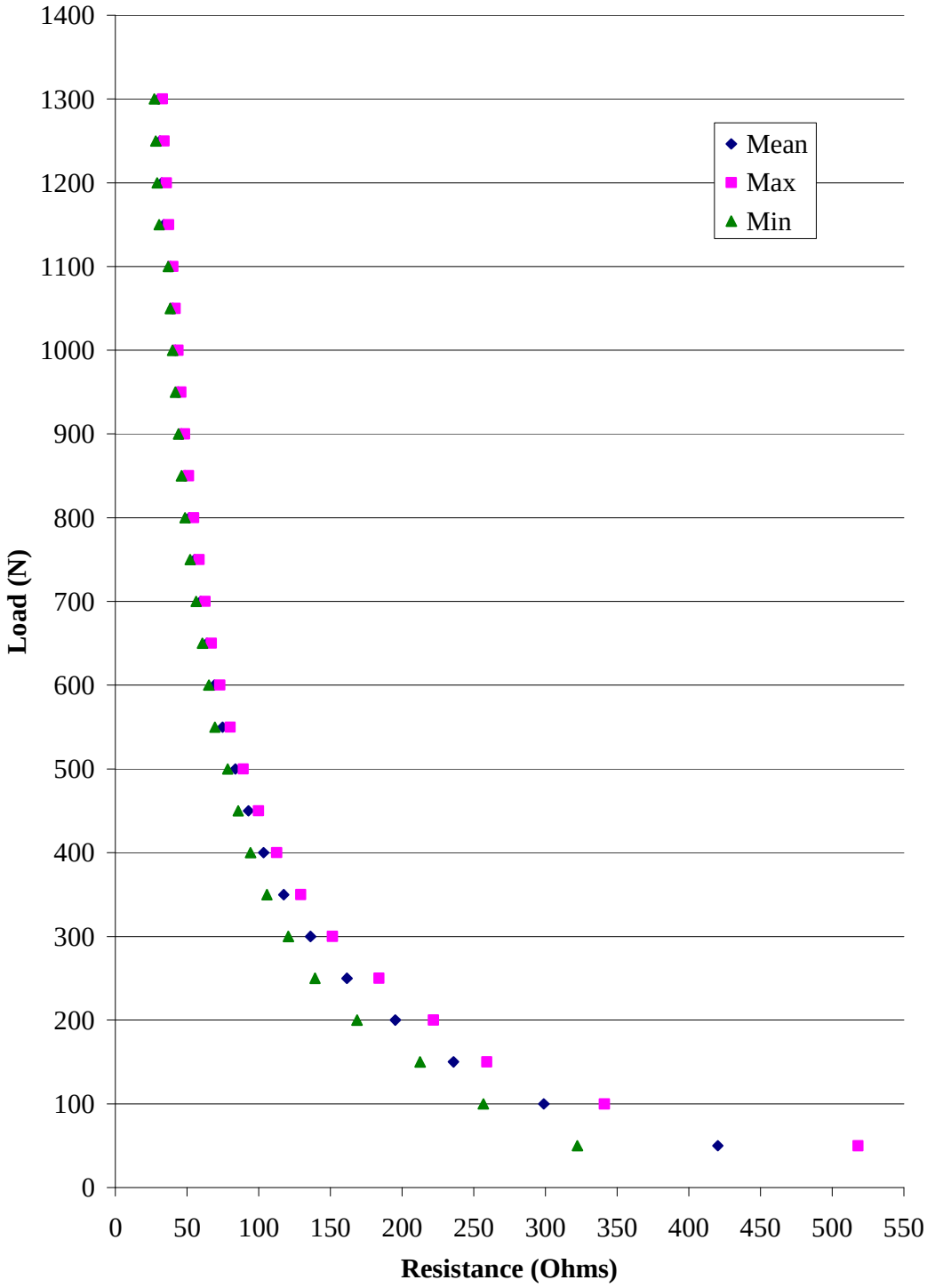

Figure 5-24. Plot of variation in measured resistance according to the applied load for the resistive force sensor. The Max and Min plots denote one standard deviation either side of the mean value.

5.3.2.4. Discussion

It is clear from Figure 5-24. that the repeatability with which reaction force measurements could be taken using the resistive force sensor was poor throughout the sensor's range of operation, limiting the accuracy with which the specimen reaction force could be determined to a maximum of approximately +/- 20-25 %. This error is significant when viewed in light of the difference in the experimentally measured reaction force between ovine specimens that underwent experimental compressive testing to failure (Described in Chapter 3) and suggested that the force sensor data would not be a useful tool for validating interfacial hFE model predictions.

5.3.3. Modifications to initial apparatus: Fabrication for ovine specimens

5.3.3.1. Introduction

Initial compressive test data suggested that the ovine specimens were of the order of ten times stiffer than the synthetic bone specimens. However, the dimensional constraints imposed by the specimen chamber and the requirement to avoid the use of metal components precluded significantly stiffening the proof of concept compression and imaging device. Calculations suggested that the stress in the various component parts of the device would still be below the published yield stress for Delrin, so that it might be possible to use the device for ovine specimens.

5.3.3.2. Methods

A modification was made to the compression and imaging device to improve the stability of the threaded deformation control and make it easier to apply smaller increments (<< 1 mm) to the applied deformation. A schematic of the modified device is show in its final form in Figure 5-25.

The modified compression and imaging device was then used to image the incremental compression of ovine bone – cement interface specimens (Described in Section 5.4.2.).

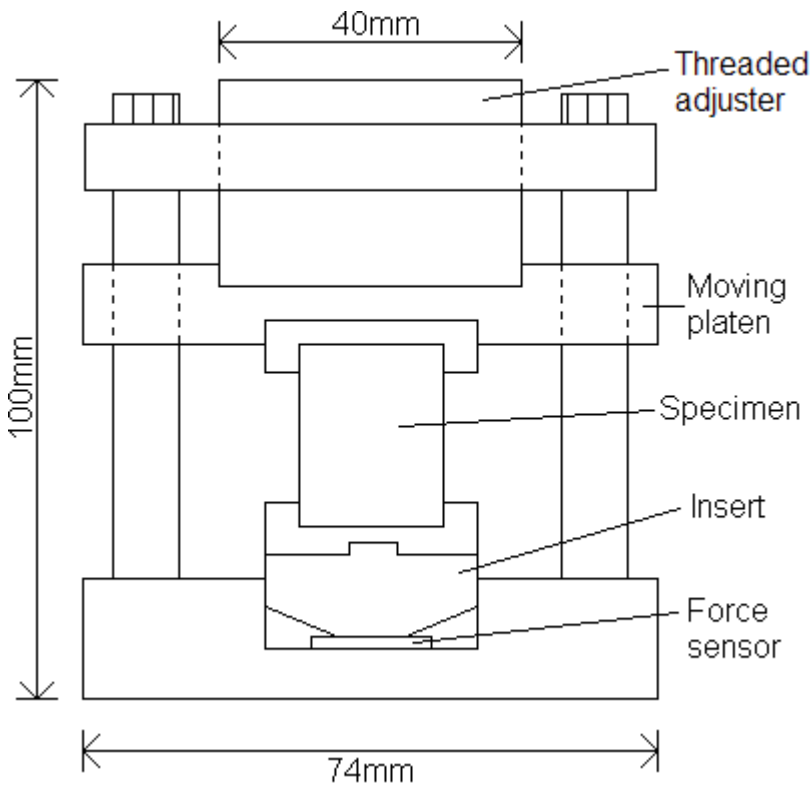

Figure 5-25. Cross-section schematic of the modified proof of concept compression and imaging device.

5.3.3.3. Results

Following a number of tests, examination of the resulting μCT images suggested that the increased stiffness of the ovine specimens caused the majority of the indicated applied deformation to occur in the compression and imaging device itself, as opposed to the specimen. The proportion of the overall deformation occurring in the specimen was not only typically less than 50%, but appeared to vary inconsistently between increments, making it difficult to counteract the reduced specimen deformation by proportionally increasing the indicated applied deformation.

5.3.3.4. Discussion

Most of the shortcomings of the proof of concept compression and imaging device were due either directly or indirectly to the dimensional constraints imposed by the available

μCT scanner. During the development and testing of the modified device, a larger μCT scanner was purchased which allowed the development of a larger and stiffer compression and imaging device from the start. For this reason, further development and testing of the modified proof of concept device ceased, and a new device was developed for the larger μCT scanner. The new device is described in the next section.

5.3.4. XtremeCT compression and imaging device

5.3.4.1. Introduction

A new clinical μCT scanner (Xtreme CT, Scanco Medical AG, Brüttisellen, Switzerland) became available during the development of the proof of concept compression and imaging device. The new scanner offered a greatly increased sample container volume and provided an opportunity to design and build a new device from the ground up to take advantage of the relaxed dimensional constraints.

The increased sample container volume allowed:

- A physically larger and stiffer device structure to enable controllable compression and imaging of ovine lumbar vertebral trabecular bone – cement interface specimens, which were of the order of ten times stiffer than the initial proof of concept specimens fabricated from the synthetic bone.
- Inclusion of metallic components as the device could be made sufficiently large to incorporate such components while keeping them clear of the μCT x-ray beam path.

5.3.4.2. Design requirements

Most of the requirements set out in Section 5.4 were still applicable. However, the enlarged sample container and utilisable space outside the scan volume changed the spatial requirements as follows:

- The limit on the maximum allowable outside diameter of the compression and imaging device increased to 126 mm.
- As a clinical research scanner, the XtremeCT μCT scanner features an open front that allows specimens to protrude from the open end of the sample container. As such, there was (effectively) no limit on the maximum length of the compression and imaging device.
- The part of the compression and imaging device containing the specimen was limited to the first 300 mm of the sample container.

5.3.4.3. Description of design

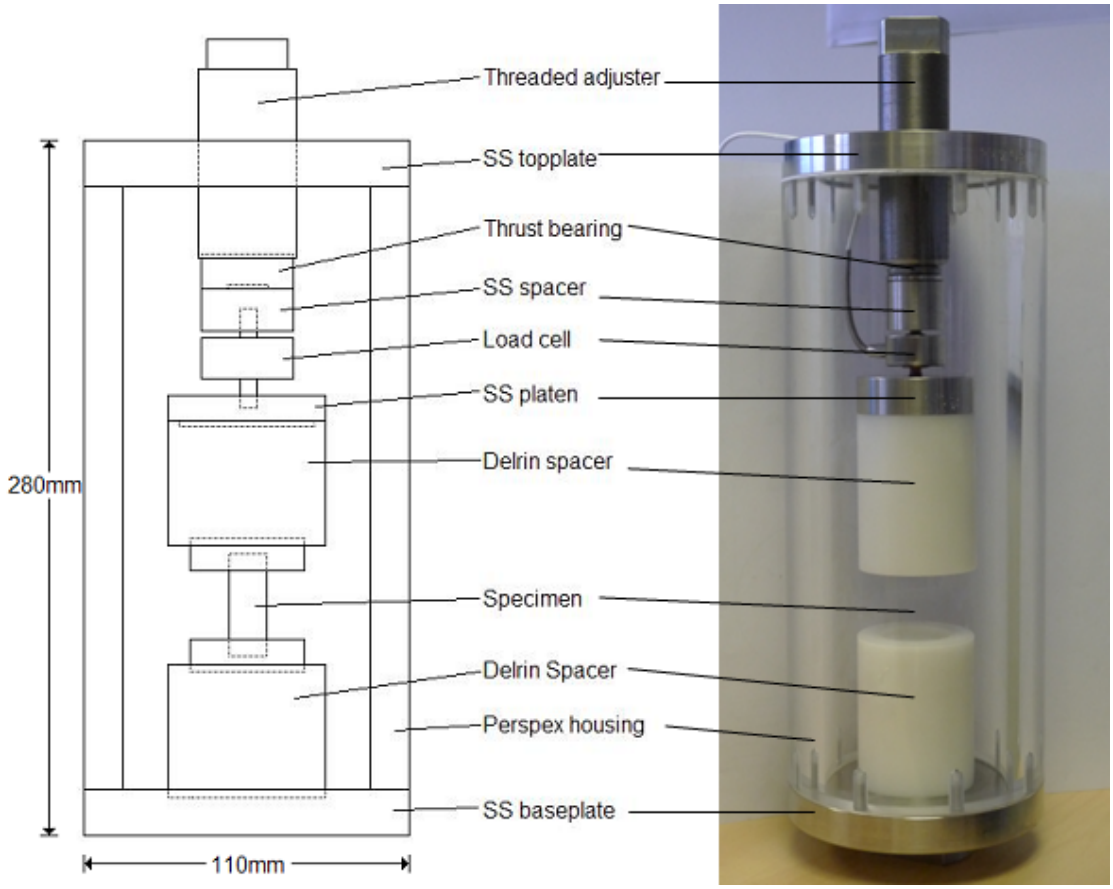

Figure 5-26. Cross-section schematic and photograph of the completed XtremeCT compression and imaging device as fabricated in-house.

The new design (Figure 5-26) was broadly based on an existing device developed in-house to allow compression and μCT imaging of whole vertebral bodies. The ability to include metal components in the design allowed the incorporation of a load cell, calibrated to work with a digital load readout, as well as a thrust bearing installed between the threaded deformation adjuster and the load cell to minimise any torque that would otherwise be applied to the specimen. This had not been necessary in the proof of concept device as the axial structural components acted as runners along which the movable platen could slide, preventing rotation. It was necessary in the redesigned device due to the switch to an external tubular structure.

5.3.4.4. Design evaluation

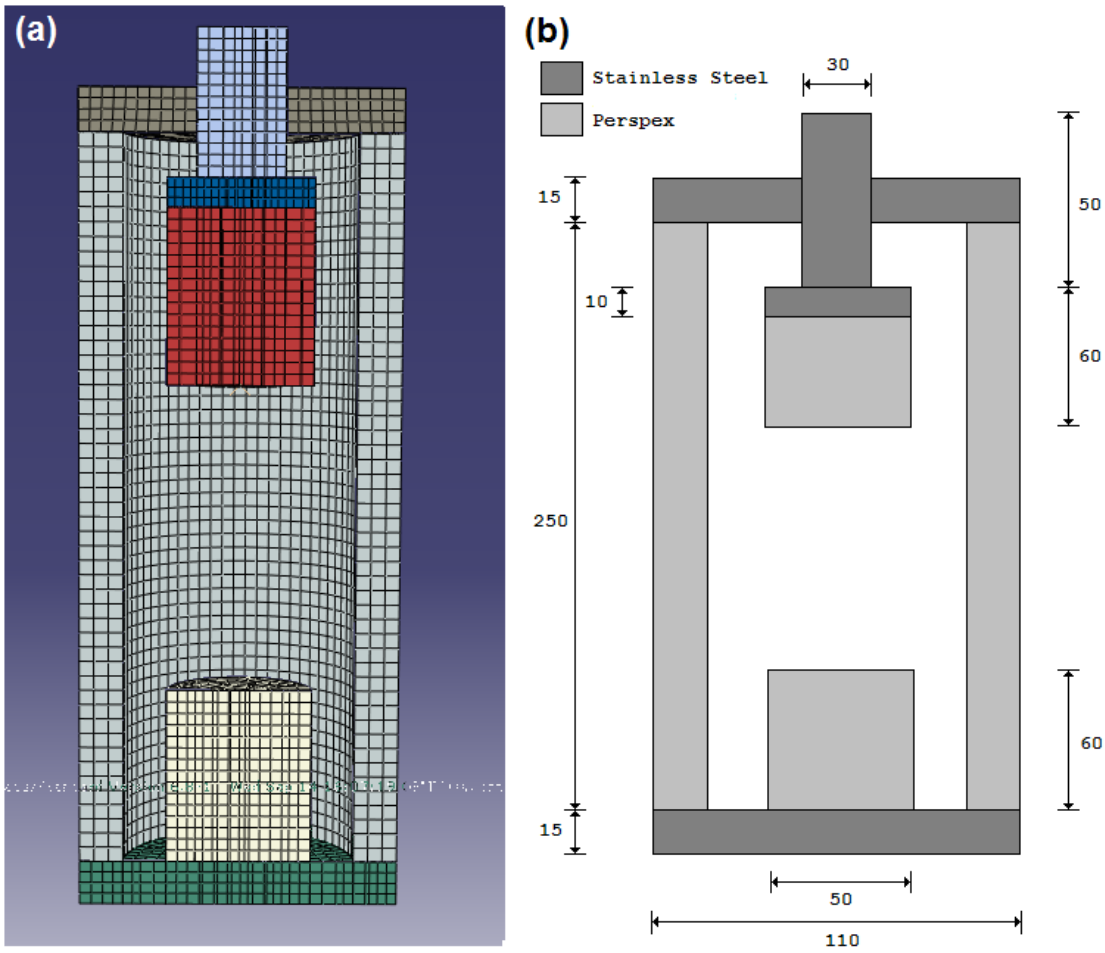

Figure 5-27. (a) Cross section of the FE model used to assist in the evaluation of the design of the XtremeCT compression and imaging device and (b) schematic showing the major dimensions.

Once the basic design had been settled, tests were carried out using a simplified finite element model of the design, constructed and solved using Abaqus CAE v6.8 (Simulia Corp, USA) (Figure 5-27) to ensure that the device would be structurally stiff enough to minimise the proportion of the indicated applied deformation occurring in the device rather than the specimen, and that the maximum stresses in the various components would remain significantly below the yield stress for the materials from which they had been fabricated. An analytical rigid plate was tied to the lower spacer and constrained with encastre boundary conditions. A 2500 N axial load was applied to a reference node in the centre of an analytical rigid plate tied to the upper spacer. This was representative

of the load required to initiate yield in an ovine lumbar vertebral trabecular bone specimen, based on previous compressive testing (discussed in Chapter 3).

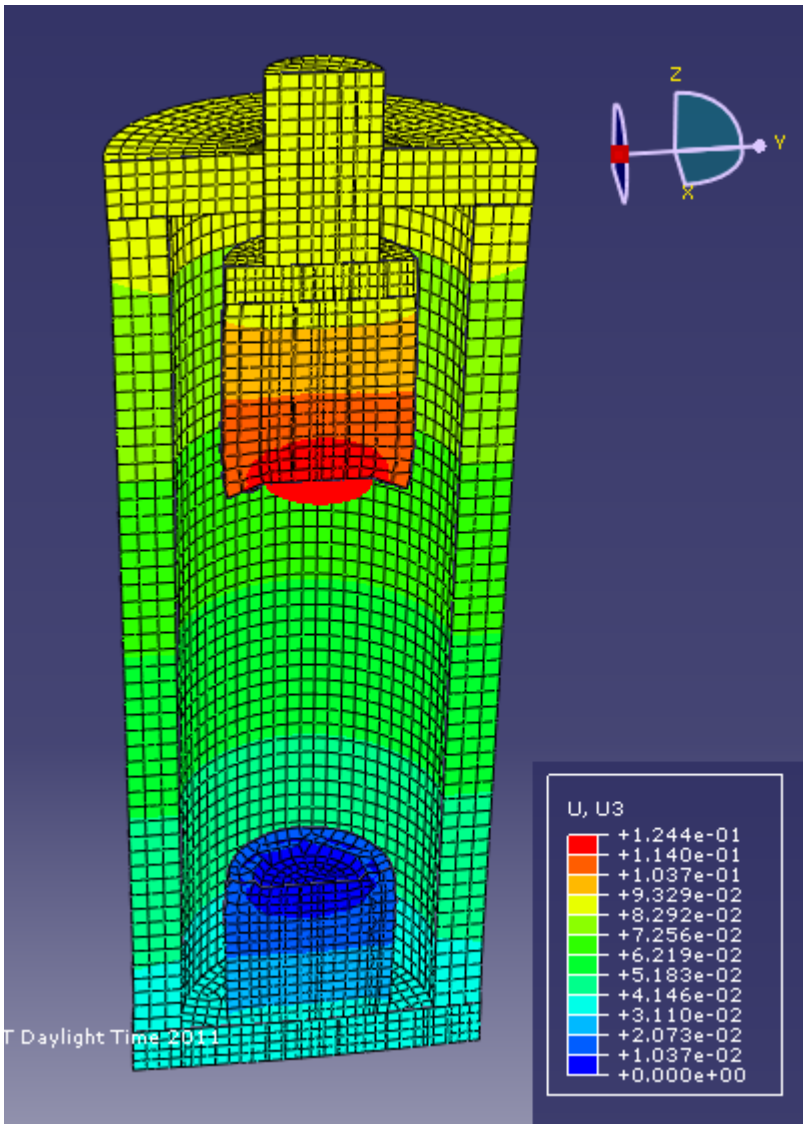

Figure 5-28. Contour plot showing FE-predicted deformation of the XtremeCT compression and imaging device in the axial (z-axis) direction under a representative reaction force for compression to failure of an ovine lumbar vertebral trabecular bone specimen.

As shown in Figure 5-28, the finite element model predicted an axial deformation of approximately 0.12 mm. Based on examination of the results of previous compressive testing of cement-augmented ovine specimens, this would equate to approximately 10-15% of the indicated deformation at the point of yield for a representative specimen. This was a five-fold decrease when compared to the proof-of-concept device, and

indicated that the new device would more easily allow controllable and repeatable deformation to failure of ovine specimens.

The device was then fabricated and assembled in house, shown in Figure 5-26.

5.4.2. Main study: μCT imaging of stepwise compressive deformation of ovine trabecular bone – cement interface specimens using XtremeCT compression and imaging device

Following commissioning, the XtremeCT compression and imaging device was used to image stepwise deformation of the three final 'break and fill' ovine lumbar vertebral trabecular bone – cement interface specimens.

5.4.2.1. Specimen preparation

The specimen to be examined was removed from frozen storage prior to each set of compression and imaging runs and allowed to thaw completely at room temperature for approximately one hour. The specimen was then seated within the XtremeCT compression and imaging device between the upper and lower Delrin spacers (See Figure 5-26), and the threaded adjuster was advanced by hand until the resistance increased sufficiently to be considered 'hand tight'.

5.4.2.2. Experimental protocol

Determination of appropriate magnitude and sub-divisions of the applied displacement

The need to complete each set of compression and imaging runs within the constraints of the laboratory opening hours limited each set of runs to a maximum of six μCT scans, with each μCT scan taking approximately one hour at the chosen image resolution of 0.082 mm^3.

For each specimen, the total deformation applied was determined by first calculating the deformation at which the specimen was expected to yield assuming a constant yield strain, based on a previously published study by Morgan and Keaveny (2001) that suggested that the apparent yield strain of human trabecular bone depended on the

anatomic site from which it was harvested. This agreed with the narrow range of yield strains determined for the wide range of un-augmented ovine lumbar vertebral trabecular bone specimens experimentally investigated in Chapter 3 (3.1 +/-0.4 %). As such, the apparent yield strain determined as part of this previous study was used (3.1 %).

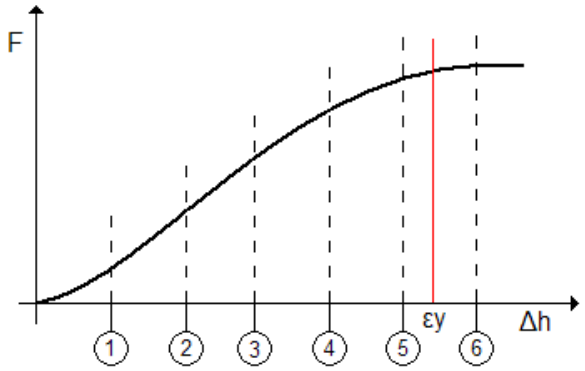

Figure 5-29. Estimated subdivisions of the proposed total applied displacement with respect to predicted apparent specimen yield (εy).

The compressive deformation at which the specimen was expected to yield was then increased by 1/12th to give the applied total deformation. It was expected that this would maximise the likelihood that yield would occur between the penultimate and final µCT scans (Figure 5-29). The total deformation was then divided by six to give the amount by which the applied deformation would be increased following each µCT scan.

XtremeCT imaging settings

The same XtremeCT scan settings were used as previously described in Section 3.3.

Experimental procedure

The experimental procedure used for the main study was similar to that used in the proof of concept study. For each of the three specimens, the specimen and XtremeCT compression and imaging device were prepared as described in Section 5.4.2.1. The load cell readout was then turned on, and the threaded adjuster was advanced until the

load cell readout indicated an applied 50 N preload. This was expected to be sufficient to ensure that the specimen was rigidly seated within the compression and imaging device, such that any further advance of the threaded adjuster would increase the applied deformation. The experimental procedure then continued as shown in Figure 5-30.

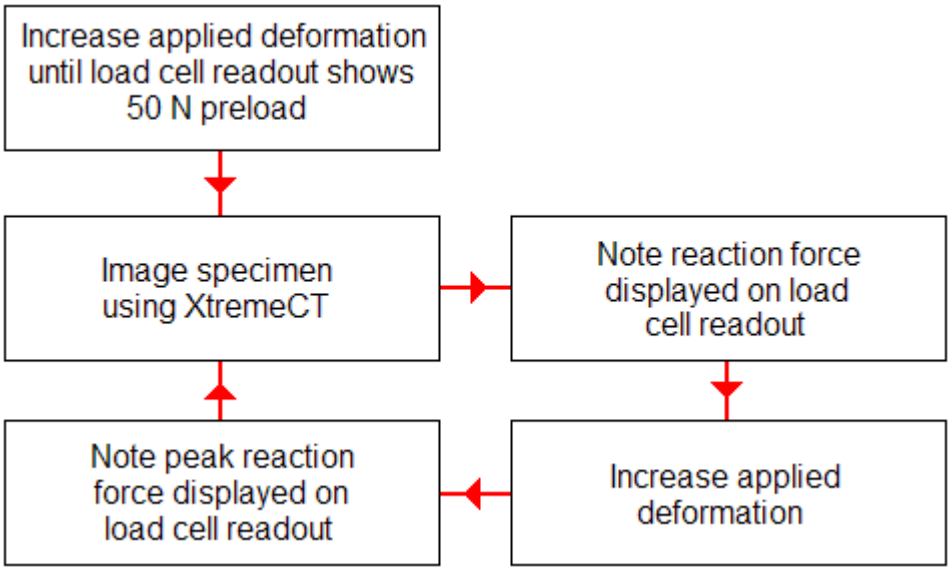

Figure 5-30. Experimental procedure for compression and µCT imaging of ovine interfacial specimens.

Preliminary analyses – Determining the actual applied deformation

Initial examination of the µCT images of the two interfacial specimens indicated that there was a disparity between the intended and actual deformations applied at each increment. The actual applied deformation was typically lower than the intended deformation at 69.22 % (S.D. 13.39) and 93.18 % (S.D. 8.87) of the intended deformation for Specimens 2 and 3 respectively. It is likely that this was due to the lack of a fine indicator scale on the XtremeCT compression and imaging device.

Accurate calculation of the interfacial specimens apparent mechanical properties required an accurate measure of the applied deformation at each increment. This was determined by examination of the specimen µCT images. For each post-increment scan, the distance in voxels between the inner end-cap faces was multiplied by the scan

resolution to give the end-cap separation. Taking the same measurement for the 50 N preload scan as a baseline and subtracting the resulting distance from the distance during each load increment gave the actual applied deformation in each case.

Preliminary analyses – Calculation of apparent specimen properties

For both Specimens 2 and 3, the apparent mechanical properties were determined in the same manner as for the un-augmented specimens studied in Chapter 4. The apparent specimen stiffness and Young's modulus was determined by taking the gradient of the straight line portion of the force/displacement and stress/strain plots respectively. The apparent specimen yield strain was determined from the stress/strain plot using the 0.2 % offset yield strain method, described in more detail in Section 3.5.

5.4.2.3. Results

Force/deformation data

The force/deformation data for Specimens 2 and 3 are shown in Figures 5-31 and 5-33 respectively. The force / deformation data for Specimen 1 was lost due to a data storage error and is not presented. The corresponding stress/strain plots for Specimens 2 and 3, including the 0.2 % offset linear intercept used to determine the yield strain, are shown in Figures 5-32 and 5-34.

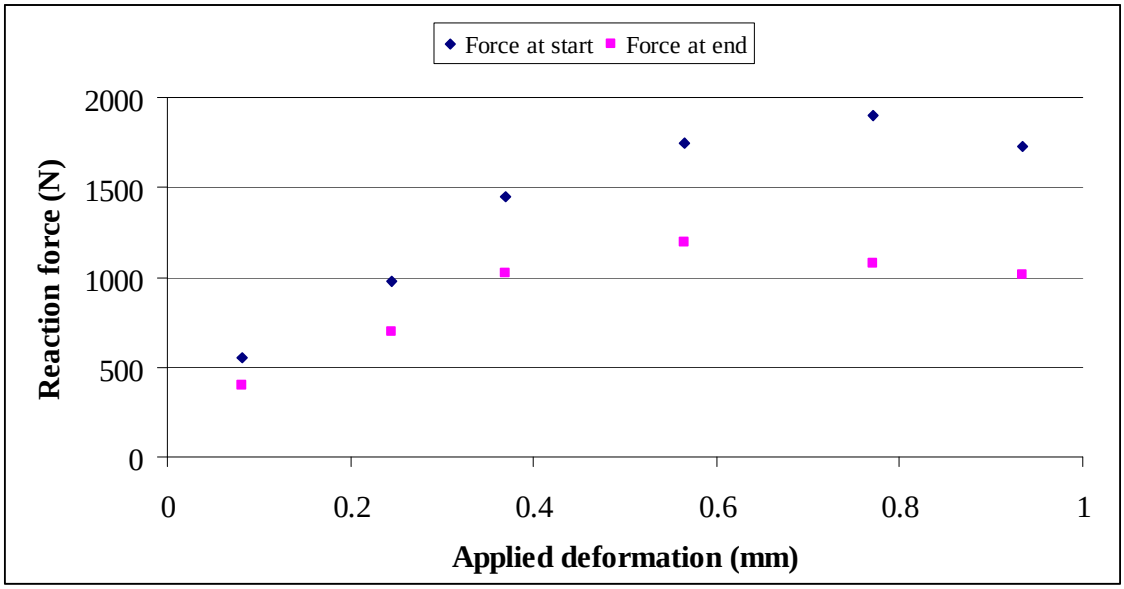

Figure 5-31 – Force/deformation plot for Specimen 2

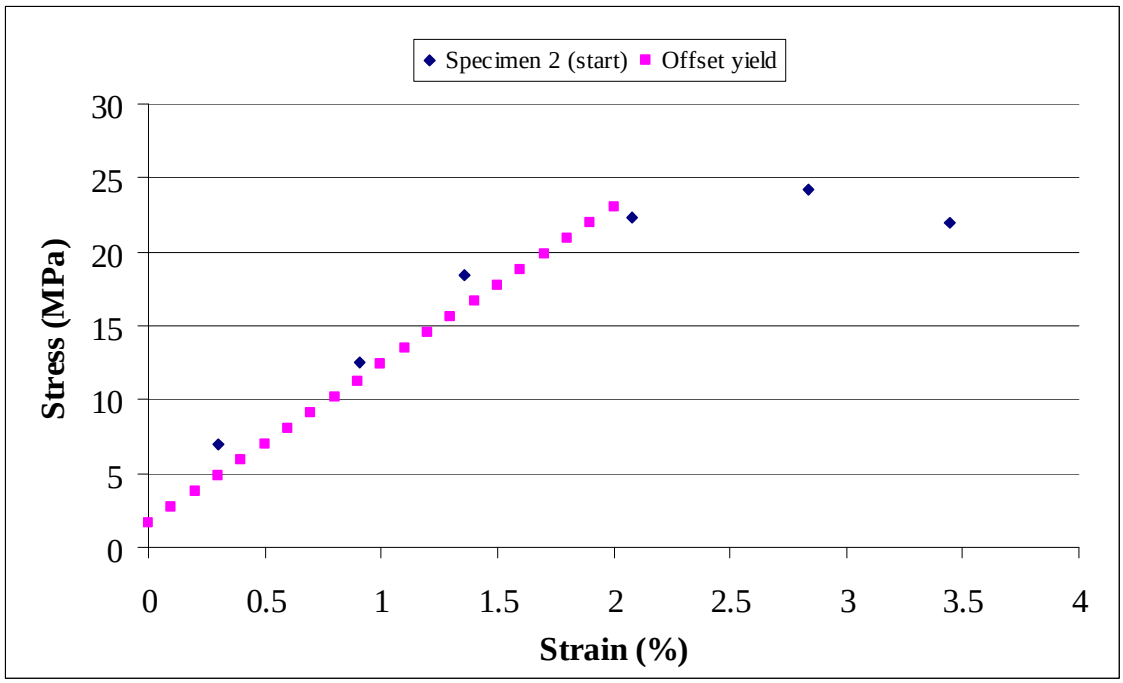

Figure 5-32 – Stress/strain plot with yield strain offset for Specimen 2

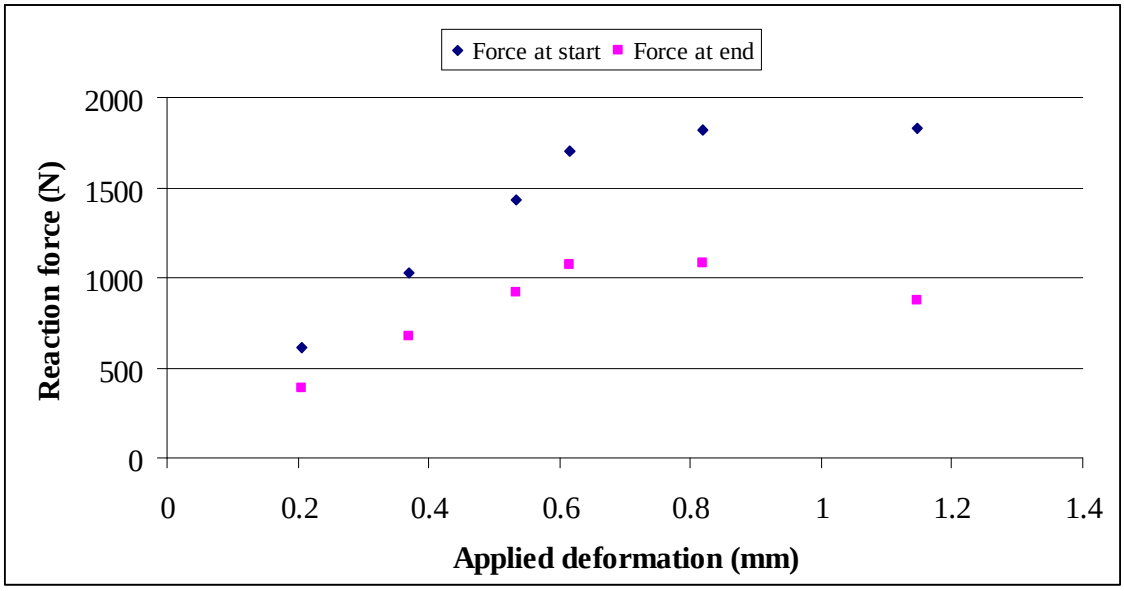

Figure 5-33 - Force/deformation plot for Specimen 3

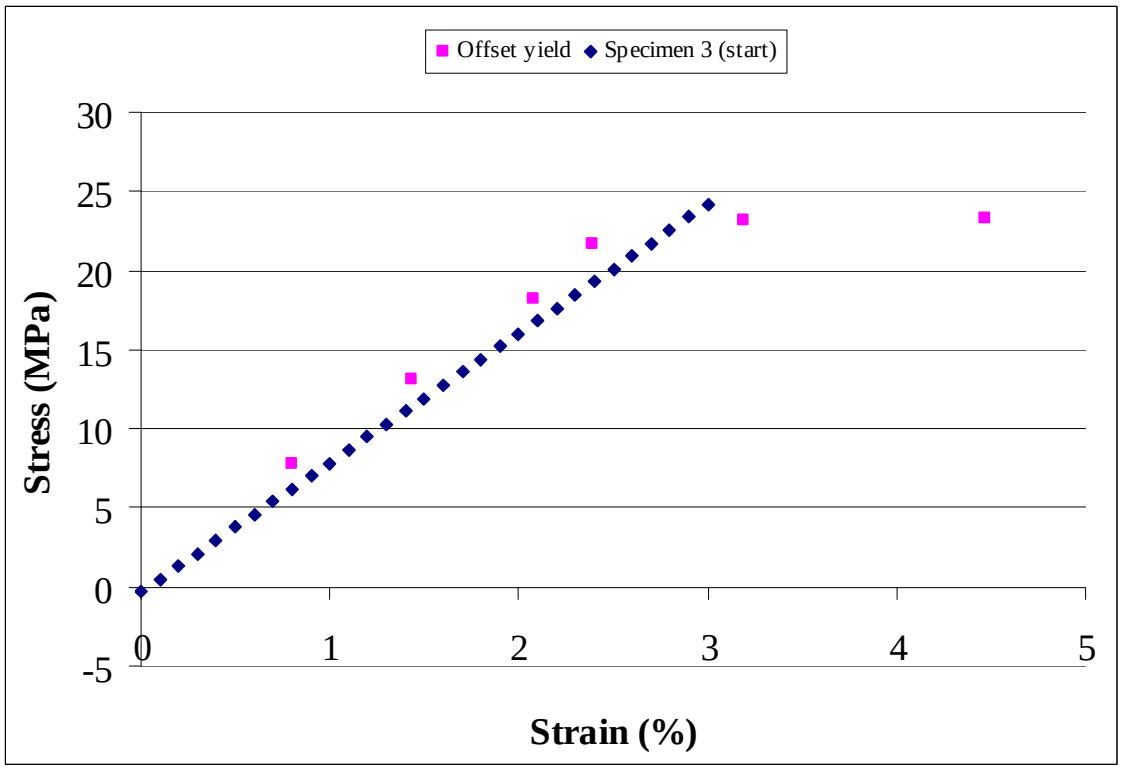

Figure 5-34 – Stress/strain plot with yield strain offset for Specimen 3

μCT images

A cross-section of Specimen 1 in the unloaded and loaded states is shown in Figure 5-35. At the maximum applied deformation trabecular failure was observed at the bone – cement interface(Figure 5-35(b)). Similar observations were seen in the other specimens at maximum load, along with some buckling of the PMMA column that was back-filled through the drill path. A more detailed quantitative analysis of the images is presented in Chapter 6.

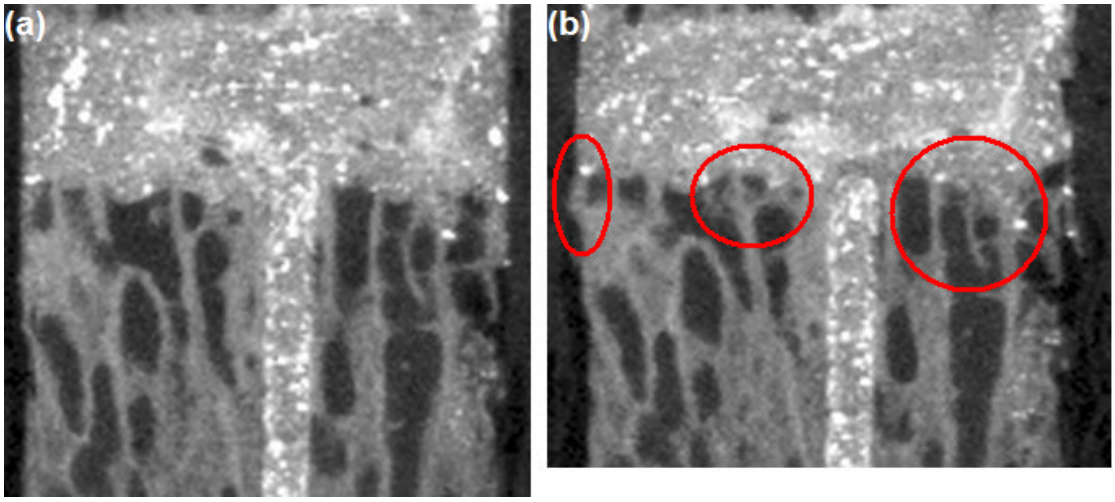

Figure 5-35. Selection from vertical cross section of μCT images of Specimen 1 at (a) zero applied deformation and (b) maximum applied deformation (1.066 mm), showing concentration of trabecular failure along the trabecular bone – cement interface (circled).

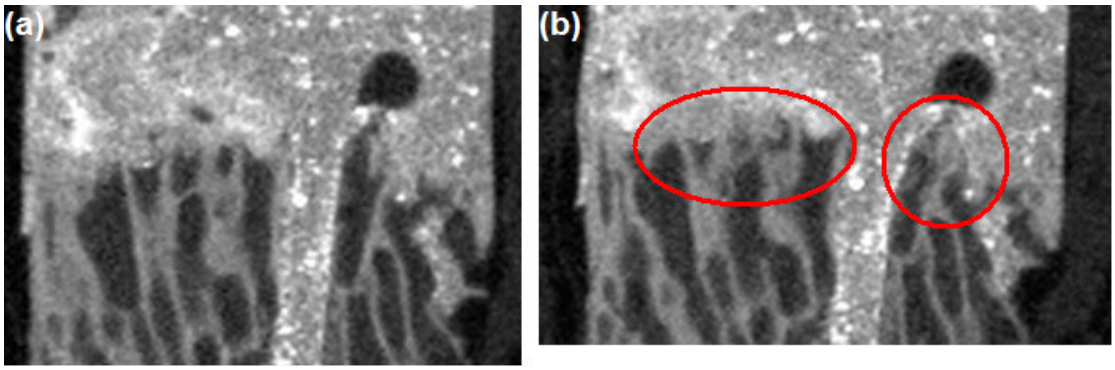

Figure 5-36. Selection from vertical cross section of μCT images of Specimen 2 at (a) zero applied deformation and (b) maximum applied deformation (0.934 mm), showing concentration of trabecular failure along the trabecular bone – cement interface (circled). Some buckling of the PMMA cement back-filled into the drill-path is also evident.

5.4.2.4. Discussion

Apparent property	Un-augmented ovine lumbar vertebral trabecular bone specimens studied previously (n = 27)	Specimen 2	Specimen 3
Stiffness (N/mm)	3685 (743)	3108	2609
Young's modulus (MPa)	956 (225)	1074	853
Yield strain (%)	3.1 (0.4)	2.4	2.9

Table 5-2 - Comparison of mean apparent specimen propeties between interfacial Specimens 2 and 3 and the un-augmented specimens studied in Chapter 3. The standard deviation across the un-augemented specimens for each apparent property are shown between parenthesis in each case.

As shown in Table 5-2., the apparent properties for both interfacial specimens fall within the range of results for the un-augmented specimens previously examined in Chapter 3 with the exception of the apparent stiffness for Specimen 3 and the apparent yield strain for Specimen 2, both of which fall outside of the lower bound of the un-augmented specimens results.

While the apparent stiffness for Specimen 3 is within the range of results for the un-augmented specimens, it lies at the lower end of the range. This finding agrees with the view expressed in several pseudo-hFE studies of the trabecular bone – cement interface (discussed in Section 2.3.3) that the bone – cement interface may behave as a region of increased compliance, more than offsetting the supposed stiffening effect due to the cement's higher Young's modulus.

The apparent yield strain for Specimen 3 is also within the range of results for the un-augmented specimens, but also lies at the lower end of the range. It is suggested that the comparatively reduced apparent yield strain for both interfacial specimens is due to stress-raising effects of interdigitation between bone and cement at the interface. This is in agreement with the initial analyses of the μCT images of the specimens in the region

of apparent yield, which appear to show trabecular failure predominantly occurring along the bone – cement interfaces (Figures 4-35 and 4-36).

	Specimen 2	Specimen 3	Deligianni et al (1994) (n = 25)
Stress relaxation (%)	29.65 (1.18)	36.19 (0.94)	26.02 (3.71)

Table 5-3 - Comparison of stress relaxation observed for interfacial Specimens 2 and 3 and cylindrical human femoral trabecular bone specimens studied by Deligianni et al (1994).

The reduction in measured reaction force between the start and end of each scan shown in Figures 5-31 and 5-33 suggests the occurrence of significant stress relaxation as the applied deformation is maintained, agreeing with previous studies (Pugh et al 1973; Linde 1994) that indicated that trabecular bone exhibits viscoelastic behaviour. In every instance, the load cell readout was stable when re-measured following each scan, suggesting that in every case specimen relaxation was complete within one hour of each increase in the applied deformation. The degree of relaxation during each scan was similar throughout the elastic range for each specimen, and only varies by 18 % between the two specimens (Table 5-3.). Both of these results agree with the findings presented by Deligianni et al (1994) in their study of cylindrical trabecular bone specimens taken from the human femoral head, and suggests that the inclusion of the cement augmentation did not significantly effect the overall viscoelastic behaviour of the interfacial specimens when compared to un-augmented trabecular bone.

5.5 Summary

The chapter presented the development of a new method for imaging cement-augmented bone specimens under incremental loading.

The new methods developed included;

- The augmentation of the specimens with sufficient cement to represent a situation similar to vertebroplasty.

- A technique for increasing the radiopacity of the cement without causing artifacts on the images.

- The design of a new testing rig to enable the specimens to be imaged under load.

6. Computational analyses of experimental results

The experimental stepwise compression to failure and μCT imaging of ovine trabecular bone – cement interfacial specimens was detailed in Chapter 5. μCT images of these interfacial specimens in their undeformed state were then used to generate specimen specific hFE models, as will be presented in Chapter 7. This study formed the second part of the work conducted to meet the second objective set out in Section 2.6.

Two methods of validating the hFE model predictions were used. Firstly, reaction force data was recorded following each increase in the applied deformation (described in Section 5.4.2.2), against which the hFE model predicted reaction forces at corresponding simulated levels of deformation were compared. Secondly, the μCT images captured following each increase in the applied deformation were used to determine the strain distribution throughout the specimens, against which the hFE model predicted strain distributions were compared. This second approach is explored in this chapter.

6.1. Digital image correlation for strain distribution measurement

In its simplest form, determining the strain distribution throughout or across the surface of specimens that are imaged as they undergo an applied deformation involves selecting a number of common points that can be identified in each of the images as the deformation is increased. Measuring the relative motion of these points from one image to the next gives the strain distribution across the image plane (Figure 6-1). This is the principle behind the digital image correlation (DIC) methods used by Janssen, Mann & Verdonschott (2008) and Waanders et al (2011), previously described in Section 2.3.3.

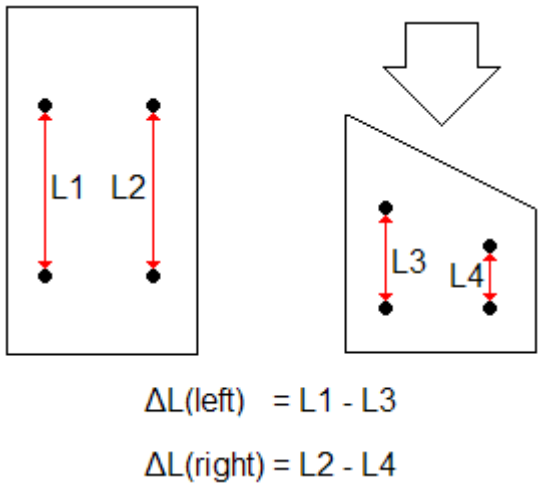

Figure 6-1. Illustration of the principle of operation of strain measurement in one dimension using image correlation

Though a useful technique, the approach as used by Janssen, Mann & Verdonschott (2008) and Waanders et al (2011) has a number of significant limitations, primarily the low resolution of the resulting strain distribution and the ability to only determine the strain distribution on the specimen surface.

The resolution with which the specimen strain-distribution can be determined is limited by the number of sampling points that are commonly identifiable from one image to the next. Achieving a higher resolution involves identifying and measuring the relative motion of a greater number of sampling points. Image correlation software has been

developed that simplifies this process by automating both aspects of the technique (Cintron and Saouma 2008). A higher resolution is achieved by replacing manually selected sampling points with a random speckle pattern, applied to an exterior planar surface of the specimen. Deformation of the specimen causes the speckle pattern to transform, and the software calculates the changes in the strain distribution between images from this transformation.

6.2 Software based digital image correlation

The software based digital image correlation approach was originally proposed and developed at the University of Southern Carolina in the 1980s (Jin and Bruck 2005). In this approach, a formula known as a similarity function is used to calculate a correlation coefficient (C_{corr}), a measure of the similarity between the pixel intensity fields across a sub-region of the undeformed image and the corresponding sub-region of the deformed image (termed subsets). A transformation, known as a shape function, is then applied to the deformed subset and varied until the correlation coefficient is maximised. It is this final shape function that describes the deformation within the deformed subset (Jin and Bruck 2005, Lava et al 2009). An illustration of the approach is shown in Figure 6-2.

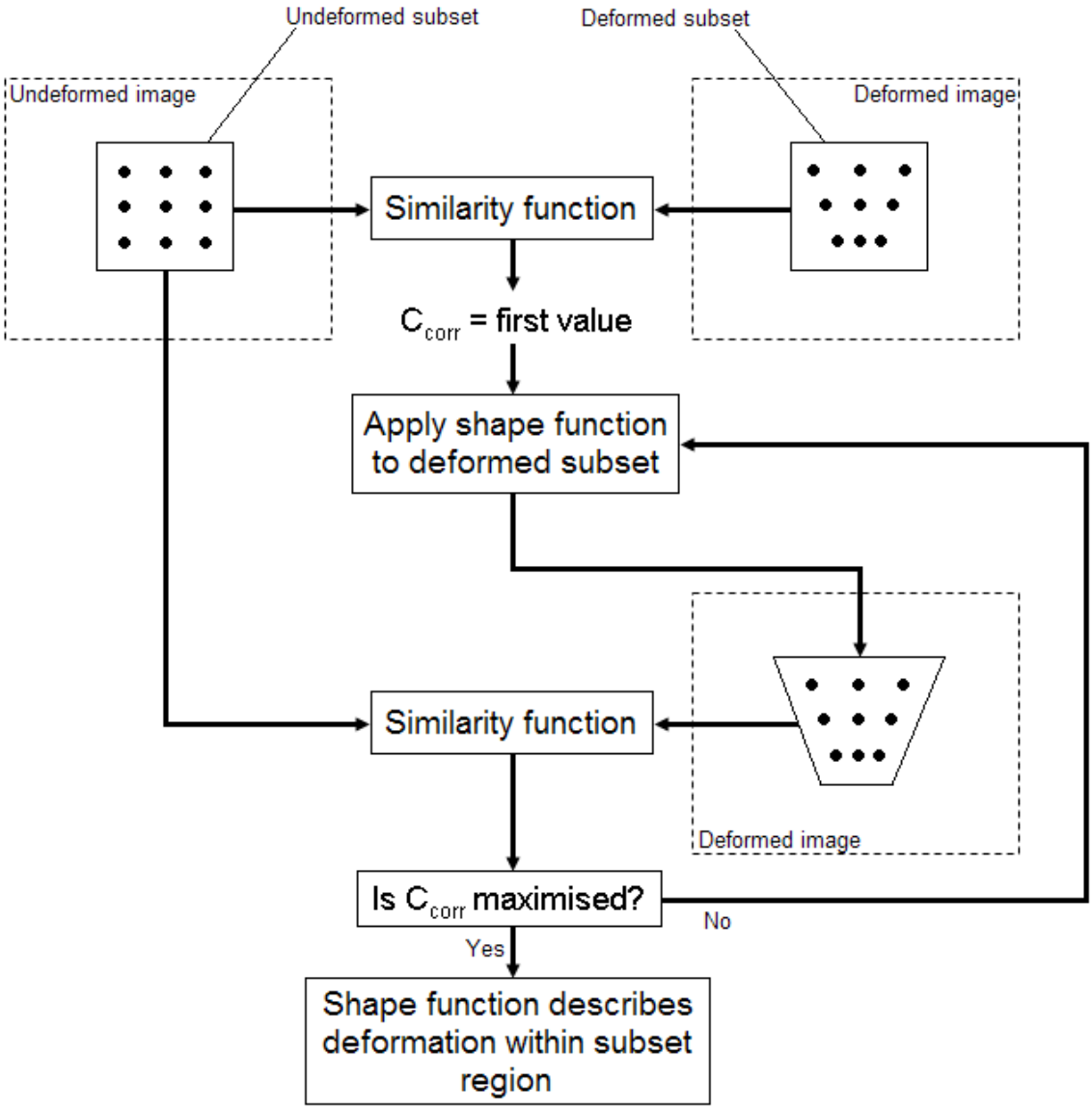

Figure 6-2 - Flowchart depicting the general form of the software based digital image correlation approach.

This process is repeated at regular intervals across the images, with both undeformed and deformed subsets moved a distance in pixels known as the step size. The subset size influences the ability of the software to accurately identify the deformed subset corresponding to each subset selected within the undeformed image, with the ideal value dependent on the spatial and size distribution of the speckle pattern and the magnitude and complexity of the deformation gradients across the deformed images (Jin and Bruck 2005). The output resolution and solution time are determined by the step size, with a larger step size producing a faster solution at the expense of a lower-resolution result (Vic2D testing guide, Version 2009, Correlated Solutions .inc).

A number of different similarity functions have been developed, including the cross-correlation coefficient and the sum of squared differences correlation coefficient, the latter of which has been shown to yield the best results when deformations become large and/or heterogeneous (Lava et al 2009).

While this approach leads to a greatly increased measurement resolution, and frees the operator from the need to manually identify, mark and track large numbers of points within the undeformed and deformed images, the use of an applied speckle pattern still limits measurement of the changing strain distribution to the specimen exterior. Previously published studies have investigated 3D DIC strain measurement in wood imaged using uCT (Forsberg et al 2010), and cancellous bone imaged using MRI (Benoit et al 2009). Based on the outcomes of these studies, it was proposed that μCT images of the trabecular bone specimens contained sufficient textural information to allow the software based DIC method to determine the strain distribution from one μCT scan to the next, as long as the same specimen region was identified in each case. Since the specimens were loaded uniaxially, by selecting μCT slices through the specimen cross-section, the internal strain distribution in 2D could be determined (Figure 6-3).

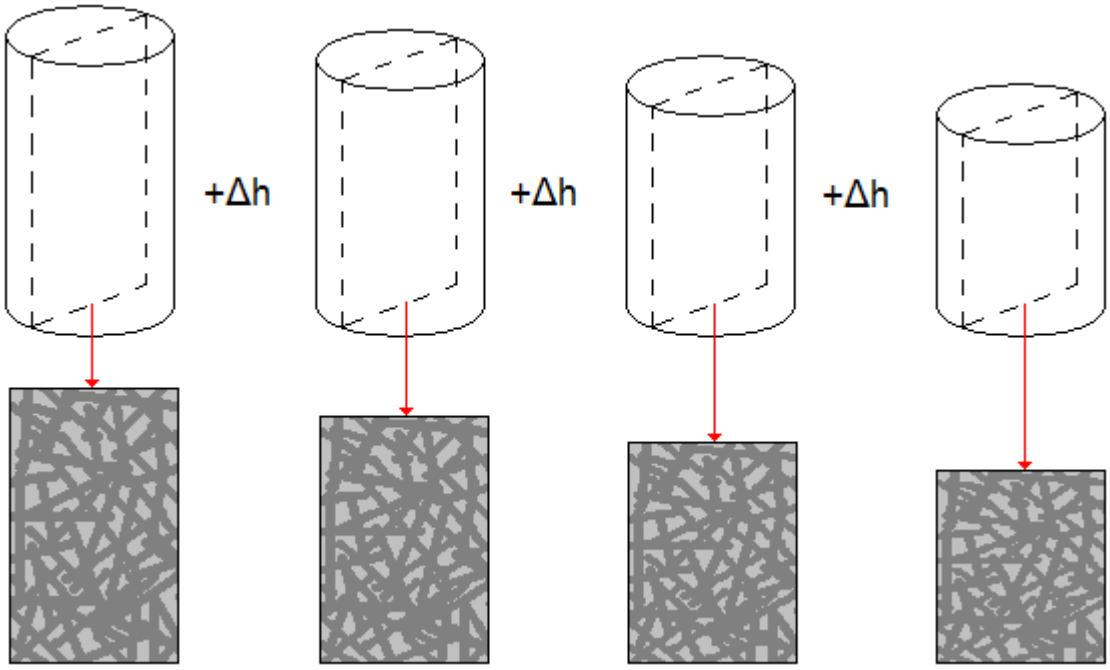

Figure 6-3. Schematic illustrating proposed extraction of 2D trabecular cross-sections from a specimen following an incrementally increased applied deformation. The resulting 2D trabecular cross-sections would be analysed using digital image correlation.

6.3. Preliminary image processing

The use of a software based DIC method required that the source images taken from each μCT scan contain the same specimen features, such that their relative motion could be tracked as the applied deformation was increased. Following selection of a target plane through each specimen, some pre-processing of the source μCT images was conducted to ensure that this was the case. Pre-processing was necessary to correct for out of plane motion and deformation of trabeculae, and specimen tilt, either due to misalignment of the μCT compression and imaging device or bending and non-concentric deformation of the specimen.

6.3.1. Correcting for specimen tilt

Initial inspection of the μCT scans indicated that the angle of part or all of the specimens with respect to the global image axes varied between scans by as much as five degrees. Two causes were identified: (a) tilt of the μCT compression and imaging device relative to the μCT scanner, which caused an arbitrary specimen tilt from one

specimen scan to the next, and (b) tilt due to non-concentric deformation of the specimen at large applied deformations. In both cases, the result of the specimen tilt was that no three adjacent μCT image slices in the plane of interest could contain the desired trabecular features identified in the undeformed μCT scan.

Attempts to minimise the tilt due to (a) by rotating the μCT scans in three-dimensions using image manipulation software resulted in an unacceptable reduction in image sharpness. Instead, a correction was applied as shown in Figure 6-4.

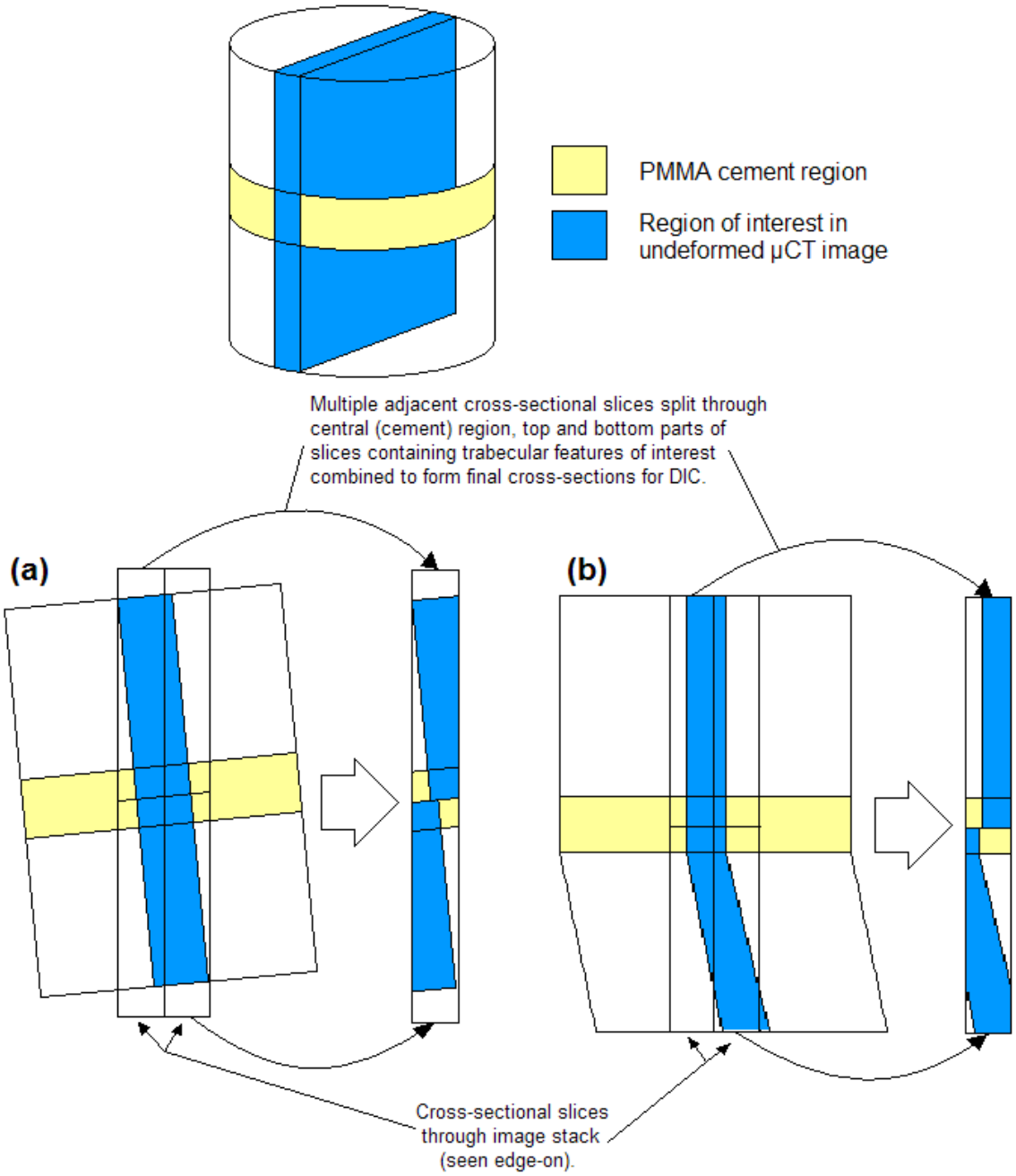

Figure 6-4. Corrections applied to counteract specimen tilt due to (a) misalignment of the compression and imaging rig and (b) non-concentric specimen deformation. The same methodology simultaneously corrected both issues. The PMMA region is highlighted in yellow. The cross-sectional region of interest is highlighted in blue.

Inspection of the µCT scans suggested that negligible deformation occurred in the cement region, even at large applied deformations. For this reason, the introduction of image discontinuities in this region was considered unimportant as the calculated strain distribution across the cement cross-section could be discounted. The µCT image slices in the plane of interest were split into top and bottom halves along the vertical (z-

direction) mid point of the cement region. The top and bottom halves from each μCT scan that contained the trabecular features from the specimen plane of interest were then combined. In each case, care was taken to ensure that both the overall specimen height and the spacing between end-caps was not altered by the procedure. Corrections were then applied for out of plane trabecular deformation.

6.3.2. Correcting for out-of-plane trabecular deformation

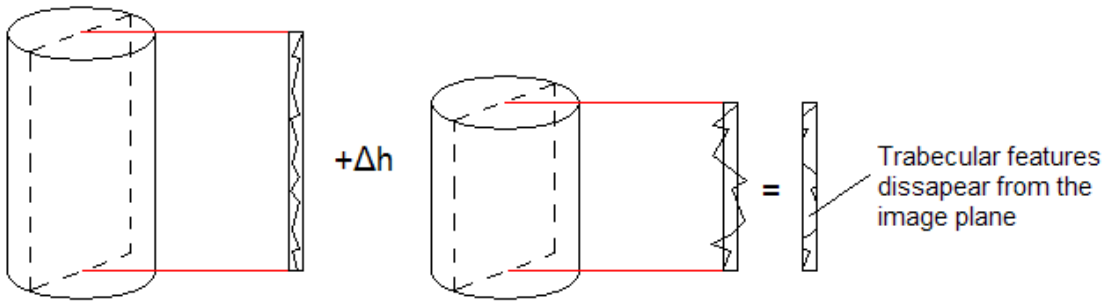

Figure 6-5. Schematic of a specimen cross section before and after an increase in the applied deformation illustrating effect of out of plane trabecular deformation.

As the applied deformation is increased, trabecular features that are visible in the selected specimen μCT image plane will deform through bending and buckling. Any deformation perpendicular to the image plane results in the features disappearing from the image and prevents further tracking of their lateral and vertical motion with respect to the image plane (Figure 6-5). As the μCT scan resolution was 0.082 mm^3, even small out of plane motion will have this effect.

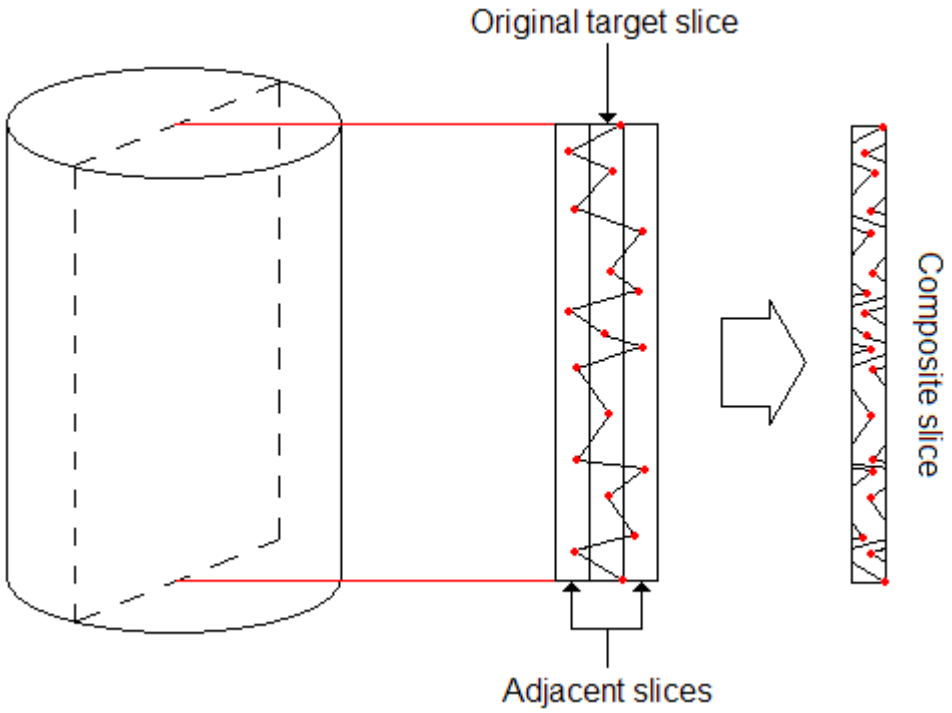

Figure 6-6. Schematic demonstrating how compositing of µCT image slices adjacent and parallel to the cross-sectional plane of interest captures trabecular features that would otherwise be lost due to out of plane trabecular deformation.

The effects of out of plane trabecular deformation were minimised by creating a composite cross-section from the selected image plane and the adjacent parallel µCT image slices (Figure 6-6) using a Matlab code developed in house. This effectively thickened the region of interest and ensured that more of the trabecular features visible in the selected undeformed cross section were included in each subsequent cross-section irrespective of any small out of plane deformation.

6.4. Computational strain characterisation

6.4.1. Methods

The computational strain characterisation of the pre-processed specimen μCT images was carried out using a commercially available two dimensional digital image correlation software package (Vic2D, Correlated Solutions, Inc. Columbia, SC 29063 – USA). Vic2D has been widely validated by comparison to a wide variety of different material and loading cases (Desai et al 2012, Kammers and Dali 2011, Palanivelu et al 2009, Lava et al 2009, Tiwari et al 2007, Wang et al 2002). The similarity function utilized by Vic2D is the sum of squared differences method, which by virtue of it's validated good performance with respect to heterogeneous deformations is expected to be the ideal choice for measurements of the discontinuous deformations observed in the μCT images.

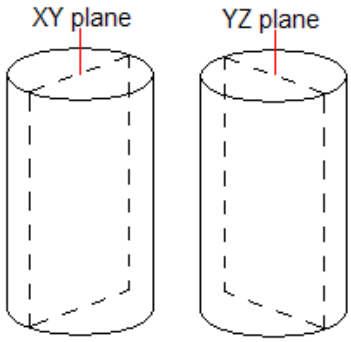

Figure 6-7. Illustration of the location of the perpendicular cross-sectional regions of interest for each specimen.

For each of the three ovine bone – cement interface specimens, two perpendicular regions of interest parallel to the specimen z-axes were identified from the undeformed μCT scans (Figure 6-7). Corrections for specimen tilt and out of plane trabecular deformation were then applied as previously described. This resulted in composite μCT images of the two perpendicular regions of interest for each specimen, at each level of applied deformation.

In addition to the undeformed and deformed specimen images, the digital image correlation software required two primary user input parameters, a reference length and

subset size, the latter of which is described in Section 6.2. The reference length is a known dimension in the image which enables the determination of absolute deformations, and in each case was specified as the distance between the inside end-cap faces. Preliminary testing indicated that a subset size of 25 pixels was the minimum value at which the software was able to determine the material deformations across the entire image at every value of applied deformation.

The analysis was run, and generated a contour plot of the strain distribution for each of the two perpendicular cross-sectional regions of interest for each specimen at each level of applied deformation. To verify that the software was able to accurately identify and track the overall specimen deformation between the undeformed and deformed images, an analysis was run to plot a contour of the displacement relative to the stationary end-cap across each of two perpendicular cross-sectional regions of interest for each specimen at each level of applied deformation.

6.4.2. Software verification results

Examples of the displacement through Specimen 1 with respect to the stationary (upper) end-cap at the maximum applied deformation determined using Vic2D over the cross-sectional region of interest in the (a) XZ plane and (b) YZ plane are shown in Figure 6-8.

Plots of the mean absolute percentage error between the applied displacement determined using Vic2D in the two perpendicular cross-sectional regions of interest and the applied displacement measured manually from the original μCT scans against increasing applied deformation are shown in Figures 6-9, 6-11 and 6-13 for Specimens 1, 2 and 3 respectively.

Plots of the mean absolute percentage error between the applied displacement determined using Vic2D in the two perpendicular cross-sectional regions of interest and the applied displacement measured manually from the original μCT scans against

increasing applied deformation, both expressed in pixels, are shown in Figures 6-10, 6-12 and 6-14 for Specimens 1, 2 and 3 respectively.

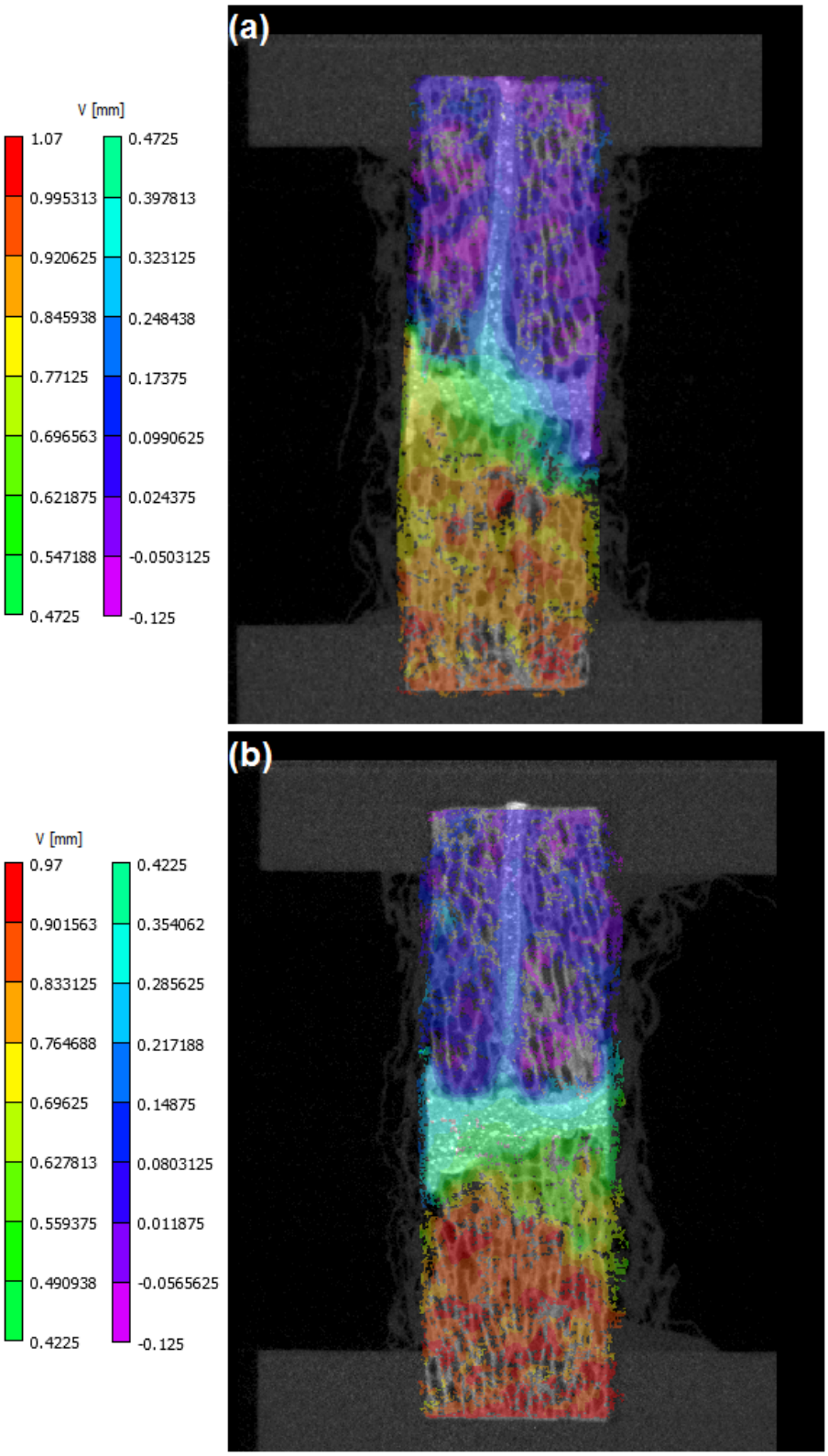

Figure 6-8. Displacement through Specimen 1 with respect to the stationary (upper) end-cap at the maximum applied deformation of 1.066 mm, determined using Vic2D over the perpendicular cross-sectional region of interest in the (a) XZ plane and (b) YZ plane.

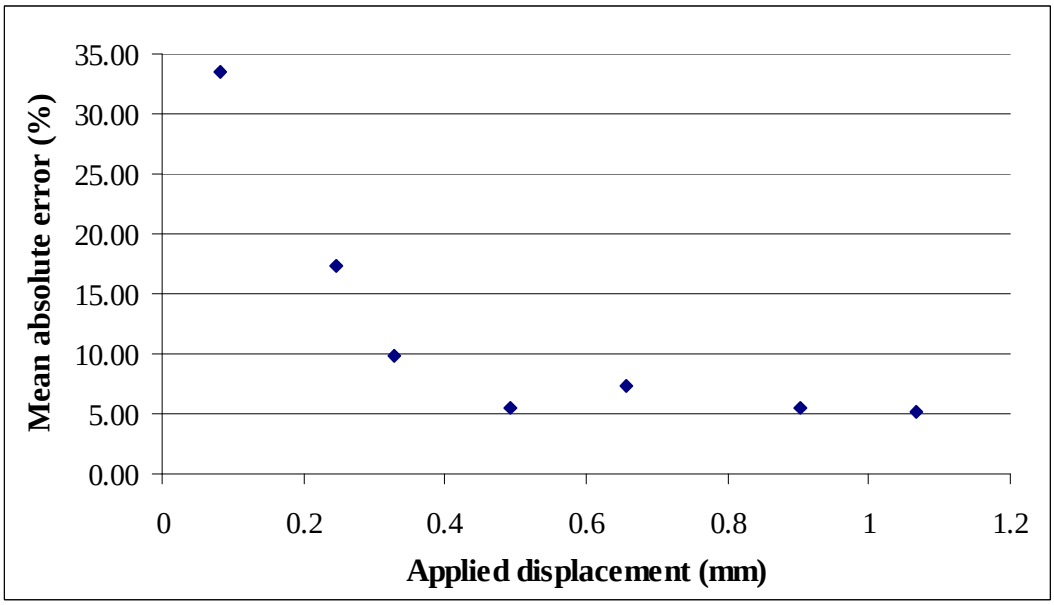

Figure 6-9. Mean absolute percentage error between the applied displacement determined using Vic2D in the two perpendicular cross-sectional regions of interest and the applied displacement measured manually from the original µCT scans plotted against increasing applied deformation for Specimen 1.

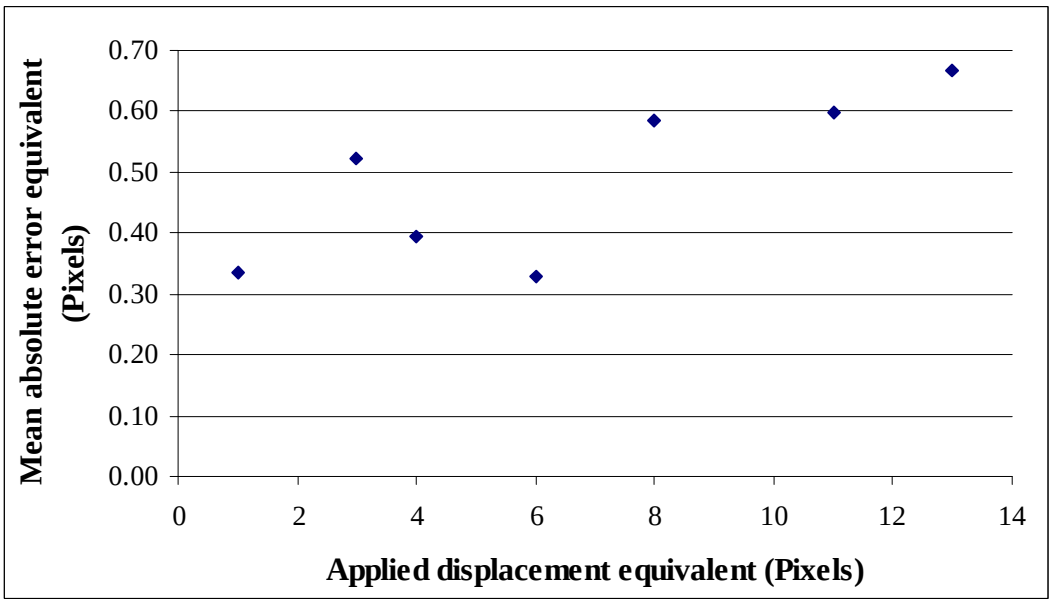

Figure 6-10. Mean absolute error between the applied displacement determined using Vic2D in the two perpendicular cross-sectional regions of interest and the applied displacement measured manually from the original µCT scans against increasing applied deformation, both expressed in pixels, for Specimen 1 (Mean = 0.49 (S.D. = 0.13))

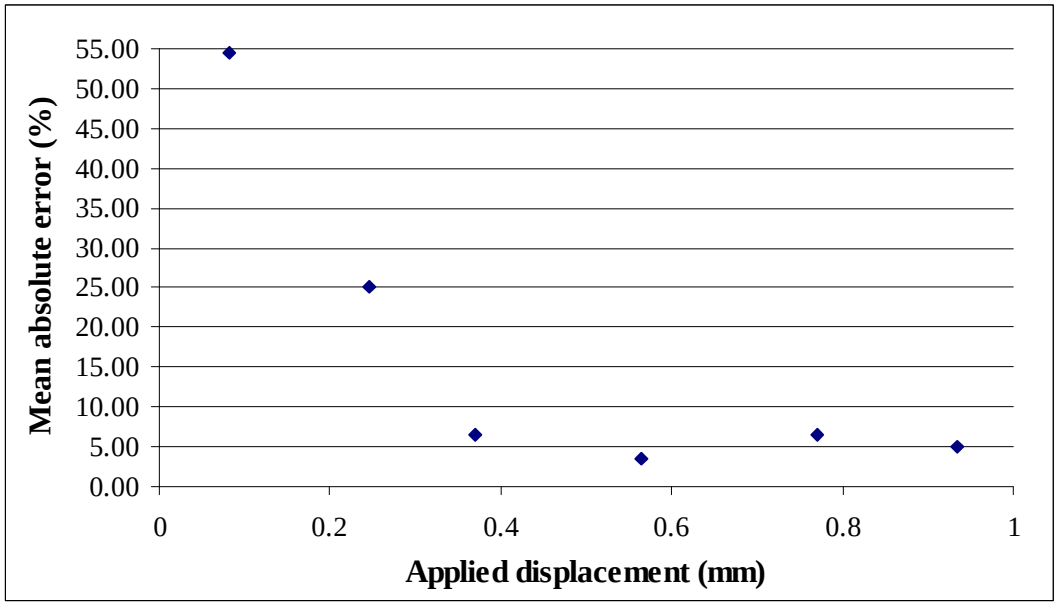

Figure 6-11. Mean absolute percentage error between the applied displacement determined using Vic2D in the two perpendicular cross-sectional regions of interest and the applied displacement measured manually from the original µCT scans plotted against increasing applied deformation for Specimen 2.

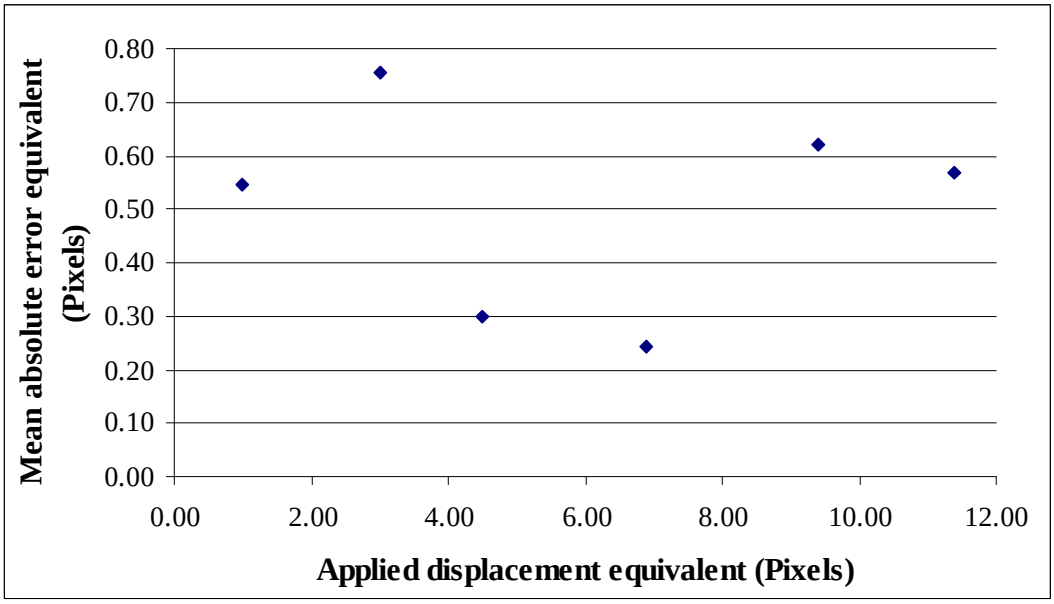

Figure 6-12. Mean absolute error between the applied displacement determined using Vic2D in the two perpendicular cross-sectional regions of interest and the applied displacement measured manually from the original µCT scans against increasing applied deformation, both expressed in pixels, for Specimen 2 (Mean = 0.51 (S.D. = 0.18))

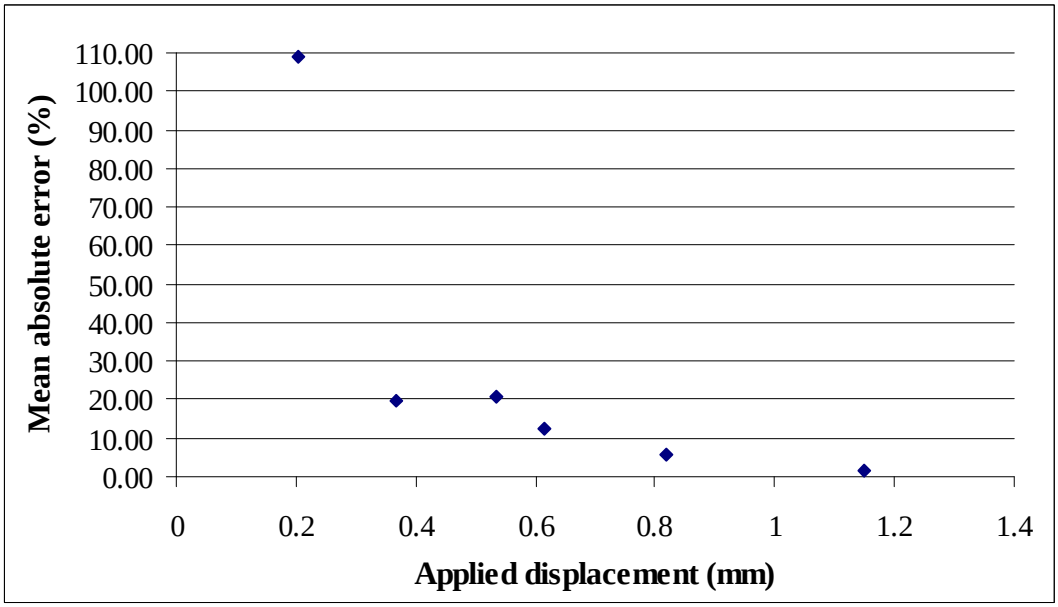

Figure 6-13. Mean absolute percentage error between the applied displacement determined using Vic2D in the two perpendicular cross-sectional regions of interest and the applied displacement measured manually from the original µCT scans plotted against increasing applied deformation for Specimen 3.

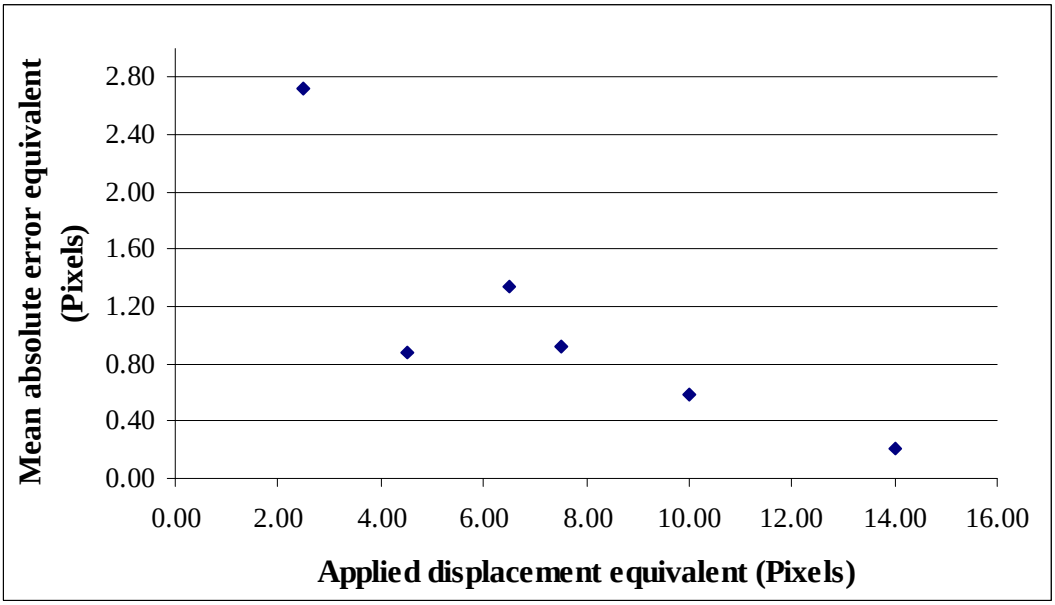

Figure 6-14. Mean absolute error between the applied displacement determined using Vic2D in the two perpendicular cross-sectional regions of interest and the applied displacement measured manually from the original µCT scans against increasing applied deformation, both expressed in pixels, for Specimen 3 (Mean = 1.11 (S.D. = 0.80))

6.4.3. Strain distribution results

The strain distribution at the maximum applied deformation over the cross-sectional regions of interest in the XZ plane and YZ plane as determined using Vic2D are shown for all three specimens in Figures 6-15 to 6-20 and a full set of strain distribution plots across both perpendicular cross-sectional regions of interest for Specimen 2 across the whole range of applied deformation are shown in Figures 6-21 and 6-22.

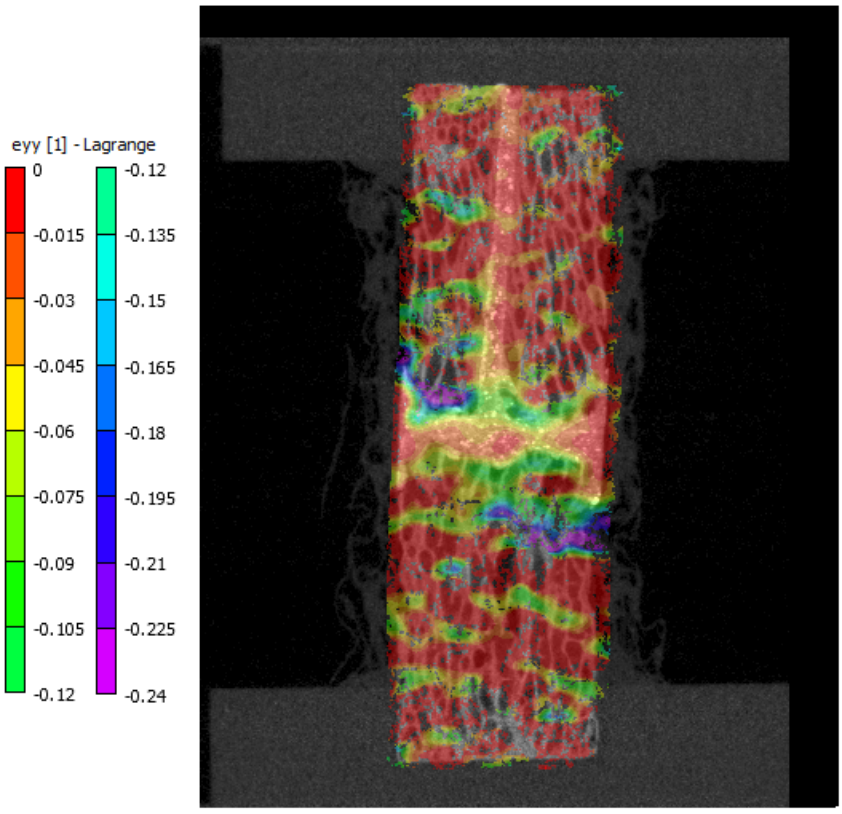

Figure 6-15. Strain distribution at the maximum applied deformation (1.066 mm) over the cross-sectional region of interest in the XZ plane for Specimen 1.

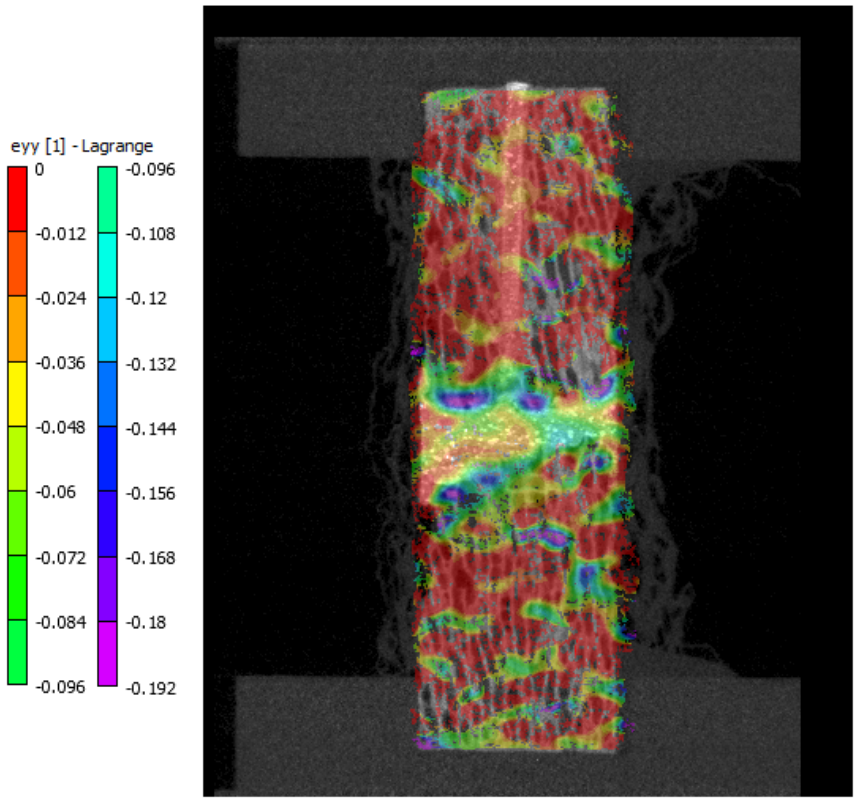

Figure 6-16. Strain distribution at the maximum applied deformation (1.066 mm) over the cross-sectional region of interest in the YZ plane for Specimen 1.

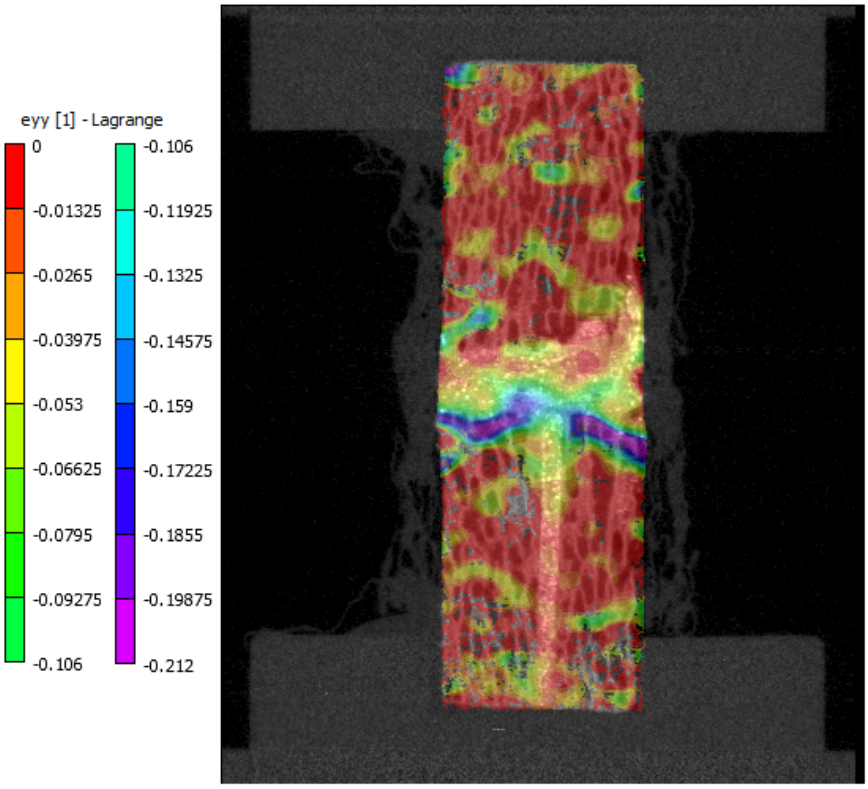

Figure 6-17. Strain distribution at the maximum applied deformation (0.934 mm) over the cross-sectional region of interest in the XZ plane for Specimen 2.

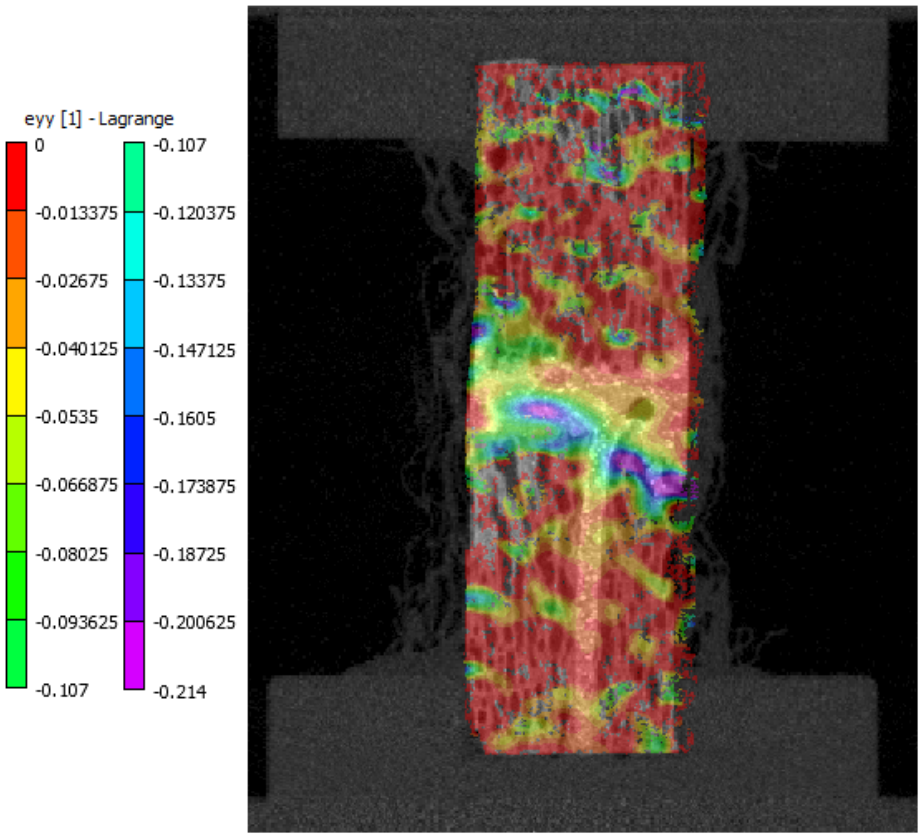

Figure 6-18. Strain distribution at the maximum applied deformation (0.934 mm) over the cross-sectional region of interest in the YZ plane for Specimen 2.

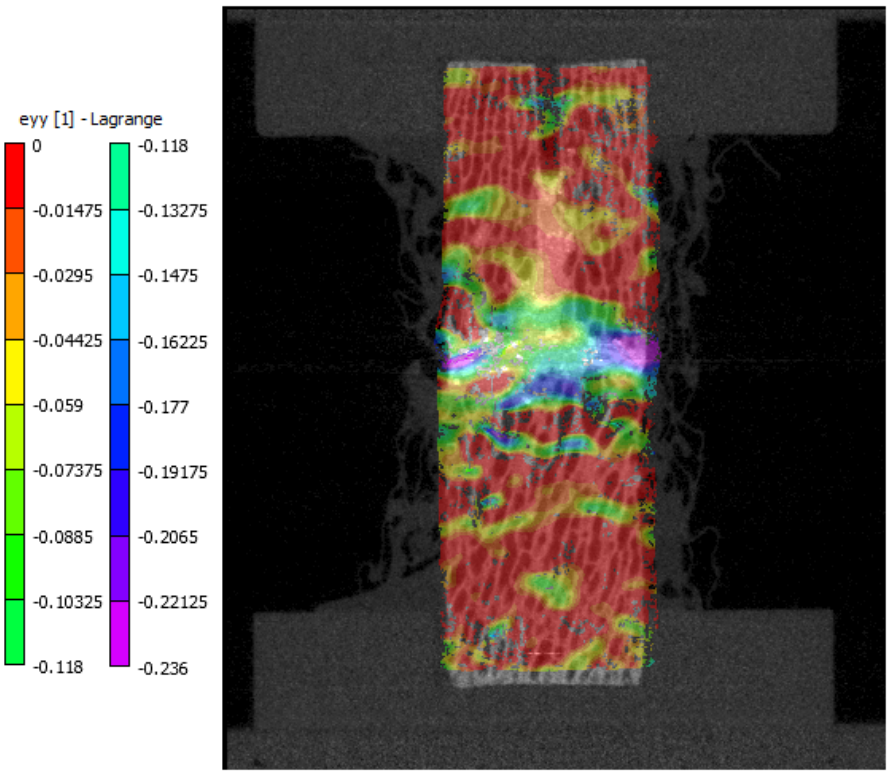

Figure 6-19. Strain distribution at the maximum applied deformation (1.148 mm) over the cross-sectional region of interest in the XZ plane for Specimen 3.

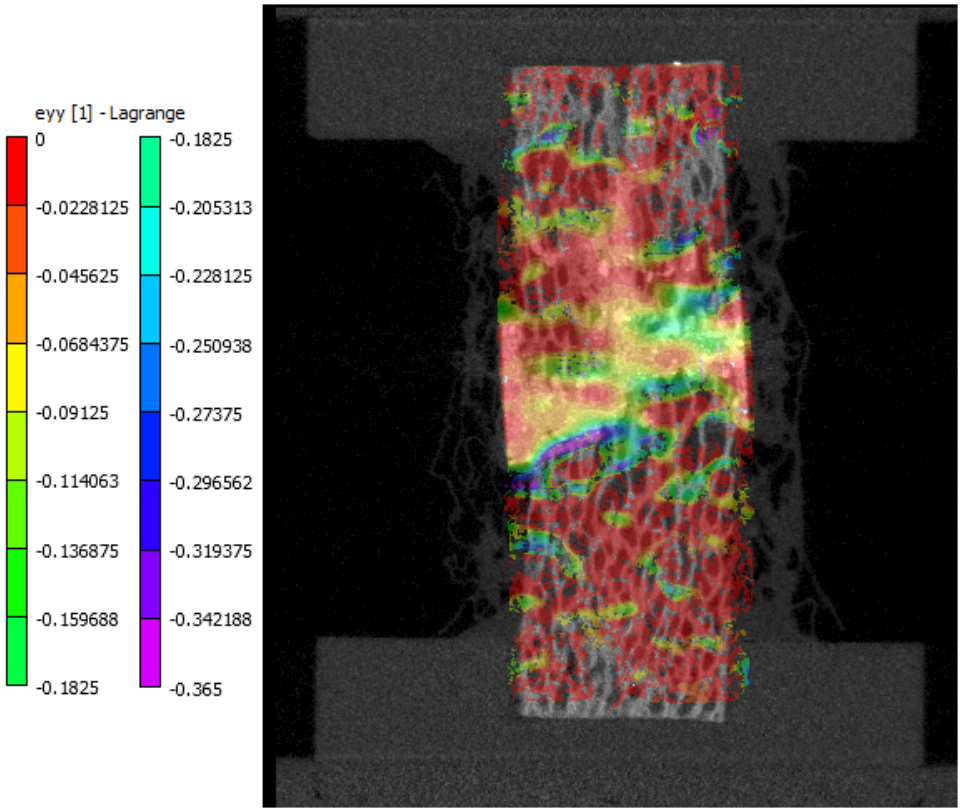

Figure 6-20. Strain distribution at the maximum applied deformation (1.148 mm) over the cross-sectional region of interest in the YZ plane for Specimen 3.

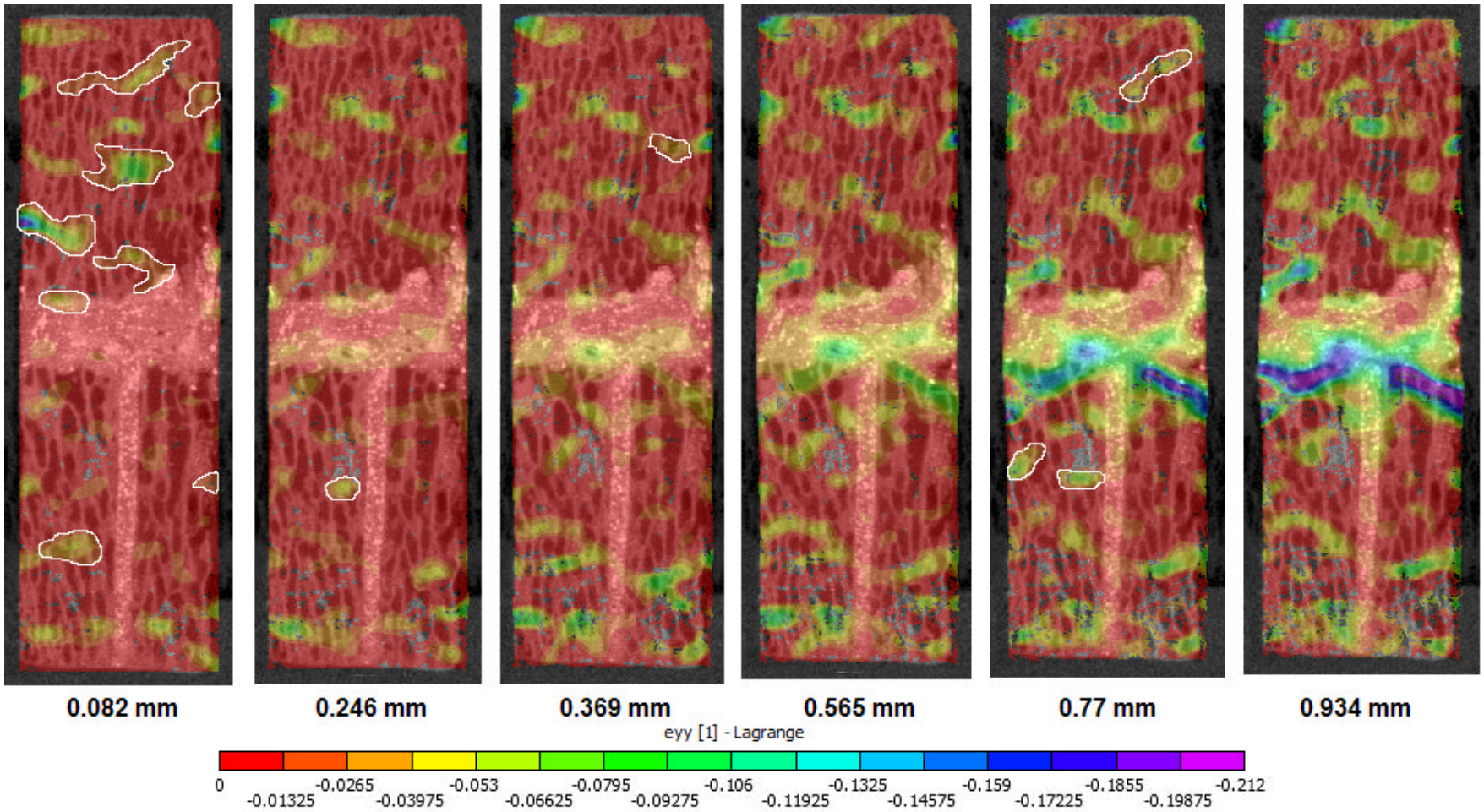

Figure 6-21. Development of strain distribution over the cross-sectional region of interest in the XZ plane for Specimen 2 as the applied deformation was increased. The applied deformation is noted directly under the strain distribution plot in each case. Regions of calculated local strain that either disappear, shrink or move markedly in the next image, following an increase in the applied deformation, are circled in white.

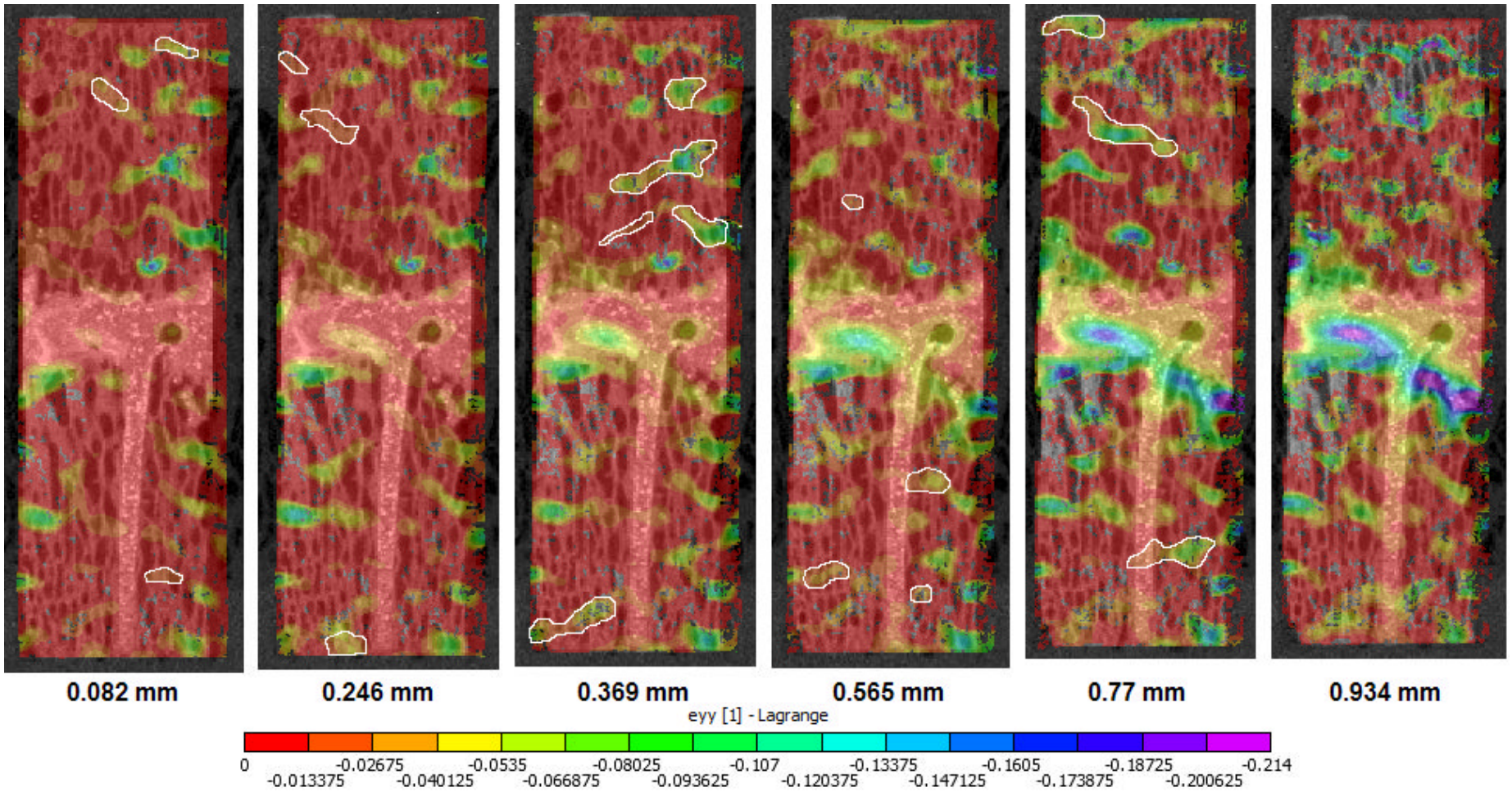

Figure 6-22. Development of strain distribution over the cross-sectional region of interest in the YZ plane for Specimen 2 as the applied deformation was increased. The applied deformation is noted directly under the strain distribution plot in each case. Regions of calculated local strain that either disappear, shrink or move markedly in the next image, following an increase in the applied deformation, are circled in white.

6.5. Discussion

6.5.1. Software verification – Determination of the applied displacement

The accuracy with which Vic2D was able to determine the transformation of the specimens from one image to the next as the applied deformation was increased was investigated by examining the accuracy with which it could determine the applied deformation in each case.

For each specimen, the average absolute percentage error between the applied deformation as calculated using Vic2D in both perpendicular cross-sectional regions of interest and the applied deformation as measured manually from the original μCT images was plotted against the latter. These plots are shown in Figures 6-9, 6-11 and 6-13 for Specimens 1, 2 and 3 respectively. In all three cases, the error was high at the lowest applied deformations, but decreased sharply as the applied deformation was increased.

This behaviour was as expected. At the lowest applied deformations, the overall change in specimen height measured only 1-3 pixels, thus any random error equivalent to a 1 pixel change in specimen height would result in a 100 % to 30 % error. As the applied deformation increased, a similar level of random error would represent a progressively smaller proportion of the overall change in specimen height, and thus the resulting percentage error would correspondingly decrease exponentially towards zero.

Though this appeared to be the case for Specimen 3, in the cases of Specimens 1 and 2 the percentage error levelled off at an error of approximately 5 %. This suggests that in the cases of Specimens 1 and 2 the random error in the processed images was greater as the applied deformation approached and exceeded the point of apparent yield than in the case of Specimen 3. Random error as discussed here is defined as any aspects of the compression and imaging process that negatively impact the ability of the digital image correlation software to accurately determine the transformation of the specimen as the

applied deformation was increased. Possible sources of random error were expected to include: specimen shift and tilt due to misalignment of the compression and imaging device between μCT scans; non-concentric deformation of the specimens that was not corrected through pre-processing of the μCT images (as described in section 6.3); or additional image artefacts introduced by the pre-processing protocol.

This notwithstanding, for all three specimens Vic2D was able to produce good agreement (=< 5 % mean absolute error) with the manually measured applied deformation above an applied deformation of approximately 0.3 mm, corresponding to 0.93 %, 1.11 % and 1.17 % strain for Specimens 1, 2 and 3 respectively.

6.5.2. Determination of the specimen strain distribution

From the strain distribution plots across the specimens (Figures 6-15 to 6-20) it can be observed that the maximum calculated compressive strains predominantly occurred at the bone – cement interface. This agreed with both initial visual inspection of the original μCT images (previously discussed in Section 5.4.2.3), and a previously published study by Tozzi et al (2012) that suggested that within bovine trabecular bone – cement interface specimens the highest local deformations primarily involved trabecular bending and buckling in the bone region adjacent to the interdigitated zone.

For the applied deformation, it was possible to undertake a direct comparison of the Vic2D software against a known benchmark. However, determining the accuracy with which the software was able to calculate the local strains, and hence the strain distribution in a similar manner would involve a large number of individual measures of local deformation across each of the cross-sectional regions of interest, for each of the three specimens. At high magnifications, the trabecular features are typically not clearly delineable and hence some measurement error would be expected.

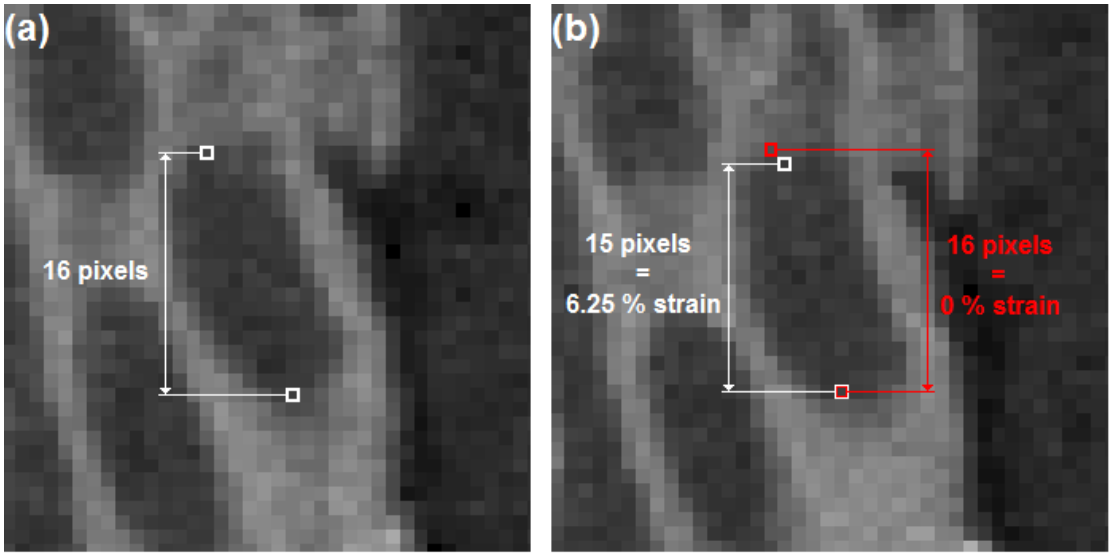

Figure 6-23. Magnified view of an extract from one of the cross-sectional regions of interest for Specimen 1 at an applied deformation of (a) 0.328 mm and (b) 0.492 mm..

An example taken from one of the cross-sectional regions of interest for Specimen 1 is shown in Figure 6-23 at two applied deformations. Over the length scale of an average trabecular cell, a difference of one pixel when choosing the points between which the measurement taken, will lead to a difference in measured strain of 6.25%.

For this reason, the strain measurement error was instead estimated based on the accuracy with which Vic2D was able to determine the applied deformation. The mean absolute error between the applied deformation in both perpendicular cross-sectional regions of interest as determined by Vic2D and the applied deformation manually measured from the original μCT images, expressed in pixels (pixel equivalent error), plotted against the applied deformation expressed in pixels, is shown in Figures 6-10, 6-12 and 6-14 for Specimens 1, 2 and 3 respectively.

While the results for Specimens 2 and 3 exhibit no clear trend with respect to pixel equivalent error as the applied deformation increased, the results for Specimen 3 exhibit a strong downward trend, suggesting that the random error present in the perpendicular cross-sectional regions of interest for Specimen 3 decreased with increasing applied deformation, though it is not understood why this was the case.

The error present in the local strains calculated using Vic2D was estimated by calculating the effect that the pixel equivalent error in the calculated applied

deformation would have over the length scale over which the software conducts the image correlation and hence calculates the local strains. The pixel equivalent error in the Vic2D determined applied deformation, averaged across the whole range of applied deformation was 0.49 pixels (0.13 S.D.), 0.51 pixels (0.18 S.D.) and 1.11 pixels (0.8 S.D.) for Specimens 1, 2 and 3 respectively. Over an image correlation subset size of 25 pixels these average pixel measurement errors would lead to an estimated average error in calculated local strains of 1.96 %, 2.04 % and 4.44 % respectively. The average for Specimen 3 was highly skewed by the particularly high error at the lowest applied deformation. If this point were ignored, the resulting average pixel equivalent error for Specimen 3 was 0.79 pixels (0.38), resulting in an estimated average error in calculated local strains of 3.16 % at applied deformations above 0.3 mm.

In Figures 6-21 and 6-22, regions of calculated local strain that are greater than the estimated error threshold but either disappear, shrink or moved markedly in the next image, following an increase in the applied deformation, are circled in white. As the calculated local strains in these regions are typically at least two times higher than the estimated error threshold they are considered unlikely to be the result of error in the image correlation process.

As discussed in Section 5.4.2.4, the reaction force measurements taken using the compression and imaging device immediately before and after each μCT scan suggested that significant stress relaxation occurred over the duration of each μCT scan. For this reason, it is proposed that the disappearance, shrinkage or movement of these regions of elevated local strain as the applied deformation increased were due to strain relaxation within the trabecular structure. It is also proposed that this strain relaxation may be one of the factors that contributed to the random error in the Vic2D based determination of the applied displacement.

In conclusion, the use of the DIC software enabled the strain fields to be visualized. The errors due to pixel size and image correlation are likely to be of the order of 2-5 %, and some additional error may be caused by strain relaxation during imaging. The most reliable strain values are likely to be obtained at the largest applied deformations, and these results will therefore be used to compare with the finite element predictions in the next chapter.

6.6. Summary

For all three interfacial bone – cement specimens, two perpendicular cross-sectional regions of interest were identified.

The cross-sectional regions of interest were extracted from the original μCT scans of each specimen at each applied deformation, correcting for specimen tilt, shift and out of plane trabecular motion as necessary.

Commercial digital image correlation software (Vic2D) was used to determine the changing strain distribution across each of the cross-sectional regions of interest as the applied deformation increased.

The ability of the digital image correlation software to accurately determine the increasing applied deformation in each case was verified by comparison with manual measurements from the original μCT images. These results were then used to estimate the accuracy with which the digital image correlation software was able to determine local strains.

7. hFE models of the bone – cement interface

A simplified analytical model of the interdigitation of trabecular bone and cement was devised and used to propose a theoretical explanation of how the underlying structural mechanics at the bone – cement interface might lead to the interfacial behaviour previously reported in a number of published studies and observed in Chapters 5 and 6.

A number of interfacial hFE models were generated from the μCT scans of ovine trabecular bone – cement specimens experimentally and computationally studied in Chapters 4 and 5 respectively, both with and without an explicitly modelled interfacial region between the bone and the cement augmentation. The analytical model predictions were used to inform the selection of the interfacial material properties assigned within a number of the hFE models that featured an explicitly modelled interfacial region.

The hFE model predictions were then quantitatively and qualitatively compared with the specimen properties derived in Chapters 4 and 5 to determine whether explicitly modelling the interfacial zone according to the analytical model predictions led to an improvement in their predictive accuracy.

This study was conducted to meet the third and final objective set out in Section 2.6.

7.1. Introduction

Analyses of the results of previous efforts to use image-based hFE modelling approaches to determine the mechanical properties of cement augmented trabecular bone specimens and whole vertebrae indicated that improving the models' predictive accuracy necessitated the development of an improved hFE representation of the interfacial region between the trabecular bone and cement augmentation.

The available evidence suggested that:
The bone – cement interface is less stiff than either pure trabecular bone or PMMA cement in the direction of the applied load (Janssen, Mann & Verdonschott 2008; Waanders et al 2009; Waanders et al 2011).
Initial failure within cement augmented trabecular bone specimens predominantly occurred adjacent to the bone – cement interface (Tozzi, Zhang & Tong 2012).
At a tissue level, individual trabecular struts most commonly failed through shear failure caused by trabecular bending and buckling (Fhyrie and Schaffler 1994; Yeni et al 2001).

In an effort to relate the observed behaviour to quantifiable mechanical failure processes at the interface, a simplified analytical model was proposed to investigate the behaviour of a trabecular strut embedded in cement (Figure 7.1).

7.2. Simplified theoretical analyses of the interface

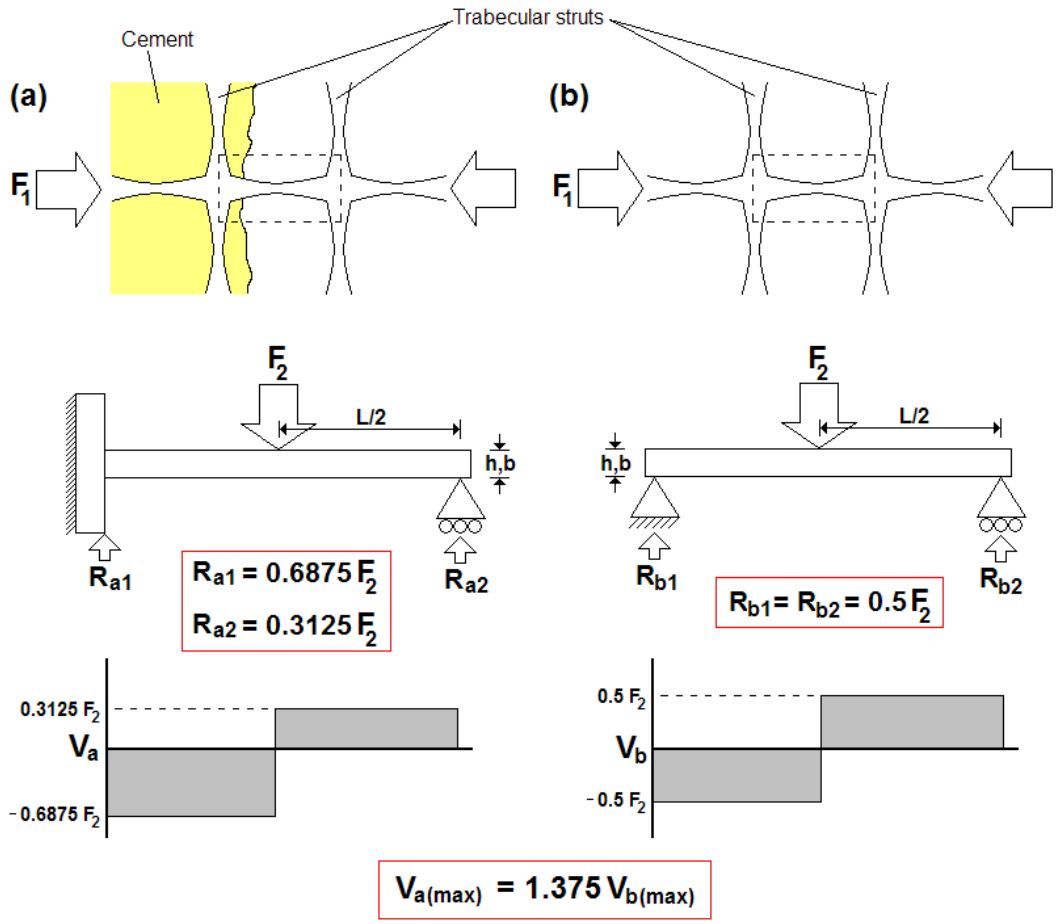

Figure 7-1. Schematic of a trabecular strut (a) embedded at one end into cement and (b) as part of the normal trabecular structure (b). Under each is a schematic of the simplified analytical representation of the region within the dashed rectangles, the calculated reaction forces at the constraints in terms of the applied load (F_2), and a sketch of the shear force along the beam length in each case (not to scale). The maximum shear force in case (a) is at the end embedded into the cement, and is 37.5% higher than the maximum shear force in case (b).

Two trabecular struts under an equal axial buckling load (F_1), one 'free' as part of the normal trabecular structure and the other embedded into the cement augmentation at one end, were considered as identical simple beams. The embedded strut was considered to behave as if it were pin jointed at the free end where it met the adjacent trabecular intersection and fixed with an encastre constraint at the end embedded into the cement to represent the increased constraint imposed by the cement (Figure 7-1a). The free strut was considered pin-jointed at both ends (Figure 7-1b). Taking advantage of the

principle of compatibility of displacement, the axial buckling load was replaced by an equivalent and equal perpendicular point load applied mid-span in both cases (F_2).

Though case (a) is statically indeterminate, the reaction forces at both the encastre and pin-jointed ends (R_{a1} & R_{a2}) were calculated in terms of the applied load F_2 by taking advantage of the principle of compatibility of displacement and the principle of superposition. The reaction forces at the pin-jointed ends for case (b) (R_{b1} & R_{b2}) were both equal to half of the applied load.

Sketching the shear force diagram for both cases demonstrated that the maximum shear force within case (a) occurred at the encastre constraint representing the interdigitation between the strut and the cement augmentation, and was 37.5 % higher than the maximum shear force within case (b). Assuming that in both cases the beams failed in shear, and at a common yield stress, the beam in case (a) would fail at an applied load equal to 0.73 times the applied load required to cause failure in case (b). It was proposed that this effect could be reproduced within a hFE representation of the bone - cement interface by modifying the properties of the bone elements adjacent to the cement region such that they would go into yield at a reduced strain when compared to the rest of the bulk trabecular bone.

Though the behaviour displayed by the analytical model is in agreement with the available evidence with respect to early trabecular failure at the bone – cement interface, the beam in case (a) is 2.42 times stiffer than the beam in case (b), directly contradicting the previous findings of Janssen, Mann & Verdonschott (2008) and Waanders et al (2009). Furthermore, the degree of constraint in-vivo provided at the ends of the trabecular struts that are not embedded into the cement by the adjacent trabecular intersection is expected to be more restrictive rotationally than the pin-jointed constraints applied in the analytical models, suggesting that the shear-failure load ratio between cases (a) and (b) lies between 1:1.375 and 1:1.

This notwithstanding, the simplified analytical model was used to inform the material properties assigned to the explicitly modeled interfacial region in a number of the subsequent hFE models. The attempt to ground the observed behaviour in theory, albeit a simplified representation, gave increased confidence that the corresponding properties

assigned to the interfacial zone were at least partially representative of the physical processes occurring at the bone – cement interface in-vivo as opposed to solely an ad-hoc adjustment.

7.3. hFE models

Specimen specific trabecular bone – cement interfacial hFE models of two ovine specimens fabricated and studied in Chapters 5 and 6 (Specimens 2 and 3) were generated. Corresponding specimen specific hFE models were generated that featured an explicitly modelled interfacial region between the elements representing the bulk trabecular bone and cement augmentation, the material properties of which were varied to explore the resulting effect on the model predictions with respect to apparent stiffness, apparent yield strain, and the strain distribution throughout the specimen. Further to this, the interfacial region was assigned material properties identical to those assigned to the bulk trabecular bone to assess the effect of the altered mesh geometry on the model predictions.

7.3.1. Mesh generation

The mesh generation procedure was identical to the process used to generate the specimen specific hFE models of un-augmented ovine trabecular bone cores described in Section 4.1.2, with the exception that additional steps were required to model the cement augmentation in all cases and in some cases the explicitly modelled interfacial region.

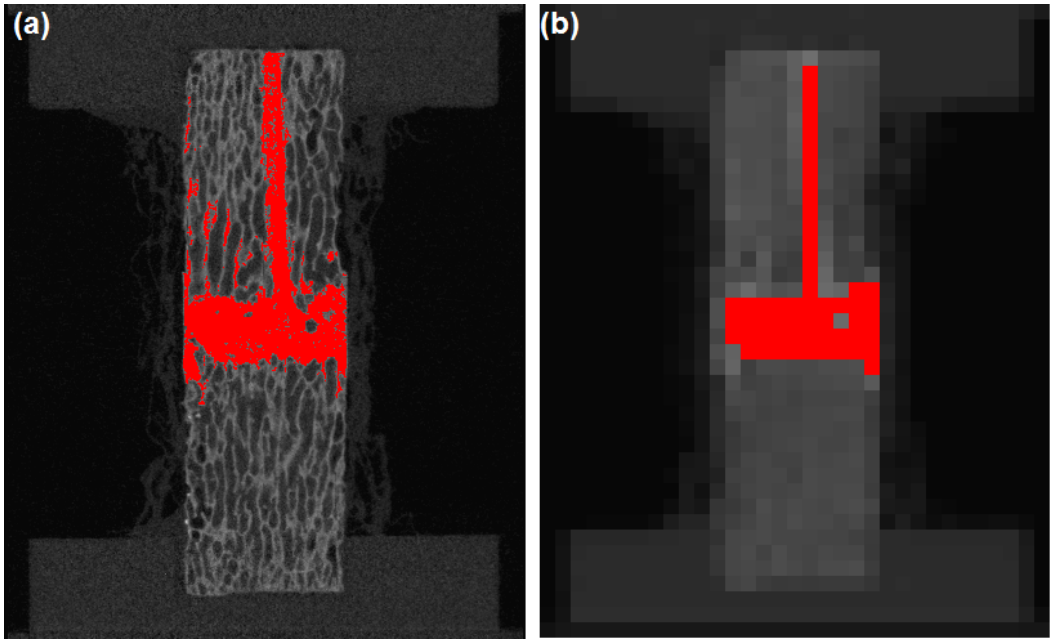

Figure 7-2. Example cross-section through the µCT images of Specimen 2 showing the masked cement augmentation at (a) 0.082 mm^3 and (b) following downsampling to an image resolution of 1 mm^3.

In the modeling process used to generate hFE models of the unaugmented specimens, the original specimen µCT images were first downsampled from their native 0.082 mm^3 resolution to a resolution of 1 mm^3. For each specimen, the downsampled images were then masked into regions comprising the different constituent materials, such as bone, Delrin end-caps and the PMMA cement used to pot the specimens into the end-caps. These collected masked regions were then converted directly into a specimen-specific hFE mesh.

In the case of the cement-augmented Specimens 2 and 3, it was difficult to accurately delineate the PMMA cement augmentation at the downsampled resolution. For this reason, the cement augmentation was masked using a grayscale thresholding approach at the original µCT image resolution (Figure 7-2a). The threshold limits were selected such as to minimize the quantity of non-cement voxels included in the resulting masks. The µCT images and superimposed cement augmentation were then downsampled to a resolution of 1mm^3, which had the effect of removing any remaining spurious features that were included in the cement masks by the thresholding operation (Figure 7-2b). For the models that did not feature an explicitly modeled interfacial region, the remainder of the mesh generation process progressed as described in Section 4.1.2.

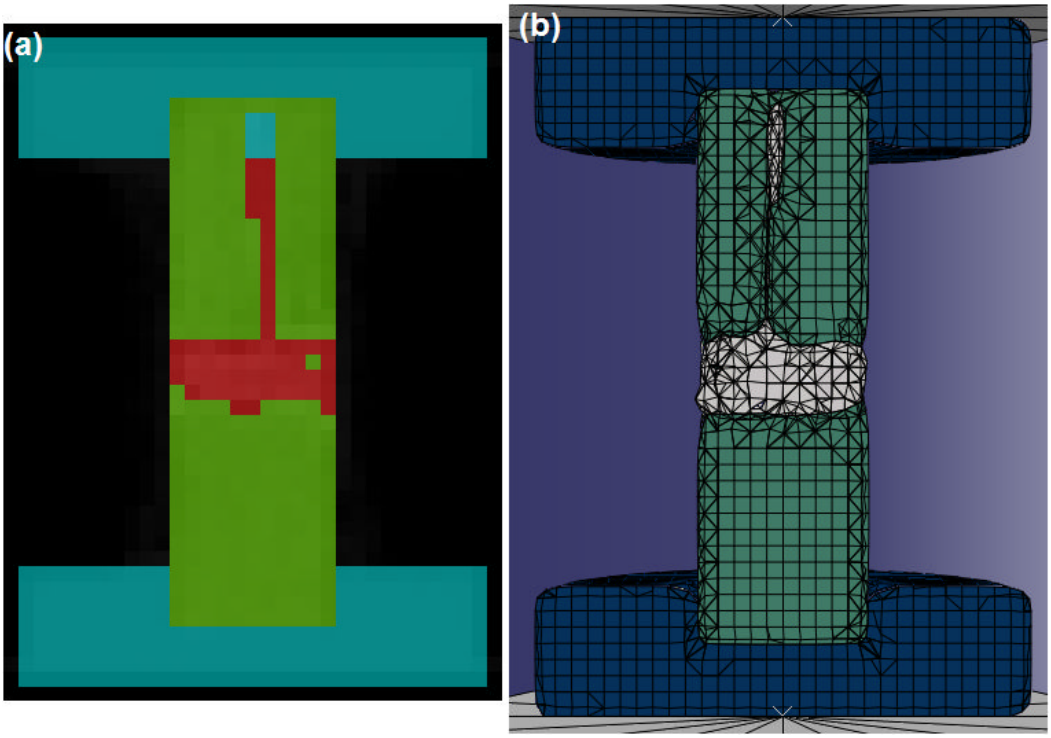

Figure 7-3. Completed (a) masks and (b) resulting hFE mesh without an explicitly modeled interface for specimen 2.

Example cross-sectional images of the completed masks and resulting hFE mesh for Specimen 2 that did not feature an explicitly modeled interface are shown in Figure 7-3a and 7-3b respectively.

For the models that did feature an explicitly modeled interfacial region, a further series of masking operations were conducted. Following the downsampling of the μCT image and the superimposed cement mask, the Delrin end-caps and trabecular bone were masked as described in Section 4.1.2. The cement mask was duplicated, and enlarged by one voxel in each direction using the dilate operation in Scan-IP. The region of the duplicate cement mask that intersected with the original cement mask and the region of the bone mask that intersected with the duplicate cement mask were then removed, resulting in a cement mask nested within an interfacial mask, nested within the bone mask. Finally the interfacial mask was trimmed level with the sides of the bone mask to preserve the original specimen diameter and the collected masks were converted directly into a hFE mesh as before.

Example cross-sectional images of the completed masks and resulting hFE mesh for Specimen 2 that featured an explicitly modeled interface are shown in Figure 7-4a and 7-4b respectively.

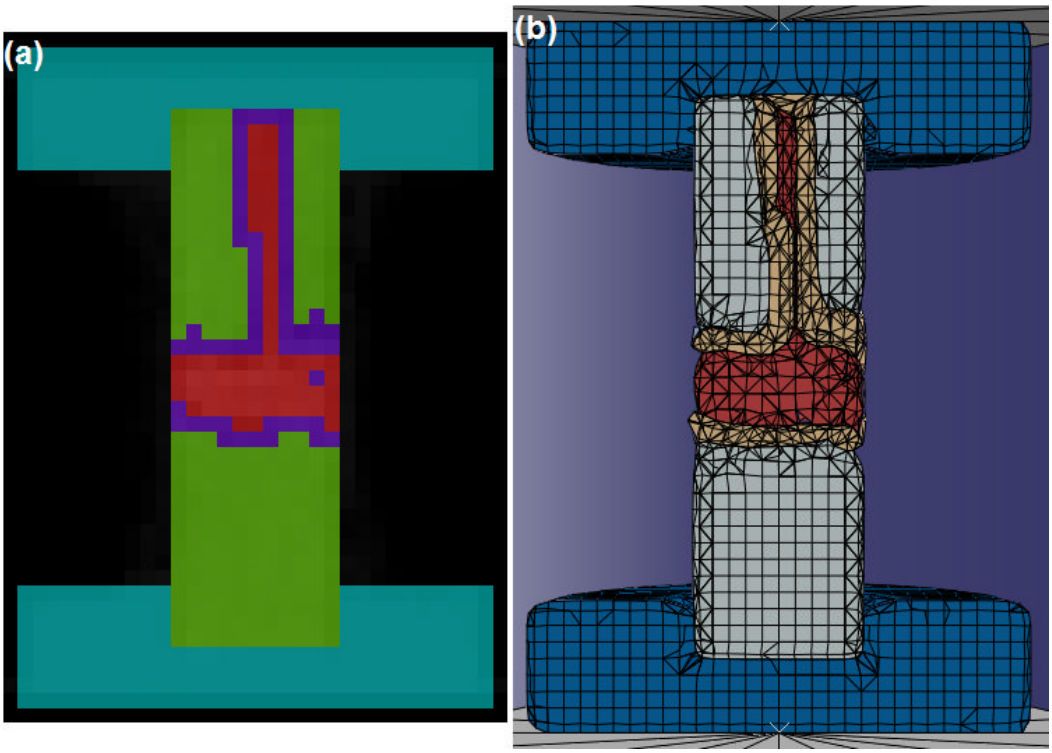

Figure 7-4. Completed (a) masks and (b) resulting hFE mesh including an explicitly modeled interface for specimen 2. The interfacial region is coloured purple in (a) and tan in (b).

In all cases, following the results of the sensitivity studies described in Section 4.2, the PMMA cement between the ends of the trabecular bone core and the Delrin end-caps was not included in the models.

7.3.2. Material properties

7.3.2.1. Bulk trabecular bone

In all of the interfacial hFE models the elements representing the main trabecular bone regions were assigned the elastic and plastic material properties derived for un-augmented ovine trabecular bone in Chapter 4. A μCT grayscale – modulus conversion factor of 45.054 and an element yield strain of 1.79 % were used.

7.3.2.2. The trabecular bone – cement interface

In the interfacial hFE models that featured an explicitly modeled interfacial region the elements representing the interfacial region were assigned a number of different elastic and plastic material properties.

For the purpose of assessing the effect on the hFE model predictions of the changes to the mesh geometry due to the inclusion of an explicitly modelled interface, the models for both specimens were initially assigned the same interfacial element material properties as for the main trabecular bone regions – a μCT grayscale – modulus conversion factor of 45.054 and an element yield strain of 1.79 %.

		Element yield strain (%)			
		1.16	**1.43**	**1.79**	**2.15**
G.S.-E x	**27.03**	1.16 % x 27.03	1.43 % x 27.03	1.79 % x 27.03	2.15 % x 27.03
	36.04	1.16 % x 36.04	1.43 % x 36.04	1.79 % x 36.04	2.15 % x 36.04
	45.054	1.16 % x 45.054	1.43 % x 45.054	1.79 % x 45.054	2.15 % x 45.054
	54.03	1.16 % x 54.03	1.43 % x 54.03	1.79 % x 54.03	2.15 % x 54.03

Table 7-1. Combinations of μCT grayscale – modulus conversion factors (G.S.-E x) and element yield strains assigned to the elements comprising the explicitly modeled bone – cement interface.

For the purpose of exploring the effect on the hFE model predictions of varying the material properties of the interface, the models for both specimens were then solved for a range of interfacial element material properties, detailed in Table 7-1. The range of element yield strains were chosen centred between the value predicted by the simplified analytical model and the value derived for un-augmented ovine trabecular bone determined in Section 4.4. The range of μCT grayscale – modulus conversion factors ranged between 60 % and 120 % of the value for un-augmented ovine trabecular bone determined in Section 4.4, such as to evaluate the contradictory suggestions of Janssen, Mann & Verdonschott (2008) and Waanders et al (2009) and the predictions of the simplified analytical model.

7.3.2.3. Delrin end-caps and PMMA cement augmentation

In all cases, the Delrin end-caps and the PMMA cement augmentation were assigned the same elastic material properties as described in Chapter 4, with a Young's modulus of 757 MPa and 2450 MPa respectively.

7.3.3. Boundary conditions

7.3.3.1. Applied constraints

In all cases, the applied constraint boundary conditions were configured according to the standard hFE model configuration described in Section 4.3.

7.3.3.2. Applied displacements

In all cases the applied incremental displacement was configured as described in Section 4.6.3.2.

In addition to this, intermediate increments were applied that corresponded with the incremental displacements applied during the experimental compression and imaging of the specimens, described in Section 5.4.2. This enabled direct comparisons to be made between the experimentally determined and hFE predicted reaction forces, and between the hFE predicted specimen strain distribution and computationally determined experimental specimen strain distribution described in Chapter 6.

7.4. Results

Comparisons between the experimentally determined and hFE predicted apparent stiffness and apparent yield strain for Specimens 2 and 3, both with and without an explicitly modeled interfacial region are shown in Figures 7-5 to 7-8. In each case, the stiffness was determined by taking the gradient of the linear part of the stress-strain data, and the yield strain was determined from the stress-strain data using the 0.2 % offset yield method as previously discussed in Section 3.5.

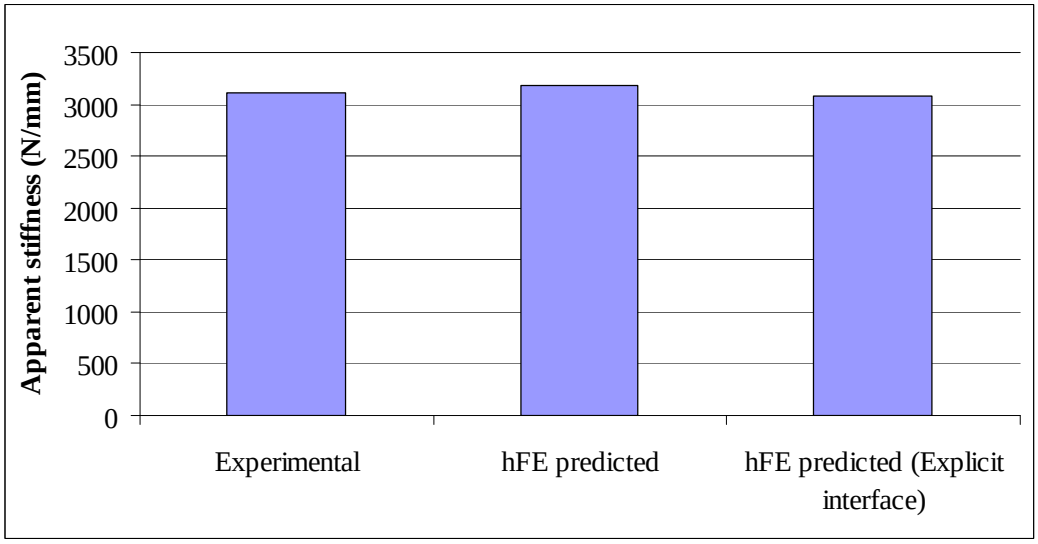

Figure 7-5. Comparison between the experimentally determined apparent stiffness and the hFE predicted apparent stiffness, both without and with an explicitly modeled interfacial region for Specimen 2.

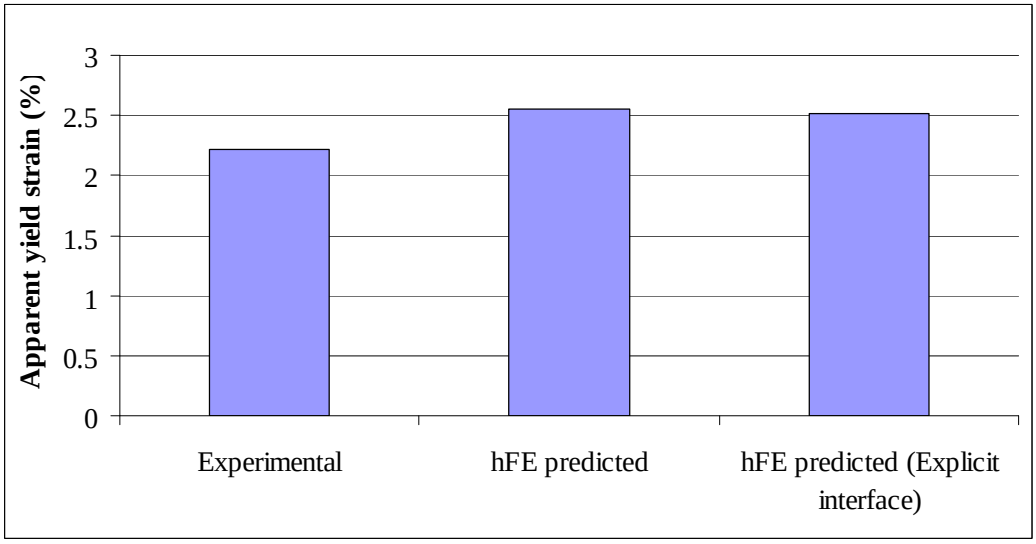

Figure 7-6. Comparison between the experimentally determined apparent yield strain and the hFE predicted apparent yield strain, both without and with an explicitly modeled interfacial region for Specimen 2.

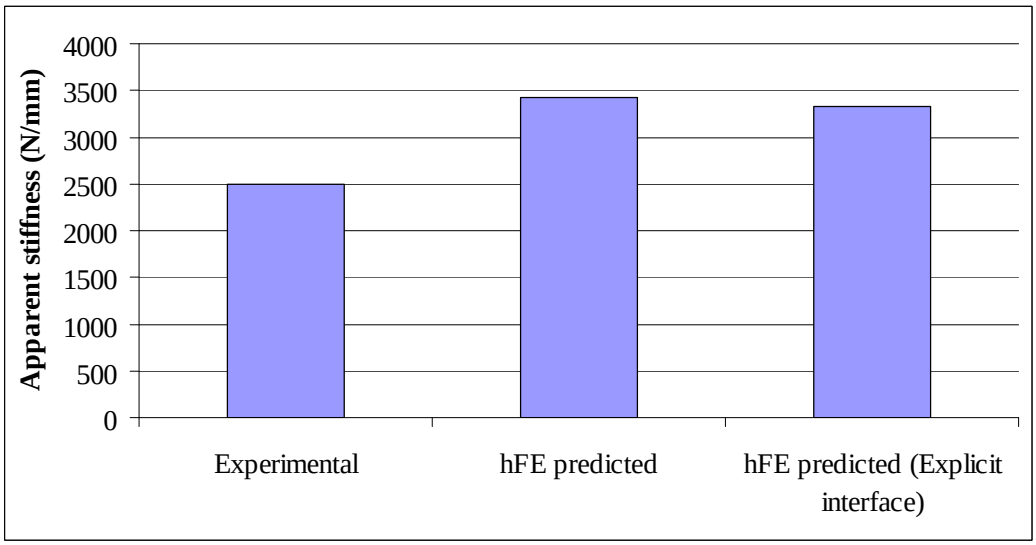

Figure 7-7. Comparison between the experimentally determined apparent stiffness and the hFE predicted apparent stiffness, both without and with an explicitly modeled interfacial region for Specimen 3.

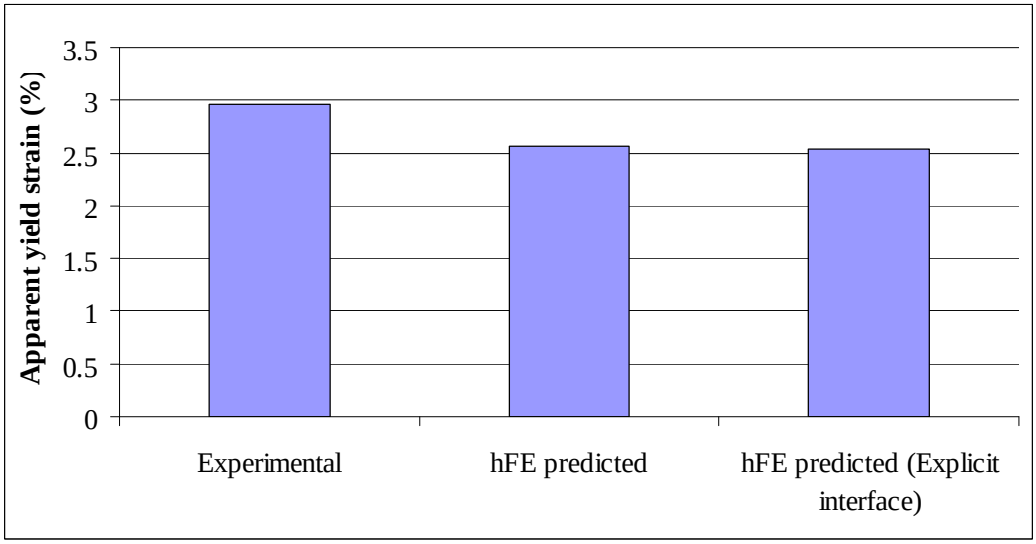

Figure 7-8. Comparison between the experimentally determined apparent yield strain and the hFE predicted apparent yield strain, both without and with an explicitly modeled interfacial region for Specimen 3.

Variation in the hFE predicted apparent stiffness for the models of Specimens 2 and 3 that feature an explicitly modelled interface are shown in Figures 7-9 to 7-11. The corners and intersections of the grid represent the hFE predicted values at each ratio of greyscale-modulus conversion factor to element yield strain. The curves that connect them were generated through third order polynomial curve fitting.

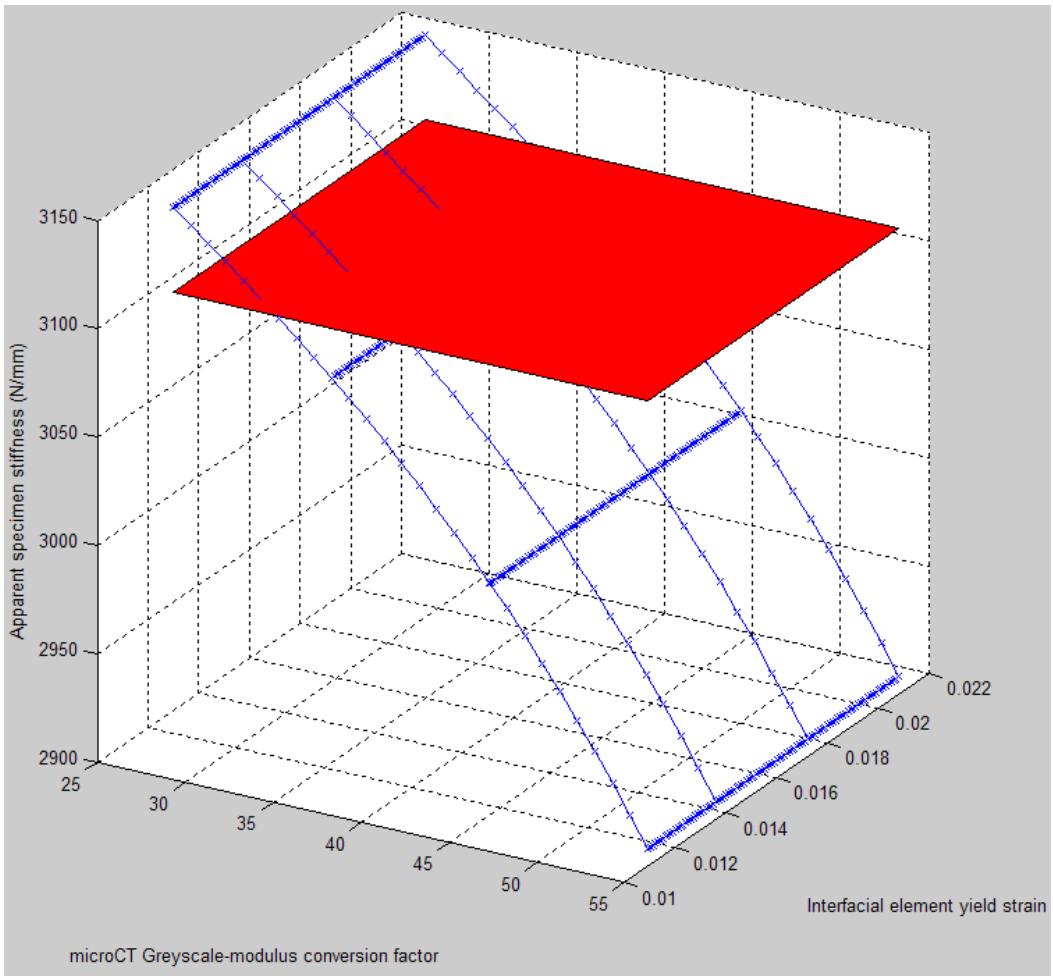

Figure 7-9. 3D plot of hFE predicted apparent stiffness for Specimen 2 (z axis) as the µCT grayscale – modulus conversion factor and element yield strain assigned to the explicitly modelled interfacial region were varied. The apparent stiffness experimentally determined for specimen 2 is shown by the red plane.

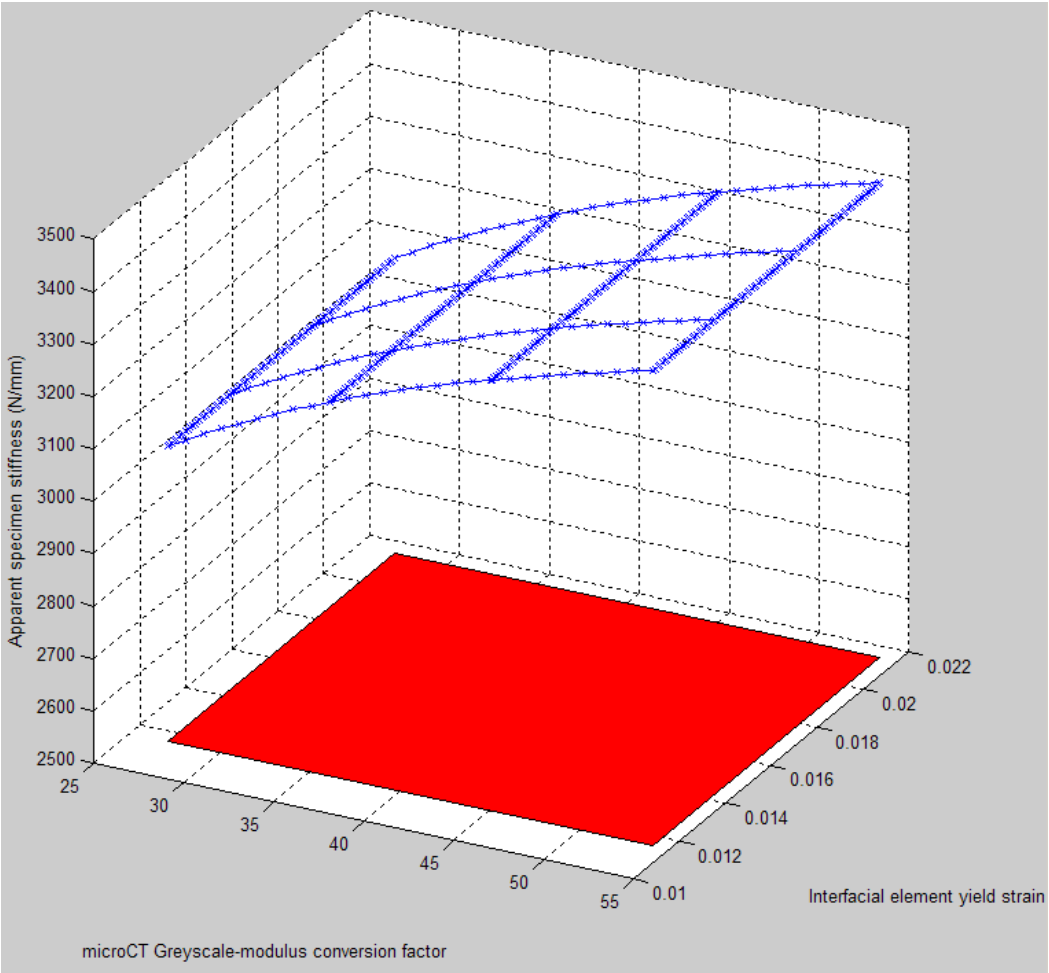

Figure 7-10. 3D plot of hFE predicted apparent stiffness for Specimen 3 (z axis) as the µCT grayscale – modulus conversion factor and element yield strain assigned to the explicitly modelled interfacial region were varied. The apparent stiffness experimentally determined for specimen 3 is shown by the red plane.

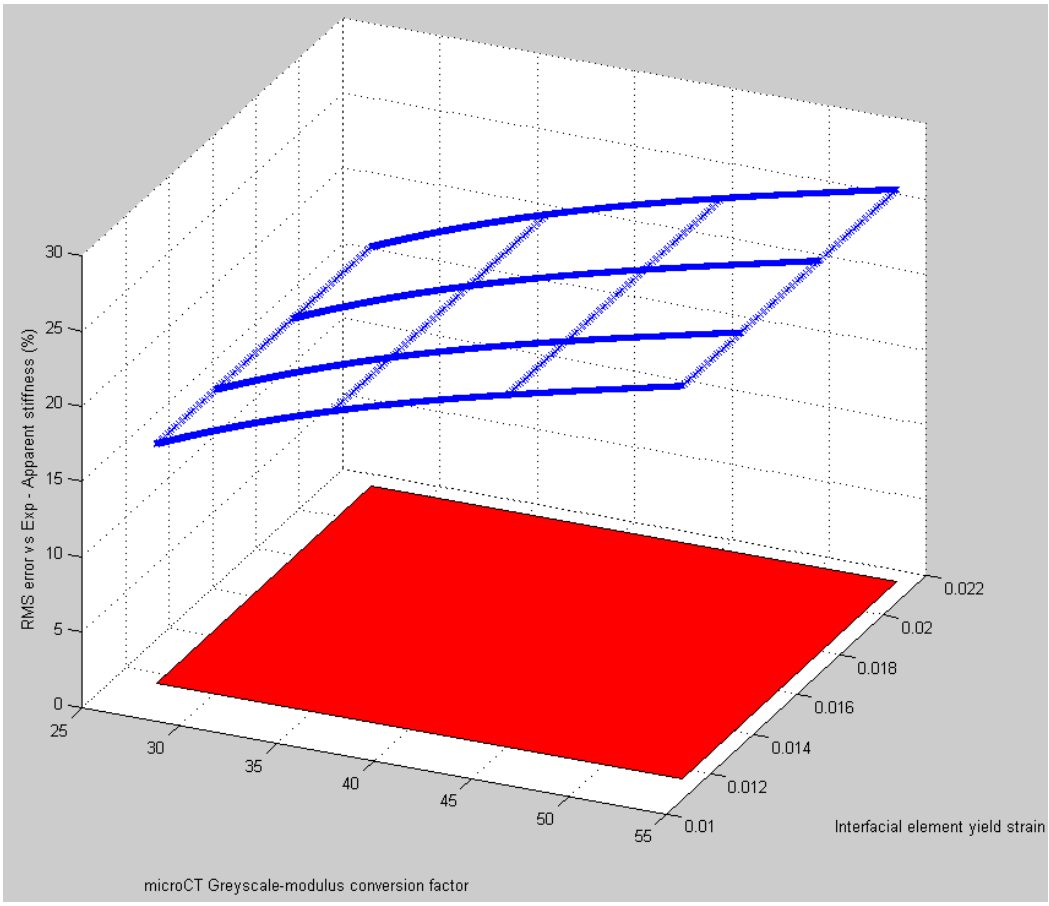

Figure 7-11. 3D plot of RMS mean percentage error between the hFE predicted apparent and experimentally determined stiffness for Specimen 2 and 3 (z axis) as the µCT grayscale – modulus conversion factor and element yield strain assigned to the explicitly modelled interfacial region were varied. The red plane represents zero RMS mean error.

Variation in the hFE predicted apparent yield strain for the models of Specimens 2 and 3 that feature an explicitly modelled interface are shown in Figures 7-12 to 7-13. In a similar manner to the previous figures, the corners and intersections of the grid represent the hFE predicted values at each ratio of greyscale-modulus conversion factor to element yield strain. The curves that connect them were generated through third order polynomial curve fitting.

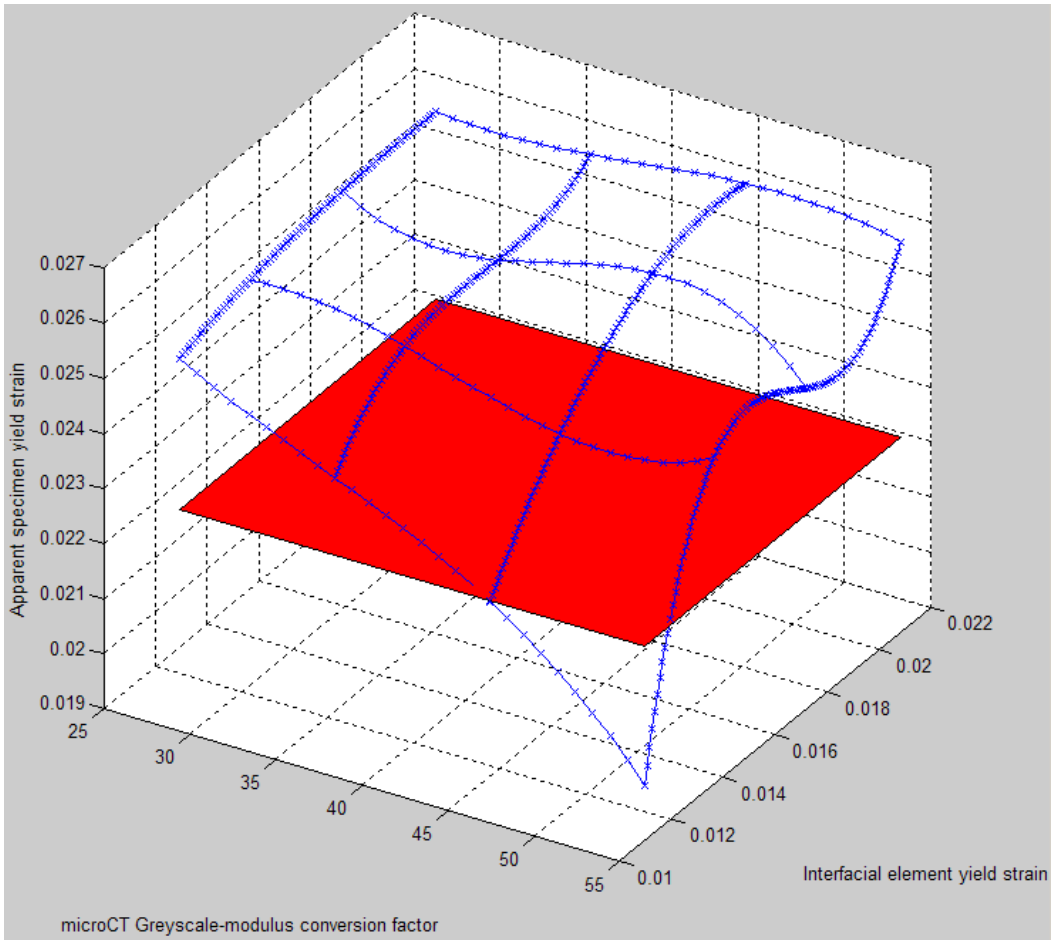

Figure 7-12. 3D plot of hFE predicted apparent yield strain for Specimen 2 (z axis) as the µCT grayscale – modulus conversion factor and element yield strain assigned to the explicitly modelled interfacial region were varied. The apparent yield strain experimentally determined for specimen 2 is shown by the red plane.

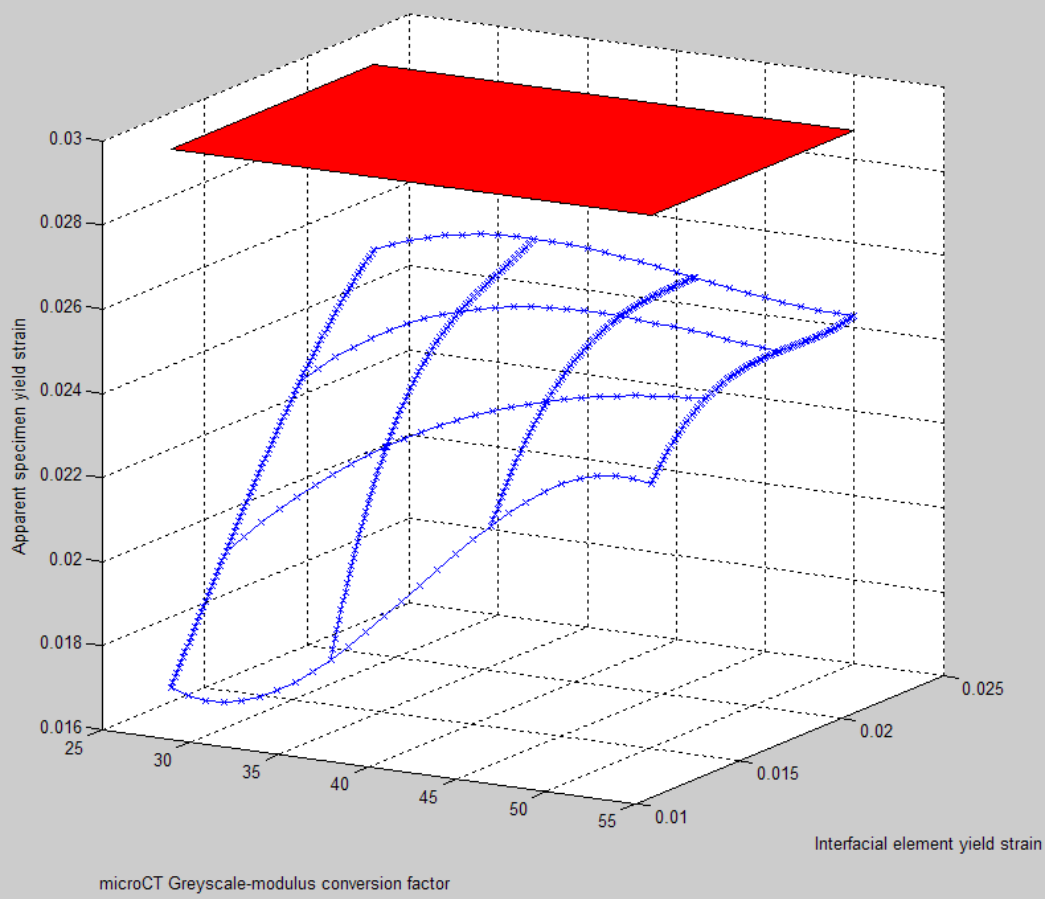

Figure 7-13. 3D plot of hFE predicted apparent yield strain for Specimen 3 (z axis) as the µCT grayscale – modulus conversion factor and element yield strain assigned to the explicitly modelled interfacial region were varied. The apparent yield strain experimentally determined for specimen 3 is shown by the red plane.

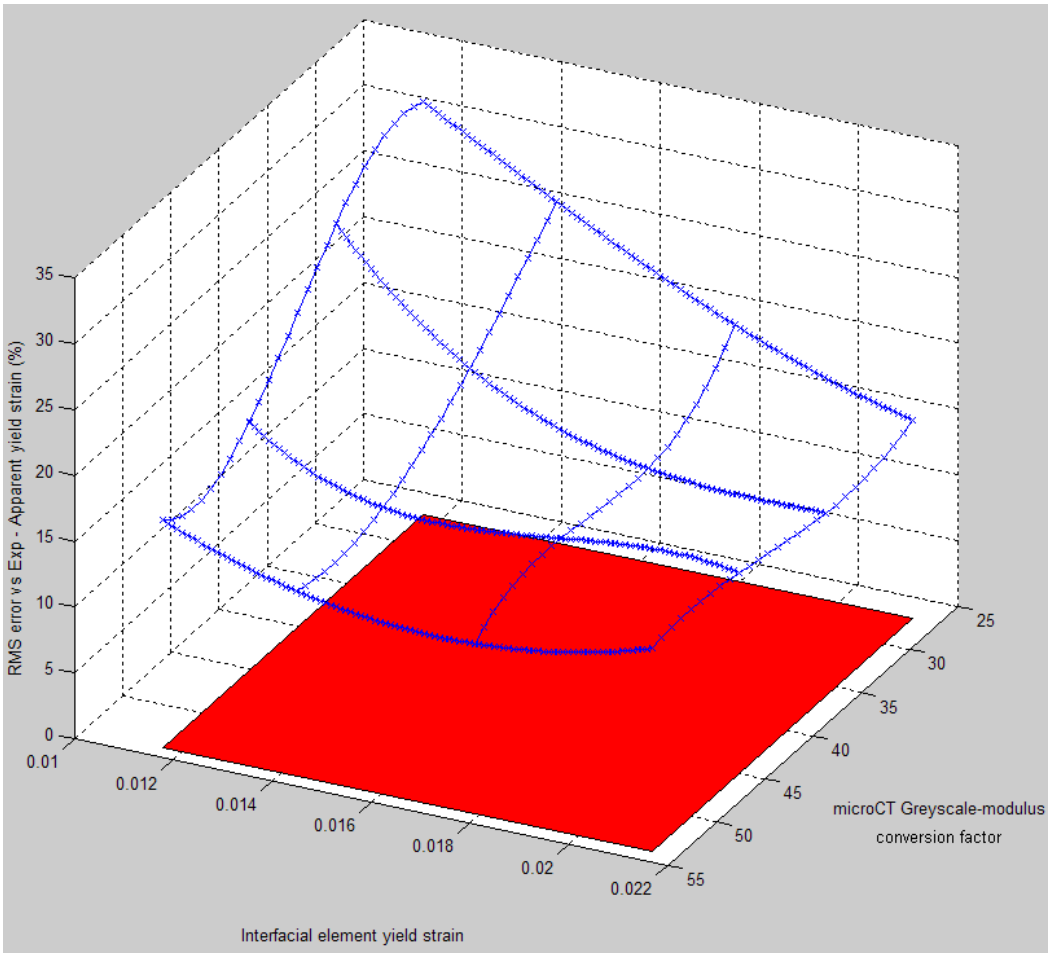

Figure 7-14. 3D plot of RMS mean percentage error between the hFE predicted apparent and experimentally determined yield strains for Specimen 2 and 3 (z axis) as the µCT grayscale – modulus conversion factor and element yield strain assigned to the explicitly modelled interfacial region were varied. The red plane represents zero RMS mean error.

Similar graphs for the variation in the hFE predicted apparent yield stress for the models of Specimens 2 and 3 that feature an explicitly modelled interface are shown in Figures 7-15 to 7-17.

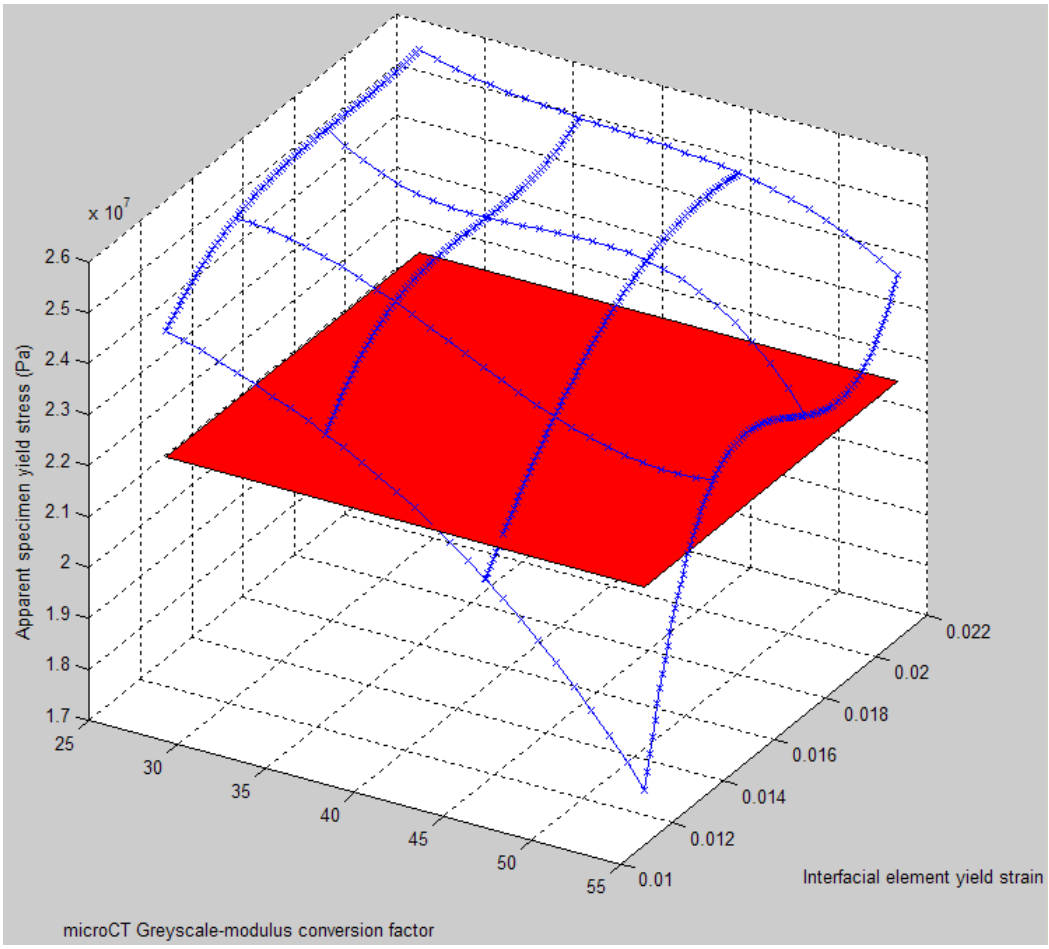

Figure 7-15. 3D plot of hFE predicted apparent yield stress for Specimen 2 (z axis) as the µCT grayscale – modulus conversion factor and element yield strain assigned to the explicitly modelled interfacial region were varied. The apparent yield stress experimentally determined for specimen 2 is shown by the red plane.

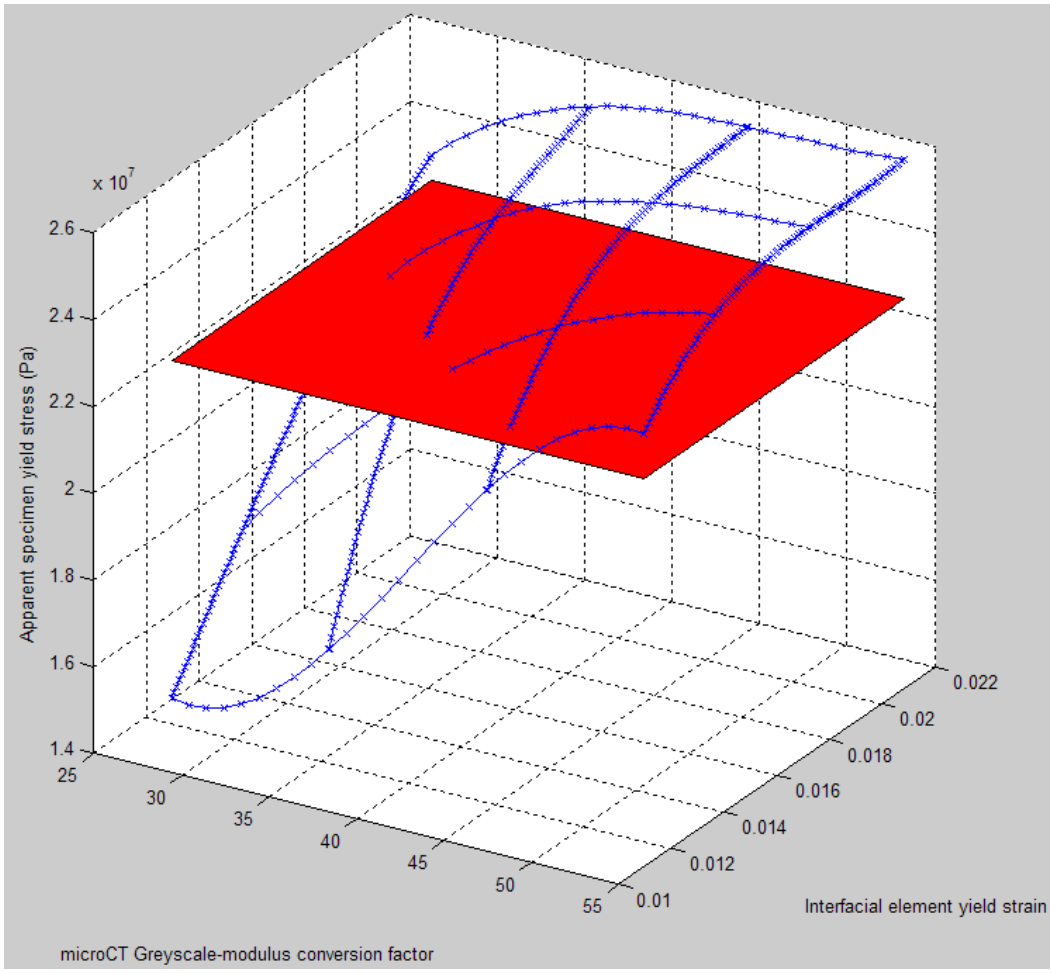

Figure 7-16. 3D plot of hFE predicted apparent yield stress for Specimen 3 (z axis) as the µCT grayscale – modulus conversion factor and element yield strain assigned to the explicitly modelled interfacial region were varied. The apparent yield stress experimentally determined for specimen 3 is shown by the red plane.

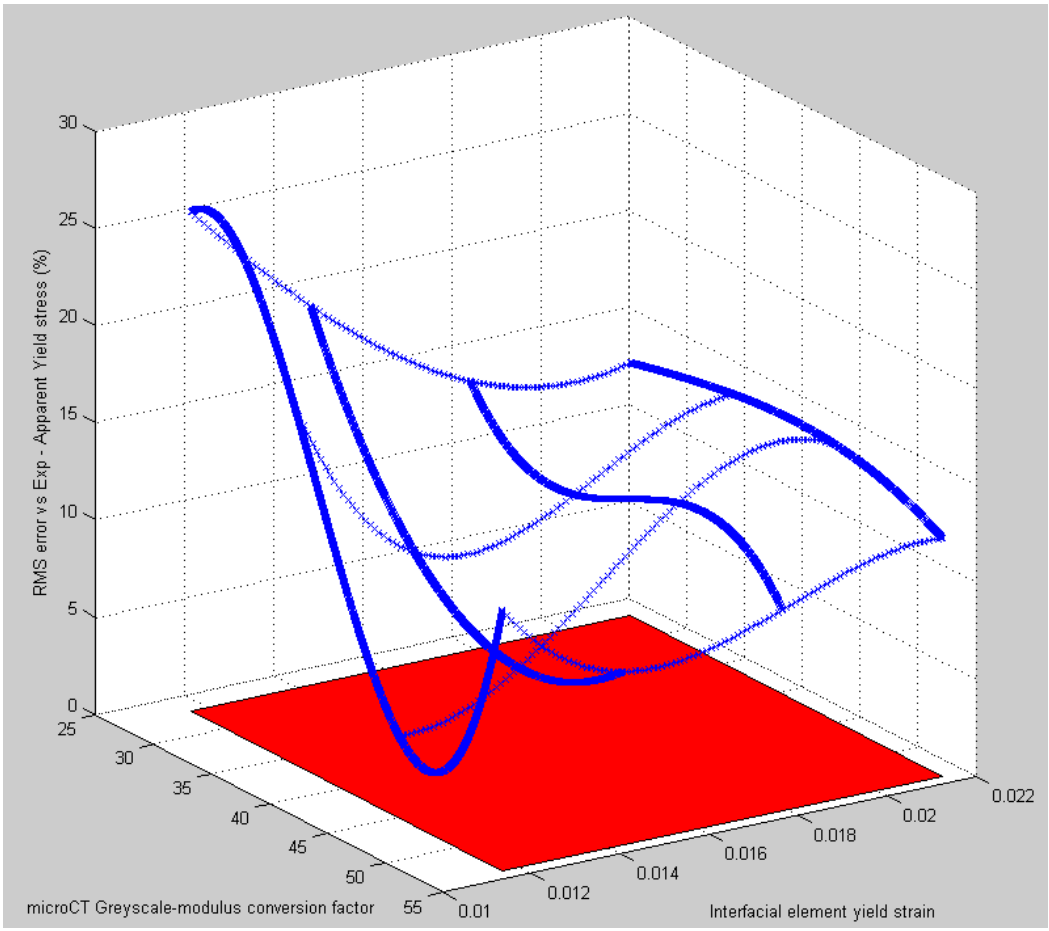

Figure 7-17. 3D plot of RMS mean percentage error between the hFE predicted apparent and experimentally determined yield stress for Specimen 2 and 3 (z axis) as the µCT grayscale – modulus conversion factor and element yield strain assigned to the explicitly modelled interfacial region were varied. The red plane represents zero RMS mean error.

The variation in the combined mean of the mean RMS percentage error between the experimentally determined and hFE predicted apparent stiffness, yield strain and yield stress for the models of Specimens 2 and 3 that feature an explicitly modelled interface is shown in Figure 7-18. The mean of the mean RMS percentage errors for both specimens in all three measured apparent properties was calculated for each ratio of greyscale-modulus conversion factor to element yield strain. Again, the curves that connect them were then generated through third order polynomial curve fitting.

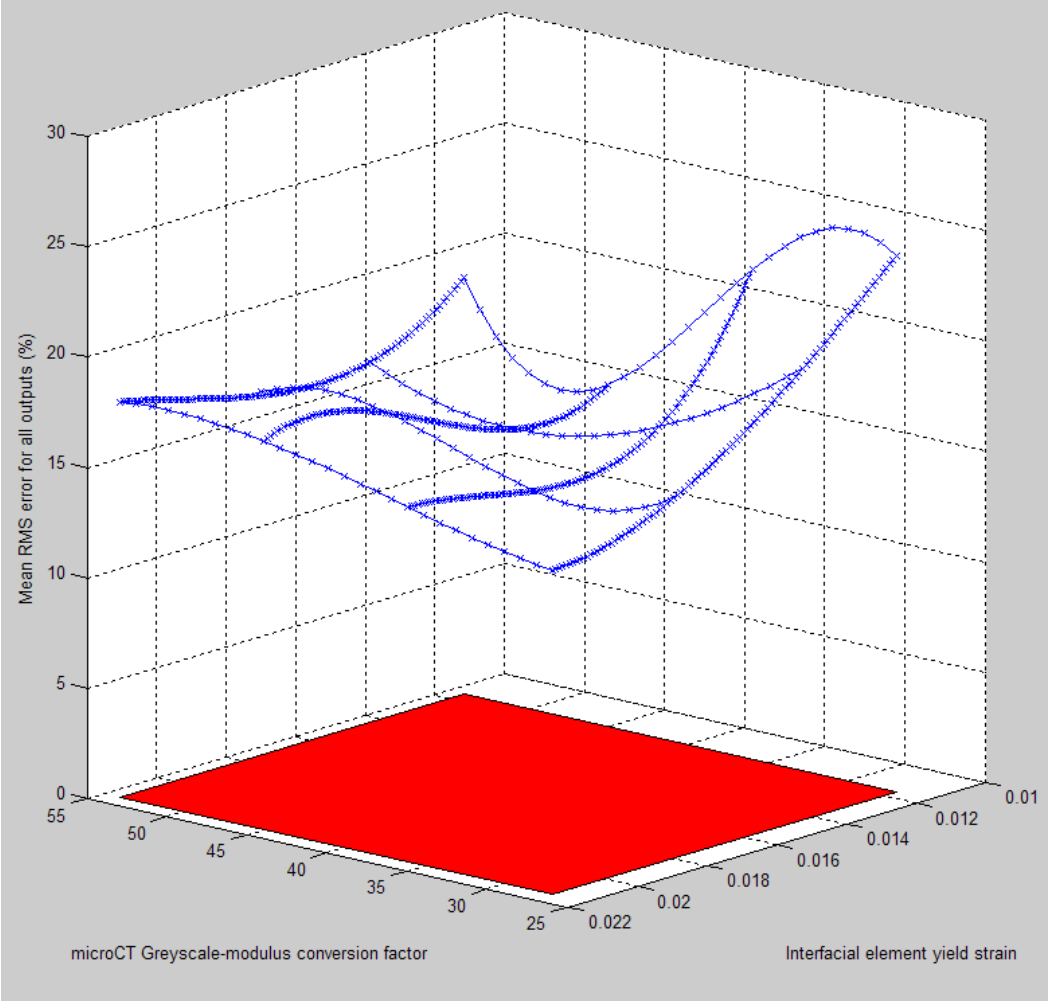

Figure 7-18. Mean of the Mean RMS percentage error between the hFE predicted apparent and experimentally determined apparent stiffness, yield strain and yield stress for Specimens 2 and 3 (z-axis) as the µCT grayscale – modulus conversion factor and element yield strain assigned to the explicitly modelled interfacial region were varied. The red plane represents zero RMS mean error.

Plots of the hFE predicted maximum principal plastic strain distribution at the maximum applied deformation for the models of Specimens 2 and 3 that featured an explicitly modelled interface are shown in Figures 7-19 to 7-26. The changes in

maximum principal plastic strain distribution as the applied greyscale-modulus conversion factor (GS->E) was varied at a common element yield strain (εyield) are shown in Figures 7-19 to 7-22. The changes in maximum principal plastic strain distribution as the applied element yield strain (εyield) was varied at a common greyscale-modulus conversion factor (GS->E) are shown in Figures 7-23 to 7-26. In each figure, the series of plots (a)-(d) use a common contour scale.

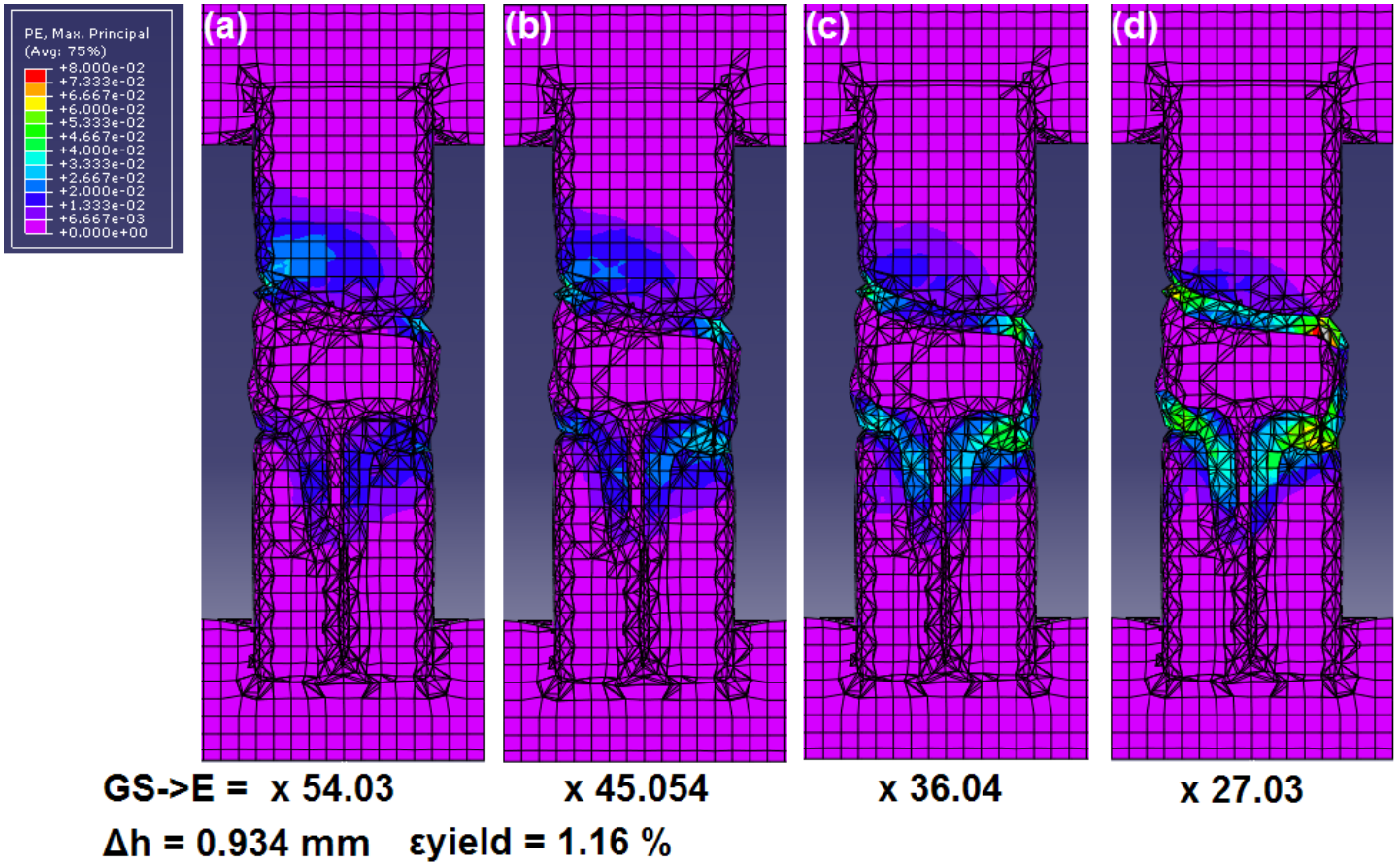

Figure 7-19. hFE predicted max principal plastic strain component plotted across the cross-section through Specimen 2 in the XZ plane at the maximum applied deformation. The grayscale-modulus conversion factor (GS->E) was varied between (a) 54.03 and (d) 27.03, at a common element yield strain (εyield) of 1.16 %. All four plots (a)-(d) are on a common contour scale (shown).

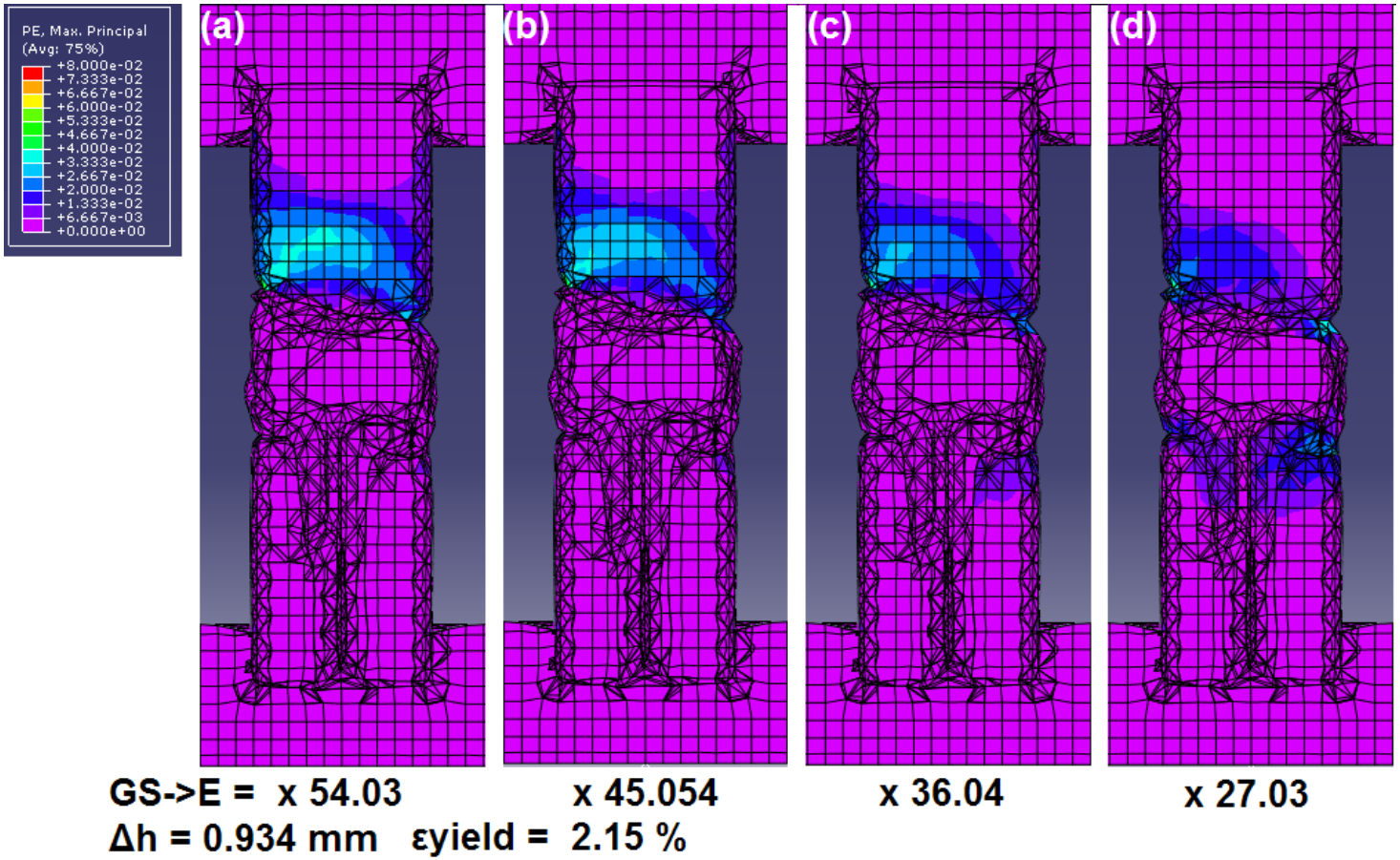

Figure 7-20. hFE predicted max principal plastic strain component plotted across the cross-section through Specimen 2 in the XZ plane at the maximum applied deformation. The grayscale-modulus conversion factor (GS->E) was varied between (a) 54.03 and (d) 27.03, at a common element yield strain (εyield) of 2.15 %. All four plots (a)-(d) are on a common contour scale (shown).

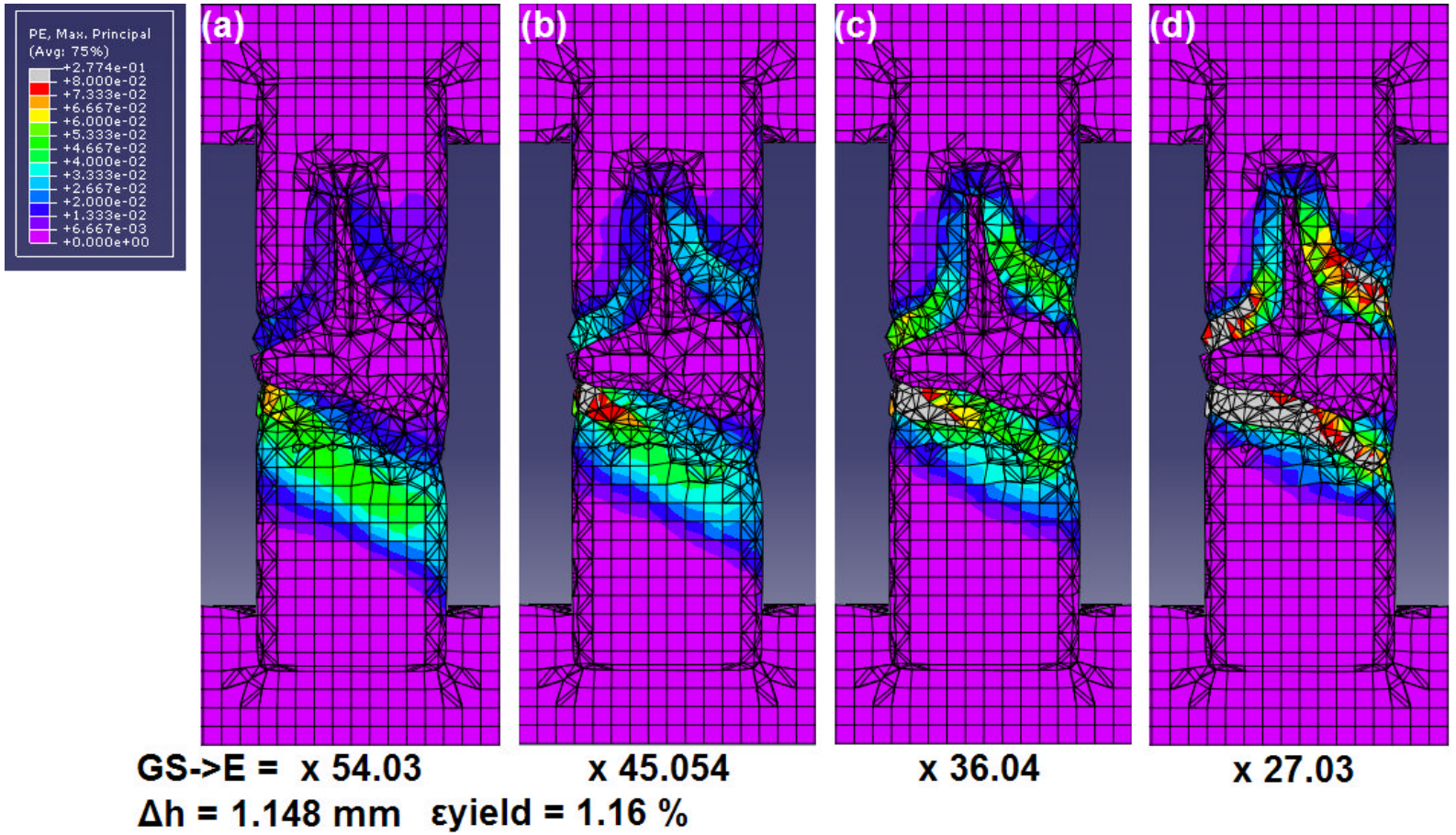

Figure 7-21. hFE predicted max principal plastic strain component plotted across the cross-section through Specimen 3 in the XZ plane at the maximum applied deformation. The grayscale-modulus conversion factor (GS->E) was varied between (a) 54.03 and (d) 27.03, at a common element yield strain (εyield) of 1.16 %. All four plots (a)-(d) are on a common contour scale (shown).

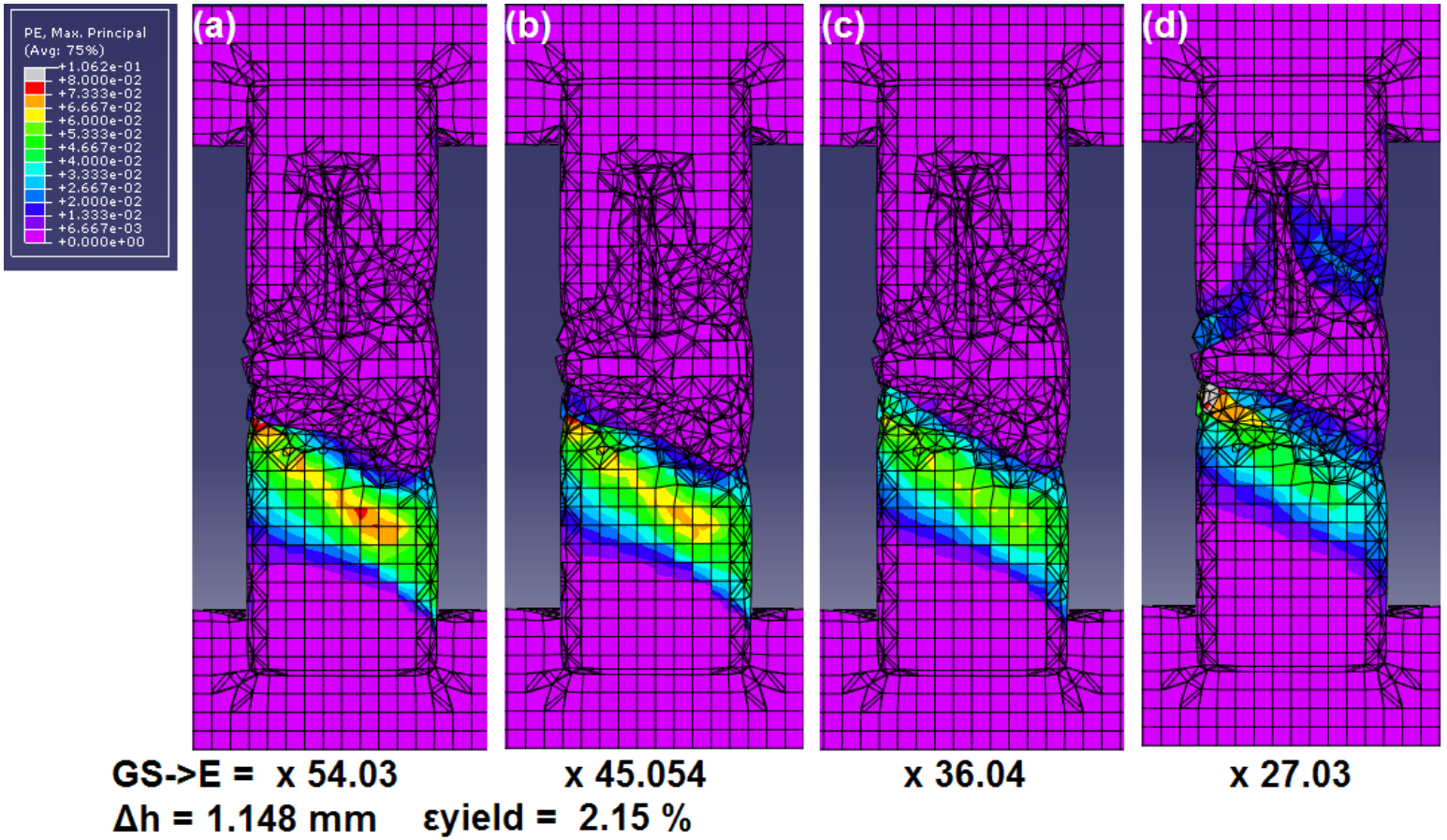

Figure 7-22. hFE predicted max principal plastic strain component plotted across the cross-section through Specimen 3 in the XZ plane at the maximum applied deformation. The grayscale-modulus conversion factor (GS->E) was varied between (a) 54.03 and (d) 27.03, at a common element yield strain (εyield) of 2.15 %. All four plots (a)-(d) are on a common contour scale (shown).

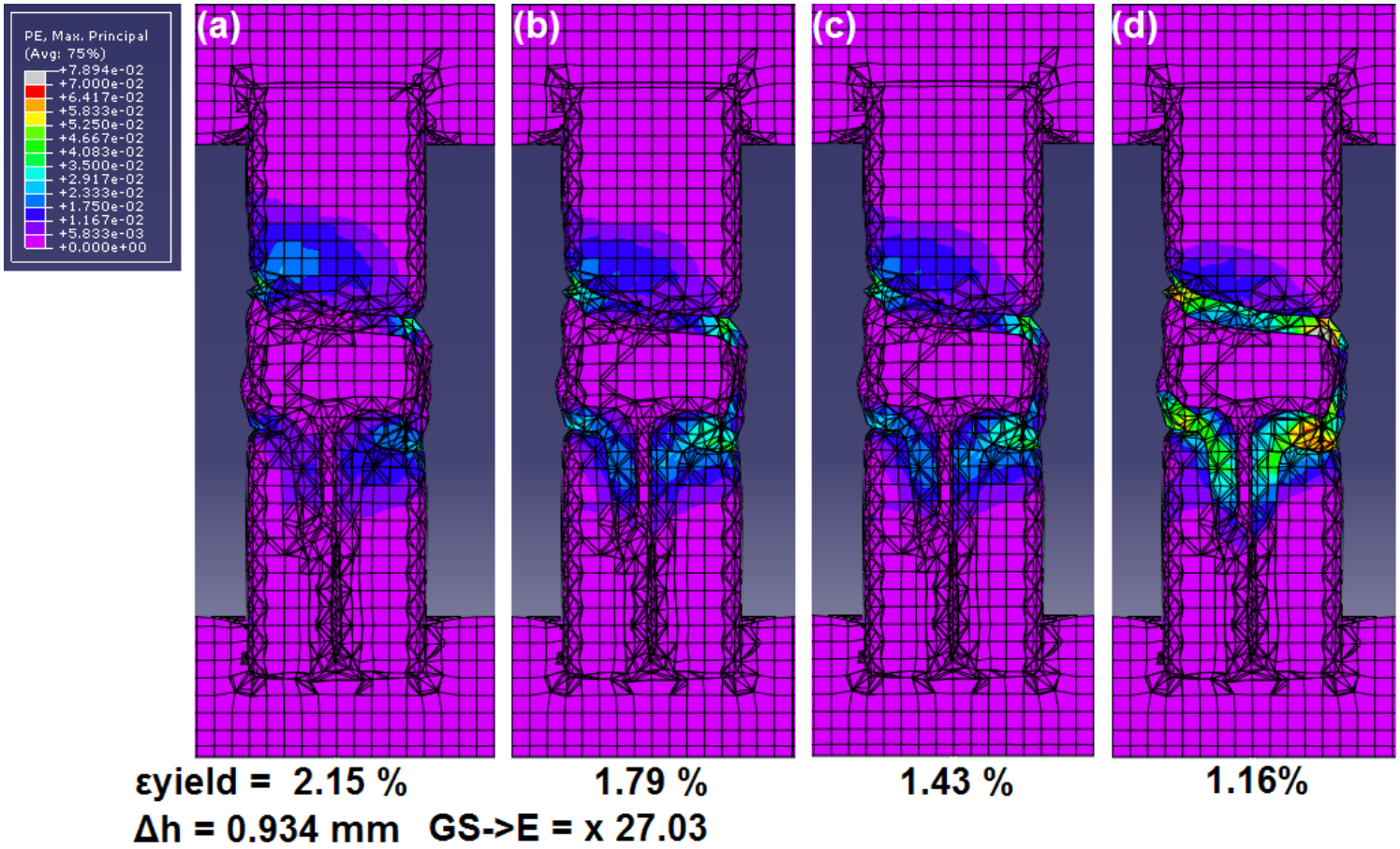

Figure 7-23. hFE predicted max principal plastic strain component plotted across the cross-section through Specimen 2 in the XZ plane at the maximum applied deformation. The element yield strain (εyield) was varied between (a) 2.15 % and (d) 1.16 %, at a common grayscale-modulus conversion factor (GS->E) of 27.03. All four plots (a)-(d) are on a common contour scale (shown).

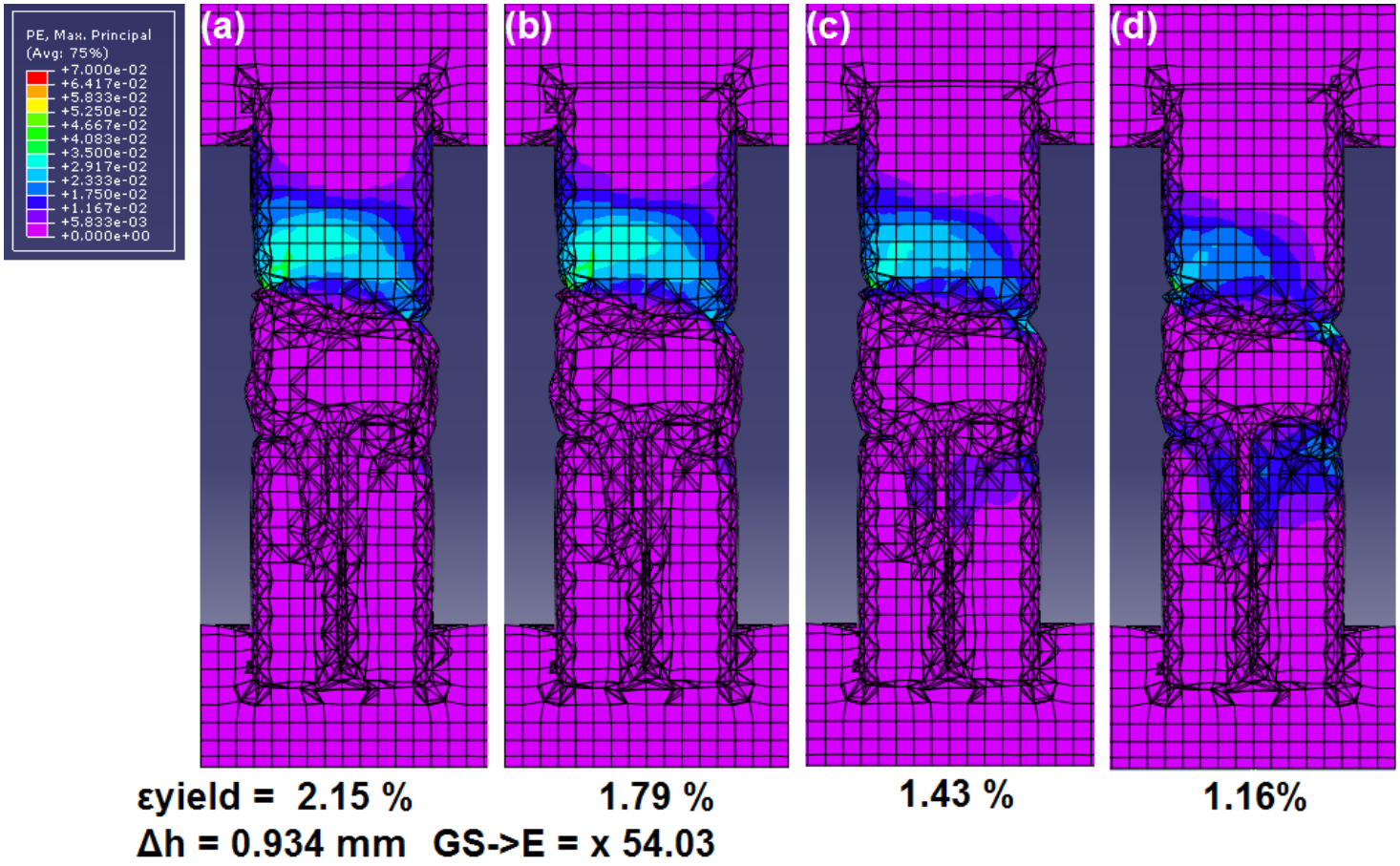

Figure 7-24. hFE predicted max principal plastic strain component plotted across the cross-section through Specimen 2 in the XZ plane at the maximum applied deformation. The element yield strain (εyield) was varied between (a) 2.15 % and (d) 1.16 %, at a common grayscale-modulus conversion factor (GS->E) of 54.03. All four plots (a)-(d) are on a common contour scale (shown).

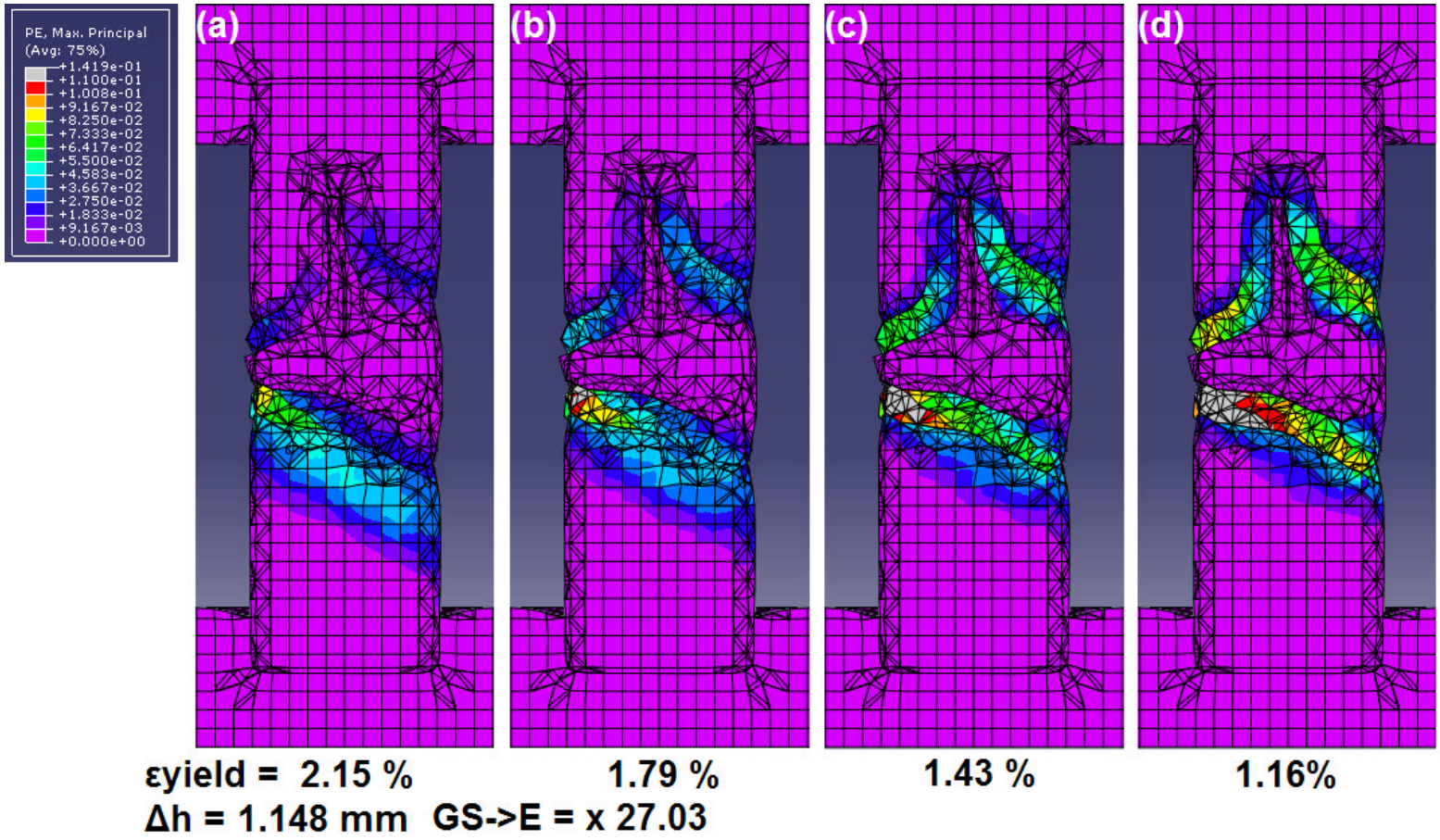

Figure 7-25. hFE predicted max principal plastic strain component plotted across the cross-section through Specimen 3 in the XZ plane at the maximum applied deformation. The element yield strain (εyield) was varied between (a) 2.15 % and (d) 1.16 %, at a common grayscale-modulus conversion factor (GS->E) of 27.03. All four plots (a)-(d) are on a common contour scale (shown).

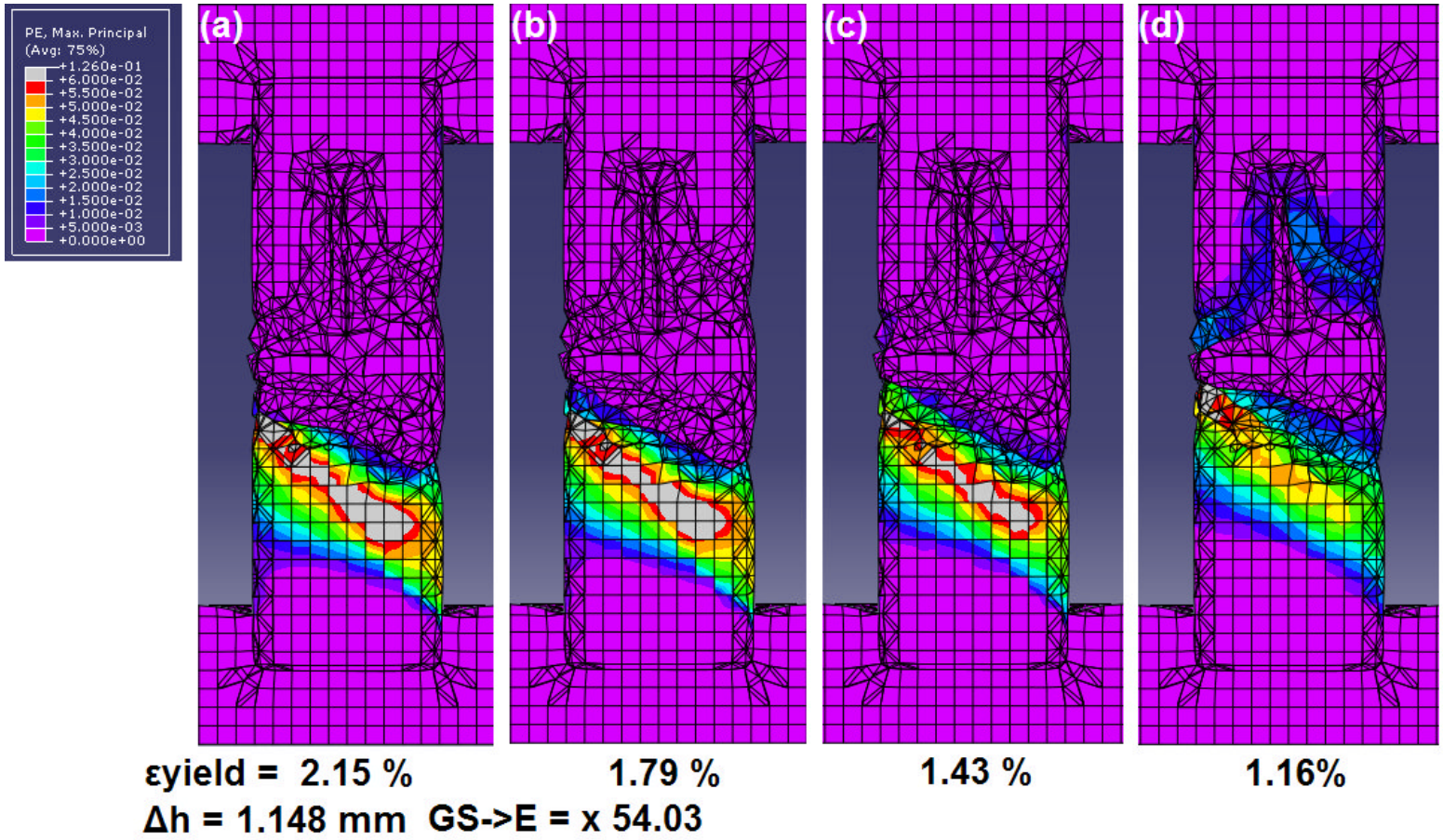

Figure 7-26. hFE predicted max principal plastic strain component plotted across the cross-section through Specimen 3 in the XZ plane at the maximum applied deformation. The element yield strain (εyield) was varied between (a) 2.15 % and (d) 1.16 %, at a common grayscale-modulus conversion factor (GS->E) of 54.03. All four plots (a)-(d) are on a common contour scale (shown).

Plots of the hFE predicted distribution of strain in the z-direction at the maximum applied deformation for the models of Specimens 2 and 3 that featured an explicitly modelled interface are shown in Figures 7-27 to 7-34. In each figure, the variation in the distribution of strain in the z-direction as the element yield strain (εyield) was varied at a common grayscale-modulus conversion factor (GS->E) is shown in plots (b)-(d) in each case. The strain distribution in the z-direction determined from the experimental tests using the Vic2D strain correlation software in shown in plot (a) in each case. In each case, the plots (a)-(e) all use a common contour scale (shown).

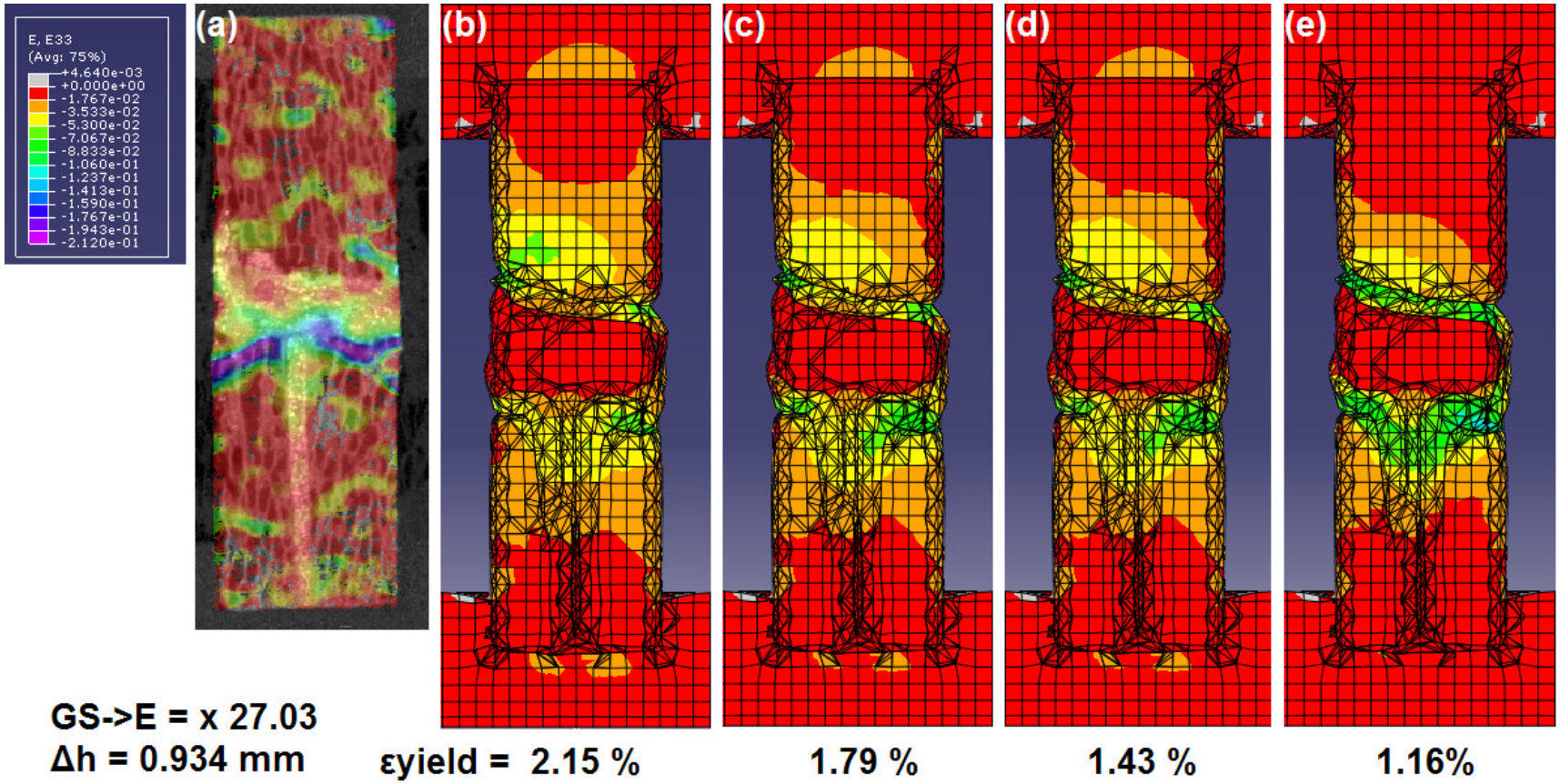

Figure 7-27. hFE predicted strain in the z-direction plotted across the cross-section through Specimen 2 in the XZ plane at the maximum applied deformation. The element yield strain (εyield) was varied between (b) 2.15 % and (e) 1.16 %, at a common grayscale-modulus conversion factor (GS->E) of 27.03. All five plots (a)-(e) are on a common contour scale (shown). The experimental specimen strain distribution through the cross section in the same plane, determined through digital image correlation using Vic2D, is shown in (a).

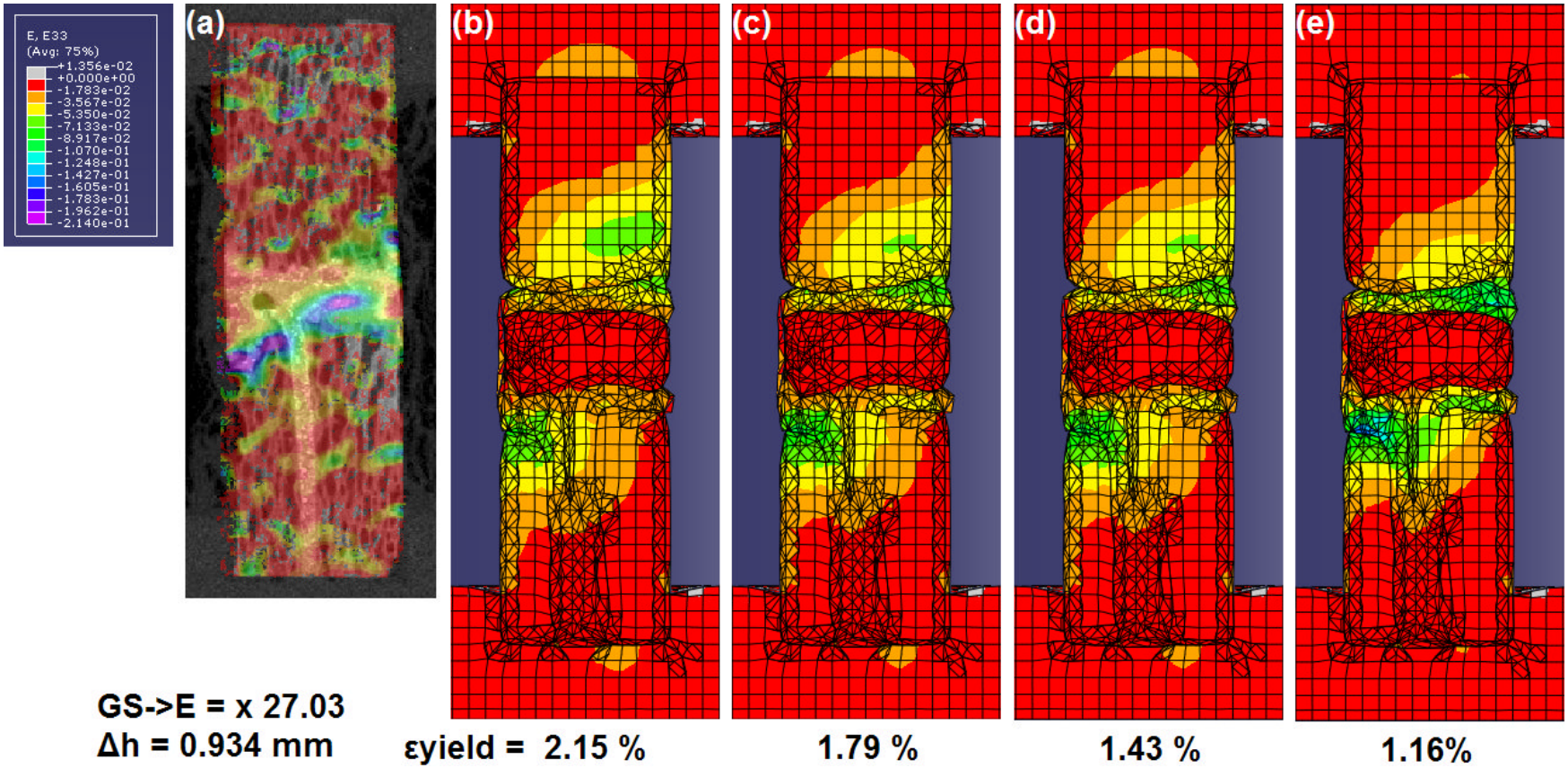

Figure 7-28. hFE predicted strain in the z-direction plotted across the cross-section through Specimen 2 in the YZ plane at the maximum applied deformation. The element yield strain (εyield) was varied between (b) 2.15 % and (e) 1.16 %, at a common grayscale-modulus conversion factor (GS->E) of 27.03. All five plots (a)-(e) are on a common contour scale (shown) are on a common contour scale (shown). The experimental specimen strain distribution through the cross section in the same plane, determined through digital image correlation using Vic2D, is shown in (a).

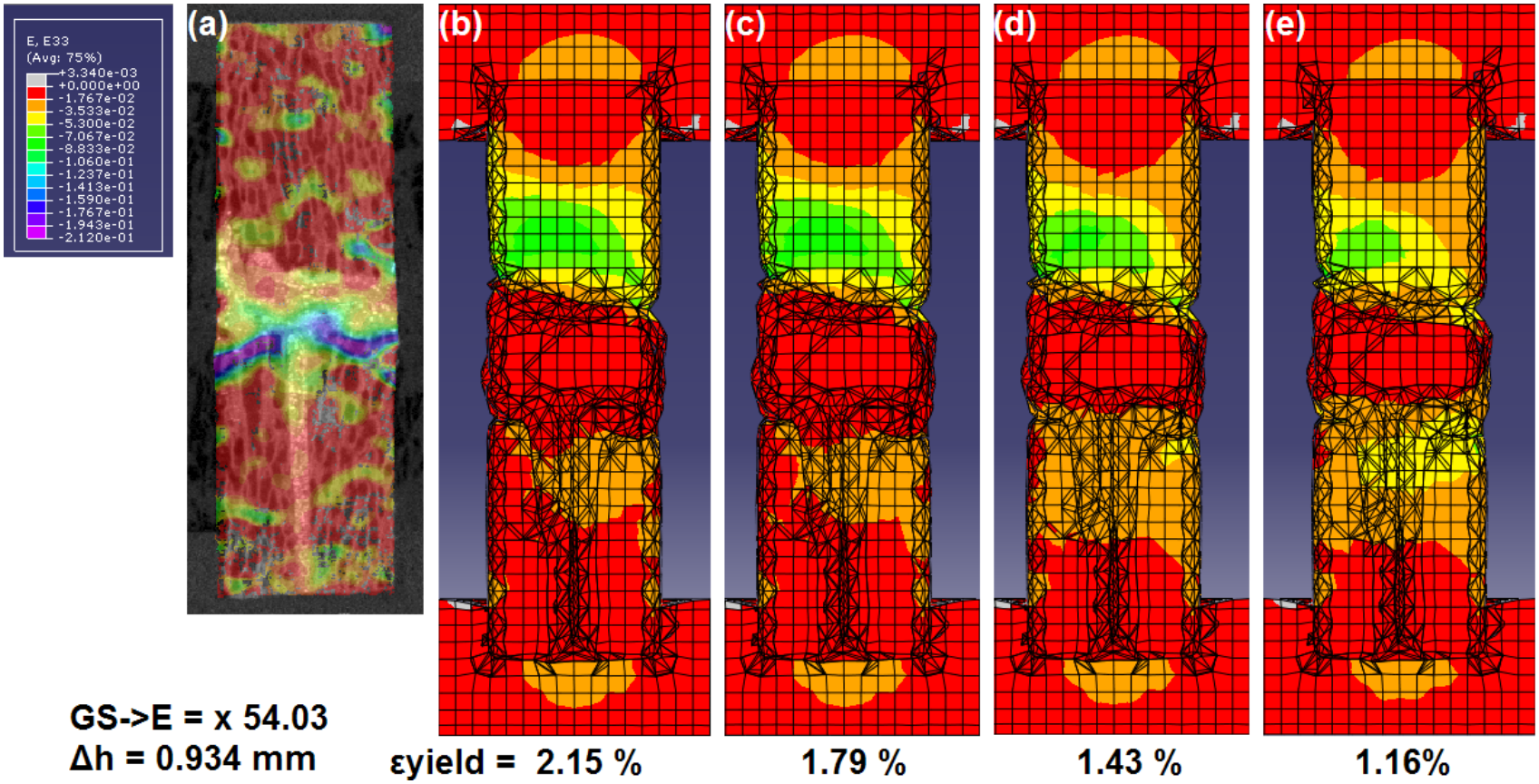

Figure 7-29. hFE predicted strain in the z-direction plotted across the cross-section through Specimen 2 in the XZ plane at the maximum applied deformation. The element yield strain (εyield) was varied between (b) 2.15 % and (e) 1.16 %, at a common grayscale-modulus conversion factor (GS->E) of 54.03. All five plots (a)-(e) are on a common contour scale (shown) are on a common contour scale (shown). The experimental specimen strain distribution through the cross section in the same plane, determined through digital image correlation using Vic2D, is shown in (a).

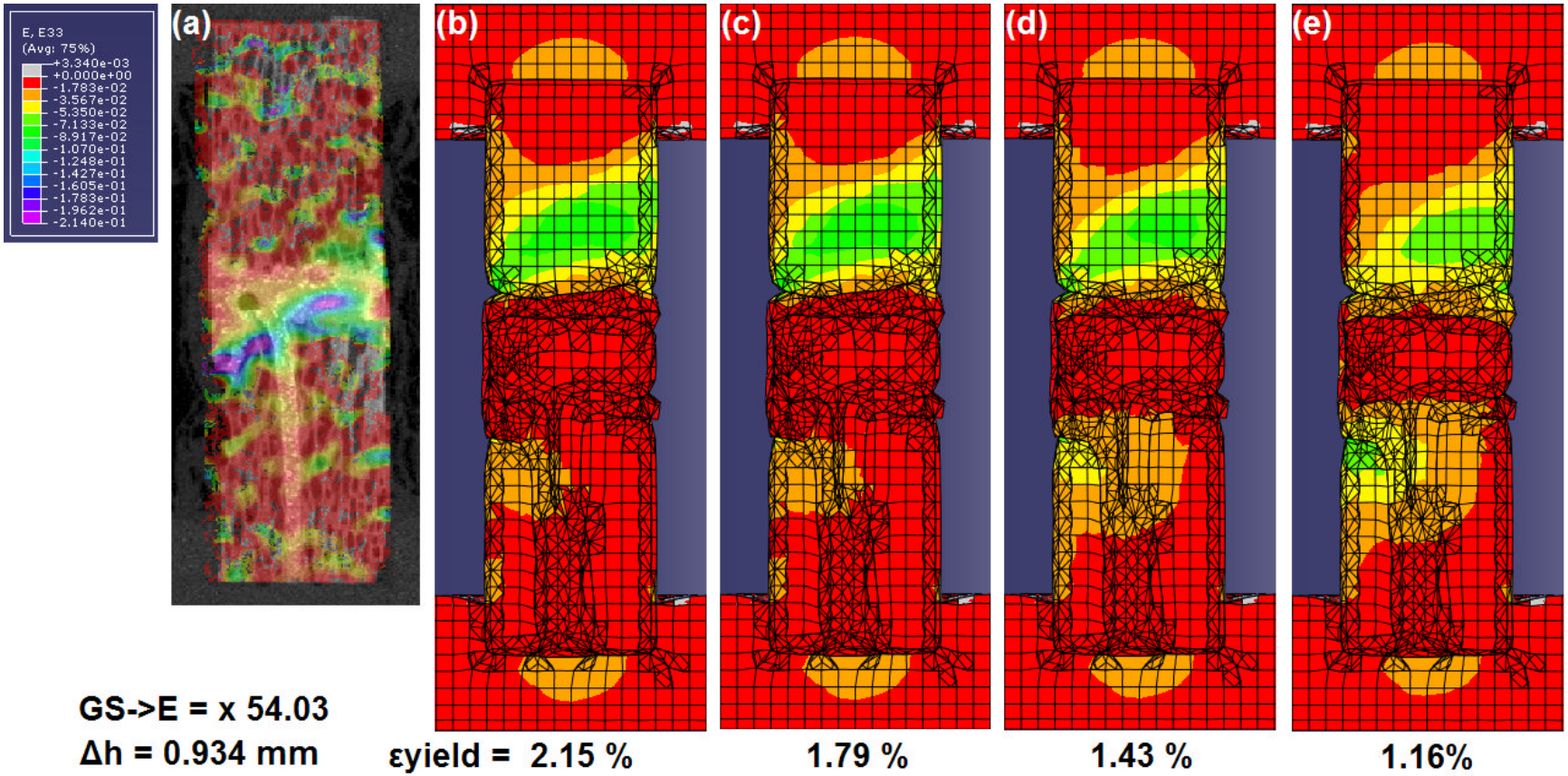

Figure 7-30. hFE predicted strain in the z-direction plotted across the cross-section through Specimen 2 in the YZ plane at the maximum applied deformation. The element yield strain (εyield) was varied between (b) 2.15 % and (e) 1.16 %, at a common grayscale-modulus conversion factor (GS->E) of 54.03. All five plots (a)-(e) are on a common contour scale (shown) are on a common contour scale (shown). The experimental specimen strain distribution through the cross section in the same plane, determined through digital image correlation using Vic2D, is shown in (a).

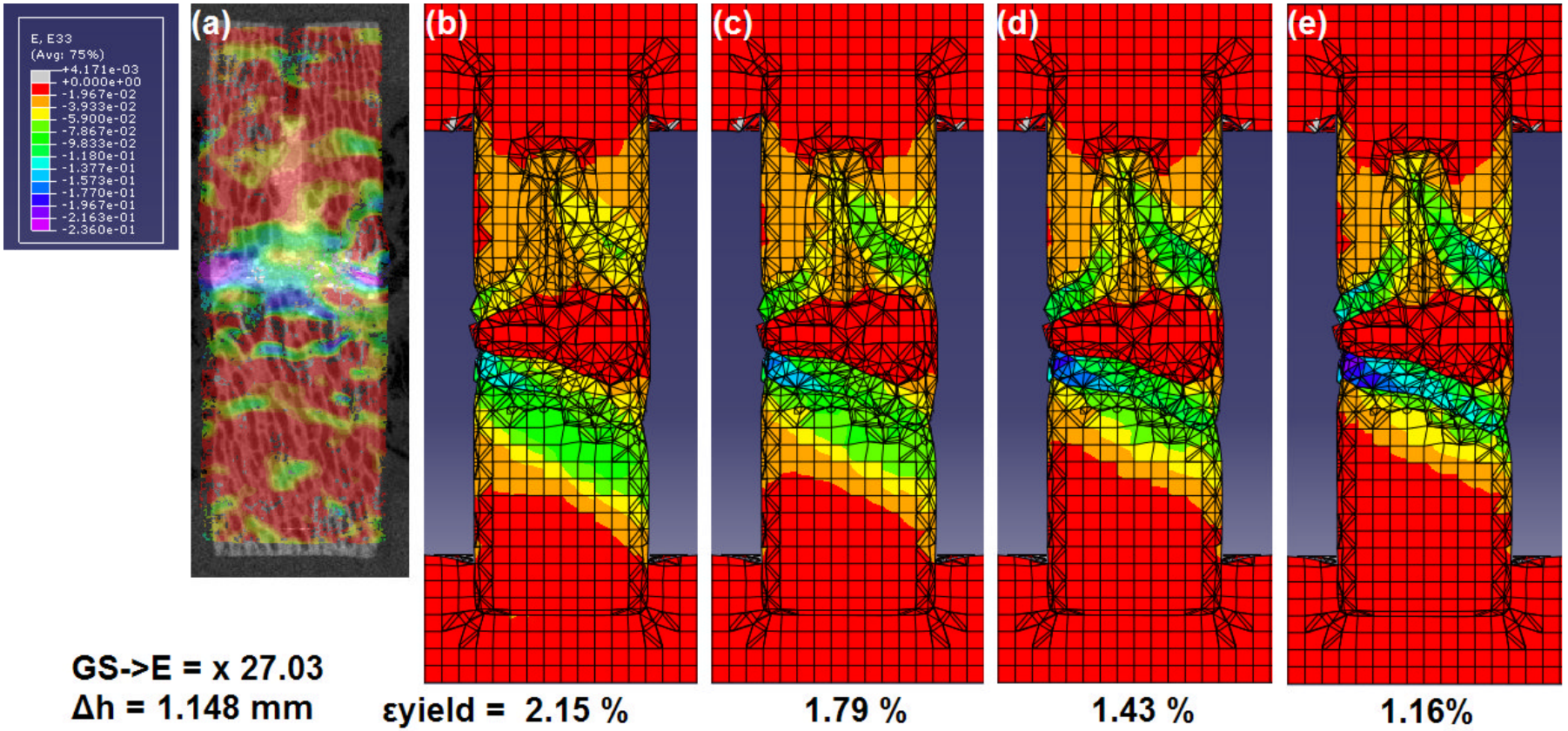

Figure 7-31. hFE predicted strain in the z-direction plotted across the cross-section through Specimen 3 in the XZ plane at the maximum applied deformation. The element yield strain (εyield) was varied between (b) 2.15 % and (e) 1.16 %, at a common grayscale-modulus conversion factor (GS->E) of 27.03. All five plots (a)-(e) are on a common contour scale (shown) are on a common contour scale (shown). The experimental specimen strain distribution through the cross section in the same plane, determined through digital image correlation using Vic2D, is shown in (a).

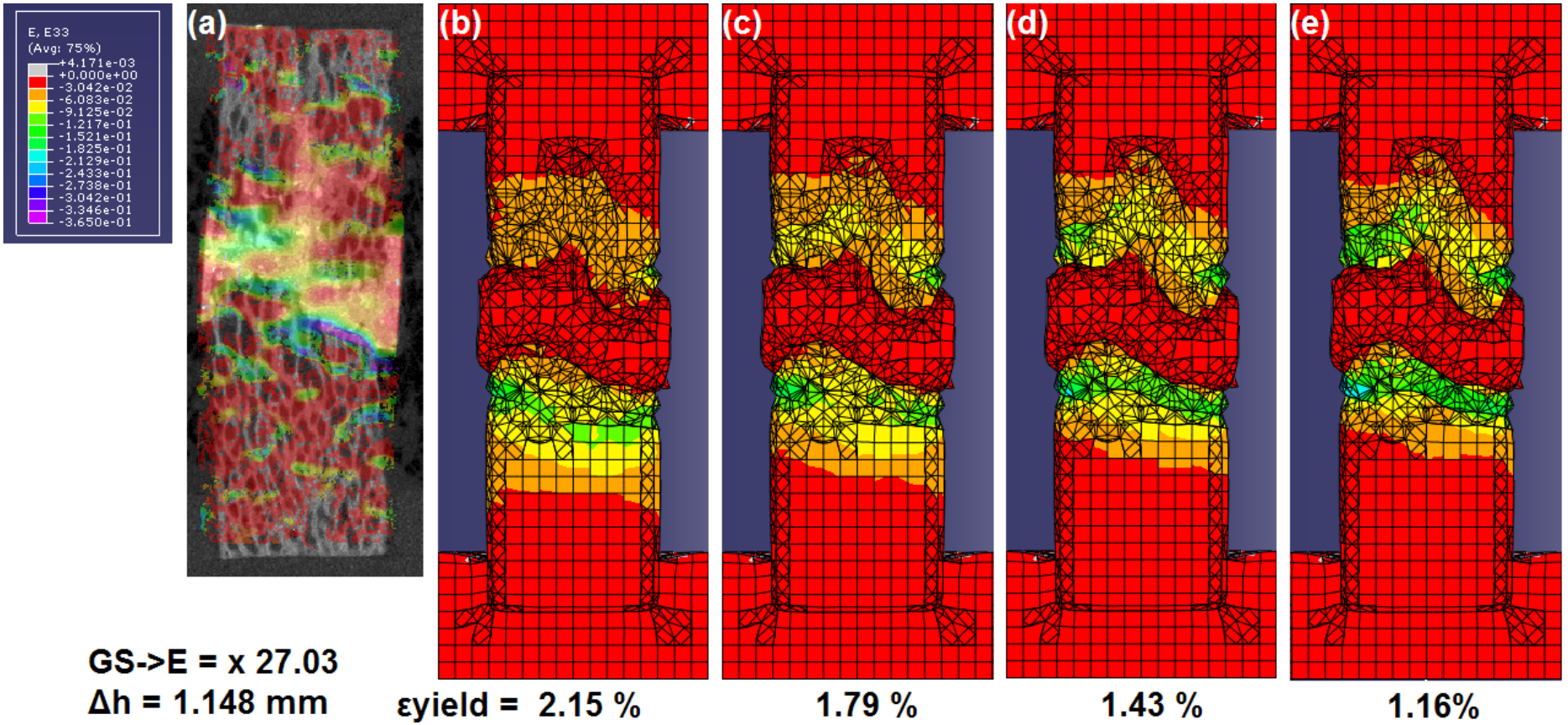

Figure 7-32. hFE predicted strain in the z-direction plotted across the cross-section through Specimen 3 in the YZ plane at the maximum applied deformation. The element yield strain (εyield) was varied between (b) 2.15 % and (e) 1.16 %, at a common grayscale-modulus conversion factor (GS->E) of 27.03. All five plots (a)-(e) are on a common contour scale (shown) are on a common contour scale (shown). The experimental specimen strain distribution through the cross section in the same plane, determined through digital image correlation using Vic2D, is shown in (a).

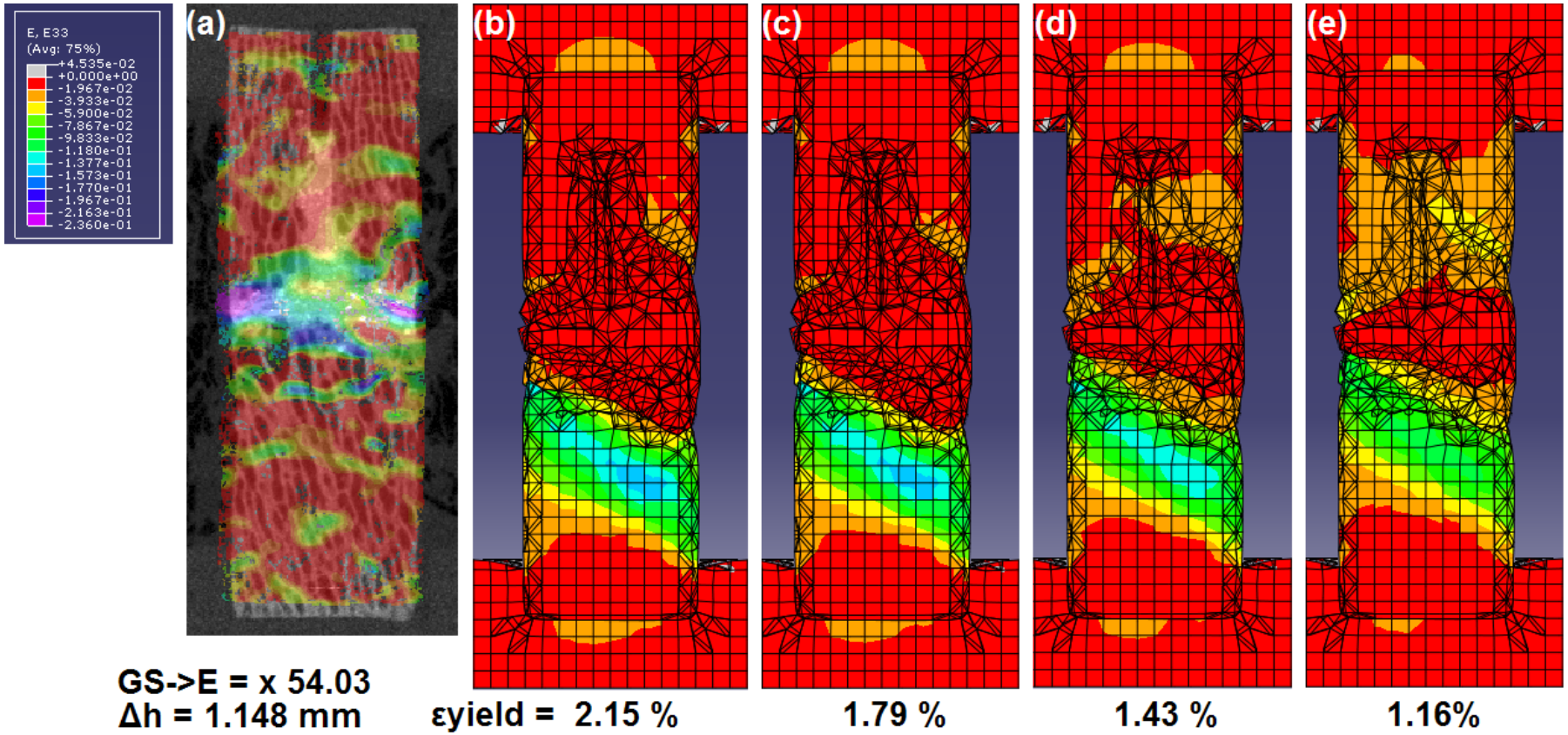

Figure 7-33. hFE predicted strain in the z-direction plotted across the cross-section through Specimen 3 in the XZ plane at the maximum applied deformation. The element yield strain (εyield) was varied between (b) 2.15 % and (e) 1.16 %, at a common grayscale-modulus conversion factor (GS->E) of 54.03. All five plots (a)-(e) are on a common contour scale (shown) are on a common contour scale (shown). The experimental specimen strain distribution through the cross section in the same plane, determined through digital image correlation using Vic2D, is shown in (a).

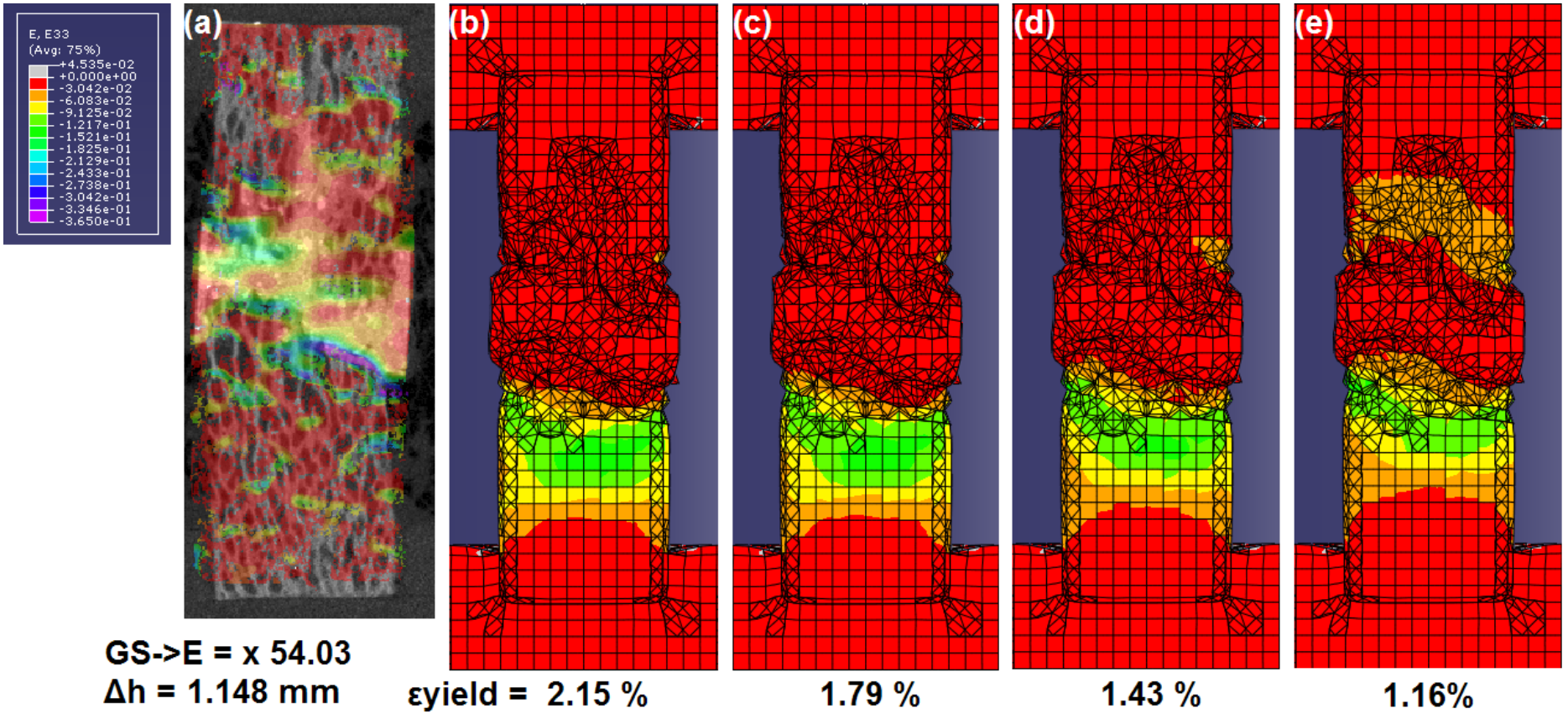

Figure 7-34. hFE predicted strain in the z-direction plotted across the cross-section through Specimen 3 in the YZ plane at the maximum applied deformation. The element yield strain (εyield) was varied between (b) 2.15 % and (e) 1.16 %, at a common grayscale-modulus conversion factor (GS->E) of 54.03. All five plots (a)-(e) are on a common contour scale (shown) are on a common contour scale (shown). The experimental specimen strain distribution through the cross section in the same plane, determined through digital image correlation using Vic2D, is shown in (a).

7.5. Discussion

7.5.1. hFE predicted apparent stiffness

Comparison between the experimentally determined and hFE predicted apparent stiffness and apparent yield strain for Specimens 2 and 3, both with and without an explicitly modeled interfacial region were shown in Figures 7-5 to 7-8. Within the models in which an explicit interfacial region was incorporated, it was assigned the grayscale-modulus conversion factor and element yield strain previously determined for un-augmented ovine trabecular bone, described in Chapter 4. This enabled the effect of the changes in the mesh geometry between the models with and without an explicit interfacial zone to be assessed.

It is clear that for both Specimens 2 and 3, the influence of the variation in mesh geometry is negligible when compared to the error between the hFE predictions of the unmodified models and the experimentally determined apparent specimen properties. In both cases the hFE predicted apparent stiffness was slightly reduced following the changes in the mesh geometry, but it is expected that this is due to the slight reduction in cross section caused by the smoothing algorithms applied by ScanIP when the mesh is generated from the downsampled and masked μCT images. This occurs at the additional contacts between the interfacial region and the adjacent bone and cement augmentation

The sensitivity of the hFE predicted apparent stiffness for Specimens 2 and 3 to the applied interfacial μCT grayscale-modulus conversion factor and element yield strain was shown in Figures 7-9 and 7-10. The hFE predicted apparent stiffness for Specimen 3 shows a decreasing sensitivity to variation in the applied interfacial grayscale-modulus conversion factor as it is increased, whereas for Specimen 2 the opposite appears to be the case. When the balance of stiffness between the interfacial region and the main trabecular bone is such that the majority of the deformation occurs in the interfacial region, the sensitivity of the apparent Specimen stiffness to the interfacial grayscale-modulus conversion factor would be expected to be at a maximum, as any

change in the hFE predicted apparent stiffness would be approximately directly proportional to the change in the grayscale-modulus conversion factor. As the stiffness of the interfacial region increases relative to the stiffness of the trabecular bone the sensitivity of the apparent specimen stiffness to a given change in the grayscale-modulus conversion factor would be expected to decrease, as a greater proportion of the overall deformation would occur in the trabecular bone. Beyond the point where the stiffness of the interfacial region was many times higher than that of the trabecular bone, a negligible proportion of the overall displacement would occur in the interfacial region. Thus the sensitivity of the apparent displacement to the interfacial grayscale-modulus conversion factor would be expected to be near zero.

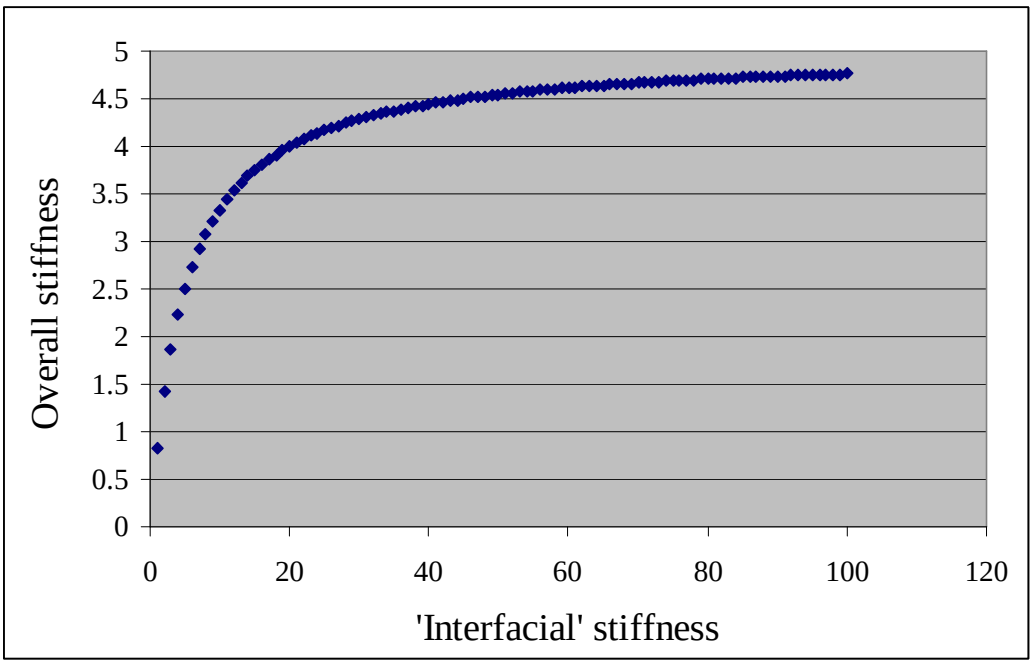

Figure 7-35. Variation in the overall stiffness of a system of three springs connected in series. The 'interfacial' (middle) spring is initially 10 times les stiff than the adjacent springs.

An illustration of this behaviour is shown in Figure 7-35, in which the overall stiffness of a system comprising three springs in series is plotted against increasing stiffness for one of the springs which is initially 10 times less stiff than the two adjacent springs.

The uniform insensitivity of the hFE predicted apparent stiffness to the element yield strain for both specimens across the whole range of applied values of grayscale-modulus conversion factor indicate that the disparity between the specimens' sensitivity response

is not due to a difference in the yield characteristics between the specimens at low applied displacements. The trends seen with respect to the hFE predicted specimen strain distribution shown in Figures 7-27 to 7-34 concur with the spring-based analogy that at higher values of interfacial grayscale-modulus conversion factor, the balance of relative deformation between the interfacial region and the adjacent trabecular bone is weighted towards the trabecular bone. In light of this, the cause of the trends displayed by Specimen 2 with respect to the sensitivity of the hFE predicted stiffness to the applied interfacial grayscale-modulus conversion factor are not as expected, and are likely due to other features of this specimen that are not captured by the spring analogy.

7.5.2. hFE predicted apparent yield strain and stress

The sensitivity of the hFE predicted apparent yield strain and stress for Specimens 2 and 3 as the applied interfacial grayscale-modulus conversion factor and element yield strain are varied were shown in Figures 7-12 to 7-17. While the trends displayed in the plots indicate that the sensitivity of the hFE predicted apparent yield stress and strain to the applied element yield strain varies greatly between the two specimens at a common grayscale-modulus conversion factor, examination of the plastic strain component distribution plots shown in Figures 7-19 to 7-26 suggest that the same underlying behaviour occurs in both cases. For a given applied interfacial grayscale-modulus conversion factor, at low values of interfacial element yield strain a greater proportion of failure occurs in the interfacial region than at higher values, where a greater proportion of failure tends to occur in the adjacent bone.

The applied interfacial grayscale-modulus conversion factor appears to affect the rate at which the balance of failure shifts from the trabecular bone to the interface, with low values leading to a gradual shift from the bone to the interface as the interfacial element yield strain is reduced, while higher values lead to a more abrupt step change, as can be seen by comparing Figures 7-23 and 7-24 with respect to Specimen 2, and Figures 7-25 and 7-26 with respect to Specimen 3.

The variation in the combined average of the RMS error between the hFE predicted apparent stiffness, yield strain and yield stress for both specimens was then considered

as the interfacial grayscale-modulus conversion factor and element yield strain were varied (Figure 7-18). It is clear that there is a range of combinations of values of interfacial grayscale-modulus conversion factor and element yield strain that achieve a minimum average error in predicted apparent properties across both specimens, corresponding to a product of the grayscale-modulus conversion factor and element yield strain approximately equal to 0.55. Application of this approach to modeling the interface in subsequent specimens will require a choice as to which combination of grayscale-modulus conversion factor and element yield strain to apply to the interfacial region.

7.5.3. hFE predicted strain distribution

As already touched upon as part of the previous discussion, the hFE predicted strain distribution plots shown in Figures 7-27 to 7-34 display the best agreement with the experimentally determined strain distribution at the lowest applied interfacial grayscale-modulus conversion factor and element yield strain.

The plots of the distribution of plastic strain throughout the models at the maximum applied displacement shown in Figures 7-12 to 7-26 display a similar trend, with the distribution of failed elements in the interfacial region and trabecular bone displaying the best agreement with that observed experimentally at the lowest applied interfacial grayscale-modulus conversion factor and element yield strain.

While the agreement is good at these values with respect to the relative strain in the interfacial region and adjacent trabecular bone, predicted regions of elevated local strain are spread over a larger region, with peak values approximately 50 % lower than those observed in the experimentally derived images. It is suggested that this is caused by the averaging effect of the downsampling of the original μCT images, which leads to lower variation in the local material properties throughout the model. Furthermore, adjacent elements are in tied contact with the surrounding elements in a way that individual trabeculae between intersections are not, limiting the possibility of large discreet changes in strain.

7.5.4. Comparison with the analytical model

Initially, it had been expected that the simplified analytical model would over-state the reduction in element yield strain required to achieve good agreement with respect to the balance of failure between the interfacial region and the adjacent trabecular bone. This was due to the exaggerated difference in the constraint boundary conditions between the interdigitated and ‘free’ trabecular struts. However, the hFE predicted plastic strain distribution plots suggest that the simplified analytical model under-predicts the reduction in element yield strain required to accurately reproduce the distribution of failure throughout the specimens. It is likely that this is due to the simplifying assumptions used in the analytical model. In reality it is unlikely that the majority of the trabeculae embedded into the cement will meet it perpendicular to the local plane of the interface. The resulting off-axis loads imposed upon them would lead to greater bending at a given applied load than predicted by the analytical model, and thus a greater chance of failure at a given apparent applied displacement.

The aim of the analytical model had been to demonstrate that there would be a difference in behaviour of the trabecular struts at the cement interface, rather than to assign specific values to this region. The outcomes from the models and comparison to the specimen image data under load indicate that this is the case, and there is a difference in behaviour of the interface region compared to the body of the bone.

7.6. Summary

- A simplified analytical model was developed to describe the mechanical behaviour of a single trabecular strut embedded into PMMA cement, in response to a bending moment resulting from the applied load.

- Specimen-specific hFE models were generated from μCT scans of the cement-augmented ovine vertebral trabecular bone cores studied experimentally and computationally in Chapters 4 and 5, which were then modified to incorporate an explicitly modeled interfacial region between the bone and cement.

- The models were solved for a range of interfacial grayscale-modulus conversion factors and element yield strains, chosen based on the predictions of the simplified analytical model.

- Averaged for both specimens, the best agreement between the experimentally determined and hFE predicted apparent properties was obtained with values of interfacial grayscale-modulus conversion factor and element yield strain whose product is approximately equal to 0.55.

- The best agreement between the experimentally determined and hFE predicted strain distribution throughout the specimens was obtained with values of element yield strain equal to 1.16 %, across the whole range of interfacial grayscale-modulus conversion factors studied.

- This was a greater reduction of the element yield strain determined for un-augmented ovine vertebral trabecular bone than predicted by the simplified analytical model, suggesting that the analytical model in fact under-states the increased likelihood of trabecular failure at the bone-cement interface.

8. Discussion

8.1. Overview

A review of previously published research that focused on the use of various hFE modelling approaches to predict the mechanical behaviour of specimens of trabecular bone or whole vertebral bodies containing cement augmentation, suggested that the poor accuracy with which the resulting hFE models stemmed from their inability to accurately reproduce the mechanical behaviour of the interface between the trabecular bone and the cement. This was due, at least in part, to the relative lack of information and experimental evidence as to the behaviour of the bone-cement interface as it deforms and yields under an applied displacement.

In an effort to better understand the behaviour of the trabecular bone – cement interface and develop a hFE modelling approach better able to accurately predict the behaviour of bone – cement interfacial specimens, three main objectives were set in this study, each of which were successfully met over a number of separate experimental and computational studies.

The first objective was to obtain the necessary μCT greyscale dependent elastic and plastic material property parameters required to construct hFE models of ovine vertebral trabecular bone, chosen for its relative similarity to human vertebral trabecular bone, using the existing image-based modelling approach described by Wilcox et al (2007) and Wijayathunga et al (2008). A number of cylindrical trabecular bone specimens were fabricated from ovine lumbar vertebrae were imaged using μCT and then tested to failure in compression. hFE models of each specimen were generated using the image-based method, which were then divided into build and validate sets. Following a series of sensitivity tests, the hFE models in the build set were tuned with respect to the applied μCT greyscale-modulus conversion factor and element yield strain to produce the best agreement between the hFE predicted and corresponding experimentally determined apparent specimen properties. This resulted in an appropriate μCT greyscale-modulus conversion factor and element yield strain of 45.054 and 1.79 %

respectively. Application of these values within the hFE models assigned to the validate set resulted in RMS errors between the hFE predicted and corresponding experimentally determined apparent stiffness and yield strain of 22.31 % and 12.6 % respectively, which is within the range of error reported in the literature.

The next objective was to obtain experimental evidence of the deformation and failure processes that occur at the trabecular bone – cement interface under an applied load. Previously published studies indicated that digital image correlation techniques were able to provide more useful data concerning the interfacial behaviour than techniques that were limited to examining the apparent specimen properties. However, the visible light based systems used in these previous studies were limited to measuring the strain distribution across the exterior surfaces of the specimens studied. To improve upon this, a device was developed that enabled μCT imaging of specimens as they underwent incremental compression to failure, in addition to measuring the apparent specimen properties. PMMA cement augmented ovine lumbar vertebral trabecular bone specimens were fabricated and imaged using μCT as they underwent incremental compression to failure within the device. This study also necessitated the development of a methodology for differentiating between the bone, marrow and cement regions, which was achieved by adding a radiopacifier with the momomer component of the cement before mixing. The resulting μCT images clearly showed that the majority of the failure within the trabecular structure occurred within the region immediately adjacent to the cement augmentation. The series of μCT images of the incremental deformation and failure of each specimen were then analysed using commercially available 2D digital image correlation software. The results suggested that in addition to the concentration of trabecular failure adjacent to the interface, the majority of the apparent elastic deformation also occurred within the interdigitated region between the trabecular bone and cement. This agreed with the previously published results obtained using the visible light based digital image correlation method.

The final objective was to use the novel experimental observations of the deformation and failure behaviour of the trabecular bone-cement interface to inform modifications to the existing image-based hFE modelling approach, aiming to improve the accuracy with which the resulting models were able to predict the behaviour of cement-augmented trabecular bone. A simple analytical model of the trabecular bone – cement interface

was developed that described the experimentally observed interfacial behaviour in terms of the proposed underlying interfacial mechanics. The analytical model suggested that the interdigitation of the trabecular bone and cement would induce failure in trabeculae at the interface at an applied load 20 % lower than that required to induce failure within un-augmented trabecular bone. Specimen-specific hFE models of the cement-augmented ovine vertebral trabecular bone specimens were generated using the existing image-based method from the μCT images previously made of the specimens in their undeformed state. The resulting hFE models were then modified to incorporate an explicitly modelled interfacial region between the trabecular bone and cement. The regions of trabecular bone were assigned material properties according to the μCT greyscale-modulus conversion factor and element yield strain relationships previously determined for un-augmented ovine vertebral trabecular bone. The interfacial region within the models was assigned a range of elastic and plastic material properties derived by modifying the μCT greyscale-modulus and element yield strain relationships previously determined for un-augmented ovine vertebral trabecular bone according to the trends displayed by the analytical model predictions and experimental observations. The results suggested that there was a range of different combinations of μCT greyscale-modulus conversion factor and element yield strain that similarly minimised the RMS error between the hFE predicted and experimentally determined apparent specimen properties. However, different combinations led to marked variation in the level of agreement between the hFE predicted and experimentally observed specimen strain distributions.

8.2. Comparison of outcomes from Chapters 5, 6 and 7

Comparisons of the variation in RMS percentage error between the hFE predicted and experimentally determined apparent properties for Specimens 2 and 3 as the combination of μCT grayscale-modulus conversion factor and element yield strain assigned to the interfacial region within the models was varied are shown in Tables 8-1 and 8-2. In Table 8-1, errors that are lower than those produced using the models within which the interfacial region was assigned standard bone properties are highlighted. This is a comparison between the experimental properties determined in Chapter 5 and the hFE properties predicted in Chapter 7. In table 8-2, combinations of the parameters that led to the best agreement between the hFE predicted and experimentally determined strain distributions are highlighted. This is a comparison between the experimental specimen strain distributions determined in Chapter 6 using digital image correlation and the hFE predicted strain distributions determined in Chapter 7.

			Element yield strain (%)			
		RMS % error hFE-Exp for	1.16	1.43	1.79	2.15
GS->E	27.03	Stiffness	**15.88**	**15.91**	**15.91**	**15.91**
		Yield strain	31.33	25.90	19.43	15.09
		Yield stress	25.69	19.51	13.85	**13.02**
	36.04	Stiffness	**20.17**	**20.17**	**20.17**	**20.17**
		Yield strain	27.97	19.18	**14.41**	**13.92**
		Yield stress	18.41	**9.58**	**10.77**	14.13
	45.054	Stiffness	23.37	23.37	**23.37**	23.37
		Yield strain	18.80	**14.49**	**15.03**	15.28
		Yield stress	**4.27**	**6.39**	**13.09**	14.19
	54.03	Stiffness	26.06	26.06	26.06	26.06
		Yield strain	17.24	**14.02**	**12.89**	15.41
		Yield stress	13.41	**8.94**	**10.34**	**12.24**

Table 8-1. Comparison of the variation in RMS error between the hFE predicted and experimentally determined apparent specimen properties for both specimens as the μCT grayscale-modulus conversion factor (GS->E) and element yield strain assigned to the interfacial region were varied. The combinations of μCT grayscale-modulus conversion factor and element yield strain that resulted in lower RMS percentage errors than when the interfacial region was assigned values derived for un-augmented ovine vertebral trabecular bone (i.e. effectively no interface) are highlighted for apparent stiffness (pink), yield strain (green) and yield stress (blue) respectively. The combination of parameters that were the same as those used in the bone are highlighted in purple.

			Element yield strain (%)			
		RMS % error hFE-Exp for	1.16	1.43	1.79	2.15
GS->E	27.03	Stiffness	**15.88**	**15.91**	15.91	15.91
		Yield strain	**31.33**	**25.90**	19.43	15.09
		Yield stress	**25.69**	**19.51**	13.85	13.02
	36.04	Stiffness	**20.17**	20.17	20.17	20.17
		Yield strain	**27.97**	19.18	14.41	13.92
		Yield stress	**18.41**	9.58	10.77	14.13
	45.054	Stiffness	23.37	23.37	**23.37**	23.37
		Yield strain	18.80	14.49	**15.03**	15.28
		Yield stress	4.27	6.39	**13.09**	14.19
	54.03	Stiffness	26.06	26.06	26.06	26.06
		Yield strain	17.24	14.02	12.89	15.41
		Yield stress	13.41	8.94	10.34	12.24

Table 8-2. Comparison of the variation in RMS error between the hFE predicted and experimentally determined apparent specimen properties for both specimens as the µCT grayscale-modulus conversion factor (GS->E) and element yield strain assigned to the interfacial region were varied. The combination of µCT grayscale-modulus conversion factor and element yield strain that resulted in the best qualitative agreement between the hFE predicted and experimentally determined strain distribution are highlighted in orange. As in Table 7-1, the combination of parameters that were the same as those used in the bone are highlighted in purple.

It is clear from the comparisons presented in Tables 8-1 and 8-2 that there is no single combination of µCT grayscale-modulus conversion factor and element yield strain that simultaneously minimizes the individual errors between the three hFE predicted and experimentally determined apparent specimen properties. Furthermore, the combinations of µCT grayscale-modulus conversion factor and element yield strain that result in the best agreement between the hFE predicted and experimentally determined specimen strain distribution coincide only with combinations that resulted in reduced RMS error with respect to the apparent specimen stiffness.

		Element yield strain (%)			
		1.16	**1.43**	**1.79**	**2.15**
GS->E	**27.03**	24.30	20.44	**16.40**	**14.67**
	36.04	22.18	**16.31**	**15.12**	**16.07**
	45.054	**15.48**	**14.75**	**17.16**	17.61
	54.03	18.91	**16.34**	**16.43**	17.90

Table 8-3. Comparison of variation in the combined mean RMS error for apparent stiffness, yield strain and yield stress, for both specimens, as the µCT grayscale-modulus conversion factor (GS->E) and element yield strain assigned to the interfacial region were varied. The combination of µCT grayscale-modulus conversion factor and element yield strain that resulted in a combined mean RMS percentage error lower than when the interfacial region was assigned those derived for un-augmented ovine vertebral trabecular bone, and those derived for un-augmented ovine lumbar vertebral trabecular bone are highlighted in olive and purple respectively.

As shown in Table 8-3, this implies that when this explicit interface modeling approach is to be used to predict the apparent properties of cement-augmented trabecular bone, there is a choice to be made with respect to the combination of µCT grayscale-modulus conversion factor and element yield strain with which the elastic and plastic material properties of the interfacial region will be determined. It is suggested that a combination of µCT grayscale-modulus conversion factor and element yield strain that results in the best agreement between the hFE predicted and experimentally determined specimen strain distribution is used (highlighted in orange in Table 8-2), even though this results in a higher combined mean RMS percentage error between the hFE predicted and experimentally determined apparent properties than that resulting from the use of the parameters derived for un-augmented ovine vertebral trabecular bone. Considering the accuracy with which the hFE models of un-augmented ovine trabecular bone studied in Chapter 4 were able to predict the apparent stiffness and yield strain properties of the corresponding experimental specimens (RMS percentage error equal to 22.3 % and 12.6 % for stiffness and yield strain respectively), it is possible that a large component of the errors discussed here is in fact due to the inaccuracy in the modeling of the adjacent trabecular bone, rather than the representation of the interfacial region.

It is suggested that good agreement between the hFE predicted and experimentally determined specimen strain distribution should be considered as the primary indicator that the models under examination are exhibiting genuinely predictive behaviour. Until now, there has been little experimental data available regarding the in-situ structural

behaviour of bone – cement interface specimens as they undergo deformation and failure. With the exception of a small number of recent studies that make use of visible light based digital image correlation methods, comparisons between finite element model predictions and corresponding experimental specimen behaviour were typically limited to the apparent properties, usually stiffness and strength. Reasonable agreement between the finite element model predictions and the experimentally determined apparent specimen properties is not a reliable indicator that the deformation and failure processes within the experimental specimens are reproduced within the finite element models, as shown in the results of this study. This is particularly true if the range of applied boundary conditions, specimen geometries and specimen material property distributions over which the finite element models and corresponding experimental specimens are compared is narrow. Consider the analogy of a specimen represented by a cubic finite element model assigned homogenous elastic and plastic material properties throughout. Even if the models material properties can be tuned so as to produce reasonable agreement with a range of experimentally determined apparent properties under a narrow range of applied finite element and experimental boundary conditions, it cannot be argued with confidence that the models accurately reproduce the specimens structural mechanics. In this case, it is likely that the finite element models material properties would require re-tuning if the applied boundary conditions or experimental specimen geometry was significantly altered.

The most important improvement in this study is the ability to make direct comparisons between the hFE predicted and experimentally determined strain distribution. Evidence that the hFE models produce reasonable agreement with the experimentally determined specimen strain distributions gives greater confidence that the models provide a reasonable approximation of the interaction between the constituent parts of the specimens. This in turn gives greater confidence that the modeling approach is not just an ad-hoc adjustment, and is likely to continue to provide reasonable agreement with corresponding experimental results under different applied boundary conditions or when used to model specimens with varied geometry or material property distributions.

8.3. Conclusions

- There is evidence that current hFE approaches used to predict the apparent mechanical properties of cement-augmented vertebrae, such as those treated using vertebroplasty, is inadequate. Analyses of the existing literature suggests that the shortcomings of the approach are most likely due to a lack of understanding of the deformation and failure processes at the trabecular bone – cement interface.

- Appropriate μCT grayscale-modulus and element yield strain relationships for ovine lumbar vertebral trabecular bone were determined for a particular combination of μCT scanner and μCT scan settings by iterative tuning of image-based hFE models of ovine lumbar vertebral trabecular bone specimens against corresponding experimentally determined apparent specimen properties. Scans of a commercially available calibrated scan phantom were then used to derive a BMD – μCT grayscale relationship for the same combination of μCT scanner and μCT scan settings, which was then substituted into the existing μCT grayscale – modulus relationship to derive a μCT scanner and scan settings independent μCT density – modulus relationship.

- A new method and test device were developed that enabled interfacial ovine lumbar vertebral trabecular bone – cement specimens to be imaged using μCT as they underwent incremental deformation to failure. This involved not only the development of a novel compression and imaging device, but also the equipment and methods required to facilitate the fabrication of appropriate test specimens, including the development of a novel cement preparation technique that improved the distribution of barium sulphate radiopacifier throughout the cement augmentation.

- 2D digital image correlation of the resulting μCT images demonstrated that within interfacial ovine lumbar vertebral trabecular bone – cement specimens the majority of the elastic deformation and failure within the specimens as the

applied deformation was increased occurs within and adjacent to the bone – cement interface.

- A simplified analytical model of the behaviour of trabecular bone struts embedded into cement was developed, and used to predict the effect of interdigitation between trabecular bone and cement on the failure characteristics of the trabeculae at the interface.

- Image based hFE models of the interfacial ovine lumbar vertebral trabecular bone specimens were generated from the previously captured μCT images and modified to incorporate an explicitly modeled interfacial region. The predictions of the simplified analytical model were used to inform the variation of the elastic and plastic material properties assigned to the trabecular bone within this region. Comparison of the hFE model predictions to the experimentally determined apparent specimen properties, and specimen strain distribution obtained through digital image correlation, demonstrated that the incorporation of an explicitly modeled interfacial region, modified as per the predictions of the simplified analytical model, produced improved agreement with the structural behaviour of the specimens.

8.4. Limitations and future work

8.4.1. Limitations

A number of limitations have been identified in the experimental and computational analyses conducted throughout this work:

- Ongoing work within the School of Mechanical Engineering within the University of Leeds has thus far indicated that μCT image grayscale-modulus relationships derived by tuning hFE models against corresponding experimentally determined apparent specimen properties are strongly dependent on the mesh resolution of the models with which they are derived. For this reason, the μCT grayscale-modulus conversion factor derived in Chapters 3 and 7 are valid only for ovine lumbar vertebral trabecular bone models generated from μCT images downsampled to a resolution of 1 mm^3.

- The ovine lumbar vertebral trabecular bone and trabecular bone – cement models were only validated against experimental specimen results obtained under axial compression. The image based modeling approach developed in this study should only be considered validated under these conditions, and care should be taken when using the same approach to model experimental boundary conditions that deviate from this.

- The final μCT grayscale-modulus conversion factor and element level yield strain derived in Chapter 7 were derived using a build set of only two specimens. The study of hFE models of unaugmented ovine lumbar vertebral trabecular bone discussed in Chapter 4 demonstrated that the component of the mechanical behaviour of the specimens that is not described by the specimens downsampled μCT grayscale distribution can vary considerably between specimens. It is possible that the interfacial specimens studied in Chapter 7 are outliers in this regard, and that the interfacial μCT grayscale-modulus and element yield strain derived using these specimens may only apply to interfacial ovine lumbar

vertebral trabecular bone specimens fabricated from lumbar vertebrae harvested from a narrow range of the ovine population.

- The experimental results determined for ovine interfacial lumbar vertebral trabecular bone specimens suggested that non-negligible viscoelastic stress and strain relaxation occurred during the approximately one hour duration of each μCT scan. It is possible that this led to non-negligible changes in the strain throughout the trabecular structure during each scan, and this may have constituted a source of error in the strain distribution analyses produced using Vic2D.

- The computational strain distribution characterization using Vic2D was only performed across perpendicular axial cross sections through the interfacial ovine lumbar vertebral trabecular bone specimens. Though efforts were made to correct for out of plane trabecular deformation, it is expected that only partial correction was achieved. Furthermore, using 2D digital image correlation across a small number of specimen cross-sections greatly limited the volume within the models throughout which the in-plane hFE predicted strain distribution was validated.

8.4.2. Recommended future work

There are two main suggested directions for the future development of the interface method developed in this study:

Firstly, it is recommended that a comprehensive exploration and validation of the interface method as it applies to interfacial ovine lumbar vertebral trabecular bone specimens be conducted. The existing equipment and methods previously described could be used to:

1. More thoroughly validate the interfacial method as it applies to interfacial ovine lumbar vertebral trabecular bone specimens by examining a larger sample of interfacial specimens. This would give more confidence in the general

applicability of the resulting interfacial μCT grayscale-modulus and element yield strain relationships.

2. Explore the validity of the interfacial method under different constraint and loading boundary conditions. A similar process to that used to analyse the interfacial ovine lumbar vertebral trabecular bone – cement specimens under axial compression could be used to derive tensile and shear properties for the interfacial region. This would greatly extend the confidence with which the method could be used within more complex model geometries.
3. The experimental specimen strain distribution could be characterized in 3D. A 3D digital image correlation software package is commercially available from the authors of Vic2D. This could be sued to provide more accurate and comprehensive specimen strain distribution data, free of the errors introduced by the manual image processing required to correct for out of plane trabecular deformation and specimen tilt and shift.

Additionally, it is recommended that a study be conducted to assess the applicability of the interface method within hFE models of cement-augmented whole vertebrae. Equipment has already been developed within the School of Mechanical Engineering at the University of Leeds that allows the incremental compression and imaging using μCT of whole vertebral bodies. In conjunction with the methods discussed in this work, this equipment could be used to:

I. Derive a μCT grayscale-modulus conversion factor appropriate for the image-based modeling of whole ovine vertebral bodies. Comparison between the μCT grayscale-modulus conversion factor derived for trabecular bone only specimens with that derived for whole vertebral bodies may give some clue as to the underlying reasons for the shortcomings of the image-based hFE modeling approach.
II. Image the incremental deformation to failure of cement-augmented whole vertebrae. It is considered that the biggest improvement and most novel development in this work is the imaging using μCT of the ovine specimens as they underwent incremental deformation to failure. This provided a unique source of information that allowed the validation of the structural behaviour of the interfacial ovine lumbar vertebral trabecular bone – cement hFE models. A source

of similar evidence of the deformation and failure processes that occur within whole vertebrae under an applied load, impossible to obtain using existing methods such as visible light based digital image correlation, would be a great boon to any researcher attempting to model or better understand the apparent-level or micromechanical properties of vertebrae.

III. Explore the application of the interfacial method developed in this work to whole cement-augmented vertebral bodies. The approach described in Chapter 4 could be used to generate hFE models directly from μCT images of the cement-augmented vertebrae studied in (II) in an unloaded state. The whole vertebral hFE models could then be modified to include an explicit interfacial region, and assigned bone material properties according either to the μCT density-modulus relationship detailed in Section 4.4, or that derived in (I). A ‘build’ subset of the whole vertebral hFE models could be tuned against the μCT data obtained in (II) in the manner described in Section 4.4 to obtain μCT density-modulus and element yield strain relationships for the interfacial region. The results could then be validated and the efficacy of the explicit interface method as applied to hFE models of cement-augmented whole vertebrae determined by assigning properties to the interfacial region within the remaining whole vertebral hFE models according to the relationships derived using the ‘build’ subset, and then comparing the model predictions to the corresponding μCT data obtained in (II).

8.4.3. Application of the explicit interface method in cement-augmented whole vertebral hFE models

Further to the suggestion for future work in Section 8.4.2.(III), a preliminary investigation was conducted using models generated as part of a previously published study by Wijayathunga et al (2008). The full model generation methodology was reported elsewhere (Wijayathunga et al 2008). Briefly, the models were generated from four prophylactically-augmented vertebrae that were subsequently tested under axial compression in the laboratory. The process used to generate the original models was identical to that used to generate the specimen specific hFE models of cement-augmented ovine trabecular bone described in Chapter 7. In the previous study, Wijayathunga et al (2008) compared the predictions from the hFE models with the experimental data and found poor agreement, with the models overestimating both the specimen stiffness and yield strength. The hFE models were then modified to incorporate an explicitly modeled interfacial region. The region of cement-augmentation within the models was too large to allow the creation of the interfacial region by dilating a duplicate of the cement mask in the same manner as was used to create the interfacial region within the ovine trabecular bone – cement interfacial hFE models, as this led to the interfacial region penetrating the vertebral endplates and wall.

Instead, following the creation of a duplicate cement mask, the original cement mask was eroded by one voxel in each direction. The intersection between the duplicate cement mask and the original cement mask was deleted from the duplicate cement mask, leaving the duplicate cement mask ‘shell’ occupying the space between the original cement mask and the surrounding bone (Figure 8-1), which was then designated as the interfacial region. The interfacial region was connected to the adjacent bone and cement augmentation using a tied contact.

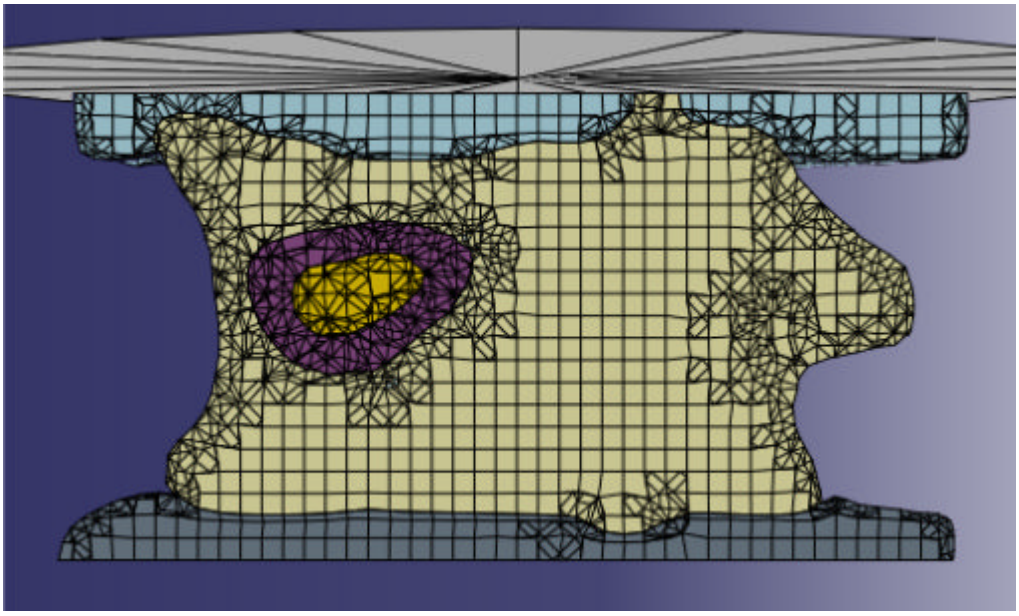

Figure 8-1. A representative example of one of the cement-augmented whole vertebral body hFE models modified to incorporate an explicitly modified interface. The original extent of the cement augmentation included the gold and purple regions. The purple region was designated as the interfacial region.

The models were configured with the same boundary conditions as in the original study, and with the exception of the interfacial region, the elastic and plastic material properties assigned throughout the models were the same as in the original study. As the underlying μCT grayscale values in the interfacial region were those of cement, an in-house developed Matlab code was used to scale down the underlying grayscale values until the mean μCT grayscale value within the interfacial region was equal to the mean μCT grayscale value for the surrounding bone in each case.

The elastic material properties were assigned to the interfacial region according to the same μCT grayscale-modulus conversion factor used in the original study, while the interfacial element yield strains were varied over a similar relative range as in the ovine trabecular bone – cement interfacial hFE models described in Chapter 7. The range of applied displacement was determined in each case in the same manner as described in Section 4.6.3. The models were solved for the chosen range of applied interfacial element yield strains, and the hFE predicted apparent stiffness and strength were determined using the same method as described in the original study.

The variation in the hFE predicted apparent stiffness and strength, as the interfacial element yield strain was varied, is shown for a representative example of one of the models (15_T12) in Figure 8-12. Plots of the maximum principal plastic strain distribution at the maximum applied deformation at the highest (original) and lowest values of interfacial element yield strain are shown in Figure 8-13.

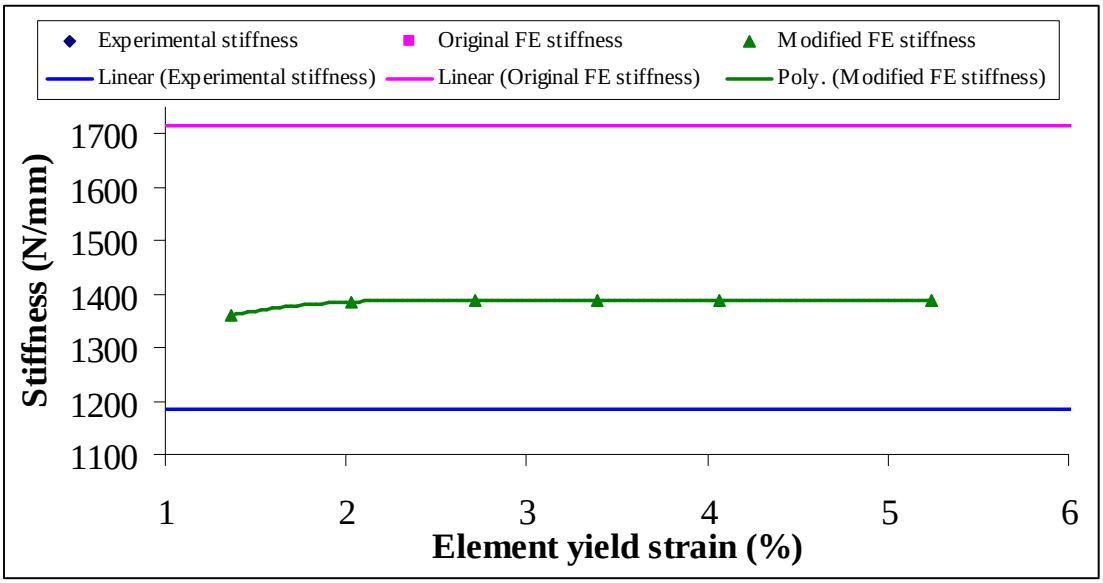

Figure 8-2. Variation in hFE predicted stiffness for a representative example of the models (15_T12) as the interfacial element yield strain was varied (green). The pink and blue horizontal lines indicate the hFE predicted apparent stiffness of the corresponding unmodified model and the corresponding experimentally determined apparent stiffness respectively.

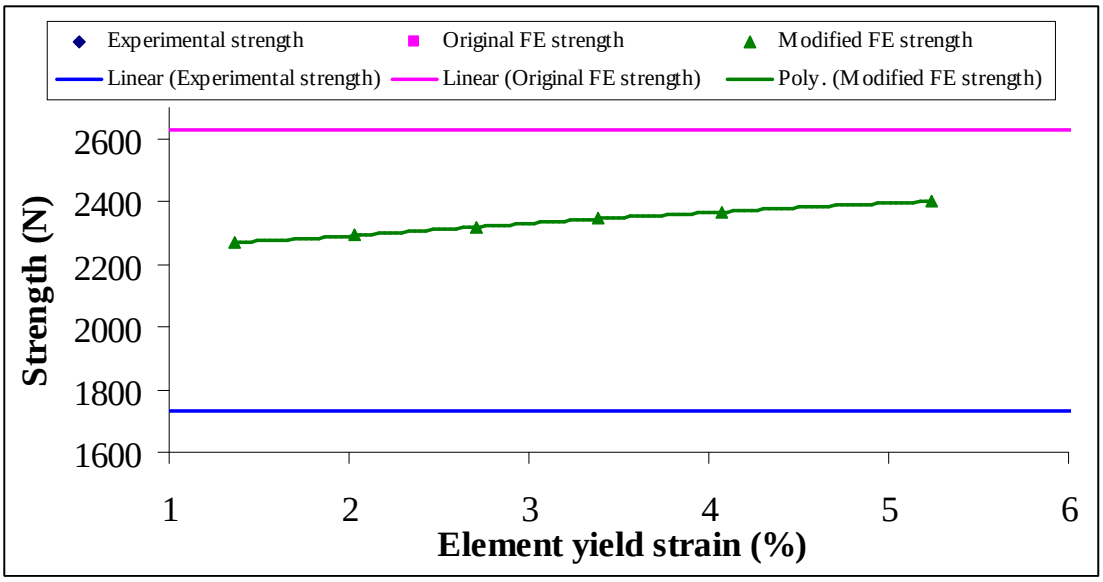

Figure 8-3. Variation in hFE predicted strength for model 15_T12 as the interfacial element yield strain was varied (green). The pink and blue horizontal lines indicate the hFE predicted apparent strength of the corresponding unmodified model and the corresponding experimentally determined apparent strength respectively.

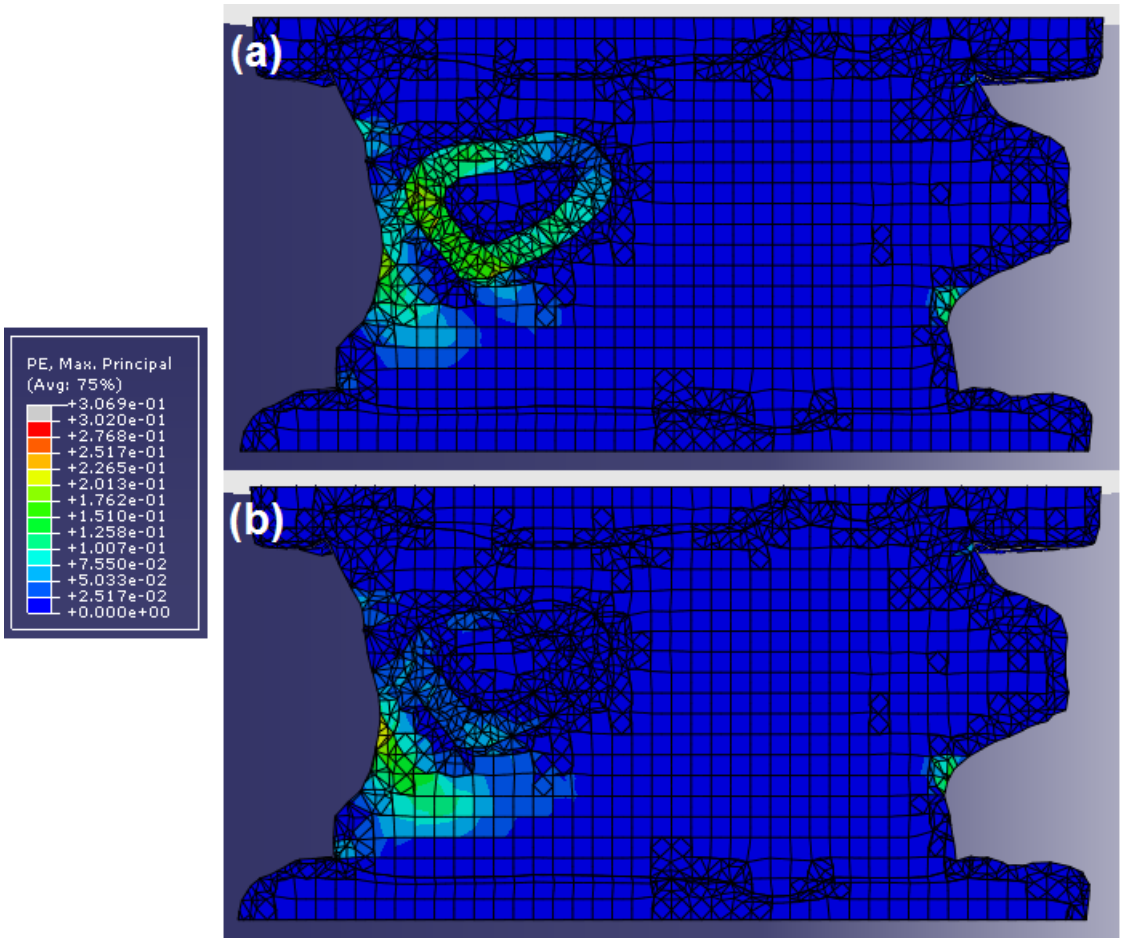

Figure 8-4. Plots of the maximum principal plastic strain distribution across model 15_T12 at an applied interfacial element yield strain equal to (a) approximately 75 % reduction compared to the original values and (b) the original values used by Wijayathunga et al (2008) throughout the rest of the vertebral bone. The colour contour scaling is the same in both images.

As can be seen in Figures 8-2 and 8-3, the incorporation of an explicitly modeled interfacial region between the trabecular bone and cement augmentation leads to a large reduction in the hFE predicted apparent stiffness and strength. It is expected that this is, for the most part, due to the marked reduction in the volume of the cement augmentation within the models. This notwithstanding, the trends displayed by the models apparent strength and stiffness predictions are similar to those displayed by the interfacial hFE models incorporating an explicitly modeled interfacial region studied in Chapter 7. This suggests that the whole vertebral body models exhibit a similar degree of sensitivity to variation of the element yield strain assigned to the interfacial region. Furthermore, the hFE predicted plastic strain distribution plots for the whole vertebral body models assigned a reduced interfacial element yield strain (an example of which is shown in Figure 8-4a) show a greater degree of similarity to the experimentally

observed failure characteristics discussed in Chapters 5 and 6 than the models in which the original element yield strain was assigned to the interfacial region.

In the absence of experimentally derived evidence of the strain and failure distribution within the original experimental specimens with which these results can be compared, it is not possible to have complete confidence that the explicit interface method improves the accuracy with which image-based hFE models of whole cement-augmented vertebrae predict the vertebral strain and failure distribution under load. The method was developed and validated using ovine trabecular bone-cement specimens that contained an effectively planar interface, perpendicular to the applied load. Within the cement-augmented whole vertebral bodies, the interface takes the form of a shell surrounding the cement region, and likely experiences a far greater degree of shear loading away from the superior and inferior interfacial regions.

A complete validation of the effect of modifying hFE models of cement-augmented whole vertebrae to include an explicitly modeled interfacial region is contingent on the experimental determination of the strain and failure distribution within and adjacent to the trabecular bone – cement interface within cement-augmented vertebrae as they undergo deformation to failure, as outlined in Section 8.4.2.(II).

References

- Aerssens, J., Boonen, S., Lowet, G., & Dequeker, J. Interspecies differences in bone composition, density, and quality: potential implications for in vivo bone research. Endocrinology, 1998, 139(2), 663-670.
- Andresen, R., Werner, HJ., Schober, HC., Contribution of the cortical shell of vertebrae to mechanical behaviour of the lumbar vertebrae with implications for predicting fracture risk, British Journal of Radiology, 1998, 71, 847, 759-765.
- Baroud, G., Nemes, J., Heini, P., Steffen, T., Load shift of the intervertebral disc after a vertebroplasty: a finite-element study, European Spine Journal, 2003, 12, 4, 421-426.
- Bayraktar, H. H., & Keaveny, T. M. Mechanisms of uniformity of yield strains for trabecular bone. Journal of Biomechanics, 2004, 37(11), 1671-1678.
- Benoit, A., Guérard, S., Gillet, B., Guillot, G., Hild, F., Mitton, D., & Roux, S. 3D analysis from micro-MRI during in situ compression on cancellous bone. Journal of Biomechanics, 2009, 42, 14, 2381-2386.
- Bevill, G., Farhamand, F., & Keaveny, T. M. Heterogeneity of yield strain in low-density versus high-density human trabecular bone. Journal of Biomechanics, 2009, 42(13), 2165-2170.
- Bilezikian, J. P., Raisz, L. G., Martin, T. J. Principles of Bone Biology, Page 31. 3rd ed. London, Academic Press, 2008.
- Boccaccio, A., Vena, P., Gastaldi, D., Franzoso, G., Pietrabissa, R., Pappalettere, C., Finite element analysis of cancellous bone failure in the vertebral body of healthy and osteoporotic subjects, Proceedings of the Institution of Mechanical Engineering Part H – Journal of Engineering in Medicine, 2008, 222, H7, 1023-1036.
- Bryant, J.D, David, T., Gaskell, P.H., King, S., Lond, G. Rheology of bovine bone marrow. Proceedings on the Institution of Mechanical Engineers Part H: Journal of Engineering in Medicine, 1989, 2003, 71-5.
- Buchbinder, R., Osborne, R. H., Ebeling, P. R., Wark, J. D., Mitchell, P., Wriedt, C., Murphy, B. A randomized trial of vertebroplasty for painful osteoporotic vertebral fractures. New England Journal of Medicine, 2009, 361,

6, 557-568.

- Buckley, JM., Leang, DC., Keaveny, TM., Sensitivity of vertebral compressive strength to endplate loading distribution, Journal of Biomedical Engineering – Transactions of the ASME, 2006, 128, 5, 641-646.
- Buckley, JM., Loo, K., Motherway, J., Comparison of quantitative computed tomography-based measures in predicting vertebral compressive strength, Bone, 2007, 40, 3, 767-774.
- Chae, SW., Lee, MK., Park, JY., Lee, TS., Park, SB., Finite element analysis and the clinical consideration for the methodology of PMMA injection in vertebroplasty, International Journal of Precision Engineering and Manufacturing, 2012, 13, 8, 1467-1472.
- Chevalier, Y., Pahr, D., Charlebois, M., Heini, P., Schneider, E., Zysset, P., Cement distribution, volume, and compliance in vertebroplasty - Some answers from an anatomy-based nonlinear finite element study, Spine, 2008, 33, 16, 1722-1730.
- Chevalier, Y., Pahr, D., Zysset, PK., The role of cortical shell and trabecular fabric in finite element analysis of the human vertebral body, Journal of Biomechanical Engineering, 2009, 131, 11, 1528-8951.
- Chevalier, Y., Zysset, PK., A patient-specific computer tomography-based finite element methodology to calculate the six dimensional stiffness matrix of human vertebral bodies, Journal of Biomechanical Engineering, 2012, 134, 5, 1528-8951.
- Christiansen, BA., Kopperdahl, DL., Kiel, DP., Keaveny, TM., Bouxsein, ML., Mechanical Contributions of the Cortical and Trabecular Compartments Contribute to Differences in Age-Related Changes in Vertebral Body Strength in Men and Women Assessed by QCT-Based Finite Element Analysis, Journal of Bone and Mineral Research, 2011, 26, 5, 974-983.
- Cintrón, R. & Saouma, V. Strain measurements with the digital image correlation system vic-2D. University of Colorado, published through the NEES hub (www.nees.org), 2008.
- Cox, B. D. Measurement of bone cement properties using self-sensing techniques. PhD thesis, 2006, University of Leeds.
- Crawford, RP., Cann, CE., Keaveny, TM., Finite element models predict in

vitro vertebral body compressive strength better than quantitative computed tomography, Bone, 2003, 33, 4, 744-750.

- Crawford, RP., Rosenberg, WS., Keaveny, TM., Quantitative computed tomography-based finite element models of the human lumbar vertebral body: Effect of element size on stiffness, damage, and fracture strength predictions, Journal of Biomedical Engineering – Transactions of the ASME, 2003, 125, 4, 434-438.
- Dall'Ara, E., Pahr, D., Varga, P., Kainberger, F., Zysset, P., QCT-based finite element models predict human vertebral strength in vitro significantly better than simulated DEXA, Osteoporosis International, 2012, 23, 2, 563-572.
- Dall'Ara, E., Schmidt, R., Pahra, D., Varga, P., Chevalier, Y., Patsch, J., Kainberger, F., Zysset, P., A nonlinear finite element model validation study based on a novel experimental technique for inducing anterior wedge-shape fractures in human vertebral bodies in vitro, Journal of Biomechanics, 2010, 43, 12, 2374-2380.
- Deligianni, D. D., Maris, A., & Missirlis, Y. F. Stress relaxation behaviour of trabecular bone specimens. Journal of Biomechanics, 1994, 27, 12, 1469-1476.
- Development of calcium phosphate cement for the augmentation of traumatically fractured porcine specimens using vertebroplasty Tarsuslugil SM, O'Hara RM,
- Desai, C. K., Basu, S., & Parameswaran, V. Determination of complex stress intensity factor for a crack in a bimaterial interface using digital image correlation. Optics and Lasers in Engineering, 2012, 50(10), 1423-1430.
- Dunne NJ, Buchanan FJ, Orr JF, Barton DC, Wilcox RK. J. Biomechanics, 46, 711-715, 2013.
- Dupont (TM). Delrin design guide - Module III, available on the Dupont website 'Knowledge centre' (http://plastics.dupont.com/plastics/pdflit/americas/delrin/230323c.pdf)
- Eswaran, SK., Gupta, A., Adams, MF., Keaveny, TM., Cortical and trabecular load sharing in the human vertebral body, Journal of Bone and Mineral Research, 2006, 21, 2, 307-314.
- Eswaran, SK., Gupta, A., Keaveny, TM., Locations of bone tissue at high risk of initial failure during compressive loading of the human vertebral body, Bone,

2007, 41, 4, 733-739.

- Evans, A. J., Jensen, M. E., Kip, K. E., DeNardo, A. J., Lawler, G. J., Negin, G. A., Dunnagan, S. A. Vertebral Compression Fractures: Pain Reduction and Improvement in Functional Mobility after Percutaneous Polymethylmethacrylate Vertebroplasty—Retrospective Report of 245 Cases1. Radiology, 2003, 226, 2, 366-372.
- F McLain, R., Yerby, S. A., & Moseley, T. A. Comparative morphometry of L4 vertebrae: comparison of large animal models for the human lumbar spine. Spine, 2002, 27(8), E200.
- Forsberg, F., Sjödahl, M., Mooser, R., Hack, E., & Wyss, P. Full Three Dimensional Strain Measurements on Wood Exposed to Three Point Bending: Analysis by Use of Digital Volume Correlation Applied to Synchrotron Radiation Micro Computed Tomography Image Data. Strain, 2010, 46, 1, 47-60.
- Fyhrie, D. P., & Schaffler, M. B. Failure mechanisms in human vertebral cancellous bone. Bone, 1994, 15, 1, 105.
- Garcia, D., Zysset, PK., Charlebois, M., Curnier, A., A three-dimensional elastic plastic damage constitutive law for bone tissue, Biomechanics and Modelling in Mechanobiology, 2009, 8, 2, 149-165.
- Garfin, S. R., Yuan, H. A. and Reiley, M. A. New technologies in spine—Kyphoplasty and vertebroplasty for the treatment of painful osteoporotic compression fractures. Spine, 2001, 26, 1511–1515.
- Guo, TF., Faleskog, J., Shih, CF., Continuum modeling of a porous solid with pressure-sensitive dilatant matrix, Journal of the Mechanics and Physics of Solids, 2008, 56, 6, 2188-2212.
- Harrigan, T. P., Jasty, M., Mann, R. W., & Harris, W. H. Limitations of the continuum assumption in cancellous bone. Journal of Biomechanics, 1988, 21, 4, 269-275.
- Harrigan, TP., Jasty, M., Mann, RW., Harris, WH., Limitations of the continuum assumption in cancellous bone. Journal of Biomechanics, 1988, 21, 4, 269-275.
- Homminga, J., Van-Rietbergen, B., Lochmüller, E. M., Weinans, H., Eckstein, F., & Huiskes, R. The osteoporotic vertebral structure is well adapted to the

loads of daily life, but not to infrequent “error” loads. Bone, 2004, 34, 3, 510-516.

- Imai, K., Ohnishi, I., Yamamoto, S., Nakamura, K., In vivo assessment of lumbar vertebral strength in elderly women using computed tomography-based nonlinear finite element model, Spine, 2008, 33, 1, 27-32.
- Janssen, D., Mann, KA., Verdonschot, N., Micro-mechanical modeling of the cement-bone interface: The effect of friction, morphology and material properties on the micromechanical response, Journal of Biomechanics, 2008, 41, 15, 3158-3163.
- Jin, H., & Bruck, H. A. Pointwise digital image correlation using genetic algorithms. Experimental Techniques, 2005, 29(1), 36-39.
- Jones, AC., Wilcox, RK., Assessment of factors influencing finite element vertebral model predictions, Journal and Biomechanical Engineering – Transactions of the ASME, 2007, 129, 6, 898-903.
- Kammers, A., & Daly, S. Experimental Investigation of Deformation Mechanisms Present in Ultrafine-Grained Metals. In MEMS and Nanotechnology, Volume 4 (pp. 105-110). 2011, Springer New York.
- Keaveny, T. M., & Hayes, W. C. A 20-year perspective on the mechanical properties of trabecular bone. Journal of Biomechanical Engineering, 1993, 115(4B), 534.
- Keaveny, T. M., Borchers, R. E., Gibson, L. J., & Hayes, W. C. Trabecular bone modulus and strength can depend on specimen geometry. Journal of Biomechanics, 1993, 26(8), 991-1000.
- Keaveny, T. M., Pinilla, T. P., Crawford, R. P., Kopperdahl, D. L., & Lou, A. Systematic and random errors in compression testing of trabecular bone. Journal of Orthopaedic Research, 2005, 15, 1, 101-110.
- Keaveny, T., Pinilla, T., Crawford, R., Kopperdahl, D., & Lou, A. Systematic and random errors in compression testing of trabecular bone. Journal of Orthopaedic Research, 1997, 15(1), 101-110.
- Kim SH, Kang HS, Choi JA, Ahn JM. Risk factors of new compression fractures in adjacent vertebrae after percutaneous vertebroplasty. Acta Radiologica, 2004, 4, 440-445.
- Kinzl, M., Boger, A., Zysset, PK., Pahr, DH., The effects of bone and pore

volume fraction on the mechanical properties of PMMA/bone biopsies extracted from augmented vertebrae, Journal of Biomechanics, 2011, 44, 15, 2732-2736.

- Kinzl, M., Boger, A., Zysset, PK., Pahr, DH., The mechanical behavior of PMMA/bone specimens extracted from augmented vertebrae: A numerical study of interface properties, PMMA shrinkage and trabecular bone damage, Journal of Biomechanics, 2012, 45, 8, 1478-1484.
- Kinzl, M., Schwiedrzik, J., Zysset, PK., Pahr, DH., An experimentally validated finite element method for augmented vertebral bodies., Clinical biomechanics (Bristol, Avon), 2013, 28, 1, 15-22.
- Kopperdahl, D. L., & Keaveny, T. M. Yield strain behavior of trabecular bone. Journal of Biomechanics, 1998, 31(7), 601-608.
- Kopperdahl, DL., Morgan, EF., Keaveny, TM., Quantitative computed tomography estimates of the mechanical properties of human vertebral trabecular bone, Journal of Orthopaedic Researech, 2002, 20, 4, 801-805.
- Kurtz, S. M., Villarraga, M. L., Zhao, K., & Edidin, A. A. Static and fatigue mechanical behavior of bone cement with elevated barium sulfate content for treatment of vertebral compression fractures. Biomaterials, 2005, 26, 17, 3699-3712.
- Lava, P., Cooreman, S., Coppieters, S., De Strycker, M., & Debruyne, D. Assessment of measuring errors in DIC using deformation fields generated by plastic FEA. Optics and Lasers in Engineering, 2009, 47(7), 747-753.
- Lewis, G., Xu, J., Rapid and reliable biomechanical screening of injectable bone cements for autonomous augmentation of osteoporotic vertebral bodies: Appropriate values of elastic constants for finite element models, Journal of Biomedica Materials Research Part B – Applied Biomaterials, 2007, 82B, 2, 408-417.
- Liebschner, MAK., Kopperdahl, DL., Rosenberg, WS., Keaveny, TM., Finite element modeling of the human thoracolumbar spine, Spine, 2003, 28, 6, 559-565.
- Liebschner, MAK., Rosenberg, WS., Keaveny, TM., Effects of bone cement volume and distribution on vertebral stiffness after vertebroplasty, Spine, 2001, 26, 14, 1547-1554.
- Lin, LI., A concordance correlation coefficient to evaluate reproducibility,

Biometrics, 1989, 45, 1, 255-268.

- Linde, F. Elastic and viscoelastic properties of trabecular bone by a compression testing approach. Danish medical bulletin, 1994, 41, 2, 119.
- Maniadakis A, Gray A. The economic burden of back pain in the UK. Pain, 2000, 84, 95-103.
- Mann, KA., Allen, MJ., Ayers, DC., Pre-yield and post-yield shear behavior of the cement-bone interface, Journal of Orthopaedic Research, 1998, 16, 3, 370-378.
- Matsumoto, T., Ohnishi, I., Bessho, M., Imai, K., Ohashi, S., Nakamura, K., Prediction of Vertebral Strength Under Loading Conditions Occurring in Activities of Daily Living Using a Computed Tomography-Based Nonlinear Finite Element Method, Spine, 2009, 34, 14, 1464-1469.
- McBroom, RJ., Hayes, WC., Edwards, WT., Goldberg, RP., White, AA., Prediction of vertebral body compressive fracture using quantitative computed-tomography. Journal of Bone and Jount Surgery – American Volume, 1985, 67A, 8, 1206-1214.
- Mirzaei, M., Zeinali, A., Razmjoo, A., Nazemi, M, On prediction of the strength levels and failure patterns of human vertebrae using quantitative computed tomography (QCT)-based finite element method, Journal of Biomechanics, 2009, 42, 11, 1584-1591.
- Mitton, D., Cendre, E., Roux, J. P., Arlot, M. E., Peix, G., Rumelhart, C., ... & Meunier, P. J. Mechanical properties of ewe vertebral cancellous bone compared with histomorphometry and high-resolution computed tomography parameters. Bone, 1998, 22(6), 651.
- Mitton, D., Rumelhart, C., Hans, D., & Meunier, P. J. The effects of density and test conditions on measured compression and shear strength of cancellous bone from the lumbar vertebrae of ewes. Medical Engineering and Physics, 1997, 19(5), 464-474.
- Mittra, E., Rubin, C., & Qin, Y. X. Interrelationship of trabecular mechanical and microstructural properties in sheep trabecular bone. Journal of Biomechanics, 2005, 38(6), 1229-1237.
- Moreo, P., Garcia-Aznar, JM., Doblare, M., A coupled viscoplastic rate-dependent damage model for the simulation of fatigue failure of cement-bone

interfaces, International Journal of Plasticity, 2007, 23, 12, 2058-2084.

- Morgan, E. F., & Keaveny, T. M. Dependence of yield strain of human trabecular bone on anatomic site. Journal of Biomechanics, 2001, 34(5), 569-577.
- Muijs, S. P. J., van Erkel, A. R., & Dijkstra, P. D. S. Treatment of painful osteoporotic vertebral compression fractures A BRIEF REVIEW OF THE EVIDENCE FOR PERCUTANEOUS VERTEBROPLASTY. Journal of Bone & Joint Surgery, British Volume, 2011, 93, 9, 1149-1153.
- Netter, F.H. Atlas of Human Anatomy. 4th ed. 2006, Saunders Elsevier, 547.
- Newman, E., Turner, A. S., & Wark, J. D. The potential of sheep for the study of osteopenia: current status and comparison with other animal models. Bone, 1995, 16(4), S277-S284.
- Pahr, DH., Zysset, PK., A comparison of enhanced continuum FE with micro FE models of human vertebral bodies, Journal of Biomechanics, 2009, 42, 4, 455-462.
- Palanivelu, S., De Pauw, S., Van Paepegem, W., Degrieck, J., Van Ackeren, J., Kakogiannis, D., ... & Vantomme, J. Validation of digital image correlation technique for impact loading applications. In Proceedings of ninth International conference on the mechanical and physical behaviour of materials under dynamic loading: Brussels, Belgium, (2009, September).
- Perez, MA., Garcia-Aznar, JM., Doblare, M., Does Increased Bone-Cement Interface Strength have Negative Consequences for Bulk Cement Integrity? A Finite Element Study, Annals of Biomedical Engineering, 2009, 37, 3, 454-466.
- Polikeit, A., Nolte, LP., Ferguson, SJ., The effect of cement augmentation on the load transfer in an osteoporotic functional spinal unit - Finite-element analysis, Spine, 2003, 28, 10, 991-996.
- Prendergast, P. J. Finite element models in tissue mechanics and orthopaedic implant design. Clinical Biomechanics, 1997, 12, 6, 343-366.
- Pugh, .JW., Rose, R.M.; Radin , E.L. Elastic and viscoelastic properties of trabecular bone – dependence on structure. Journal of Biomechanics, 1973, 6, 5, 475.
- Punmia, B.C., Jain, A. K. & Jain A.K. Mechanics of Materials, Page 14, New Dehli, Firewall Media, 2002.

- Rohlmann, A., Boustani, HN., Bergmann, G., Zander, T., A probabilistic finite element analysis of the stresses in the augmented vertebral body after vertebroplasty, European Spine Journal, 2010, 19, 9, 1585-1595.
- Ross, P. D., Ettinger, B., Davis, J. W., Melton III, L. J., Wasnich, R. D. Evaluation of adverse health outcomes associated with vertebral deformities. Osteoporos. Int., 1991, 1, 134–140.
- Sapin-de Brosses, E., Jolivet, E., Travert, C., Mitton, D., Skalli, W., Prediction of the Vertebral Strength Using a Finite Element Model Derived From Low-Dose Biplanar Imaging Benefits of Subject-Specific Material Properties, Spine, 2012, 37, 3, E156-E162.
- Scanco Medical AG, Brüttisellen, Switzerland. General FAQ: Support, available on the Scanco Medical website (http://www.scanco.ch/en/support/faq-general.html)
- Sun, K., & Liebschner, M. A. Evolution of vertebroplasty: a biomechanical perspective. Annals of biomedical engineering, 2004, 32, 1, 77-91.
- Sun, K., Liebschner, MAK., Biomechanical efficacy of prophylactic vertebroplasty with respect to initial bone mineral density, Second Joint EMBS-BMES Conference 2002, Vols 1-3, Conference Proceedings: Bioengineering – Integrative Methodologies, New Technologies, 2002, 2495-2496.
- Tarsuslugil, S. Computational modelling of spinal burst fractures for the development of calcium phosphate cement. Ph.D. thesis, 2011, University of Leeds.
- Teo, J., Wang, SC., Teoh, SH., Preliminary study on biomechanics of vertebroplasty - A computational fluid dynamics and solid mechanics combined approach, Spine, 2007, 32, 12, 1320-1328.
- Theodorou, D. J., Theodorou, S. J., Duncan, T. D., Garfin, S. R., & Wong, W. H. Percutaneous balloon kyphoplasty for the correction of spinal deformity in painful vertebral body compression fractures. Clinical imaging, 2002, 26, 1, 1-5.
- Tiwari, V., Sutton, M. A., & McNeill, S. R. Assessment of high speed imaging systems for 2D and 3D deformation measurements: methodology development and validation. Experimental mechanics, 2007, 47(4), 561-579.
- Tozzi, G., Zhang, QH., Tong, J,. 3D real-time micromechanical compressive behaviour of bone-cement interface: Experimental and finite element studies,

Journal of Biomechanics, 2012, 45, 2, 356-363.

- Travert, C., Jolivet, E., Sapin-de Brosses, E., Mitton, D., Skalli, W., Sensitivity of patient-specific vertebral finite element model from low dose imaging to material properties and loading conditions, Medical and Biological Engineering and Computing, 2011, 49, 12, 1355-1361.
- Trout, A. T., & Kallmes, D. F. Does vertebroplasty cause incident vertebral fractures? A review of available data. American journal of neuroradiology, 2006, 27, 7, 1397-1403.
- Tschirhart, C. E., Roth, S. E., Whyne, C. M. Biomechanical assessment of stability in the metastatic spine following percutaneous vertebroplasty: effects of cement distribution patterns and volume. Journal of biomechanics, 2005, 38, 8, 1582-1590.
- Ulrich, D., Van Rietbergen, B., Laib, A., Ruegsegger, P., The ability of three-dimensional structural indices to reflect mechanical aspects of trabecular bone, Bone, 1999, 25, 1, 55-60.
- Uppin AA, Hirsch JA, Centenera LV et al. Occurrences of new vertebral body fracture after percutaneous vertebroplasty in patients with osteoporosis. Radiology, 2003, 226, 119-124.
- Van Tulder M. Chapter 1: Introduction. European Spine Journal, 2006, 15, s2, S134-S135.
- Vic2D testing guide, Version 2009, Correlated Solutions .inc.
- Villarraga, ML., Bellezza, AJ., Harrigan, TP., Cripton, PA., Kurtz, SM., Edidin, AA., The biomechanical effects of kyphoplasty on treated and adjacent nontreated vertebral bodies, Journal of Spinal Disorders and Techniques, 2005, 18, 1, 84-91.
- Vossou, CG., Provatidis, CG., Investigating mesh parameters to achieve clinically applicable finite element analysis of vertebrae, 8TH IEEE International Conference on Bioinformatics and Bioengineering, Vols 1 and , 2008, 1124-1129.
- Waanders, D., Janssen, D., Bertoldi, K., Mann, KA., Verdonschot, N., Mixed-mode loading of the cement-bone interface: a finite element study, Computer Methods in Biomechanics and Biomedical Engineering, 2011, 14, 2, 145-155.
- Waanders, D., Janssen, D., Miller, MA., Mann, KA., Verdonschot, N., Fatigue

creep damage at the cement-bone interface: An experimental and a micro-mechanical finite element study, Journal of Biomechanics, 2009, 42, 15, 2513-2519.

- Wang, C. C., Deng, J. M., Ateshian, G. A., & Hung, C. T. An automated approach for direct measurement of two-dimensional strain distributions within articular cartilage under unconfined compression. TRANSACTIONS-AMERICAN SOCIETY OF MECHANICAL ENGINEERS JOURNAL OF BIOMECHANICAL ENGINEERING, 2002, 124(5), 557-567.
- Wang, X., Sanyal, A., Cawthon, PM., Palermo, L., Jekir, M., Christensen, J., Ensrud, KE., Cummings, SR., Orwoll, E., Black, DM., Keaveny, TM., Prediction of New Clinical Vertebral Fractures in Elderly Men Using Finite Element Analysis of CT Scans, Journal of Bone and Mineral Research, 2012, 27, 4, 808-816.
- Wang, Y., Liu, G., Li, T., Xiao, Y., Han, Q., Xu, R., & Li, Y. Morphometric Comparison of the Lumbar Cancellous Bone of Sheep, Deer, and Humans. Comparative Medicine, 2010, 60(5), 374.
- Watts NB, Harris ST, Genant HK. Treatment of painful osteoporotic vertebral fractures with percutaneous vertebroplasty or kyphoplasty. Osteoporosis, 2001, 12, 429–437.
- Whitehouse WJ, The quantitative morphology of anisotropic trabecular bone. J Microsc, 1974, 101:153–168
- Whyne, CM., Hu, SS., Lotz, JC., Parametric finite element analysis of vertebral bodies affected by tumors, Journal of Biomechanics, 2001, 34, 10, 1317-1324.
- Wijayathunga, VN., Jones, AC., Oakland, RJ., Furtado, NR., Hall, RM., Wilcox, RK., Development of specimen-specific finite element models of human vertebrae for the analysis of vertebroplasty, Proceedings of the Institution of Mechanical Engineers Part H – Journal of Engineering in Medicine, 2008, 222, H2, 221-228.
- Wilcox, R. K. The biomechanics of vertebroplasty: a review. Proceedings of the Institution of Mechanical Engineers, Part H: Journal of Engineering in Medicine, 2004, 218, 1, 1-10.
- Wilcox, RK., The influence of material property and morphological parameters on specimen-specific finite element models of porcine vertebral bodies, Journal

of Biomechanics, 2007, 40, 3, 669-673.

- Yeni, Y. N., Hou, F. J., Vashishth, D., & Fyhrie, D. P. Trabecular shear stress in human vertebral cancellous bone: intra-and inter-individual variations. Journal of biomechanics, 2001, 34, 10, 1341.
- Zarrinkalam, M. R., Beard, H., Schultz, C. G., & Moore, R. J. Validation of the sheep as a large animal model for the study of vertebral osteoporosis. European Spine Journal, 2008, 18(2), 244-253.
- Zeinali, A., Hashemi, B., Akhlaghpoor, S., Noninvasive prediction of vertebral body compressive strength using nonlinear finite element method and an image based technique, Physica Medica, 2010, 26, 2, 88-97.
- Zhang, LC., Yang, GJ., Wu, LJ., Yu, BF., The biomechanical effects of osteoporosis vertebral augmentation with cancellous bone granules or bone cement on treated and adjacent non-treated vertebral bodies: A finite element evaluation, Clinical Biomechanics, 2010, 25, 2, 166-172.
- Zhao, Y. Finite element modelling of cement augmentation and fixation for orthopaedic applications. Ph.D. Thesis, 2010, University of Leeds.
- Zhao, Y., Brown, KAR., Jin, ZM., Wilcox, RK., Trabecular Level Analysis of Bone Cement Augmentation: A Comparative Experimental and Finite Element Study, Annals of Biomedical Engineering, 2012, 40, 10, 2168-2176.
- Zysset, PK., A review of morphology-elasticity relationships in human trabecular bone: theories and experiments, Journal of Biomechanics, 2003, 36, 10, 1469-1485.